

---

# Neutron, X-ray, and Optical Studies of Multiferroic Materials

---



Alexander J. Hearmon  
Corpus Christi College  
University of Oxford

A thesis submitted for the degree of  
*Doctor of Philosophy*  
Trinity Term 2013









# Neutron, X-ray, and Optical Studies of Multiferroic Materials

Alexander J. Hearmon

Corpus Christi College, University of Oxford

A thesis submitted for the degree of *Doctor of Philosophy*, Trinity Term 2013

---

Developing a greater understanding of multiferroic materials, particularly those in which a strong coupling is exhibited between magnetic and electrical orderings, is of great importance if potential applications are to be realised. This thesis reports new experimental findings on several multiferroics using the techniques of X-ray and neutron diffraction together with nonlinear optical experiments.

Spherical neutron polarimetry measurements on  $\text{RbFe}(\text{MoO}_4)_2$  show how this system's chiral magnetic structure can be controlled by an external electric field. Consideration is given to the axial distortion that the crystal structure makes, and the effect that this has on the stabilised magnetic structures. A ferroaxial coupling is invoked to explain, from a symmetry point of view, the spin driven multiferroicity in this proper screw system.

The charge ordering in  $\text{YbFe}_2\text{O}_4$  is examined by a detailed imaging of reciprocal space measured by elastic X-ray diffraction. Continuous helices of scattering are observed above the three-dimensional ordering transition temperature, whereas the intensity is concentrated onto separated maxima below this. The low temperature data are modelled using a simple oxygen displacement pattern, generalised to an incommensurate structure. The observed incommensurability implies that  $\text{YbFe}_2\text{O}_4$  cannot be truly ferroelectric.

The low field magnetic structures of a Y-type hexaferrite  $\text{Ba}_{0.5}\text{Sr}_{1.5}\text{Zn}_2\text{Fe}_{12}\text{O}_{22}$  are observed in a resonant soft X-ray diffraction study. In zero field the system is helimagnetic, and with small applied fields peaks corresponding to a new phase appear. Energy calculations are used to suggest a suitable magnetic structure for the new phase and to show how this relates to the known commensurate phases that are present in low fields.

Finally, an experimental setup designed to measure second harmonic generation from non-centrosymmetric crystals is presented, along with static measurements on the multiferroic system  $\text{MnWO}_4$ . An optical pump / second harmonic probe study is then undertaken, with the result that a pump induced enhancement in the efficiency of the second harmonic generation is observed.



---

## Acknowledgements

---

I have been fortunate in having the opportunity to work with some fantastic people during my DPhil, and I would like to thank them for making my time as a research student so enjoyable. Firstly I am indebted to my supervisor, Paolo Radaelli, for sharing with me his insight into condensed matter physics, as well as his continual good humour, optimism (particularly during the late nights at Diamond) and encouragement. It has also been a pleasure to work with the other members of the group and people further afield in Oxford Physics: in particular Roger Johnson, Federica Fabrizi, Ben Williams, Natasha Perks, Benjamin Mahler, Sungkyun Choi, Lucian Pascut, James Lloyd-Hughes, Paul Goddard, Radu Coldea and John Chalker; I thank them for all the numerous discussions that have contributed so much to my knowledge of the subject, and the time they have given in answering my questions.

Thanks are due to Andrea Cavalleri and his group (past and present) in Oxford, especially Nicky Dean, Vikaran Khanna, and Ekaterina Moehr for letting me share their lab in the Clarendon and patiently answering my many questions about optics.

I would like to acknowledge helpful support from David Allan, Kirsten Christensen, Matthias Gutmann, and Harriott Nowell on beamline I19; and Paul Steadman, Raymond Fan, Alexey Dobrynin, and particularly Mark Susmuth on I10. Alessandro Bombardi and Tom Beale also provided very valuable assistance during the Diamond beamtimes. I am grateful to have had the opportunity to work with Jane Brown and Laurent Chapon at the ILL, and to have collaborated with Sergey Streltsov and Kun Cao who undertook theoretical calculations on  $\text{RbFe}(\text{MoO}_4)_2$ .

None of this work would have been possible without top quality samples, and for this I sincerely thank Dharmalingam Prabhakaran who has always been extremely happy to provide these, as well as Keith Belcher and Bob Watkins for their excellent sample preparation, and Sang-Wook Cheong's group for providing the hexaferrite crystals.

I would like to thank the EPSRC and Diamond Light Source for funding my studies, and Corpus Christi College for their generosity in awarding me a senior scholarship and for providing conference funds. I have had the opportunity to meet many interesting people during my time at Corpus, many of whom are now close friends, and they shall be sorely missed.

I owe a great deal of gratitude to those who have taught me over the years: Carol Blyth, who first sparked my interest in physics while I was at Aylesbury Grammar School and whose infectious enthusiasm for the subject will always remain with me, and my undergraduate tutors Paul Ewart, Huw Davies and Fabian Essler for inspiring me to continue into research. Finally I would like to thank my parents, Martin and Deborah, for their steadfast encouragement of my studies, and my fiancée Natalie for her constant friendship, love, and support.



*for my family, with love*



---

# Contents

---

<b>1</b>	<b>Introduction</b>	<b>1</b>
1.1	‘Ferroic’ materials	3
1.1.1	Ferromagnetism	4
1.1.2	Ferroelectricity	6
1.1.3	Ferroelasticity and ferrotoroidicity	7
1.2	Multiferroics	8
1.3	Plan of the thesis	9
<b>2</b>	<b>Experimental techniques</b>	<b>11</b>
2.1	Introduction	11
2.2	The interaction of X-rays with condensed matter systems	11
2.2.1	Interaction of a collection of electrons with an electromagnetic field	12
2.2.2	Transition probabilities	13
2.2.3	Non-resonant scattering	14
2.2.4	Resonant scattering	18
2.3	X-ray instrumentation	21
2.3.1	Laboratory sources	21
2.3.2	The synchrotron source	23
2.4	The interaction of neutrons with condensed matter systems	28
2.4.1	Elastic neutron diffraction from nuclei	29
2.4.2	Magnetic diffraction of polarised neutrons	30
2.4.3	The neutron as a chiral probe	32
2.4.4	The S-matrix	32
2.4.5	The polarised neutron spin-flip cross sections	33
2.4.6	Spherical neutron polarimetry	35
2.5	Neutron instrumentation	37
2.5.1	Research reactors	37
2.5.2	Beamline D3	37
2.5.3	Orient Express	39
2.6	Second harmonic generation	40
2.6.1	SHG in determining point group symmetries	40
2.6.2	Laser light sources	42

<b>3</b>	<b>Multiferroicity in ferroaxial <math>\text{RbFe}(\text{MoO}_4)_2</math></b>	<b>45</b>
3.1	Introduction . . . . .	45
3.2	The structural transition in $\text{RbFe}(\text{MoO}_4)_2$ . . . . .	46
3.2.1	Axial distortions in $\text{RbFe}(\text{MoO}_4)_2$ . . . . .	46
3.2.2	Ferroaxiality . . . . .	47
3.3	Magnetic ordering . . . . .	48
3.4	Ferroelectricity . . . . .	49
3.4.1	Experimental arrangement . . . . .	50
3.4.2	Integrating the pyroelectric current measurements . . . . .	50
3.4.3	Results . . . . .	51
3.5	Energy calculations . . . . .	52
3.5.1	Definitions . . . . .	52
3.5.2	Symmetric exchange energies . . . . .	54
3.5.3	The free energy and coupling to an electric field . . . . .	58
3.6	Spherical neutron polarimetry . . . . .	60
3.6.1	Magnetic structure factor . . . . .	60
3.6.2	Diffractometer angles . . . . .	64
3.6.3	Calculation of the neutron intensities and polarimetry components . . . . .	65
3.6.4	The polarimetry components . . . . .	66
3.7	Results . . . . .	67
3.7.1	Temperature dependence of the magnetic peaks . . . . .	68
3.7.2	Field cooling data . . . . .	68
3.7.3	Zero field cooling data . . . . .	72
3.7.4	Hysteresis measurements . . . . .	74
3.8	Conclusion . . . . .	74
<b>4</b>	<b>Charge ordering in <math>\text{YbFe}_2\text{O}_4</math></b>	<b>77</b>
4.1	Introduction . . . . .	77
4.1.1	Crystal structure and geometrical frustration . . . . .	78
4.1.2	Charge ordering . . . . .	79
4.1.3	Magnetic ordering . . . . .	82
4.1.4	The use of X-ray diffraction in examining charge ordering . . . . .	82
4.2	Diffraction from periodic atomic displacements . . . . .	83
4.2.1	Equivalence of the supercell and propagation vector descriptions . . . . .	85
4.3	X-ray diffraction data . . . . .	87
4.3.1	Laboratory measurements . . . . .	87
4.3.2	Synchrotron radiation measurements . . . . .	88
4.3.3	Discussion . . . . .	93
4.4	The low temperature structure and oxygen displacement model . . . . .	94
4.4.1	Oxygen displacements in the commensurate picture . . . . .	95
4.4.2	Propagation vectors for the commensurate structure . . . . .	97
4.4.3	Generalisation to an incommensurate model . . . . .	98
4.4.4	Intensity calculations . . . . .	102
4.5	Conclusion . . . . .	109



<b>5</b>	<b>The low field phase diagram of <math>\text{Ba}_{0.5}\text{Sr}_{1.5}\text{Zn}_2\text{Fe}_{12}\text{O}_{22}</math> hexaferrite</b>	<b>111</b>
5.1	Introduction . . . . .	111
5.1.1	Crystal structure . . . . .	112
5.1.2	Magnetic structures . . . . .	113
5.2	Magnetisation measurements . . . . .	115
5.2.1	Experimental details . . . . .	115
5.2.2	Results . . . . .	116
5.3	Resonant X-ray scattering . . . . .	116
5.3.1	Experimental details . . . . .	117
5.3.2	Results . . . . .	121
5.4	Low field phase diagram . . . . .	125
5.5	Energy calculations for the various phases . . . . .	128
5.5.1	Helical phase (zero field) . . . . .	128
5.5.2	‘4-fan’ phase . . . . .	129
5.5.3	‘2-fan’ phase . . . . .	130
5.5.4	Ferrimagnetic phase . . . . .	131
5.5.5	Possible explanation for the $\mathbf{q} = (0, 0, 1)$ peaks: a ‘6-fan’ phase . . .	131
5.6	Model for the room temperature phase diagram . . . . .	132
5.7	Model for the phase diagram at low temperatures . . . . .	135
5.8	Intensity calculations . . . . .	136
5.9	Conclusion . . . . .	139
<b>6</b>	<b>Nonlinear optical measurements on <math>\text{MnWO}_4</math></b>	<b>141</b>
6.1	Introduction . . . . .	141
6.2	Design of the experiment . . . . .	141
6.3	Static measurements on $\text{MnWO}_4$ . . . . .	144
6.3.1	Introduction to $\text{MnWO}_4$ . . . . .	144
6.3.2	Results and discussion . . . . .	146
6.4	Pump-probe measurements on $\text{MnWO}_4$ . . . . .	147
6.4.1	The pump-probe setup . . . . .	147
6.4.2	Results . . . . .	149
6.4.3	Discussion . . . . .	151
6.5	Conclusion and further work . . . . .	152
<b>A</b>	<b>Calculation of the hexaferrite scattering intensities</b>	<b>155</b>
A.1	Fourier descriptions of the commensurate magnetic structures . . . . .	155
A.2	X-ray intensities . . . . .	157
A.2.1	6-fan structure . . . . .	158
A.2.2	4-fan structure . . . . .	159
A.2.3	2-fan structure . . . . .	160
	<b>References</b>	<b>160</b>



---

## List of Figures

---

1.1	Ferromagnetism vs. paramagnetism . . . . .	3
1.2	Inversion and time reversal operators . . . . .	4
1.3	Ferroic orderings under time reversal and spatial inversion . . . . .	5
2.1	Geometry of Bragg scattering . . . . .	18
2.2	Thomson vs. resonant scattering . . . . .	19
2.3	Photograph of the SuperNova diffractometer . . . . .	21
2.4	Conventional four circle diffractometer angles . . . . .	22
2.5	Undulator radiation . . . . .	24
2.6	The RASOR end station . . . . .	27
2.7	Neutron chirality . . . . .	33
2.8	Schematic diagram of the CRYOPAD . . . . .	38
2.9	Schematic of the SHG process at an atomic level . . . . .	41
3.1	Crystal structure of $\text{RbFe}(\text{MoO}_4)_2$ . . . . .	46
3.2	Axial vectors describing angular momentum and structural distortions . . . . .	47
3.3	Magnetic structures in $\text{RbFe}(\text{MoO}_4)_2$ . . . . .	49
3.4	Experimental arrangement for measuring pyroelectric currents . . . . .	50
3.5	Ferroelectric polarisation measurements . . . . .	52
3.6	Positive and negative staggered triangular chirality . . . . .	53
3.7	Staggered and macroscopic triangular chiralities . . . . .	54
3.8	The various exchange paths in $\text{RbFe}(\text{MoO}_4)_2$ . . . . .	55
3.9	Energies of the different magnetic configurations . . . . .	58
3.10	Geometry of the neutron scattering experiment . . . . .	63
3.11	Temperature dependence of the magnetic intensity . . . . .	67
3.12	Calculated vs. measured polarimetry components . . . . .	69
3.13	Polarimetry components measured under different field cooling conditions . . . . .	70
3.14	Magnetic structures under positive / negative field cooling . . . . .	71
3.15	Improved fits calculated with variable magnetic domain populations . . . . .	72
3.16	Comparison of calculated / measured zero field cooling components . . . . .	73
3.17	Hysteresis observed in the polarimetry components . . . . .	73
4.1	Crystal structure of $\text{YbFe}_2\text{O}_4$ . . . . .	78
4.2	Frustration on a triangular lattice . . . . .	79
4.3	Charge ordered supercells . . . . .	80
4.4	The six W-layers . . . . .	81
4.5	Periodic displacement patterns on a square lattice . . . . .	84
4.6	Intensity maps in the $a^*b^*$ plane . . . . .	88
4.7	Intensity map of the $(h, -7/3, l)$ plane . . . . .	89

4.8	Intensity profile along the $(1/3, -5/3, l)$ rod . . . . .	90
4.9	Fourier transforms of the $(1/3, -5/3, l)$ intensity oscillations . . . . .	91
4.10	Radius of a satellite helix . . . . .	91
4.11	Three-dimensional reciprocal space isointensity plots . . . . .	92
4.12	$(h, 1/3, 12)$ peaks at 150 K and 360 K . . . . .	94
4.13	Commensurate oxygen displacement patterns . . . . .	95
4.14	Displacement patterns within the FeO layers . . . . .	96
4.15	Oxygen tetrahedra in the commensurate displacement pattern . . . . .	96
4.16	Satellite helices arising from commensurate propagation vectors . . . . .	98
4.17	Representation of an incommensurate pattern . . . . .	99
4.18	Propagation vectors related by symmetry . . . . .	100
4.19	Satellite helices arising from different incommensurate propagation vectors . . . . .	101
4.20	Combination of $\mathbf{q}_1$ and $\mathbf{q}_2$ modes to give a single intensity map . . . . .	106
4.21	Background subtraction . . . . .	107
4.22	$(1/3, -2/3, l)$ satellites . . . . .	107
4.23	$(1/3, 1/3, l)$ satellites . . . . .	108
4.24	$(-7/3, 2/3, l)$ satellites . . . . .	108
5.1	Crystal structure of the Y-type hexaferrites . . . . .	113
5.2	Previously reported magnetic structures. . . . .	114
5.3	SQUID magnetisation measurements . . . . .	116
5.4	The RASOR sample mount . . . . .	118
5.5	Electromagnet characterisation . . . . .	119
5.6	$\eta$ -scan to characterise polarisation analyser leakthrough . . . . .	120
5.7	A room temperature $l$ -scan . . . . .	122
5.8	Energy scan of the magnetic satellite . . . . .	123
5.9	Room temperature $l$ -scans at various magnetic fields . . . . .	124
5.10	165 K $l$ -scans at various magnetic fields . . . . .	125
5.11	50 K $l$ -scans at various magnetic fields . . . . .	126
5.12	Low field phase diagram . . . . .	128
5.13	Intensities of the $(0, 0, 3)$ peaks . . . . .	129
5.14	Spin block arrangement in the helical phase . . . . .	130
5.15	Structure of the ‘6-fan’ phase . . . . .	131
5.16	Fits to the peak at $(0, 0, \approx 3.5)$ . . . . .	133
5.17	Energies of the room temperature phases . . . . .	134
5.18	Energies of the 165 K phases . . . . .	136
5.19	Measured and calculated intensities for two $l$ -scans . . . . .	138
6.1	Schematic arrangement of the static SHG experiment . . . . .	142
6.2	The crystal structure of $\text{MnWO}_4$ . . . . .	145
6.3	Static intensity plots . . . . .	147
6.4	Temperature dependence of $\chi_{yxx}$ and $\chi_{x'z'z'}$ components . . . . .	148
6.5	Schematic of the pump-probe experimental arrangement . . . . .	149
6.6	Pump-probe trace of $\chi_{x'z'z'}$ . . . . .	150
6.7	The effect of varying the probe intensity . . . . .	151
6.8	Pump-probe intensity maps taken at time zero . . . . .	152

---

## List of Tables

---

3.1	The four sets of allowed parameters in $\text{RbFe}(\text{MoO}_4)_2$ . . . . .	60
3.2	Coefficients for the analytical approximations to two Bessel functions . . . .	64
3.3	Connection between the chiralities, diffraction peaks, and structure factors .	67
3.4	Details of the magnetic satellites measured in field cooling experiments . . .	68
4.1	X-ray atomic form factors for Yb, Fe, and O . . . . .	105
5.1	Satellites observed for the various phases . . . . .	127
6.1	Non-zero susceptibility tensor elements . . . . .	146



# Chapter 1

---

## Introduction

---

A large portion of research in condensed matter systems is focussed on understanding how materials develop long range order in response to changes in external parameters such as temperature, pressure, or electric and magnetic fields. Scientists have at their disposal a wealth of different degrees of freedom within an extremely diverse range of materials: thus these systems may exhibit ordering in the spatial arrangement of their constituent atoms or ions, or in the arrangement of any magnetic or electric dipole moments belonging to these constituents. Ordering may also appear in the arrangement of atomic orbitals or in toroidal moments. In addition, more exotic degrees of freedom can be important, such as the order leading to correlation in the behaviour of electrons within a superconductor, or the correlation of atomic wavefunctions within a superfluid. In all cases, the orderings that appear within these materials lead to certain symmetries being broken. Understanding the symmetry of the ordered phase is vitally important as this knowledge places strong restrictions on the physical properties that a material may exhibit.

The motivation for this research is driven, in large part, by the desire to find new materials whose orderings can be exploited in technologically useful applications. There are obvious benefits, for example, in developing an understanding of superconductivity in existing systems that show this effect so that the knowledge can be applied in the search for new systems with improved properties (for example, a higher transition temperature). In a similar way, research into materials that exhibit magnetic ordering has extremely important applications in the development and improvement of future data storage devices. Going beyond this, recent years have started to see the exploitation of materials which exhibit multiple orderings, and of the interplay between these. This gives intriguing new possibilities for novel applications, since the multiple orderings may work together to improve significantly the properties of devices. An example would be the comparison between existing computer hard disk technology, which relies on the generation of magnetic fields requiring moderate currents in coils of a relatively large size to write the data in the form

of a magnetic ordering on the surface, with a device in which the data could instead be written by an electric field but still stored robustly in the system's magnetism. The latter has distinct advantages in that no large currents are required to write the data (improving energy efficiency) and that electric fields can be more easily localised than magnetic fields which would allow an increase in the storage density. However, a material in which this could work would not only require both electrical *and* magnetic orderings, but also a significant coupling between the two such that the material would respond to changes in the electrical ordering by adjusting its magnetic structure. It is candidate materials for this type of application that are the subject of this thesis: I shall therefore, in essence, be concerned with materials with multiple and coupled ordered regimes, an understanding of which may help pave the way toward future applications.

It is fortunate that the symmetry breaking that accompanies the onset of an ordered phase can be measured very sensitively by a number of well-developed experimental techniques. All of the systems studied in the present work are *crystals* (*i.e.* certain symmetries have already been broken in arranging the constituent atoms in a periodic way) and therefore diffraction techniques, which provide direct information on the periodicity of these structures via their Fourier transforms, are highly suited to their study. Furthermore, periodic superstructures that arise in addition to the crystal structure, such as orderings of any magnetic spins or electric charges that may be present, also lend themselves very well to being examined with diffraction methods. X-ray and neutron scattering are typically the techniques of choice, since both provide detailed information about the crystal structure and both probes may also interact with the arrangement of magnetic moments. However the two interactions are fundamentally different in that neutrons are sensitive to the positions of the nuclei and the unpaired spins present in the solid, whereas X-rays are scattered by the electron cloud surrounding the atoms. The energy of the X-rays can also be tuned to coincide with atomic transitions, from which further information (for example, resulting from charge or orbital ordering) can be gained in an experiment. Modern high intensity sources such as the Diamond Light Source synchrotron and the Institut Laue–Langevin research reactor, as well as continually advancing the available instrumentation with which to collect data, have contributed greatly to the power of this technique. In addition, a further method of determining the symmetry of a material exists in optical *second harmonic generation*. This is a laboratory-scale experiment that is often extremely sensitive to changes in the point group symmetry of both crystallographic and magnetic orderings, and is therefore able to complement diffraction measurements.

In the remainder of this chapter I shall discuss magnetic and electrical orderings (the two ‘ferroic’ orders relevant for the experimental work I have undertaken), and explain how



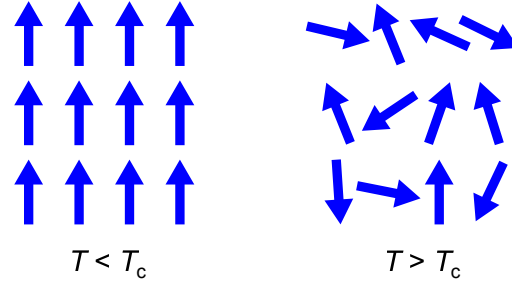


**Figure 1.1:** Schematic representation of a lattice of XY-spins, below and above the critical temperature for a ferromagnetic transition,  $T_c$ .

these come together in so-called *multiferroic* materials. I shall then give an outline plan for the remainder of the thesis.

## 1.1 ‘Ferroic’ materials

Ferroic materials exhibit phase transitions at some critical temperature  $T_c$ , below which the order parameter becomes non-zero and long range order (up to the level of domains) is present throughout the system, without the need to apply any external stimulus field. In addition, all ferroics are coupled to the external field and this field can be used to switch the long range order. In the example of the paramagnetic-ferromagnetic transition, shown schematically in figure 1.1 with a two-dimensional lattice of XY-spins, the random arrangement of spins in the paramagnetic phase is symmetry broken to the ferromagnetic phase as it is cooled through  $T_c$ . A magnetic field could then be applied across the sample to set the direction along which the spins align.

The system is said to have undergone *spontaneous symmetry breaking* because the rotational invariance present in the paramagnetic phase is no longer present in the ferromagnetic one, and a spontaneous magnetisation along the direction of the spins will result<sup>1</sup>. It is often energetically favourable for a system to form individually ordered domains rather than exhibiting the same ordering throughout the whole crystal. In the case of a ferromagnet, these domains will have magnetisations pointing in different directions in order to minimise the energy associated with the dipolar field. Ferroic systems also tend to show hysteresis effects; the behaviour of the system in response to an external field depends on the history of the system.

<sup>1</sup>This magnetisation is non-zero only below the transition temperature and this quantity may therefore be used to describe the transition as an *order parameter*, which is coupled to the external field.

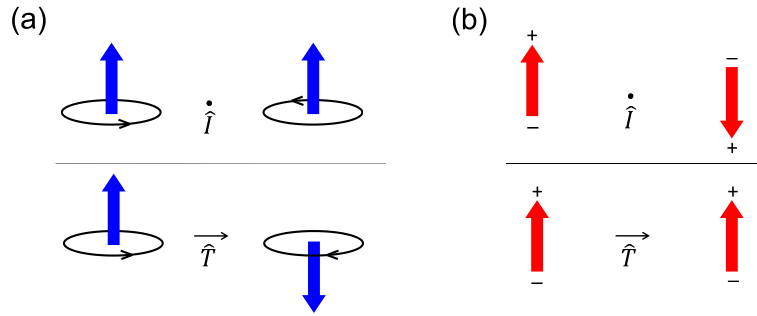


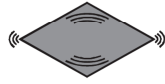
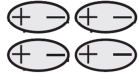
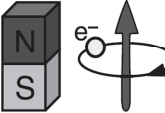
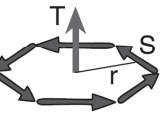
**Figure 1.2:** Transformation of (a) magnetic dipoles, and (b) electric dipoles, under the spatial inversion and time reversal operators.

Two symmetry operations are of central importance in discussing the ferroic properties of materials: the spatial inversion operator,  $\hat{I}$ , and the time reversal operator,  $\hat{T}$ . As can be seen in figure 1.2, the two operators act differently on magnetic and electric dipole moments. The direction of a magnetic moment, which arises from electronic angular momenta (represented by the circulating black arrows in the figure) and is therefore an axial vector, is unchanged by inversion but its direction is flipped by time reversal. Conversely, an electric dipole moment is invariant under time reversal (the charges are static) but changes sign upon spatial inversion: hence the electric dipole moment is a polar vector. The way in which a vector behaves under  $\hat{I}$  in fact *defines* whether that vector is axial or polar: thus, any vector which changes sign under  $\hat{I}$  is polar, and any vector whose sign remains unchanged is axial.

The four principal types of ferroic ordering (ferromagnetism, ferroelectricity, ferroelasticity, and ferrotoroidicity) can each be characterised by the operations that leave the ordering invariant, as shown in figure 1.3.

### 1.1.1 Ferromagnetism

Ferromagnetism is the oldest known ferroic ordering, and indeed it is from the behaviour of the ‘ferrous’ metal oxides showing this effect due to the iron moments that we generalise to other ‘ferroicities’ (which often have nothing to do with iron). An example of a fictitious ferromagnetic system was shown in figure 1.1 with the lattice of spins aligning along a certain direction below  $T_c$ . Often these materials also show *magnetostriction*, a phenomenon in which the physical size of a material changes slightly with the spin ordering. (Anti)ferromagnetic properties appear because of significant *exchange interactions* between nearby spins.

Time \ Space	Invariant	Change
Invariant	Ferroelastic 	Ferroelectric 
Change	Ferromagnetic 	Ferrotoroidic 

**Figure 1.3:** The properties of the four principal ferroic orderings under time reversal and spatial inversion (after [1]). © IOP Publishing. Reproduced by permission of IOP Publishing. All rights reserved.

The exchange interaction is essentially quantum mechanical in nature, arising from the fact that for identical particles the quantum mechanical wavefunction must either remain the same (*i.e.* be symmetric) or gain a minus sign (be antisymmetric) if the particles are exchanged. This is because, for identical particles, all physically observable phenomena (which depend on the modulus of the wavefunction) must remain unchanged upon particle exchange. Further, the spin statistics theorem states that identical *fermions* must behave *antisymmetrically* under exchange (this is equivalent to stating that fermions must obey the Pauli exclusion principle). Considering the simple picture of two electrons a and b at positions  $\mathbf{r}_1$  and  $\mathbf{r}_2$ , the wavefunction describing the system may, following [2], be written in one of the following two forms:

$$\psi_S = \frac{1}{\sqrt{2}} [\phi_a(\mathbf{r}_1)\phi_b(\mathbf{r}_2) + \phi_a(\mathbf{r}_2)\phi_b(\mathbf{r}_1)] \chi_S, \quad \text{or} \quad (1.1)$$

$$\psi_T = \frac{1}{\sqrt{2}} [\phi_a(\mathbf{r}_1)\phi_b(\mathbf{r}_2) - \phi_a(\mathbf{r}_2)\phi_b(\mathbf{r}_1)] \chi_T, \quad (1.2)$$

where the  $\phi$ 's are spatial wavefunctions of the individual electrons, and  $\chi_{S,T}$  are the normalised spin parts (either singlet or triplet). In general there is a difference in energy between these two states, and it is this difference that appears in the Hamiltonian,  $\mathcal{H}$ . Conventionally,  $J$  parametrises the difference in energies and is equal to the integral

$$\frac{E_S - E_T}{2} = -J_{ab} := \int d^3\mathbf{r}_1 d^3\mathbf{r}_2 \phi_a^*(\mathbf{r}_1)\phi_b^*(\mathbf{r}_2)\mathcal{H}\phi_a(\mathbf{r}_2)\phi_b(\mathbf{r}_1). \quad (1.3)$$

However, for practical purposes the quantity  $\mathbf{S}_a \cdot \mathbf{S}_b$  can be used to determine whether or not the two electrons are in a triplet or singlet state<sup>2</sup>. Therefore the energy of the two-electron

<sup>2</sup>This is because  $\mathbf{S}_1 \cdot \mathbf{S}_2 = \frac{1}{2} [(\mathbf{S}_1 + \mathbf{S}_2)^2 - \mathbf{S}_1^2 - \mathbf{S}_2^2] = \frac{1}{4}$  for a triplet state, or  $-\frac{3}{4}$  for a singlet state.

system can be written in the form

$$E = \frac{1}{4}(E_S + 3E_T) - (E_S - E_T)\mathbf{S}_a \cdot \mathbf{S}_b = E_T \text{ or } E_S. \quad (1.4)$$

This can be written as a constant plus a spin-dependent part, motivating the term in the Hamiltonian  $\mathcal{H}_{\text{exchange}} = \sum_{ij} J_{ij} \mathbf{S}_i \cdot \mathbf{S}_j$ . Note that the convention used here has  $J_{ij} > 0$  favouring an antiferromagnetic arrangement between the  $i$ th and  $j$ th spins, and  $J_{ij} < 0$  favouring a ferromagnetic one. To describe a transition from a paramagnetic to a ferromagnetic state it is necessary to consider a model in which only nearest neighbour  $J$ 's are non-zero; in more complex systems it is often necessary to take into account interactions beyond the nearest neighbours and this can give rise to a variety of interesting magnetic structures such as helimagnets.

In order for the above mechanism to work it is necessary for there to be spatial overlap between the orbitals belonging to neighbouring magnetic ions. However, it is often the case that strong exchange interactions are still present even when this overlap is missing, and this can be explained by *superexchange*, in which the exchange interaction is mediated by a non-magnetic ion (typically oxygen) that is positioned between the magnetic species. For example, the electron spin occupying a transition metal  $d$ -orbital may overlap with a neighbouring oxygen  $p$ -orbital, which in turn overlaps with the neighbouring transition metal's  $d$ -orbital. The degree of overlap depends on the metal-oxygen-metal bond angle and therefore the crystal structure strongly influences the size (and sign) of the exchange constants.

### 1.1.2 Ferroelectricity

There are various ways in which the electrical properties of certain systems may change under an external stimulus. In *piezoelectric* materials, a mechanical stress applied to the material will result in the onset of an electrical polarisation (and conversely application of a polarising electric field will lead to a strain within the crystal). *Pyroelectrics* are materials whose electrical polarisation changes with temperature. However, only in *ferroelectrics* is there the onset of a spontaneous switchable polarisation below the critical temperature: thus the direction of the electrical polarisation may be changed with an external electric field in complete analogy to the ferromagnetic case. In fact, it is far from obvious how one can define a unique electrical polarisation in a charge-neutral periodic structure at all (this is discussed in greater depth in [3]). However, a *change* in polarisation as measured, for example, when one reverses the direction of a polling field can easily be understood to be uniquely valued and is the physically relevant quantity that one obtains in experiment. Whilst ferromagnetism has been around for centuries, ferroelectric behaviour is a more

recent discovery [4] and there are various mechanisms that can give rise to the effect [5], discussed below.

In *proper ferroelectrics*, the spontaneous polarisation occurs as a direct consequence of a structural transition that results in a lower energy (and polar) state. Well-known examples of materials where this happens are  $\text{BaTiO}_3$  [6] where the energy is lowered due to covalent bonding that occurs between the oxygen and the  $3d^0$  titanium orbitals resulting in a deformation, and also  $\text{BiFeO}_3$  [7] and  $\text{BiMnO}_3$  in which the  $6s^2$  lone pairs on the Bi become ordered below  $T_c$  [8].

*Improper ferroelectrics*, by contrast, are materials in which the ferroelectric polarisation appears as a result of some other ordering. An example of this behaviour can be found in mixed valence compounds such as  $\text{RFe}_2\text{O}_4$  (the subject of chapter 4), where the different iron species ( $\text{Fe}^{2+}$  and  $\text{Fe}^{3+}$ ) that are present in equal quantities to ensure charge neutrality can order in various ways, some of which result in a net polarisation. A further example is to be found in  $\text{TbMnO}_3$ , in which it is energetically favourable for the lattice to distort below the transition temperature in response to the magnetic structure [9]. As a side effect of this transition electric dipole moments are set up between the ions. Since the crystal symmetry is such that these do not cancel out, the material develops a macroscopic electrical polarisation.

### 1.1.3 Ferroelasticity and ferrotoroidicity

*Ferroelastics* exhibit a spontaneous strain below the transition temperature. In one recent example it was predicted that  $\text{K}_{0.6}\text{Fe}_{0.6}^{\text{II}}\text{Fe}_{0.4}^{\text{III}}\text{F}_3$ , a compound forming a charge ordered ground state, ought also to show a lattice strain as a result of distortions introduced by the charge ordering and behave ferroelastically [10]. Just as an external electric field can be used to change the polarisation of a ferroelectric in such a way as to show hysteresis, so an external stress applied to a ferroelastic sample should show hysteresis in the strain.

*Ferrotoroidic* materials possess below  $T_c$  a toroidal moment,  $\mathbf{T}$ : this is a vector associated with a vortex of spins as shown in figure 1.3. Because of this, toroidal moments change sign under both time reversal (flipping the direction of the spins) and spatial inversion (changing the position of the spins)<sup>3</sup>. The associated fields that can be used to control the toroidal moments are ‘source vectors’ [11],  $\mathbf{S} = \mathbf{E} \times \mathbf{H}$ , although other vectors fields (such as a magnetic field gradient [12]) with the correct symmetry properties can also be used.

<sup>3</sup>Ferrotoroidic arrangements are therefore intrinsically magnetoelectric (see section 1.2). In a simple picture, application of an external magnetic field  $\mathbf{H}$  in the plane of the spin vortex will lead to an energy difference between spins on either side of the vortex. The system may therefore respond by becoming electrically polarised along this direction, leading to a polarisation that is orthogonal to both  $\mathbf{T}$  and  $\mathbf{H}$ .

Ferrotoroidicity will not be of further concern in the present work (but is included here for completeness); it is discussed further in [1, 13, 14].

## 1.2 Multiferroics

Having introduced the two ferroic orderings associated with magnetism and electricity, *multiferroics*<sup>4</sup> are those materials that exhibit simultaneously both of these ferroic orderings in the same phase. They may also exhibit a ‘magnetoelectric effect’, *i.e.* where an electric polarisation can be induced by an applied magnetic field, or vice versa. Research into this class of materials led to pioneering work in the 1950s-1960s (see, for example, [15, 16]) and more recently these materials have once again become the subject of intense interest in condensed matter physics [17]. In particular, the discovery in 2003 by Kimura *et al.* that a relatively small ferroelectric polarisation in  $\text{TbMnO}_3$  could be switched by a magnetic field [9] (see also [18]) sparked a great deal of interest in spin driven multiferroicity.

Multiferroics can be broadly divided into two classes based upon the nature of the magnetic and ferroelectric transitions. In *type-I* multiferroics, the transitions occur independently of one another and at separate critical temperatures. Whilst the ferroelectric polarisations in such materials tend to be quite large and the transitions tend to occur at relatively high temperatures (as is the case for  $\text{BiFeO}_3$ ), the disadvantage from the point of view of practical applications is that this means the coupling between the two orderings is weak. Therefore it is difficult to influence the behaviour of one ordering by changing the other with some external field. Conversely, in *type-II* multiferroics it is the magnetic ordering itself that breaks the inversion symmetry (a necessary condition for a ferroelectric polarisation to develop). Thus the magnetism may be thought of as ‘inducing’ the ferroelectricity, and as such there is a very strong coupling between the two that is of great interest for potential applications. However, to date only materials with relatively low polarisations have been reported (although this looks set to change as new multiferroics, such as  $\text{CaMn}_7\text{O}_{12}$  [19], continue to be the focus of research), and the temperatures at which the transitions occur are, in most cases, still rather low for practical applications.

Despite such promising technological ideas on the horizon, it is an unfortunate consequence of the physics behind multiferroicity that means that new multiferroic materials have so far proved relatively difficult to find. This is because, as explained in [5], the covalent bonding that is often the mechanism behind proper ferroelectricity requires empty electron states in the transition metal *d*-shell which the oxygen electrons can occupy. This is incompatible with magnetism on the transition metal ions as this requires the presence

---

<sup>4</sup>For the purposes of this thesis this is assumed to mean *magnetoelectric* multiferroics.

of unpaired spins within these energy levels. However, as research into novel forms of developing electrical polarisations continues, hope is growing that practical applications of this fascinating class of materials will soon be within reach. Indeed, multiferroics have recently been used to demonstrate practical devices both in thin films (see [20] and references therein, also [21,22]) and bulk crystals [23].

### 1.3 Plan of the thesis

The main focus of this work will be the three multiferroic systems  $\text{RbFe}(\text{MoO}_4)_2$ ,  $\text{YbFe}_2\text{O}_4$ , and a Y-type Ba-hexaferrite. The former is studied using polarised neutrons to examine in detail the different magnetic structures that are present, and it is shown how these can be controlled by an external electric field. This system is also used to develop ideas of ‘ferroaxiality’, a symmetry based argument that can allow a ferroelectric polarisation to appear due to a proper screw magnetic structure. The latter two systems are studied using X-ray diffraction. Detailed hard X-ray elastic scattering data collected on  $\text{YbFe}_2\text{O}_4$  are used to infer information concerning the precise nature of the charge ordering present in this system by reciprocal space imaging. Following this, a model is developed to explain the incommensurate charge ordering observed at low temperatures to which one is sensitive in the diffraction experiment because of the effect it has on the oxygen positions. A soft X-ray diffraction study carried out on the hexaferrite clarifies the complex phase diagram that has been reported at low applied magnetic fields, and evidence for a new phase is presented and a corresponding magnetic structure suggested. Finally, work on the development and testing of a new nonlinear optics experimental setup is presented, along with both static and time-resolved second harmonic generation data collected on the multiferroic  $\text{MnWO}_4$ .

In chapter 2 the key techniques of neutron and X-ray diffraction, as well as the fundamentals of nonlinear optics, are discussed. Chapters 3, 4, 5, and 6 then present a detailed introduction to each of the above materials, more experimental details relevant to each particular chapter, as well as results, models, and conclusions that can be drawn from the work.





## Chapter 2

---

### Experimental techniques

---

#### 2.1 Introduction

All of the experimental techniques employed for the work presented in this thesis share a common foundation, in that they all rely upon exploiting the precise nature of the interaction between radiation and a condensed matter system to inform us about some structural aspect of that system. The three techniques described in this section are X-ray diffraction, neutron diffraction, and the nonlinear optical process of second harmonic generation. These techniques are useful because they are sensitive to particular orderings that occur in the systems in question as a result of symmetry breaking. All of the samples studied in this thesis are crystalline, so have already broken certain translational and rotational symmetries. In addition, extra symmetry breaking may occur as superstructures (due to magnetism or ionic displacements) develop.

This chapter will set out the fundamentals of these techniques, beginning with X-rays and then neutrons. As these are both scattering techniques, the relevant quantity to calculate for these two types of radiation is the *cross section*, which is proportional to the scattered intensities and may therefore be directly compared to experimental data. Finally, second harmonic generation will be discussed as a technique from which to learn extra information about the point symmetries that may not always be readily available from diffraction techniques. As well as explaining the theoretical basis for these techniques, this chapter will also briefly discuss the various pieces of instrumentation used for the experiments.

#### 2.2 The interaction of X-rays with condensed matter systems

X-rays are very useful for the study of crystalline materials because their wavelength is of the order of typical interatomic spacings, and they therefore readily diffract from them. The exact details of this diffraction, for example its dependence on the polarisation of the X-rays

and the energy they have, can be used to learn a great deal about the system being studied. In this section the interaction between X-rays and electrons is considered, at first in general and then specialising to the case of crystals. Following this is a discussion of resonant X-ray scattering, before the instrumentation used for the X-ray scattering experiments is introduced.

### 2.2.1 Interaction of a collection of electrons with an electromagnetic field

As a starting point, consider the Hamiltonian for a system of electrons interacting with an electromagnetic field. This may be written

$$\begin{aligned} \mathcal{H} = & \sum_j \frac{1}{2m} \left[ \mathbf{p}_j - \frac{e}{c} \mathbf{A}(\mathbf{r}_j) \right]^2 + \sum_{i>j} V(|\mathbf{r}_j - \mathbf{r}_i|) - \frac{e\hbar}{2mc} \sum_j \mathbf{s}_j \cdot [\nabla \times \mathbf{A}(\mathbf{r}_j)] \\ & - \frac{e\hbar}{2m^2c^2} \sum_j \mathbf{s}_j \cdot \left\{ \mathbf{E}(\mathbf{r}_j) \times \left[ \mathbf{p}_j - \frac{e}{c} \mathbf{A}(\mathbf{r}_j) \right] \right\} + \mathcal{H}_{\text{rad}}. \end{aligned} \quad (2.1)$$

As pointed out in [24], the vector potential  $\mathbf{A}(\mathbf{r})$  describing the radiation field is linear in photon creation and annihilation operators [respectively denoted  $\hat{c}_\lambda^\dagger(\boldsymbol{\kappa})$  and  $\hat{c}_\lambda(\boldsymbol{\kappa})$ , where  $\boldsymbol{\kappa}$  is the wavevector of the photon and  $\lambda = \sigma, \pi$  describes its transverse polarisation state], and takes the form

$$\mathbf{A}(\mathbf{r}) = \sum_{\boldsymbol{\kappa}, \lambda} \sqrt{\frac{2\pi\hbar c^2}{V_0\omega_{\boldsymbol{\kappa}}}} \left[ \boldsymbol{\epsilon}_\lambda(\boldsymbol{\kappa}) \hat{c}_\lambda(\boldsymbol{\kappa}) e^{i\boldsymbol{\kappa} \cdot \mathbf{r}} + \boldsymbol{\epsilon}_\lambda^*(\boldsymbol{\kappa}) \hat{c}_\lambda^\dagger(\boldsymbol{\kappa}) e^{-i\boldsymbol{\kappa} \cdot \mathbf{r}} \right]. \quad (2.2)$$

Here,  $V_0$  is the quantisation volume,  $\omega_{\boldsymbol{\kappa}}$  is the frequency of the photon with wavevector  $\boldsymbol{\kappa}$ , and the  $\boldsymbol{\epsilon}_\lambda(\boldsymbol{\kappa})$  are the corresponding polarisation (unit) vectors. Because the radiation is polarised in a transverse direction (*i.e.* orthogonally to its direction of propagation), we have  $\boldsymbol{\kappa} \cdot \boldsymbol{\epsilon}_\lambda(\boldsymbol{\kappa}) = 0$ .

The result of this is that scattering (a process which requires a product of two photon operators: annihilation together with creation) is only described in first order perturbation theory by terms quadratic in  $\mathbf{A}$ , or in second order perturbation theory by terms linear in  $\mathbf{A}$ . We restrict ourselves to considering terms up to second order in  $(v/c)$  (*i.e.* this is a non-relativistic treatment). The first term in the Hamiltonian [equation (2.1)] is the kinetic energy for the  $n$  electrons ( $j = 1, 2, \dots, n$ ) where the canonical momentum  $\mathbf{p} - \frac{e}{c} \mathbf{A}$  is appropriate for electrons within an electromagnetic field of vector potential  $\mathbf{A}(\mathbf{r})$ . The second term represents the Coulomb interaction between pairs of electrons and is a function of their separation, and the third term is due to the interaction of the electron's spin,  $\mathbf{s}$ , with the magnetic field  $\mathbf{B} = \nabla \times \mathbf{A}$ . The fourth term describes the spin-orbit interaction between the electron's spin and the magnetic field set up due to the electron's orbital

motion in an electric field<sup>1</sup>. This term may be expanded, using  $\mathbf{E} = -\nabla\phi - \frac{\dot{\mathbf{A}}}{c}$  where  $\phi$  is the electrostatic potential (due to the electrons, as opposed to the radiation field) and  $\mathbf{A}$  is the vector potential associated with the radiation field, to give

$$\mathcal{H}_{\text{SO}} = -\frac{e\hbar}{2m^2c^2} \sum_j \mathbf{s}_j \cdot \left[ -(\nabla\phi_j \times \mathbf{p}_j) + \left( \frac{e}{c^2} \dot{\mathbf{A}}_j \times \mathbf{A}_j \right) - \left( \frac{1}{c} \dot{\mathbf{A}}_j \times \mathbf{p}_j \right) + \left( \frac{e}{c} \nabla\phi \times \mathbf{A}_j \right) \right], \quad (2.3)$$

where  $\phi_j \equiv \phi(\mathbf{r}_j)$  and  $\mathbf{A}_j \equiv \mathbf{A}(\mathbf{r}_j)$ . The final term in equation (2.1),  $\mathcal{H}_{\text{rad}}$ , describes the energy of the electromagnetic field itself.

Since the spin-orbit term is of order  $(v/c)^2$  already [24], for the present derivation I shall ignore contributions to the scattering coming from the second order perturbations from the spin-orbit term, as these will be of order  $(v/c)^4$ . Thus only first order terms will be considered, which, if we are to have scattering, requires terms in the Hamiltonian that are quadratic in  $\mathbf{A}$ . Therefore, neglecting the third and fourth terms in equation (2.3), the total Hamiltonian may be written in the following form:

$$\mathcal{H} = \mathcal{H}_0 + \mathcal{H}_1 + \mathcal{H}_{\text{rad}}, \quad (2.4)$$

where

$$\mathcal{H}_0 = \sum_j \frac{1}{2m} \mathbf{p}_j^2 + \sum_{i>j} V(|\mathbf{r}_j - \mathbf{r}_i|) + \frac{e\hbar}{2m^2c^2} \sum_j \mathbf{s}_j \cdot [\nabla\phi(\mathbf{r}_j) \times \mathbf{p}_j] \quad (2.5)$$

is the part that is unperturbed by the radiation field, and where

$$\begin{aligned} \mathcal{H}_1 = & \sum_j \frac{e^2}{2mc^2} [\mathbf{A}(\mathbf{r}_j)]^2 - \sum_j \frac{e}{2mc} [\mathbf{p}_j \cdot \mathbf{A}(\mathbf{r}_j) + \mathbf{A}(\mathbf{r}_j) \cdot \mathbf{p}_j] \\ & - \frac{e\hbar}{2mc} \sum_j \mathbf{s}_j \cdot [\nabla \times \mathbf{A}(\mathbf{r}_j)] - \frac{e\hbar}{2m^2c^2} \sum_j \mathbf{s}_j \cdot \left[ \frac{e}{c^2} \dot{\mathbf{A}}(\mathbf{r}_j) \times \mathbf{A}(\mathbf{r}_j) \right] \end{aligned} \quad (2.6)$$

is the perturbation due to the interaction between the radiation field and the electrons. Note that the first and fourth terms in this perturbation are quadratic in  $\mathbf{A}$  and therefore correspond to scattering at first order in the perturbation, whereas the second and third terms are linear in  $\mathbf{A}$ , resulting in scattering at second order in the perturbation.

### 2.2.2 Transition probabilities

If the interaction energies are sufficiently small that they may be treated as a perturbation to the unperturbed states, the Fermi Golden Rule may be used to calculate the probability per unit time of interaction (transition),  $W$ . To first order in the perturbation, this rate is simply given by

$$W^{(1)} = \frac{2\pi}{\hbar} \left| \langle f | \mathcal{H}^{(\text{per})} | i \rangle \right|^2 \delta(E_i - E_f), \quad (2.7)$$

---

<sup>1</sup>An electron moving with velocity  $\mathbf{v}$  in an electric field  $\mathbf{E}$  results in a magnetic field  $\mathbf{B} = -\frac{\mathbf{v} \times \mathbf{E}}{c^2} = \frac{\mathbf{E} \times \mathbf{p}}{mc^2}$ .

whereas to second order in the perturbation, the appropriate formula is

$$W^{(2)} = \frac{2\pi}{\hbar} \left| \sum_n \frac{\langle f | \mathcal{H}^{(\text{per})} | n \rangle \langle n | \mathcal{H}^{(\text{per})} | i \rangle}{E_i - E_n} \right|^2 \delta(E_i - E_f), \quad (2.8)$$

with  $\mathcal{H}^{(\text{per})}$  equal to the perturbing part of the Hamiltonian. These formulae give the rates for a transition between an initial state  $|i\rangle \equiv |a; \mathbf{k}, \rho\rangle$  (*i.e.* the state comprising the collection of electrons described by  $|a\rangle$  together with a single photon with wavevector  $\mathbf{k}$  and polarisation state  $\rho$ ) and final state  $|f\rangle \equiv |b; \mathbf{k}', \rho'\rangle$  (*i.e.* the collection of electrons described by  $|b\rangle$  and a single photon with wavevector  $\mathbf{k}'$  and polarisation state  $\rho'$ ). Note that  $|a\rangle$  and  $|b\rangle$  are eigenstates of the unperturbed Hamiltonian  $\mathcal{H}_0$ , with energies  $E_a$  and  $E_b$  respectively. The delta functions included in these formulae ensure that energy is conserved, with  $E_i = E_a + \hbar\omega_{\mathbf{k}}$  and  $E_f = E_b + \hbar\omega_{\mathbf{k}'}$ .

### 2.2.3 Non-resonant scattering

The scattering term arising from first order perturbation theory is given by the above formula with

$$\mathcal{H}^{(\text{per})} = \sum_j \frac{e^2}{2mc^2} [\mathbf{A}(\mathbf{r}_j)]^2 - \frac{e\hbar}{2m^2c^2} \sum_j \mathbf{s}_j \cdot \left[ \frac{e}{c^2} \dot{\mathbf{A}}(\mathbf{r}_j) \times \mathbf{A}(\mathbf{r}_j) \right]. \quad (2.9)$$

Thus the matrix element appearing in  $W^{(1)}$  is

$$\left\langle b; \mathbf{k}', \rho' \left| \sum_j \frac{e^2}{2mc^2} [\mathbf{A}(\mathbf{r}_j)]^2 \right| a; \mathbf{k}, \rho \right\rangle - \left\langle b; \mathbf{k}', \rho' \left| \frac{e\hbar}{2m^2c^2} \sum_j \mathbf{s}_j \cdot \left[ \frac{e}{c^2} \dot{\mathbf{A}}(\mathbf{r}_j) \times \mathbf{A}(\mathbf{r}_j) \right] \right| a; \mathbf{k}, \rho \right\rangle. \quad (2.10)$$

The first of these terms, as explained in the next section, gives rise to the basic Thomson scattering from a collection of electrons. The second term is more complex and results in a non-resonant contribution to the magnetic scattering from the set of magnetic moments  $\mathbf{s}_j$  [25, 26]. For the work presented in this thesis the technique of non-resonant magnetic scattering is not used and this term will not be considered further.

#### 2.2.3.1 Thomson scattering

It is assumed that the radiation incident onto and diffracted from the sample is monochromatic, and therefore may be described by the single wavevector and polarisation states  $\mathbf{k}, \rho$  and  $\mathbf{k}', \rho'$  respectively. Additionally, it is assumed that the scattering occurs only from the electron charges in the sample, and not through interaction with their magnetism. The

relevant matrix element to be evaluated is therefore

$$M = \left\langle b; \mathbf{k}', \rho' \left| \sum_j \frac{e^2}{2mc^2} \left\{ \sum_{\kappa, \lambda} \sqrt{\frac{2\pi\hbar c^2}{V_0\omega_\kappa}} \left[ \epsilon_\lambda(\kappa) \hat{c}_\lambda(\kappa) e^{i\kappa \cdot \mathbf{r}} + \epsilon_\lambda^*(\kappa) \hat{c}_\lambda^\dagger(\kappa) e^{-i\kappa \cdot \mathbf{r}} \right] \right\} \right| a; \mathbf{k}, \rho \right\rangle. \quad (2.11)$$

Since, in the Born approximation, the incident and exit photon states may be described by plane waves ( $\propto e^{-i\mathbf{k} \cdot \mathbf{r}}$  or  $\propto e^{-i\mathbf{k}' \cdot \mathbf{r}}$ ), and since we require (for a scattering process) creation of the  $\mathbf{k}', \rho'$  photon and annihilation of the  $\mathbf{k}, \rho$  photon, the summation over  $\kappa$  leaves only

$$M = \left\langle b \left| \sum_j \frac{e^2}{2mc^2} \left[ \sqrt{\frac{2\pi\hbar c^2}{V_0\omega_{\mathbf{k}}}} \epsilon_\rho(\mathbf{k}) \hat{c}_\rho(\mathbf{k}) e^{-i\mathbf{k} \cdot \mathbf{r}_j} + \sqrt{\frac{2\pi\hbar c^2}{V_0\omega_{\mathbf{k}'}}} \epsilon_{\rho'}^*(\mathbf{k}') \hat{c}_{\rho'}(\mathbf{k}') e^{i\mathbf{k}' \cdot \mathbf{r}_j} \right] \right| a \right\rangle. \quad (2.12)$$

This can be further simplified by imposing the condition that, for a scattering process, only terms containing one creation and one annihilation operator will be non-zero. Thus only the cross terms survive when squaring the above, giving

$$M = \left\langle b \left| \sum_j \frac{e^2}{mc^2} \frac{2\pi\hbar c^2}{V_0\sqrt{\omega_{\mathbf{k}}\omega_{\mathbf{k}'}}} e^{i(\mathbf{k}' - \mathbf{k}) \cdot \mathbf{r}_j} \epsilon_\rho(\mathbf{k}) \cdot \epsilon_{\rho'}^*(\mathbf{k}') \right| a \right\rangle. \quad (2.13)$$

Let us now assume that the scattering process is *elastic*, such that  $|b\rangle = |a\rangle$  (*i.e.* the state of the electrons is not changed by the interaction) and  $\omega_{\mathbf{k}} = \omega_{\mathbf{k}'} \equiv \omega$ . Then, using the shorthand  $\mathbf{Q} = \mathbf{k}' - \mathbf{k}$  for the scattering vector,

$$M = \frac{e^2}{mc^2} \frac{2\pi\hbar c^2}{V_0\omega} \left\langle a \left| \sum_j e^{i\mathbf{Q} \cdot \mathbf{r}_j} \right| a \right\rangle \epsilon \cdot \epsilon', \quad (2.14)$$

where  $\epsilon = \epsilon_\rho(\mathbf{k})$  and  $\epsilon' = \epsilon_{\rho'}^*(\mathbf{k}')$ . The transition probability for Thomson scattering is therefore

$$W^{(1)} = \frac{2\pi}{\hbar} \frac{e^4}{m^2 c^4} \frac{4\pi^2 \hbar^2 c^4}{V_0^2 \omega^2} \left| \sum_j e^{i\mathbf{Q} \cdot \mathbf{r}_j} \right|^2 |\epsilon \cdot \epsilon'|^2 \delta(E_i - E_f) \quad (2.15)$$

$$= \frac{8\pi^3 e^4 \hbar}{V_0^2 \omega^2 m^2} \left| \sum_j e^{i\mathbf{Q} \cdot \mathbf{r}_j} \right|^2 |\epsilon \cdot \epsilon'|^2 \delta(E_i - E_f). \quad (2.16)$$

From the transition probability  $W$ , the cross section is defined by multiplying by the photon density of states  $g = \frac{V_0}{8\pi^3} \frac{\omega^2}{\hbar c^3}$  and dividing by the incident flux  $I_0 = c/V_0$ , to give

$$\left( \frac{d^2\sigma}{d\Omega dE_f} \right)_{\text{Thomson}} = r_0^2 \left| \sum_j e^{i\mathbf{Q} \cdot \mathbf{r}_j} \right|^2 |\epsilon \cdot \epsilon'|^2 \delta(E_i - E_f), \quad (2.17)$$

where  $r_0 := e^2/(mc^2)$  is the Thomson scattering length.

### 2.2.3.2 Bragg scattering

The formalism introduced in the previous section can now be extended to the case where there are a number of different atoms, each associated with a distribution of electrons from which the X-rays will scatter. The position of the  $j$ th electron,  $\mathbf{r}_j$ , can be written as a sum of two terms:  $\mathbf{r}_l$ , the position vector of the associated atomic centre, and  $\mathbf{r}_m$ , the position vector of the electron relative to this. Thus we may make the replacement

$$\sum_j e^{i\mathbf{Q}\cdot\mathbf{r}_j} \longrightarrow \sum_l \sum_m e^{i\mathbf{Q}\cdot(\mathbf{r}_l+\mathbf{r}_m)}, \quad (2.18)$$

which gives the following cross section for scattering from electrons associated with a collection of atoms:

$$\left( \frac{d^2\sigma}{d\Omega dE_f} \right)_{\text{atoms}} = r_0^2 \left| \sum_l e^{i\mathbf{Q}\cdot\mathbf{r}_l} \sum_m e^{i\mathbf{Q}\cdot\mathbf{r}_m} \right|^2 |\boldsymbol{\epsilon} \cdot \boldsymbol{\epsilon}'|^2 \delta(E_i - E_f), \quad (2.19)$$

where the second summation is understood to run over all of the electrons making up the atom [often this is replaced by an integral over a continuous charge distribution function,  $\rho(\mathbf{r})$ ]. For convenience this second summation is simply written as a function of the scattering vector  $\mathbf{Q}$  (this function will be specific to the type of atom or ion in question, so the function carries a label  $l$ ). This function is known as the *form factor*,  $f_l(\mathbf{Q})$ , and its values are tabulated in [27]. Roughly speaking it is proportional to the atomic number,  $Z$ , of the atom it describes. Thus the cross section may now be written

$$\left( \frac{d^2\sigma}{d\Omega dE_f} \right)_{\text{atoms}} = r_0^2 \left| \sum_l f_l(\mathbf{Q}) e^{i\mathbf{Q}\cdot\mathbf{r}_l} \right|^2 |\boldsymbol{\epsilon} \cdot \boldsymbol{\epsilon}'|^2 \delta(E_i - E_f), \quad (2.20)$$

the summation running over all the atoms in the part of the sample exposed to the X-ray beam.

For the study of solids one is very often interested in the scattering resulting from a periodic array of atoms as found in a crystal. If this is the case then a further simplification can be made that exploits the periodicity of the structure: the atomic positions may be written  $\mathbf{r}_l = \mathbf{R}_n + \mathbf{r}_p$ . In so doing we consider the crystal structure as being generated by a basis of atoms convoluted with a set of lattice points at position vectors  $\mathbf{R}_n$ . In each unit cell, the atoms in the basis have position vectors  $\mathbf{r}_p$  relative to the lattice point belonging to that unit cell. In a similar way to before, we may split the summation over  $l$  into a pair of summations over  $n$  and  $p$  to express the cross section as:

$$\left( \frac{d^2\sigma}{d\Omega dE_f} \right)_{\text{crystal}} = r_0^2 \left| \sum_n e^{i\mathbf{Q}\cdot\mathbf{R}_n} \right|^2 \left| \sum_p f_p(\mathbf{Q}) e^{i\mathbf{Q}\cdot\mathbf{r}_p} \right|^2 |\boldsymbol{\epsilon} \cdot \boldsymbol{\epsilon}'|^2 \delta(E_i - E_f). \quad (2.21)$$

The phase factors  $e^{i\mathbf{Q}\cdot\mathbf{R}_n}$ , when summed over  $n$ , will tend to cancel out in general (this is because the  $\mathbf{R}_n$  describe points which are positioned equally apart in space). Therefore this term always goes to zero *unless*

$$\mathbf{Q} \cdot \mathbf{R}_n = 2\pi \times \text{integer}, \quad (2.22)$$

in which case all of the phases are unity and add constructively. Hence the summation may be recast as a delta function [28], giving

$$\left( \frac{d^2\sigma}{d\Omega dE_f} \right)_{\text{crystal}} = \frac{(2\pi)^3}{V_{\text{cell}}} N_{\text{cell}} \delta^{(3)}(\mathbf{Q} - \mathbf{G}) r_0^2 \left| \sum_j f_j(\mathbf{Q}) e^{i\mathbf{Q}\cdot\mathbf{r}_j} \right|^2 |\boldsymbol{\epsilon} \cdot \boldsymbol{\epsilon}'|^2 \delta(E_i - E_f), \quad (2.23)$$

where there are  $N_{\text{cell}}$  unit cells, each of volume  $V_{\text{cell}}$ , contributing to the scattering, and the sum runs over the  $j$  atoms in the basis. The vector  $\mathbf{G}$  is used to denote those values of  $\mathbf{Q}$  satisfying equation (2.22). The collection of vectors  $\mathbf{G}$  describe an array of points in Fourier space ('reciprocal space') and are therefore said to make up the 'reciprocal lattice'.

For a three-dimensional crystal whose real space lattice vectors are written as a linear combination of three basis vectors as  $\mathbf{R} = n_1\mathbf{a} + n_2\mathbf{b} + n_3\mathbf{c}$  with  $n_{1,2,3} \in \mathbb{Z}$ , the reciprocal lattice vectors can similarly be expanded in a reciprocal basis as  $\mathbf{G} = h\mathbf{a}^* + k\mathbf{b}^* + l\mathbf{c}^*$  with  $h, k, l \in \mathbb{Z}$ . The basis vectors of the reciprocal lattice can be generated from those of the direct lattice via the following relations:

$$\mathbf{a}^* = \frac{2\pi}{V_{\text{cell}}}(\mathbf{b} \times \mathbf{c}), \quad \mathbf{b}^* = \frac{2\pi}{V_{\text{cell}}}(\mathbf{c} \times \mathbf{a}), \quad \mathbf{c}^* = \frac{2\pi}{V_{\text{cell}}}(\mathbf{a} \times \mathbf{b}), \quad (2.24)$$

where  $V_{\text{cell}} = \mathbf{a} \cdot (\mathbf{b} \times \mathbf{c})$ . Equation (2.23) shows that the cross section is only non-zero when  $\mathbf{Q} = \mathbf{G}$ : thus one can measure a peak in scattered intensity if the scattering geometry is positioned for the correct  $\mathbf{Q}$ . This is known as a *Bragg peak*. For a perfect crystal the delta function in equation (2.23) would suggest infinitely sharp Bragg peaks, but deviations from a perfectly crystalline structure, together with finite correlation lengths in the beam, deviations from a perfectly monochromatic beam, or finite crystal size mean that these peaks are always broadened to some extent.

The factor  $|\boldsymbol{\epsilon} \cdot \boldsymbol{\epsilon}'|^2$  appearing in the cross section is known as the *polarisation factor*. The contribution this term makes depends on the source of X-rays used:

$$|\boldsymbol{\epsilon} \cdot \boldsymbol{\epsilon}'|^2 = \begin{cases} 1, & \text{synchrotron: } \sigma \rightarrow \sigma \text{ scattering,} \\ \cos^2(2\theta), & \text{synchrotron: } \pi \rightarrow \pi \text{ scattering,} \\ \frac{1}{2}(1 + \cos^2(2\theta)), & \text{unpolarised source,} \end{cases} \quad (2.25)$$

where  $2\theta$  is the scattering angle, and the linear polarisation directions are  $\sigma$  (perpendicular to the scattering plane), or  $\pi$  (parallel to the scattering plane). These are depicted in figure 2.1.

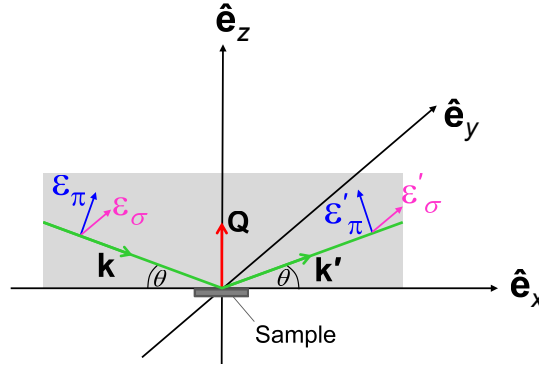


**Figure 2.1:** Geometry of Bragg scattering. The scattering plane, containing the three vectors  $\mathbf{k}$ ,  $\mathbf{k}'$ , and  $\mathbf{Q} = \mathbf{k}' - \mathbf{k}$  is shown shaded. The directions of the linear polarisation states  $\epsilon_\sigma$  and  $\epsilon_\pi$  are shown for the incident and scattered beams. A Cartesian coordinate system of basis vectors  $\hat{\mathbf{e}}_{x,y,z}$  is also shown, and the scattering angle is  $2\theta$ .

### 2.2.4 Resonant scattering

Returning to the perturbation theory described above, the second order transition rate is given in equation (2.8) as:

$$W^{(2)} = \frac{2\pi}{\hbar} \left| \sum_n \frac{\langle f | \mathcal{H}^{(\text{per})} | n \rangle \langle n | \mathcal{H}^{(\text{per})} | i \rangle}{E_i - E_n} \right|^2 \delta(E_i - E_f) \quad (2.26)$$

where the summation is over the set of all intermediate states  $|n\rangle$  which are of energy  $E_n$ , and

$$\mathcal{H}^{(\text{per})} = - \sum_j \frac{e}{mc} \mathbf{A}(\mathbf{r}_j) \cdot \mathbf{p}_j - \frac{e\hbar}{2mc} \sum_j \mathbf{s}_j \cdot [\nabla \times \mathbf{A}(\mathbf{r}_j)]. \quad (2.27)$$

The resonant process may therefore be thought of in terms of an electron absorbing an incident photon and being promoted from the ground state  $|a\rangle$  to an intermediate state  $|n\rangle$  (which, by the Pauli exclusion principle, must be unoccupied). The electron then undergoes the reverse, making a transition from  $|n\rangle$  to  $|a\rangle$  and emitting the scattered photon in the process (see figure 2.2). The dominant transition in such a process is the electric dipole (E1) transition [29], and this is all that will be considered here. For the case of iron, the corresponding atomic transitions are from the core  $2p$  states to the (empty)  $3d$  valence states. Most of the terms in the summation over intermediate states are suppressed by the denominator in the transition rate,  $E_i - E_n$ . However, if the energy of the incident beam is tuned such that this denominator tends to zero, a strong resonant enhancement of the cross section will result.

Following Hill and McMorro [30], it is possible to define a resonant magnetic form factor which is of practical use in calculating the scattered intensities and polarisations. Only a



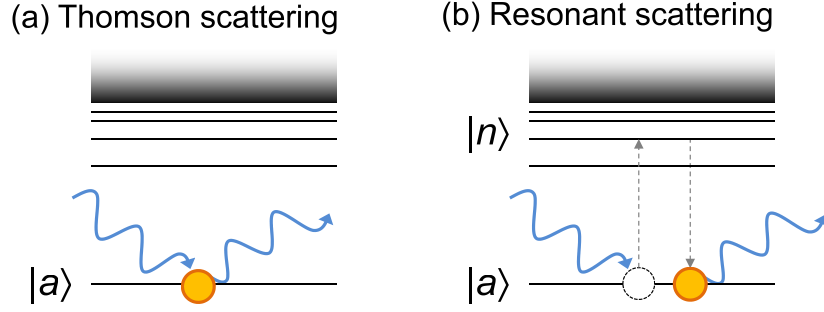


**Figure 2.2:** Thomson vs. resonant scattering (after [28]). In (a), the electron radiates the outgoing X-rays in response to the electric field felt by the incident beam, whereas in (b) the incident energy is precisely tuned to the energy between two atomic levels, allowing the electron to make a virtual transition to the higher level and radiate the outgoing X-ray photon as it returns to the ground state.

brief outline is presented here (further details can be found in [30, 31]) of some of the steps in its derivation. The resonant contribution to the scattering depends on the precise nature of the intermediate atomic states, which we expect to be affected by magnetic interactions (thus resonant scattering is really an *indirect* probe of the magnetism, since fundamentally it probes electronic states). These states are described by spherical harmonics  $Y_{LM}(\vartheta, \varphi)$  and the resonant form factor depends on these, and the beam polarisations, in the following way:

$$f_{\text{RES}} \propto \sum_{M=-1,0,1} \left[ \epsilon' \cdot \mathbf{Y}_{1M}(\hat{\mathbf{k}}') \epsilon \cdot \mathbf{Y}_{1M}(\hat{\mathbf{k}}) \right], \quad (2.28)$$

where  $\mathbf{Y}_{LM}(\hat{\mathbf{r}}) = Y_{LM}\hat{\mathbf{r}}$  are the vector spherical harmonics. If a magnetic ion with moment  $\mathbf{z}_j$  is present, these terms may be written in the following form [32]:

$$\epsilon' \cdot \mathbf{Y}_{1\pm 1}(\hat{\mathbf{k}}') \epsilon \cdot \mathbf{Y}_{1\pm 1}(\hat{\mathbf{k}}) = \frac{3\pi}{16} \left[ \epsilon' \cdot \epsilon \mp i(\epsilon' \times \epsilon) \cdot \mathbf{z}_j - (\epsilon' \cdot \mathbf{z}_j)(\epsilon \cdot \mathbf{z}_j) \right] \quad (2.29)$$

for  $M = \pm 1$ , and

$$\epsilon' \cdot \mathbf{Y}_{10}(\hat{\mathbf{k}}') \epsilon \cdot \mathbf{Y}_{10}(\hat{\mathbf{k}}) = \frac{3\pi}{8} [(\epsilon' \cdot \mathbf{z}_j)(\epsilon \cdot \mathbf{z}_j)] \quad (2.30)$$

for  $M = 0$ . Thus, the magnetic resonant scattering form factor for the  $j$ th magnetic ion can be written

$$f_{j,\text{RES}} = (\epsilon' \cdot \epsilon)F^{(0)} - i(\epsilon' \times \epsilon) \cdot \mathbf{z}_j F^{(1)} + (\epsilon' \cdot \mathbf{z}_j)(\epsilon \cdot \mathbf{z}_j)F^{(2)}, \quad (2.31)$$

where  $F^{(0),(1),(2)}$  are constants that depend on the atomic properties (and also the incident X-ray wavelength). The first term in this expression does not depend on the magnetic moment, and simply adds a contribution to the charge scattering (the polarisation factor being the same as for the Bragg scattering case above). The second term depends linearly

on the magnetic moment and gives rise to first order magnetic satellite peaks, whereas the final term depends on the moment quadratically and results in second order satellites. Once the magnetic form factor is calculated then the magnetic resonant scattering cross section can be expressed in a form very similar to before:

$$\left( \frac{d^2\sigma}{d\Omega dE_f} \right)_{\text{Resonant magnetic}} = \left| \sum_j f_{j,\text{RES}} e^{i\mathbf{Q}\cdot\mathbf{r}_j} \right|^2 \delta(E_i - E_f). \quad (2.32)$$

The magnetic resonant scattering form factor can also be written in such a way as to conveniently emphasise its polarisation dependence [30]. To do this, a matrix representation is used containing the elements

$$\begin{bmatrix} \epsilon_\sigma \rightarrow \epsilon_\sigma & \epsilon_\sigma \rightarrow \epsilon_\pi \\ \epsilon_\pi \rightarrow \epsilon_\sigma & \epsilon_\pi \rightarrow \epsilon_\pi \end{bmatrix},$$

where the notation  $\epsilon_\sigma \rightarrow \epsilon_\pi$  means the polarisation state of the incident photon is  $\sigma$ , and that of the scattered photon is  $\pi$ , *etc.* (see figure 2.1 for the definitions of these polarisation states). In this way, equation (2.31) may equivalently be written<sup>2</sup>

$$\begin{aligned} f_{j,\text{RES}} = & F^{(0)} \begin{bmatrix} 1 & 0 \\ 0 & \cos 2\theta \end{bmatrix} - iF^{(1)} \begin{bmatrix} 0 & z_{j1} \cos \theta - z_{j3} \sin \theta \\ -z_{j3} \sin \theta - z_{j1} \cos \theta & z_{j2} \sin 2\theta \end{bmatrix} \\ & + F^{(2)} \begin{bmatrix} z_{j2}^2 & z_{j2}(z_{j1} \sin \theta + z_{j3} \cos \theta) \\ -z_{j2}(z_{j1} \sin \theta - z_{j3} \cos \theta) & -\cos^2 \theta (z_{j1}^2 \tan^2 \theta + z_{j3}^2) \end{bmatrix}, \end{aligned} \quad (2.33)$$

where  $\theta$  is half of the scattering angle, and the magnetic moment  $\mathbf{z}_j = (z_{j1}, z_{j2}, z_{j3})$  is defined with respect to the Cartesian basis of figure 2.1. Since the second and third terms allow the polarisation to be rotated in the scattering process (leading to off-diagonal terms in the matrices), whereas the charge scattering does not, polarisation analysis is a useful technique for separating out these two contributions. This is particularly true for the case where the magnetic satellites overlap in reciprocal space with charge peaks, since without polarisation analysis it is very difficult to distinguish these two contributions. If there is no such overlap (for example in an incommensurate magnetic structure), then the satellites originate solely from the magnetic terms in equation (2.31) (plus a very small contribution from the non-resonant term).

Other contributions to the resonant scattering cross section, such as those arising from electric quadrupole transitions, have been calculated (see, for example, [30]). However, they will not be considered in the work presented here since the electric dipole terms are dominant.

<sup>2</sup>This formalism uses the polarisation basis vectors  $\epsilon_\sigma$  and  $\epsilon_\pi$ . It is sometimes more convenient, however, to work in the basis of circular left / right polarisation states, particularly since circularly polarised X-rays are sensitive to both magnetic [33] and crystal [34] chirality.

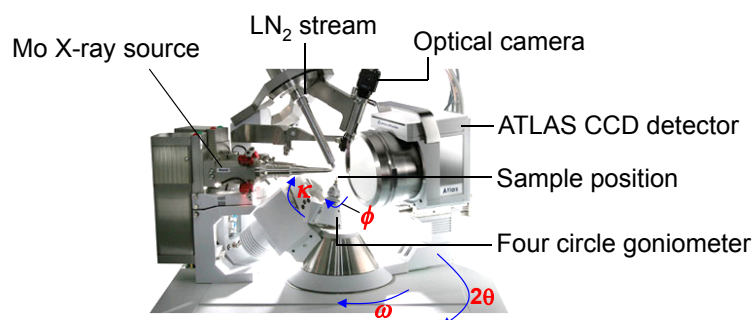


**Figure 2.3:** Photograph of the SuperNova diffractometer (inside the safety shielding) with the key components labelled. The arrows indicate the positive direction of each circle of rotation.

## 2.3 X-ray instrumentation

### 2.3.1 Laboratory sources

An Agilent Technologies ‘SuperNova’ X-ray diffractometer is employed to assess crystal quality in advance of synchrotron experiments, and to determine the orientation of the samples. It uses a high flux ‘Mova’ molybdenum 50 W X-ray source, whose beam size is  $\approx 300 \mu\text{m}$  in diameter (the beam is unpolarised). The sample is mounted onto a four circle kappa geometry goniometer, which is optionally positioned within the gas stream of a nitrogen or helium jet for cooling. A camera is mounted above the sample position to allow accurate alignment of the sample into the beam. The ATLAS area detector consists of a phosphorescent screen which generates light in response to the scattered X-rays. Behind this screen a fibre optic taper transmits the light onto the active surface of a CCD chip. The detector is capable of registering a 32 bit intensity at each of the  $2048 \times 2048$  pixels, but in order to keep the file sizes manageable the raw data is typically binned into  $2 \times 2$  blocks and compressed. The detector is mounted on a moveable arm which allows it to move away from the goniometer while the crystal orientation is changed (avoiding potential collisions), but it can then move inwards to subtend a large solid angle to the sample while collecting data. A photo of the diffractometer can be seen in figure 2.3.

In the conventional four circle design for a diffractometer, the angles  $\phi$ ,  $\omega$ , and  $\chi$  are used to position the sample. As shown in figure 2.4, the  $\chi$  circle is tilted at an angle  $\omega + \theta$  to the primary beam direction, and around this  $\chi$  circle moves the sample stage which itself is capable of rotating by an angle  $\phi$  about its axis. The detector is then set to make an angle  $2\theta$  with respect to the straight through beam, and a further ‘virtual’ angle  $\psi$  is used to refer to the degree of sample rotation about the scattering vector  $\mathbf{Q}$ . Whilst such a setup allows the sample to be positioned almost arbitrarily, it has the disadvantage that the large

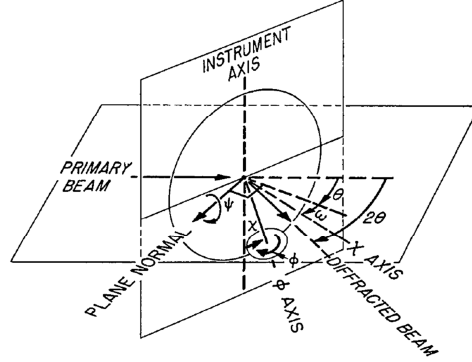


**Figure 2.4:** Conventional four circle diffractometer angles (all of which are shown in the first quadrant), after [35]. © International Union of Crystallography. Reproduced by permission. All rights reserved.

$\chi$  circle will often intercept the X-ray beams. To overcome this problem, the  $\chi$  circle can be replaced with a  $\kappa$  rotation, inclined at an angle  $\alpha \approx 50^\circ$  to the horizontal and attached to the  $\omega$  rotation (see figure 2.3).

To index a general reflection requires knowledge of the diffractometer angles and the scattering vector  $\mathbf{Q} = \mathbf{k}' - \mathbf{k}$ . It is then possible to relate  $\mathbf{Q}$  to the peak index  $(h, k, l) = h\mathbf{a}^* + k\mathbf{b}^* + l\mathbf{c}^*$  by

$$\begin{pmatrix} |\mathbf{Q}| \\ 0 \\ 0 \end{pmatrix} = \mathbf{\Omega K \Phi U B} \begin{pmatrix} h \\ k \\ l \end{pmatrix}, \quad (2.34)$$

where the (in general non-orthogonal) matrix  $\mathbf{B}$  converts from the reciprocal basis vectors  $\{\mathbf{a}^*, \mathbf{b}^*, \mathbf{c}^*\}$  to a set of Cartesian axes rigidly attached to the crystal. The matrix  $\mathbf{U}$  then rotates the sample from this Cartesian set of axes onto an equivalent set rigidly attached to the goniometer head (*i.e.* allowing for the fact that the crystal may be mounted with an arbitrary orientation) [35]. The matrices  $\mathbf{\Phi}$ ,  $\mathbf{K}$ , and  $\mathbf{\Omega}$  then rotate about the  $\phi$ ,  $\kappa$ , and  $\omega$  axes such that the scattering vector now points along the  $x$  direction (parallel to the direction of propagation of the straight through beam). The matrix  $\mathbf{UB}$  is generally not known in advance of the experiment, so the diffractometer software (CrysAlis Pro [36]) continually processes the data during collection and uses a least squares technique to find the  $\mathbf{UB}$  that most accurately indexes the greatest number of reflections consistently. Alternatively, if the sample is mounted in a specific orientation (for example at a central facilities experiment) the  $\mathbf{UB}$  matrix can be calculated from the position of two reflections and a knowledge of the lattice parameters.

One particularly useful feature of the CrysAlis software is its ability to convert the data from the raw images obtained on the CCD detector into reciprocal space intensity maps (these reciprocal space images are used extensively in chapter 4). Essentially this

works by indexing the entire set of pixels across all images in a data set [in fractional  $(h, k, l)$  coordinates] and then mapping the intensities from appropriate pixels belonging to a particular plane in reciprocal space [for example: the  $(h, k, 0)$  plane] into the new image.

### 2.3.2 The synchrotron source

The synchrotron X-ray experiments detailed in this thesis were carried out at the Diamond Light Source, Harwell, UK ('Diamond'). Synchrotron radiation has many advantages over laboratory sources: in particular it is far more intense<sup>3</sup>, can be tuned to a specific energy, and the polarisation of the X-rays can be arbitrarily set. At a fundamental level, a synchrotron light source works by accelerating a beam of charged particles (typically electrons) up to relativistic speeds. The electrons are directed through a series of strong magnetic fields, which due to the Lorentz force cause them to change their direction and emit Bremsstrahlung radiation tangentially to their motion in the process. Typically this radiation is in the X-ray part of the electromagnetic spectrum, although a very wide range of photon energies (down to the infrared) can be produced.

At Diamond, electrons are generated by an electron gun: a heated metal cathode close to a positively charged anode. They then pass along a linear accelerator (linac), reaching an energy of 100 MeV. Following this they enter the booster synchrotron where a series of straight sections of beam pipe (all held under ultra high vacuum) are connected via bending magnets to form a loop. The electrons circulate, gaining energy as they repeatedly pass through a radio frequency (RF) cavity, until they reach 3 GeV (the strength of the booster synchrotron bending magnets is coupled to the electrons' energy to ensure they remain on the same path on each loop). Other magnets (quadrupoles and sextupoles) are used to focus the beam and keep the electrons together in 'bunches'. Once at 3 GeV the electrons are released into the storage ring, in which they circulate for several hours at the same nominal energy. Diamond operates in continuous top-up mode, meaning that every few minutes the electron bunches in the storage ring that are most depleted are replenished, maintaining an approximately constant storage ring beam current of  $\approx 300$  mA.

Situated between the bending magnets of the storage ring are straight sections, around which arrays of magnets called *insertion devices* can be placed. These consist of alternating north and south poles of permanent magnets, which force the electrons to follow a highly oscillatory path emitting X-rays as they do so. These devices are therefore named 'wigglers' and 'undulators', and undulators (the relevant source of X-rays for the work presented in this thesis) are discussed further in the next section. Useful radiation can also be obtained

<sup>3</sup>Typical fluxes are  $9 \times 10^8$  photons  $\text{s}^{-1} \text{mm}^{-2}$  for the Mo 'SuperNova' laboratory source, and  $1.7 \times 10^{14}$  photons  $\text{s}^{-1} \text{mm}^{-2}$  for hard X-rays generated on beamline I19 at the Diamond Light Source [37].

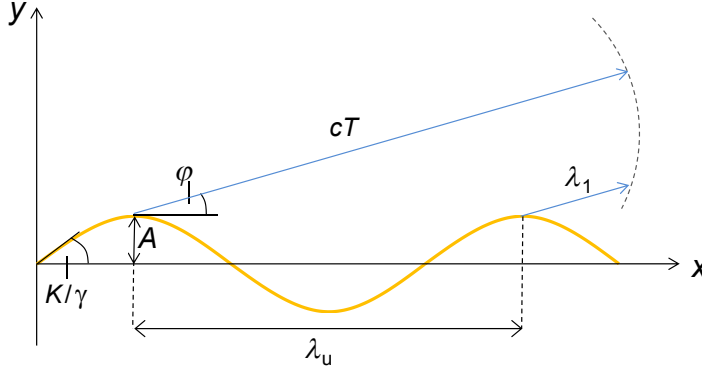


**Figure 2.5:** The geometry of undulator radiation: the electrons follow the curved orange path and radiate light tangentially. The light radiated at two positions one wavelength apart is indicated by the blue arrows.

directly from the bending magnets, although it is not as intense as light produced by insertion devices.

### 2.3.2.1 Undulator radiation

Undulator radiation differs from wiggler radiation in that it adds in a constructive way from one period of the insertion device to the next. Therefore, whilst the radiation generated by a wiggler may be viewed simply as that generated from a series of independent bending magnets, the energy spectrum for an undulator is centred around a fundamental wavelength and its harmonics, as is demonstrated in the following.

Let the spatial repeat distance of the undulator be  $\lambda_u$ , with associated wavevector  $k_u = 2\pi/\lambda_u$ , and consider an electron passing along part of the undulator as shown by the orange path in figure 2.5. With an amplitude of oscillation  $A$ , the path may be written  $y \approx A \sin(k_u x)$ , although in reality the curves are circular since they are describing an electron moving within a magnetic field of strength  $\mathbf{B}$  directed perpendicular to the diagram. Such electrons experience a Lorentz force  $\mathbf{F} = -e\mathbf{v} \times \mathbf{B}$  where  $\mathbf{v}$  is the velocity of the electron. The equation of motion for relativistic electrons is  $\gamma m a = evB$  where  $\gamma := (1 - \frac{v^2}{c^2})^{-1/2}$  and where  $a = v^2/\rho$  is the acceleration for motion in a circle. Thus the radius of the circle is given by

$$\rho = \frac{\gamma mc}{eB} \quad (2.35)$$

which scales inversely with the magnetic field  $B$  as expected.

By expanding the motion described by the sinusoidal path,

$$y \approx A \sin(k_u x) = A \cos \left[ k_u \left( x - \frac{\lambda_u}{4} \right) \right] \approx A - \frac{Ak_u^2}{2} \left( x - \frac{\lambda_u}{4} \right)^2, \quad (2.36)$$

we can compare this to the equation of a circle centred at  $x = \lambda_u/4$ ,  $y = A - \rho$ :

$$(y - A + \rho)^2 + \left(x - \frac{\lambda_u}{4}\right)^2 = \rho^2 \quad \Rightarrow \quad y \approx A - \frac{1}{2} \left( \frac{x - \lambda_u/4}{\rho} \right), \quad (2.37)$$

having assumed that  $y$  is small (*i.e.* the amplitude of oscillation is small). Therefore the radius of curvature is given by

$$\rho \approx \frac{1}{Ak_u^2}. \quad (2.38)$$

The angle of maximum deviation of the electrons from the  $x$ -axis is equal to  $K/\gamma$  (this is the definition of the parameter  $K$  which is used to characterise the undulator), which is equal to  $Ak_u$  (this can be obtained by evaluating  $\frac{dy}{dx}$  at  $x = 0$  for small angles of deviation). Thus we may substitute into equation (2.35) to obtain a working equation for the parameter  $K$ :

$$K = \frac{eB}{mck_u} \approx 0.932 \lambda_u[\text{cm}] B[\text{T}]. \quad (2.39)$$

Let the time taken (in the electron's frame of reference) for the electron to travel one complete spatial period of the undulator be  $T$ . Then, as shown in figure 2.5, one will obtain constructive interference if

$$n\lambda_1 = cT - \lambda_u \cos \varphi, \quad n \in \mathbb{Z}, \quad (2.40)$$

where  $\lambda_1$  is the fundamental wavelength emitted by the undulator. We have  $T = \frac{S}{v}$  where  $S$  is the length of the electron's path over one spatial period, given by

$$S = \int_0^{\lambda_u} dx \left[ 1 + \left( \frac{dy}{dx} \right)^2 \right]^{1/2} \quad (2.41)$$

$$\approx \int_0^{\lambda_u} dx \left[ 1 + \frac{1}{2} A^2 k_u^2 \cos^2(k_u x) \right] \quad (2.42)$$

assuming the amplitude of oscillation is small. This can be evaluated to give

$$S = \lambda_u \left( 1 + \frac{1}{4} A^2 k_u^2 \right) = \lambda_u \left( 1 + \frac{K^2}{4\gamma^2} \right), \quad (2.43)$$

so that, from equation (2.40), the undulator will produce wavelengths given by

$$\lambda_n = \frac{c\lambda_u}{vn} \left( 1 + \frac{K^2}{4\gamma^2} \right) - \frac{\lambda_u}{n} \cos \varphi \quad (2.44)$$

$$\approx \frac{\lambda_u}{2\gamma^2 n} \left( 1 + \frac{K^2}{2} + \gamma^2 \varphi^2 \right), \quad (2.45)$$

assuming that the angle between the emitted radiation and the undulator axis,  $\varphi$ , is small. Equation (2.45) is known as the 'undulator equation' and shows how the emitted wavelengths can be tuned by varying the parameter  $K$  (in practice this is achieved by changing

the undulator gap, which varies the magnetic field  $B$ ). Further considerations of the motion of the electrons within the undulator limit the harmonics that may be generated to reach an on-axis observer to odd values of  $n$  only. At Diamond, electrons in the storage ring have  $\gamma \approx 5870$ , so taking typical values of  $B = 0.5$  T and  $\lambda_u = 1$  cm, a fundamental X-ray wavelength of  $1.8$  Å can be obtained from the undulator.

Whilst the above would suggest that there exist specific wavelengths at which there will be constructive interference, in reality limitations on the number of undulator periods limit the length of the X-ray pulse train, which in turn limits the frequency distribution of the radiation. Thus, it can be shown that an undulator containing  $N$  magnet periods produces radiation of bandwidth

$$\frac{\Delta\lambda}{\lambda_n} \sim \frac{1}{nN}. \quad (2.46)$$

Therefore monochromation of the beam is important, as well as the obvious need to remove the unwanted harmonics produced by the undulator.

Finally, it is also possible to construct more complicated arrangements of the magnets within an undulator, such that the electrons are forced to follow a helical path. Using this technique one can produce intense beams of circularly polarised light, typically with a polarisation exceeding 99%, of either handedness.

### 2.3.2.2 Beamline I19

Elastic X-ray diffraction experiments were undertaken on the hard X-ray beamline I19 at Diamond [37] to study samples of  $\text{YbFe}_2\text{O}_4$  (see chapter 4). The undulator generates linearly polarised X-rays of wavelength  $0.6889$  Å, which are passed through a double bounce monochromator, slits, and focussing mirrors to bring the beam down to approximately  $170 \times 85$  µm at the sample position. A  $\text{LN}_2$  cryostream was used to cool the samples down to 150 K, and additionally the samples could be heated up as far as 360 K. The samples were mounted onto a microloop which was attached to a four circle diffractometer. A Rigaku Saturn 724 CCD area detector was used to collect the X-ray reflections, and subsequent analysis began by indexing the reflections as described for the SuperNova diffractometer above in section 2.3.1.

### 2.3.2.3 Beamline I10

This beamline is optimised for soft X-ray diffraction experiments, as employed to study hexaferrite samples (see chapter 5). The beamline's undulators are capable of producing X-rays with energy close to the iron resonance, which was used to carry out elastic resonant X-ray scattering. The undulators are also optimised to produce both linear (horizontally or vertically polarised) or circular (left handed or right handed) light, and it is straightforward



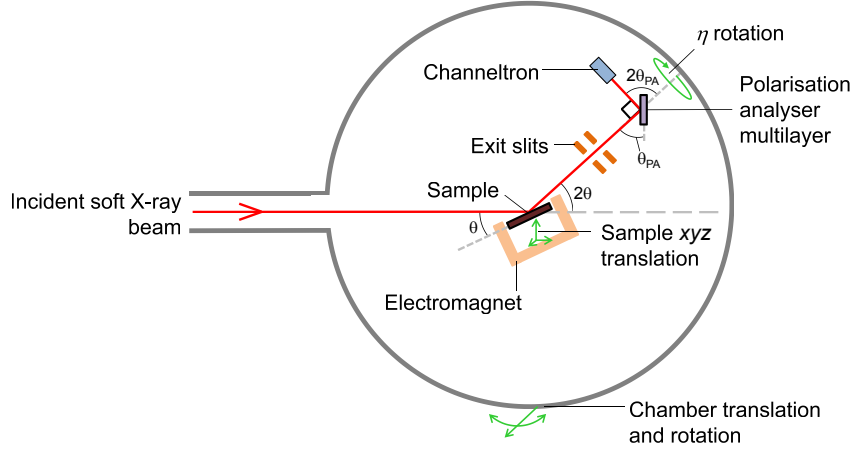


**Figure 2.6:** Simplified diagram of the RASOR end station on beamline I10, showing the key rotations / translations, polarisation analyser, and position of the electromagnet around the sample.

to switch between any of these polarisations during an experiment by adjusting the phase between the different rows of undulator magnets. A plane grating monochromator is used and various focussing mirrors and slits are employed to shape the beam before it arrives at the experimental station.

Unlike the case of hard X-rays as generated, for example, on beamline I19, soft X-rays are strongly attenuated by air. Therefore the entire experiment is designed to take place in ultra high vacuum, and to this end a purpose built diffractometer chamber, RASOR<sup>4</sup>, is used to house the sample and the detectors (figure 2.6 and [38]). The RASOR end station contains a Janis LHe cryostat which allows the sample to be cooled to 12 K. The diffractometer operates mainly in a  $\theta$ - $2\theta$  geometry, with an additional small  $\chi$  rotation (limited to  $\pm 4^\circ$ ) which can be used to correct for misalignment in the sample mounting. The detector arm also has the capability to analyse the polarisation of the scattered beam. For the work presented in this thesis, this is carried out with an analyser multilayer whose  $d$ -spacing is optimised for the Fe  $L_{2,3}$  edges, and a channeltron (electron multiplier) detector. The detector and analyser crystal can be rotated about the  $\eta$ -axis to access different exit polarisations (further details are given in section 5.3). The cryostat has the option of an electromagnet fitting which allows a magnetic field to be applied across the sample. Both the sample and chamber can be translated or rotated in various directions (as shown in the figure) to align the instrument.

<sup>4</sup>Reflectivity and Advanced Scattering from Ordered Regimes.

## 2.4 The interaction of neutrons with condensed matter systems

There are several properties of neutrons that make them a very well-suited probe for the study of condensed matter systems. Neutrons travelling at slow (nonrelativistic) speeds have a de Broglie wavelength  $\lambda = 2\pi\hbar/(mv)$  which is equal to  $1.5 \text{ \AA}$  (a typical interatomic distance in condensed matter) when  $v \approx 2.64 \times 10^3 \text{ ms}^{-1}$ , so they are ideal for use in diffraction studies of crystals. In addition (although not used in the present work), neutrons' energies are on a scale suitable for probing collective excitations (such as phonons) in inelastic scattering experiments. Importantly, the magnetic moment of the neutron  $\mu_n = -1.913 \dots \mu_N$ , where  $\mu_N$  is the nuclear magneton, allows it to interact with the magnetic moments of ions making up a crystal, revealing detailed information about the magnetic structure. Finally, the fact that the neutron carries no electric charge means it can penetrate deeply into matter. Diffraction studies with neutrons are often complementary to those with X-rays: in particular, neutrons have traditionally been the probe of choice to study complex magnetic structures, and this is still partly the case today although advances in X-ray science continue to challenge this rôle.

Proceeding in a similar fashion to the scattering theory presented in section 2.2, the starting point is the Hamiltonian for the sample / neutron system:

$$\mathcal{H} = \mathcal{H}_0 + \frac{\mathbf{p}^2}{2m} + V(\mathbf{r}) \quad (2.47)$$

where  $\mathcal{H}_0$  is the (unperturbed) Hamiltonian of the sample, the kinetic energy of the neutron is  $\mathbf{p}^2/(2m)$  and  $V(\mathbf{r})$  is the interaction energy between the sample and the neutron. The eigenstates of  $\mathcal{H}_0$  (*i.e.* the states describing the sample without the perturbation due to the neutron) are written  $|\Psi\rangle$ . As with the case of X-ray scattering, in first order perturbation theory the transition probability per unit time is given by

$$W^{(1)} = \frac{2\pi}{\hbar} |\langle f|V(\mathbf{r})|i\rangle|^2 \delta(E_i - E_f), \quad (2.48)$$

where  $|i\rangle = |\mathbf{k}_i, \chi_i, \Psi_a(E_a)\rangle$  describes the initial state of the system, in which the sample is in state  $|\Psi_a\rangle$  with energy  $E_a$ , and the neutron has wavevector  $\mathbf{k}_i$  and spin  $\chi_i$ . Similarly  $|f\rangle = |\mathbf{k}_f, \chi_f, \Psi_b(E_b)\rangle$ . We have  $E_i = E_a + \mathbf{p}_i^2/(2m)$ ,  $E_f = E_b + \mathbf{p}_f^2/(2m)$ , and the delta function in equation (2.48) ensures that energy is conserved.

As for X-rays, the cross section is obtained by multiplying this transition probability rate by the neutron density of states  $g_{\mathbf{k}_f, \chi_f}(E_f)$  [where  $E_f = \mathbf{p}_f^2/(2m)$ ] and dividing by the incident flux  $I_0$ . The density of states in wavevector interval  $dk_f$  and solid angle  $d\Omega$  is given by

$$g = \frac{V_0}{8\pi^3} k_f^2 dk_f d\Omega = \frac{V_0}{8\pi^3} k_f^2 \frac{mdE_f}{\hbar^2 k_f} d\Omega, \quad (2.49)$$

and the flux is  $I_0 = v/V_0 = \hbar k_i/(V_0 m)$ . Therefore

$$\left(\frac{d\sigma}{d\Omega dE_f}\right)_{\mathbf{k}_i, \chi_i, a \rightarrow \mathbf{k}_f, \chi_f, b} = V_0^2 \left(\frac{m}{2\pi\hbar^2}\right)^2 \frac{k_f}{k_i} |\langle \mathbf{k}_f, \chi_f, \Psi_b(E_b) | V(\mathbf{r}) | \mathbf{k}_i, \chi_i, \Psi_a(E_a) \rangle|^2 \delta(E_i - E_f). \quad (2.50)$$

Since the state of the sample is not determined in an experiment, averaging over all of the initial states  $a$  of the sample and summing over all final states  $b$  that are allowed gives

$$\begin{aligned} \left(\frac{d\sigma}{d\Omega dE_f}\right)_{\mathbf{k}_i, \chi_i \rightarrow \mathbf{k}_f, \chi_f} = \\ V_0^2 \left(\frac{m}{2\pi\hbar^2}\right)^2 \frac{k_f}{k_i} \sum_a P(|\Psi_a\rangle) \sum_b |\langle \mathbf{k}_f, \chi_f, \Psi_b(E_b) | V(\mathbf{r}) | \mathbf{k}_i, \chi_i, \Psi_a(E_a) \rangle|^2 \delta(E_i - E_f), \end{aligned} \quad (2.51)$$

where the function  $P(|\Psi_a\rangle)$  gives the probability of the initial sample state  $|\Psi_a\rangle$  occurring. This is the most general form of the neutron scattering cross section. In the following, two special cases will be considered: firstly the case of elastic scattering from the nuclei in a crystal, and secondly the case of elastic magnetic scattering of polarised neutrons.

### 2.4.1 Elastic neutron diffraction from nuclei

For nuclear scattering, the interaction potential between the neutron and nucleus is short ranged and, following [39], may therefore be approximated by the *Fermi pseudopotential*

$$V_{\text{nuclear}}(\mathbf{r}) = \frac{2\pi\hbar^2}{m} \sum_j b_j \delta^{(3)}(\mathbf{r} - \mathbf{r}_j), \quad (2.52)$$

where the summation runs over the  $j = 1, \dots, n$  nuclei in the part of the sample illuminated by the neutron beam. In this expression,  $b_j$  (which depends on the particular isotope) is known as the *scattering length* and parametrises how strongly the neutron will interact with the  $j$ th nucleus. If the scattering is elastic ( $k_f = k_i$ , and the scattering does not change the sample state) and unpolarised (*i.e.* averaged over all spin states), equation (2.51) reduces to

$$\left(\frac{d\sigma}{d\Omega dE_f}\right)_{\text{elastic, nuclear}} = V_0^2 \left(\frac{m}{2\pi\hbar^2}\right)^2 |M|^2 \delta(E_i - E_f) \quad (2.53)$$

where the matrix element

$$M = \frac{2\pi\hbar^2}{mV_0} \sum_j b_j \int d^3\mathbf{r} e^{i\mathbf{k}' \cdot \mathbf{r}} \delta^{(3)}(\mathbf{r} - \mathbf{r}_j) e^{-i\mathbf{k} \cdot \mathbf{r}} \quad (2.54)$$

assuming that the incident and exit neutron beams can be described by plane waves (of the form  $V_0^{-1/2} e^{-i\mathbf{k} \cdot \mathbf{r}}$ ) in the same way as the X-ray scattering treatment above, and neglecting

the Debye Waller factor that would account for thermal motion of the nuclei. Therefore the final cross section is given by

$$\left(\frac{d\sigma}{d\Omega dE_f}\right)_{\text{elastic, nuclear}} = \left| \sum_j b_j e^{i\mathbf{Q}\cdot\mathbf{r}_j} \right|^2 \delta(E_i - E_f). \quad (2.55)$$

In analogy to the elastic X-ray scattering case, if the nuclei are arranged into a crystal structure, this may be expressed as

$$\left(\frac{d\sigma}{d\Omega dE_f}\right)_{\text{elastic, coherent}} = \frac{(2\pi)^3}{V_{\text{cell}}} N_{\text{cell}} \delta^{(3)}(\mathbf{Q} - \mathbf{G}) \left| \sum_j b_j e^{i\mathbf{Q}\cdot\mathbf{R}_j} \right|^2 \delta(E_i - E_f) \quad (2.56)$$

where, as before,  $\mathbf{G}$  is a reciprocal lattice vector. Note that this is the *coherent* contribution to the scattering: there will also be an *incoherent* part which arises from differences in the scattering lengths, for example due to different isotopes.

## 2.4.2 Magnetic diffraction of polarised neutrons

As well as interacting with atomic nuclei, neutrons are sensitive to magnetism in solids arising from unpaired electrons carrying a net spin or orbital magnetic moment. This is because the neutron itself possesses a magnetic moment  $\boldsymbol{\mu}_n = -\gamma\mu_N\boldsymbol{\sigma}$  which will interact with the electron's magnetic moment  $\boldsymbol{\mu}_e = -2\mu_B\mathbf{S}$ , where  $\gamma = 1.9132$  and  $\mu_N = e\hbar/(2m_p)$ ,  $\mu_B = e\hbar/(2m_e)$  are respectively the nuclear and Bohr magnetons, and  $\boldsymbol{\sigma}$  is the Pauli spin operator. The interaction potential due to this magnetism may be written as

$$V_{\text{magnetic}}(\mathbf{r}) = -\boldsymbol{\mu}_n \cdot \mathbf{B}(\mathbf{r}), \quad (2.57)$$

where  $\mathbf{B}(\mathbf{r})$  is the magnetic field set up by the ensemble of atoms and is given by<sup>5</sup>

$$\mathbf{B}(\mathbf{r}) = \frac{\mu_0}{4\pi} \sum_j \left\{ \nabla \times \left[ \boldsymbol{\mu}_{e,j} \times \frac{(\mathbf{r} - \mathbf{r}_j)}{|\mathbf{r} - \mathbf{r}_j|^3} \right] - \frac{2\mu_B}{\hbar} \mathbf{p}_j \times \frac{(\mathbf{r} - \mathbf{r}_j)}{|\mathbf{r} - \mathbf{r}_j|^3} \right\}, \quad (2.58)$$

where  $\mathbf{r}_j$ ,  $\mathbf{p}_j$ , and  $\boldsymbol{\mu}_{e,j}$  are respectively the position, momentum, and magnetic moment of the unpaired electrons belonging to the  $j$ th atom. Thus, the magnetic interaction potential is

$$V_{\text{magnetic}}(\mathbf{r}) = V_{\text{spin}}(\mathbf{r}) + V_{\text{orbit}}(\mathbf{r}), \quad (2.59)$$

<sup>5</sup>The first of these terms (due to the electron's spin moment) comes from the curl of the magnetic vector potential  $\mathbf{A}$  set up by a point dipole moment:  $\mathbf{A}(\mathbf{r}) = \frac{\mu_0}{4\pi} \frac{\boldsymbol{\mu} \times \mathbf{r}}{|\mathbf{r}|^3}$ ; the second (from the orbital moment) is from the Biot-Savart law for a point charge, setting up a magnetic field  $\mathbf{B}(\mathbf{r}) = -\frac{\mu_0}{4\pi} e\mathbf{v} \times \frac{\mathbf{r}}{|\mathbf{r}|^3}$ .

where

$$V_{\text{spin}}(\mathbf{r}) = -\frac{\mu_0}{4\pi} \boldsymbol{\mu}_n \cdot \sum_j \nabla \times \left[ \boldsymbol{\mu}_{e,j} \times \left( \frac{\mathbf{r} - \mathbf{r}_j}{|\mathbf{r} - \mathbf{r}_j|^3} \right) \right], \quad (2.60)$$

$$V_{\text{orbit}}(\mathbf{r}) = \frac{\mu_0}{4\pi} \boldsymbol{\mu}_n \cdot \sum_j \frac{2\mu_B}{\hbar} \mathbf{p}_j \times \left( \frac{\mathbf{r} - \mathbf{r}_j}{|\mathbf{r} - \mathbf{r}_j|^3} \right). \quad (2.61)$$

The elastic scattering cross section depends on the matrix element,  $M$ , which is given by

$$M = \langle \mathbf{k}_f, \chi_f | V_{\text{magnetic}}(\mathbf{r}) | \mathbf{k}_i, \chi_i \rangle = \langle \chi_f | V_{\text{magnetic}}(\mathbf{Q}) | \chi_i \rangle, \quad (2.62)$$

where  $V_{\text{magnetic}}(\mathbf{Q})$  is the Fourier transform of  $V_{\text{magnetic}}(\mathbf{r})$ , which may be shown<sup>6</sup> to be

$$V_{\text{magnetic}}(\mathbf{Q}) = V_{\text{spin}}(\mathbf{Q}) + V_{\text{orbit}}(\mathbf{Q}), \quad (2.63)$$

where

$$V_{\text{spin}}(\mathbf{Q}) = -\mu_0 \boldsymbol{\mu}_n \cdot \sum_j e^{i\mathbf{Q} \cdot \mathbf{r}_j} \hat{\mathbf{Q}} \times (\boldsymbol{\mu}_{e,j} \times \hat{\mathbf{Q}}), \quad (2.64)$$

$$V_{\text{orbit}}(\mathbf{Q}) = \mu_0 \boldsymbol{\mu}_n \cdot \sum_j e^{i\mathbf{Q} \cdot \mathbf{r}_j} \frac{2i\mu_B}{\hbar|\mathbf{Q}|} (\mathbf{p}_j \times \hat{\mathbf{Q}}). \quad (2.65)$$

For practical calculations, this may be written in an alternative form as

$$V_{\text{magnetic}}(\mathbf{Q}) = \gamma \mu_N \mu_0 \boldsymbol{\sigma} \cdot \mathbf{M}_{\perp}(\mathbf{Q}), \quad (2.66)$$

where  $\mathbf{M}_{\perp}(\mathbf{Q})$  is the *magnetic interaction vector*:

$$\mathbf{M}_{\perp}(\mathbf{Q}) = 2\mu_B \sum_j e^{i\mathbf{Q} \cdot \mathbf{r}_j} \left[ \hat{\mathbf{Q}} \times (\mathbf{s}_j \times \hat{\mathbf{Q}}) + \frac{i}{\hbar|\mathbf{Q}|} (\mathbf{p}_j \times \hat{\mathbf{Q}}) \right] \quad (2.67)$$

$$= \hat{\mathbf{Q}} \times [\mathbf{M}(\mathbf{Q}) \times \hat{\mathbf{Q}}]. \quad (2.68)$$

In this expression,  $\mathbf{M}(\mathbf{Q})$  is the *magnetic structure factor* and is given by the Fourier transform of the magnetisation distribution function<sup>7</sup>,  $\mathbf{M}(\mathbf{r})$ . Assuming spin-only scattering, or both spin and orbital scattering within the dipole approximation, this is conventionally written

$$\mathbf{M}(\mathbf{Q}) = \sum_j f_j^{\text{mag}}(\mathbf{Q}) \boldsymbol{\mu}_j e^{i\mathbf{Q} \cdot \mathbf{r}_j}, \quad (2.69)$$

the summation running over the magnetic ions in the crystal (labelled by  $j$ ). In this expression,  $f_j^{\text{mag}}(\mathbf{Q})$  is known as the *magnetic form factor* and is the Fourier transform of the

<sup>6</sup>This can be seen by considering the following relations, worked out in [39]:

$\nabla \times \left( \mathbf{m} \times \frac{\mathbf{r}}{|\mathbf{r}|^3} \right) = \frac{1}{2\pi^2} \int d^3\mathbf{q} [\hat{\mathbf{q}} \times (\mathbf{m} \times \hat{\mathbf{q}})] e^{i\mathbf{q} \cdot \mathbf{r}}$ , and  $\int d^3\mathbf{r} \frac{\mathbf{r}}{|\mathbf{r}|^3} e^{i\mathbf{q} \cdot \mathbf{r}} = 4\pi i \frac{\mathbf{q}}{|\mathbf{q}|^2}$ .

<sup>7</sup>For the spin part of the potential it is immediately apparent from equation (2.67) that this is the case. For the orbital part, the result  $\frac{i}{\hbar|\mathbf{Q}|} \sum_j e^{i\mathbf{Q} \cdot \mathbf{r}_j} (\mathbf{p}_j \times \hat{\mathbf{Q}}) = -\frac{1}{2\mu_B} \hat{\mathbf{Q}} \times [\mathbf{M}_{\text{orbit}}(\mathbf{Q}) \times \hat{\mathbf{Q}}]$ , where  $\mathbf{M}_{\text{orbit}}(\mathbf{Q})$  is the Fourier transform of the orbital magnetisation density (again proved in [39]), is required.

magnetisation distribution function due to the  $j$ th atom, and  $\boldsymbol{\mu}_j$  is the magnetic moment associated with this atom. Thus, the cross section for elastic magnetic neutron scattering is given by

$$\left(\frac{d\sigma}{d\Omega dE_f}\right)_{\text{elastic, magnetic}} = \left(\frac{m}{2\pi\hbar^2}\right)^2 |M|^2 \delta(E_i - E_f), \quad (2.70)$$

where the matrix element is

$$M = \gamma\mu_N\mu_0 \langle \chi_f | \boldsymbol{\sigma} \cdot \mathbf{M}_\perp(\mathbf{Q}) | \chi_i \rangle. \quad (2.71)$$

The value of this matrix element will depend on the neutron spins (*i.e.* the polarisation of the beam). After a brief digression to discuss chirality, its dependence on the neutron polarisations will be evaluated.

### 2.4.3 The neutron as a chiral probe

The experimental work presented in this thesis relies in part on the neutron being sensitive to the *chiral* properties of magnetic structures. By chirality, I take to mean (by definition) the phenomenon exhibited by systems that exist in two distinct enantiomorphic states that are interconnected by space inversion but *not* by time reversal symmetry combined with any proper spatial rotation and translation [40, 41].

A moving neutron is associated with a pair of vectors: a polar vector  $\mathbf{p}$  describing its linear momentum (inversion odd and time reversal odd), together with an axial vector  $\mathbf{s}$  describing its spin angular momentum (inversion even and time reversal odd) [42]. Imagining the simple picture of a neutron polarised along the direction of its linear momentum, as in figure 2.7, it becomes obvious that the neutron itself can exist in two distinct enantiomorphic states and is therefore able to interact with chiral structures in a way that depends explicitly on their chirality. For this to work, one must use *polarised* neutrons as the probe of choice as a depolarised beam will not have a well-defined axial (spin) vector associated with it.

### 2.4.4 The S-matrix

Let  $|\chi_i\rangle$  denote the initial neutron spin state. The spin state after the neutron has interacted with the sample,  $|\chi_f\rangle$ , is related to the initial spin state by the **S**-matrix:

$$|\chi_f\rangle = \mathbf{S}|\chi_i\rangle. \quad (2.72)$$

Taking as the basis states  $|+\rangle$  to denote polarisation along the  $\hat{\mathbf{e}}_z$  direction and  $|-\rangle$  to denote polarisation along  $-\hat{\mathbf{e}}_z$ , a general state may be expanded as  $|\chi_i\rangle = a_i|+\rangle + b_i|-\rangle$

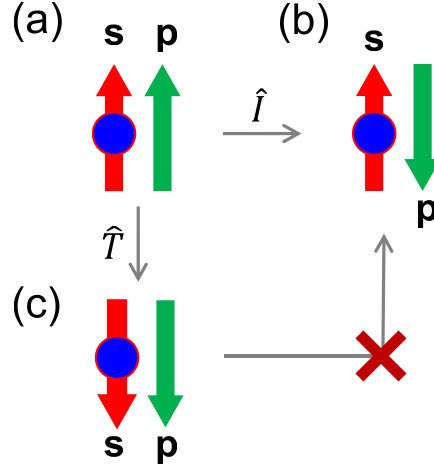


**Figure 2.7:** In (a) a neutron is shown polarised such that its spin vector  $\mathbf{s}$  is parallel to its linear momentum  $\mathbf{p}$ . Under spatial inversion, the sign of  $\mathbf{p}$  changes but that of  $\mathbf{s}$  remains the same. This state, depicted in (b), cannot be reached from the state in (a) by a combination of time reversal [shown in (c)] and proper rotation, and is therefore a distinct ‘enantiomer’.

(and similarly  $|\chi_f\rangle = a_f|+\rangle + b_f|-\rangle$ ). In such a basis, the  $\mathbf{S}$ -matrix may be expressed in component form as

$$\begin{pmatrix} a_f \\ b_f \end{pmatrix} = \begin{bmatrix} a_{11} & a_{12} \\ a_{21} & a_{22} \end{bmatrix} \begin{pmatrix} a_i \\ b_i \end{pmatrix}. \quad (2.73)$$

This matrix, being Hermitian, may be decomposed (rather suggestively) into two parts as follows:

$$\begin{bmatrix} a_{11} & a_{12} \\ a_{21} & a_{22} \end{bmatrix} = \begin{bmatrix} \beta & 0 \\ 0 & \beta \end{bmatrix} + \begin{bmatrix} A_z & A_x - iA_y \\ A_x + iA_y & -A_z \end{bmatrix}, \quad (2.74)$$

and in so doing the  $\mathbf{S}$ -matrix may be written

$$\mathbf{S} = \beta \mathbb{I} + \mathbf{A} \cdot \boldsymbol{\sigma}, \quad (2.75)$$

where  $\mathbb{I}$  is the identity matrix,  $\boldsymbol{\sigma} = (\sigma_x, \sigma_y, \sigma_z)$  is the vector of Pauli spin matrices,  $\mathbf{A} = (A_x, A_y, A_z)$  is a vector and  $\beta$  is a scalar.

#### 2.4.5 The polarised neutron spin-flip cross sections

Physical meaning is now attached to the quantities  $\beta$  and  $\mathbf{A}$  introduced in the previous section. Since the  $\mathbf{S}$ -matrix connects the initial spin state of the neutron to the final spin state, it clearly needs to describe interactions between the neutron and the sample.

The first term on the right of equation (2.75) describes processes in which the neutron spin couples to a scalar and its direction of polarisation is therefore unchanged. This is

simply the nuclear scattering process derived in section 2.4.1, *i.e.*

$$\beta_{\text{nuclear}}(\mathbf{Q}) = N(\mathbf{Q}) := \sum_j b_j e^{i\mathbf{Q} \cdot \mathbf{R}_j}. \quad (2.76)$$

The second term on the right of equation (2.75) involves a coupling between the spin of the neutron (described by the Pauli spin matrices) and a vectorial quantity  $\mathbf{A}$  which must therefore be connected to magnetism within the sample. There are two contributions to  $\mathbf{A}$ : the first comes from the magnetic moments carried by the nuclei  $\mathbf{I}_j$  and may be written

$$\mathbf{A}_{\text{nuclear}}(\mathbf{Q}) = \sum_j b_j \mathbf{I}_j e^{i\mathbf{Q} \cdot \mathbf{R}_j}, \quad (2.77)$$

whereas the second comes from the interaction between the magnetic moments of the electrons and the neutron, and was derived in section 2.4.2:

$$\mathbf{A}_{\text{magnetic}}(\mathbf{Q}) = \mathbf{M}_{\perp}(\mathbf{Q}) \quad (2.78)$$

where  $\mathbf{M}_{\perp}(\mathbf{Q})$  is defined in equation (2.68). Usually the nuclear spins are disordered such that the term described by  $\mathbf{A}_{\text{nuclear}}$  in equation (2.77) leads to incoherent scattering. It will therefore be neglected from this point onwards. Applying these considerations, the  $\mathbf{S}$ -matrix for the scattering of a single neutron by an ensemble of atoms may be expressed in the following form:

$$\mathbf{S} = \begin{bmatrix} N(\mathbf{Q}) + M_{\perp z}(\mathbf{Q}) & M_{\perp x}(\mathbf{Q}) - iM_{\perp y}(\mathbf{Q}) \\ M_{\perp x}(\mathbf{Q}) + iM_{\perp y}(\mathbf{Q}) & N(\mathbf{Q}) - M_{\perp z}(\mathbf{Q}) \end{bmatrix}. \quad (2.79)$$

In the remainder of this section, this will be used to derive the combined nuclear and magnetic scattering cross section, with neutron polarisation dependence.

The starting point is equation (2.51). Assuming the Born approximation (incident and exit wavefunctions may be considered plane waves) together with elastic scattering (the state of the sample is unchanged), the cross section becomes

$$\left( \frac{d\sigma}{d\Omega dE_f} \right) = \left( \frac{m}{2\pi\hbar^2} \right)^2 |M|^2 \delta(E_i - E_f), \quad (2.80)$$

and the matrix element  $M$  may be written

$$M = \langle \mathbf{k}_f, \chi_f | V(\mathbf{r}) | \mathbf{k}_i, \chi_i \rangle = \langle \chi_f | V(\mathbf{Q}) | \chi_i \rangle, \quad (2.81)$$

where  $V(\mathbf{Q})$  is the Fourier transform of the interaction potential  $V(\mathbf{r})$ . Since, by definition, the action of this potential is to change the spin state of the neutron from  $|\chi_i\rangle$  to  $|\chi_f\rangle$ , we have

$$|\chi_f\rangle = V(\mathbf{Q})|\chi_i\rangle, \quad (2.82)$$



or, expressed in the  $|\pm\rangle$  basis,

$$\begin{pmatrix} a_f \\ b_f \end{pmatrix} = \mathbf{S} \begin{pmatrix} a_i \\ b_i \end{pmatrix}. \quad (2.83)$$

Thus,

$$|M|^2 = \begin{pmatrix} a_f^* & b_f^* \end{pmatrix} \mathbf{S} \begin{pmatrix} a_i \\ b_i \end{pmatrix} \begin{pmatrix} a_i^* & b_i^* \end{pmatrix} \mathbf{S}^\dagger \begin{pmatrix} a_f \\ b_f \end{pmatrix}. \quad (2.84)$$

Substituting in the  $\mathbf{S}$ -matrix from equation (2.79), we may evaluate this quantity for the four spin-flip processes  $|\pm\rangle \rightarrow |\pm\rangle$ . To do this, one chooses the  $a_{i,f}$  and  $b_{i,f}$  appropriately [for example, a  $|+\rangle \rightarrow |-\rangle$  process requires  $(a_i, b_i) = (1, 0)$  and  $(a_f, b_f) = (0, 1)$ ] to obtain [43]:

$$|M|_{+\rightarrow+}^2 = |N(\mathbf{Q}) + M_{\perp z}(\mathbf{Q})|^2, \quad (2.85)$$

$$|M|_{+\rightarrow-}^2 = |M_{\perp x}(\mathbf{Q}) + iM_{\perp y}(\mathbf{Q})|^2, \quad (2.86)$$

$$|M|_{-\rightarrow+}^2 = |M_{\perp x}(\mathbf{Q}) - iM_{\perp y}(\mathbf{Q})|^2, \quad (2.87)$$

$$|M|_{-\rightarrow-}^2 = |N(\mathbf{Q}) - M_{\perp z}(\mathbf{Q})|^2. \quad (2.88)$$

## 2.4.6 Spherical neutron polarimetry

From the spin-flip cross sections derived in the previous section it is straightforward to generalise to arbitrary polarisations. If the incident neutron beam is polarised perfectly along the  $\pm\hat{\mathbf{e}}_z$  direction respectively, we have [dropping the ' $(\mathbf{Q})$ ' notation]:

$$|\chi_f\rangle = (N \pm M_{\perp z})|+\rangle + (M_{\perp x} \pm iM_{\perp y})|-\rangle, \quad (2.89)$$

$$|M|_{\pm\rightarrow\text{all}}^2 = |N \pm M_{\perp z}|^2 + |M_{\perp x} \pm iM_{\perp y}|^2 \quad (2.90)$$

$$= \langle\chi_f|\chi_f\rangle. \quad (2.91)$$

Now, for arbitrary incident polarisation  $\mathbf{P}$ , chose  $\hat{\mathbf{e}}_z$  parallel to the quantisation axis, *i.e.*  $\hat{\mathbf{e}}_z \parallel \mathbf{P}$ . Since the beam will not be perfectly polarised along this direction, we have in general a fraction  $\frac{1+P}{2}$  of the incident neutrons in a spin state parallel to  $\hat{\mathbf{e}}_z$  and a fraction  $\frac{1-P}{2}$  of the incident neutrons in a spin state parallel to  $-\hat{\mathbf{e}}_z$ . Therefore

$$\begin{aligned} |M|_{\mathbf{P}\rightarrow\text{all}}^2 &= \left(\frac{1+P}{2}\right) (|N + M_{\perp z}|^2 + |M_{\perp x} + iM_{\perp y}|^2) \\ &\quad + \left(\frac{1-P}{2}\right) (|N - M_{\perp z}|^2 + |M_{\perp x} - iM_{\perp y}|^2), \end{aligned} \quad (2.92)$$

which, after simplification and considering similar equations for the cases of neutrons polarised parallel to  $\hat{\mathbf{e}}_x$  and  $\hat{\mathbf{e}}_y$ , results in

$$|M|_{\mathbf{P}\rightarrow\text{all}}^2 = NN^* + \mathbf{M}_{\perp} \cdot \mathbf{M}_{\perp}^* + \mathbf{P} \cdot (N\mathbf{M}_{\perp}^* + N^*\mathbf{M}_{\perp}) - i\mathbf{P} \cdot (\mathbf{M}_{\perp} \times \mathbf{M}_{\perp}^*) = I. \quad (2.93)$$

This formula can be used to determine the scattered intensity (to all polarisation channels) for arbitrary incident polarisation direction  $\mathbf{P}$ .

In a spherical neutron polarimetry experiment, however, it is possible not only to set the polarisation  $\mathbf{P}$  of the incident beam but also to analyse the polarisation  $\mathbf{P}'$  of the scattered beam. It is therefore necessary to calculate the expectation of the scattered polarisation:

$$\mathbf{P}' = \frac{\langle \chi_f | \boldsymbol{\sigma} | \chi_f \rangle}{\langle \chi_f | \chi_f \rangle} = \frac{\langle \chi_f | \boldsymbol{\sigma} | \chi_f \rangle}{I}. \quad (2.94)$$

Calculating the three components of  $\mathbf{P}'$  separately for each of the three Pauli matrices then gives

$$\begin{aligned} I\mathbf{P}' = & \mathbf{P}(NN^*) - \mathbf{P}(\mathbf{M}_\perp \cdot \mathbf{M}_\perp^*) + N\mathbf{M}_\perp^* + N^*\mathbf{M}_\perp + \mathbf{M}_\perp(\mathbf{P} \cdot \mathbf{M}_\perp^*) + \mathbf{M}_\perp^*(\mathbf{P} \cdot \mathbf{M}_\perp) \\ & + i\mathbf{P} \times (N\mathbf{M}_\perp^* - N^*\mathbf{M}_\perp) + i(\mathbf{M}_\perp \times \mathbf{M}_\perp^*). \end{aligned} \quad (2.95)$$

Equations (2.93) and (2.95) can be used together to calculate the scattered intensity from and into arbitrary polarisation states, based on knowledge of the nuclear and magnetic structure factors. Conversely, if these polarimetry data are measured in experiment, then by these equations (known as the ‘Blume-Maleev equations’ [44,45]) one may infer information about the form(s) of the nuclear or magnetic structure factors: this is fundamental to the work presented in chapter 3. As pointed out in [46] and [47], these equations contain terms in pure nuclear scattering ( $\propto NN^*$ ) that conserve the incident polarisation; ‘normal’ magnetic scattering ( $\propto \mathbf{M}_\perp \cdot \mathbf{M}_\perp^*$ ) which flips the polarisation except its component along the magnetic interaction vector; nuclear-magnetic interference terms (mixing  $N$  and  $\mathbf{M}_\perp$ ); and, perhaps most importantly for the present work, ‘chiral’ magnetic scattering ( $\propto \mathbf{M}_\perp \times \mathbf{M}_\perp^*$  which is only non-zero for chiral magnetic structures) which *creates* polarisation along the direction of the scattering vector.

So far I have followed the derivation used by Blume and Maleev [44,45], in which the so-called ‘Blume convention’ is used for the direction of the scattering vector:  $\mathbf{Q}^{(\text{Blume})} := \mathbf{k}_i - \mathbf{k}_f$ . This convention is opposite in sign to the ‘crystallography convention’ which is used throughout the other parts of this thesis. Since, by equations (2.76) and (2.69), a change in the sign of  $\mathbf{Q}$  is equivalent to interchanging  $N \leftrightarrow N^*$  and  $\mathbf{M}_\perp \leftrightarrow \mathbf{M}_\perp^*$ , the only effect is to change the signs of the cross product terms. Thus, in the crystallography convention, the appropriate equations are:

$$I = NN^* + \mathbf{M}_\perp \cdot \mathbf{M}_\perp^* + \mathbf{P} \cdot (N\mathbf{M}_\perp^* + N^*\mathbf{M}_\perp) + i\mathbf{P} \cdot (\mathbf{M}_\perp \times \mathbf{M}_\perp^*), \quad (2.96)$$

and

$$\begin{aligned} I\mathbf{P}' = & \mathbf{P}(NN^*) - \mathbf{P}(\mathbf{M}_\perp \cdot \mathbf{M}_\perp^*) + N\mathbf{M}_\perp^* + N^*\mathbf{M}_\perp + \mathbf{M}_\perp(\mathbf{P} \cdot \mathbf{M}_\perp^*) + \mathbf{M}_\perp^*(\mathbf{P} \cdot \mathbf{M}_\perp) \\ & - i\mathbf{P} \times (N\mathbf{M}_\perp^* - N^*\mathbf{M}_\perp) - i(\mathbf{M}_\perp \times \mathbf{M}_\perp^*). \end{aligned} \quad (2.97)$$

## 2.5 Neutron instrumentation

Neutrons for scientific research are produced either by spallation or from a research reactor. A spallation source (such as the ISIS neutron source, Harwell, UK) generates a pulsed neutron beam by firing proton bunches at a heavy metal target. The time structure of such a beam means that neutrons can be separated easily by wavelength by measuring the time of flight for the neutron to reach the detector. The work presented in chapter 3 of this thesis, however, used a neutron beam originating from a research reactor, specifically the Institut Laue–Langevin (ILL) in Grenoble, France.

### 2.5.1 Research reactors

Nuclear reactors generate neutrons by the nuclear fission of  $^{235}\text{U}$ , a process that releases neutrons (although some of these are absorbed by further uranium nuclei to sustain the reaction). A research reactor is designed to produce a very high neutron flux (in contrast to a power reactor) that can be directed along wave guides to the experimental stations. Before entering the wave guides, the neutrons are passed through a moderator. This slows down the neutrons to speeds (and therefore wavelengths) that are suitable for studying condensed matter systems. The ILL has several different moderators, whose temperatures are chosen depending on the needs of the beamlines that view them. The ILL is currently the most intense neutron source in the world, producing  $1.5 \times 10^{15}$  neutrons  $\text{s}^{-1} \text{cm}^{-2}$ , and the beam is continuous in contrast to spallation sources.

### 2.5.2 Beamline D3

The D3 diffractometer at the ILL uses as a source the hot neutron (2000 °C) moderator H4. The neutrons are monochromatised using diffraction from a polarising Heusler monochromator. This works because, as shown by equations (2.85) and (2.88), the scattered intensity from a magnetic crystal is given by

$$I_{\pm} \propto [N(\mathbf{Q}) \pm M_{\perp z}(\mathbf{Q})]^2, \quad (2.98)$$

where the  $+$  ( $-$ ) indicates scattering of spin-up (-down) neutrons respectively. The materials from which polarising monochromators are made, such as the Heusler alloys, are chosen to have the size of the nuclear scattering [parametrised by  $N(\mathbf{Q})$ ] equal to the magnetic part [parametrised by  $M_{\perp z}(\mathbf{Q})$ ]. In this way, equation (2.98) will give zero scattered intensity for spin-down neutrons, but will be maximum for spin-up neutrons. In other words there is constructive interference between the nuclear and magnetic scattering only when the neutrons are spin-up; otherwise there is destructive interference and no scattered intensity.

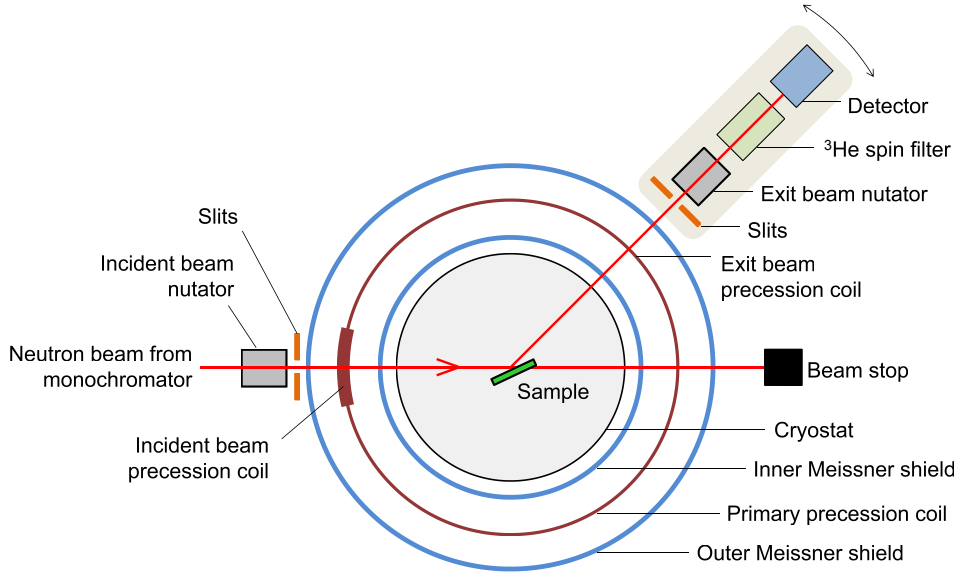


**Figure 2.8:** Schematic diagram of the CRYOPAD (Cryogenic Polarisation Analysis Device) setup. Both the detector arm and sample stage can rotate about the central axis of the device.

This results in a polarised beam of neutrons. The drawback of this technique is that one compromises on the neutron flux, with a typical intensity of  $10^7$  neutrons  $\text{cm}^{-2} \text{s}^{-1}$  incident on the sample.

The monochromatised beam then passes into the CRYOPAD (Cryogenic Polarisation Analysis Device) in order to measure the polarimetry components: a schematic diagram of the experimental arrangement is shown in figure 2.8. Central to the device's operation are the two thin superconducting niobium Meissner shields, which are transparent to neutrons (and do not change their polarisation) but separate the space into three magnetically independent regions [48]. Firstly, the polarised incident beam passes through a nutator: a device which uses magnetic fields to rotate the neutron spins adiabatically<sup>8</sup> to an arbitrary angle from the vertical ( $Z$ -axis). After passing through some slits, the neutrons enter the region between the two Meissner shields, which contains precession coils whose fields make the neutrons undergo Larmor precession about the horizontal axis. In CRYOPAD-III, the incident and exit beam precession coils are completely decoupled [49]. By adjusting the nutator and the precession coil current, the neutron polarisation can be set to be along the  $X$ -,  $Y$ -, or  $Z$ -axes as required. The neutrons then enter the zero field region enclosed by the inner Meissner shield and occupied by the 'Orange' cryostat and sample, and undergo

<sup>8</sup>*i.e.* the change of the magnetic field direction (as seen by the neutron) is slow compared to the neutron's Larmor frequency.

diffraction. In this region the neutron spin direction does not change except for any interaction with the magnetism in the sample. Upon exiting the zero field region, the reverse process occurs of adjusting the neutron spin in a known way, so as to align those neutrons which are polarised in the direction of interest onto the axis of a  $^3\text{He}$  spin filter. Only those neutrons polarised in the correct direction are permitted through the filter and contribute to the intensity measured by the detector.

The spin filter relies on the fact that, for a  $^3\text{He}$  nucleus, the neutron absorption is very strong if the spins of the neutron and the nucleus are antiparallel ( $\sigma_{\text{abs}} = 5931$  barns at  $1 \text{ \AA}$  wavelengths), whereas  $\sigma_{\text{abs}} \approx 0$  if the spins are aligned. Thus, by enclosing polarised  $^3\text{He}$  gas inside a cell that can in turn be placed inside a specially designed surround in front of the detector with a magnetic field to maintain the polarisation (‘Decpol’, [50]), one has a way of spin filtering the neutrons that pass through<sup>9</sup>. Because the  $^3\text{He}$  nuclei become depolarised over time, it is necessary to replace the cell on the order of every 100 hours. The detector used on D3 is a single 5 cm diameter  $^3\text{He}$  gas-filled detector: the incident neutrons generate charged particles in the detector either by forcing the  $^3\text{He}$  nuclei to recoil and ionise, or by undertaking a nuclear reaction. These charged particles are detected as a peak in the voltage across the anode / cathode, proportional to the number of neutrons being detected.

In an actual experiment, the quantities that are measured are *polarimetry components*, which are related to the neutron intensities in given polarisation directions by

$$P_{i \rightarrow j} := \frac{I_{i \rightarrow j} - I_{i \rightarrow -j}}{I_{i \rightarrow j} + I_{i \rightarrow -j}}, \quad (2.99)$$

where  $i, j = X, Y, Z$ . The measured polarimetry components must be corrected for the polarising efficiency of the  $^3\text{He}$  cells which changes over time: this is done automatically by the data acquisition software on D3. In addition the software also corrects the measurements for background (for example, arising from the imperfect polarisation of the beam leaving the monochromator), and when measuring a particular polarimetry component intelligently divides the time between measurements of the two intensities according to their relative sizes, in order to obtain the best statistics.

### 2.5.3 Orient Express

Orient Express is a neutron Laue diffractometer, also located at the ILL. It was used to align the  $\text{RbFe}(\text{MoO}_4)_2$  sample (the focus of chapter 3). This beamline illuminates the

<sup>9</sup>This works because the  $^3\text{He}$  nucleus (a spin-1/2 particle) can capture a neutron (also spin-1/2) to form a spin-0  $^4\text{He}$  nucleus, but only if the two spin-1/2’s are antiparallel in order to conserve spin. The  $^3\text{He}$  gas is polarised indirectly via  $^{85}\text{Rb}$  atoms, which are optically pumped into a specific hyperfine state. These spin polarised atoms then transfer their polarisation to the  $^3\text{He}$  nuclei.

sample with a ‘white’ neutron beam (*i.e.* one containing a broad continuum of different wavelengths) and collects the diffraction pattern from the sample on a large area neutron scintillator coupled to a CCD. The pattern of diffraction spots is directly related to the orientation that the sample has, so this provides an efficient way of adjusting the sample position until a desired orientation is obtained. Further information about the instrument can be found in [51].

## 2.6 Second harmonic generation

The final experimental technique discussed in this chapter is that of optical second harmonic generation (SHG). The following two sections introduce the theory of SHG explaining why it is a useful probe of condensed matter systems, and present details of the laser source used for the experiments.

### 2.6.1 SHG in determining point group symmetries

In linear optics, the electrical polarisation set up inside a material is proportional to the size of the electric field, and these two time varying vector quantities are related by  $\mathbf{P} = \epsilon_0 \chi \mathbf{E}$  where  $\chi$  is the susceptibility matrix. However, once one applies an oscillating electrical field whose strength is of a similar order to that binding the electrons into an atom, nonlinear (anharmonic) effects can also become important. In particular, one can imagine a situation in which multiple photons are absorbed, promoting an electron temporarily from its ground state to an excited state within the atom, before it returns to its ground state radiating light as it does so. This process is shown schematically, for the case where two photons are absorbed, in figure 2.9. Because such high strengths of field (of order  $10^5 \text{ V cm}^{-1}$ ) are needed, the development of the laser was necessary before nonlinear optical effects could be observed [52].

Each of the transitions made by the electron may be either of electric dipole (ED) or magnetic dipole (MD) type<sup>10</sup>. Since the strongest of these is the ED transition, in the following it will be assumed that the incident laser beam leads to atomic transitions that are ED type, whereas the electron may radiate in either a single ED or MD transition. An ED transition will lead to a nonlinear polarisation  $\mathbf{P} = (P_x, P_y, P_z)$ , which in its general form has components given by<sup>11</sup>:

$$P_i \propto \chi_{ij}^{\text{ED},1} E_j + \chi_{ijk}^{\text{ED},2} E_j E_k + \chi_{ijkl}^{\text{ED},3} E_j E_k E_l + \dots \quad (2.100)$$

<sup>10</sup>Higher orders will not be considered here.

<sup>11</sup>In this and the following, summation convention is used whereby repeated indices are assumed to be summed over all their values  $\{x, y, z\}$ .

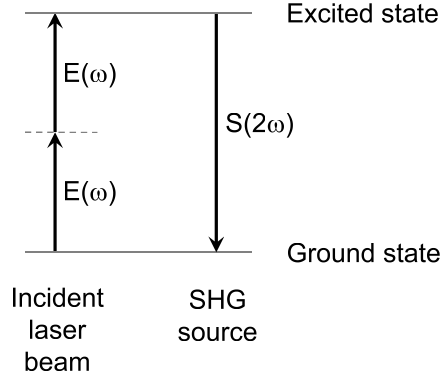


**Figure 2.9:** Schematic of the SHG process at an atomic level.

Similarly, MD transitions lead to a nonlinear magnetisation  $\mathbf{M} = (M_x, M_y, M_z)$  whose components are given by

$$M_i \propto \chi_{ij}^{\text{MD},1} E_j + \chi_{ijk}^{\text{MD},2} E_j E_k + \chi_{ijkl}^{\text{MD},3} E_j E_k E_l + \dots \quad (2.101)$$

The higher order terms in this expansion correspond to nonlinear processes in which two (or generally  $n$ ) photons of frequency  $\omega$  are absorbed by an electron in making a transition to an excited atomic state within the material. The electron then returns to its ground state, radiating a single photon of frequency  $2\omega$  (or  $n\omega$ ).

In optical SHG experiments, elements of the second order susceptibility tensors  $\chi_{ijk}^{\text{ED}}$  and  $\chi_{ijk}^{\text{MD}}$  (dropping the ‘2’ labels) are measured by examining the polarisation dependence of the second harmonic signal. The reason why one should want to measure these components is because, in determining which components of the tensors are non-zero, one typically imposes quite serious restrictions on the possible point symmetry of the material. Thus, SHG is a convenient way to determine the point group (whether crystallographic or magnetic) belonging to a particular system. Since SHG relies on atomic transitions within the material being studied, it is to be expected that the efficiency of the process will vary dramatically with the wavelength of the incident (fundamental) light. In particular, if the energy is tuned to an atomic transition then a large resonant enhancement of the SHG will be expected.

The ED or MD radiative transitions that occur in an SHG process allow one to construct a source term,  $\mathbf{S}(2\omega)$ , from which the radiated intensity may be calculated:  $I(2\omega) \propto |\mathbf{S}(2\omega)|^2$ . The source term is related to the nonlinear polarisation  $\mathbf{P}(2\omega)$  and nonlinear magnetisation  $\mathbf{M}(2\omega)$  via [53]:

$$\mathbf{S}(2\omega) = \mu_0 \frac{\partial \mathbf{P}(2\omega)}{\partial t^2} + \mu_0 \left[ \nabla \times \frac{\partial \mathbf{M}(2\omega)}{\partial t} \right]. \quad (2.102)$$

The free energy associated with the SHG is written

$$F_{\text{SHG}} = - [\chi_{ijk}^{\text{ED}} E_i^*(2\omega) E_j(\omega) E_k(\omega) + \chi_{ijk}^{\text{MD}} H_i^*(2\omega) E_j(\omega) E_k(\omega) + \text{c.c.}] . \quad (2.103)$$

The free energy must be invariant under those symmetry operations that leave the sample invariant, in particular those of time reversal and spatial inversion symmetries. This immediately imposes constraints on the allowed non-zero components of the nonlinear susceptibility tensors. This is true in general: Neumann's principle states that any symmetry element exhibited by the point group of a crystal must also be obeyed by the tensor describing any physical property of the crystal, whether that tensor describes magnetic phenomena [54] or other properties such as mechanical strain [55].

If time reversal symmetry is present, for example in SHG due to symmetry breaking by the crystallographic structure, then the susceptibility tensors must be time-reversal-invariant (*i*-type). Non-time-reversal-invariant (*c*-type) tensors are allowed if, for example, the SHG occurs as a result of symmetry breaking due to the magnetic ordering within a crystal. Inversion symmetry places further restrictions on the symmetry of the tensors. In particular,  $\chi_{ijk}^{\text{ED}}$  must be zero if inversion symmetry is present. In the first term of equation (2.103),  $E_i^*$ ,  $E_j$ , and  $E_k$  will all change sign under inversion, but by Neumann's principle  $\chi_{ijk}^{\text{ED}}$  cannot – it must therefore be zero if  $F_{\text{SHG}}$  is to remain the same. However,  $\chi_{ijk}^{\text{MD}}$  is not subject to this restriction, and can sometimes lead to SHG when there is inversion symmetry in the crystal. If time reversal *combined with* inversion is a symmetry operation of the crystal then both ED and MD contributions to the SHG susceptibility must vanish. In a similar way to this, one can consider the effect of any other point symmetries on the tensor components, and use this information to determine which components should be non-zero. Conversely, the existence of certain tensor components as measured experimentally can be used to determine (or rule out) point symmetries.

Finally, this sensitivity to the point group symmetry may be used in time-resolved optical experiments, where an optical ‘pump’ pulse perturbs the state of the sample some time  $\Delta t$  before the arrival of a ‘probe’ pulse, which is tuned to an energy at which SHG occurs. By varying  $\Delta t$  and observing the effect on the SHG, one is able to build up a picture of how the pump affects the crystallographic and/or magnetic symmetries of the sample.

### 2.6.2 Laser light sources

The experiments presented in chapter 6 were all carried out using the 800 nm output from a Ti:sapphire femtosecond laser system. This pulsed source has a repetition rate of 1 kHz and pulse duration of  $\approx 120$  fs. SHG processes tend to be very wavelength dependent, and it is therefore desirable to be able to adjust the wavelength of the light incident on the



sample. This is achieved by means of an *optical parametric amplifier* (OPA). Such a system combines a pump beam of frequency  $\omega_p$  with a weaker signal beam of frequency  $\omega_s$  in a nonlinear medium.

Consider the expression for the second order polarisation [the second term on the right of equation (2.100)], but for the case where photons of two different frequencies  $\omega_p$  and  $\omega_s$  are present. The electric field will therefore contain two frequency components:  $E(t) = E_p e^{-i\omega_p t} + E_s e^{-i\omega_s t} + \text{c.c.}$  and if the electric field is oriented so as to excite a particular tensor element  $\chi^{(2)}$  there will be a nonlinear polarisation given by

$$P^{(2)}(t) \propto E(t)E^*(t) \quad (2.104)$$

$$\begin{aligned} &= \text{constant} + E_p^2 e^{-2i\omega_p t} + E_s^2 e^{-2i\omega_s t} \\ &\quad + 2E_s E_p e^{-i(\omega_p + \omega_s)t} + 2E_p E_s^* e^{-i(\omega_p - \omega_s)t} + \text{c.c.} \end{aligned} \quad (2.105)$$

In addition to the standard frequency doubled terms, this also gives rise to sum frequency and difference frequency terms, and will lead to extra beams being generated at these frequencies. In an OPA, the difference frequency beam is known as an ‘idler’ with frequency  $\omega_i$ , and energy conservation requires that

$$\hbar\omega_p = \hbar\omega_s + \hbar\omega_i. \quad (2.106)$$

The OPAs used here are two-stage TOPAS-C’s from Light Conversion, optimised for the near infrared. Two stages of amplification are necessary to minimise deviations from the phase matching condition required for efficient nonlinear processes. A small portion of the incident 800 nm light is used to generate a white light continuum in a sapphire crystal (this is due to a highly nonlinear process in which the pulse spectrum is broadened [56]). The 800 nm light is then filtered out leaving only the broadened spectrum. In the first amplification stage, this continuum is directed into a  $\beta$ -barium borate (BBO) crystal and mixed with some of the 800 nm light. As the continuum is dispersed in time, only light whose frequency is such that it arrives at the same instant as the 800 nm pulse is amplified to produce the desired wavelength. A delay stage is used to adjust the relative arrival times of the continuum and 800 nm pulses: in this way a specific wavelength can be generated for the signal beam that is incident on the second amplification stage. Here, another BBO crystal is used to mix the 800 nm pump and the signal beam. This leads to beams of frequencies  $\omega_p$ ,  $\omega_s$ ,  $\omega_{p+s}$  and  $\omega_i$  all leaving the BBO in a collinear arrangement. A dichroic mirror is then used to separate out the pump and sum frequency beams before the signal and idler beams leave the OPA (these are separated further downstream with additional dichroic mirrors). The OPAs are able to generate signal beams with wavelengths between 1180 and 1620 nm, and idler beams between 1620 and 2680 nm.

For the work presented in this thesis, the signal beam from one OPA at 1220 nm was used for the SHG, with the 800 nm output from the laser used in addition for time-resolved experiments to pump the samples. Further details of the experimental setup beyond the generation of laser light will be presented in chapter [6](#).

## Chapter 3

---

# Multiferroicity in ferroaxial $\text{RbFe}(\text{MoO}_4)_2$

---

### 3.1 Introduction

In ‘type-II’ multiferroics, ferroelectricity appears as a consequence of the magnetic ordering which is responsible for breaking inversion symmetry within the crystal. Such materials are of particular interest in applications, since they clearly have a strong coupling between the magnetic and ferroelectric orderings. Of the type-II materials, the cycloidal multiferroics (such as  $\text{TbMnO}_3$  [9],  $\text{Ni}_3\text{V}_2\text{O}_8$  [57], and  $\text{MnWO}_4$ , the subject of chapter 6) have been well-studied. In these systems the spins rotate within a plane that contains the propagation direction of the incommensurate modulation. This allows a ferroelectric polarisation to be induced by the ‘inverse Dzyaloshinskii-Moriya interaction’, and it has the form  $\mathbf{P} \propto \hat{\mathbf{r}}_{ij} \times (\mathbf{S}_i \times \mathbf{S}_j)$  where  $\hat{\mathbf{r}}_{ij}$  is a polar vector connecting adjacent spins in the cycloid  $\mathbf{S}_i$  and  $\mathbf{S}_j$  [58, 59].

The range of candidate materials that may exhibit spin driven ferroelectricity extends beyond the cycloidal multiferroics, however. An interesting line of research has developed specifically on the magnetochiral or proper screw systems, in which the atomic spins rotate perpendicularly to the propagation direction of the screw; the above mechanism predicts zero polarisation in this case. One mechanism that *can* lead to an electrical polarisation here is a coupling to the crystal structure if it has ‘axial’ symmetry. This is known as ‘ferroaxial coupling’ and invokes a coupling between the magnetic ordering and a rotational distortion in the crystal structure to support a ferroelectric polarisation in the system.

These ideas are explored in depth in this chapter, using the relatively simple system of  $\text{RbFe}(\text{MoO}_4)_2$  (RFMO) as a test of the interplay between the different orderings (magnetic, electric, and structural). The main experimental technique of this chapter, spherical neutron polarimetry, is used to investigate how RFMO’s magnetic structure changes with the direction of the ferroelectric polarisation in the material (controlled by an applied electric field). RFMO is a particularly appropriate system upon which to test the ideas of ferroaxial

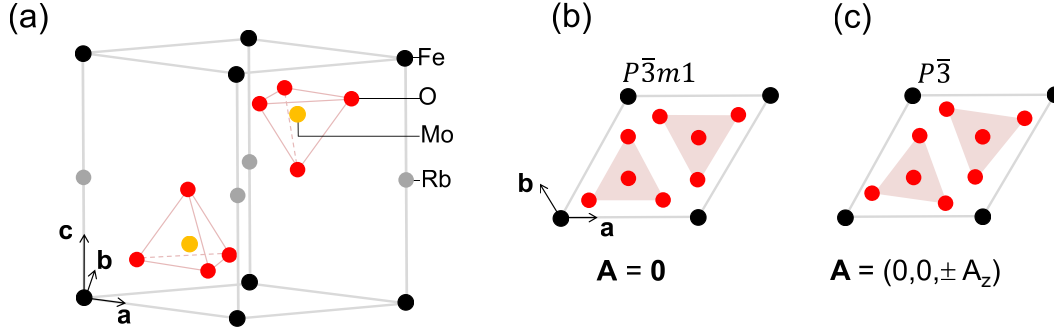


**Figure 3.1:** (a) The crystal structure of  $\text{RbFe}(\text{MoO}_4)_2$  [one unit cell is drawn]. (b) A view of the crystal structure with  $\mathbf{c}$  pointing out of the page, at a temperature above that of the structural (axial) transition  $T_c$ . Below  $T_c$  there is a rotation of the  $\text{MoO}_4$  tetrahedra [shown in (c)], associated with a non-zero axial vector  $\mathbf{A}$ . The mirror planes that were present in the parent phase are lost and consequently the symmetry is reduced from  $P\bar{3}m1$  to  $P\bar{3}$ .

coupling, since a direct link can be made between the structural distortion and the strength of the various magnetic exchange pathways. As a prelude to the experimental findings, I consider the exchange interaction energies for different structural domains and use them to determine which magnetic structures are favoured. The results of this work may be readily generalised to other more complex ferroaxial multiferroics, for example  $\text{Cu}_2\text{Nb}_2\text{O}_8$  [60] and  $\text{CaMn}_7\text{O}_{12}$  [19].

## 3.2 The structural transition in $\text{RbFe}(\text{MoO}_4)_2$

### 3.2.1 Axial distortions in $\text{RbFe}(\text{MoO}_4)_2$

The crystal structure of RFMO is shown in figure 3.1(a). It consists of a single magnetic Fe ion per unit cell, in between which are located  $\text{MoO}_4$  tetrahedra (two per unit cell). Rb ions, which take no part in any structural changes and do not contribute to the magnetism of the sample, are positioned between the two tetrahedra.

Below  $T_c = 190$  K, RFMO undergoes a structural transition in which the  $\text{MoO}_4$  tetrahedra rotate about an axis  $\hat{\mathbf{n}} \parallel \mathbf{c}$ , lowering the symmetry from  $P\bar{3}m1$  to  $P\bar{3}$  [61, 62]. This is shown in figures 3.1(b) for  $T > T_c$ , and 3.1(c) for  $T < T_c$ . These structural rotations may be parametrised by an axial vector,  $\mathbf{A}$ . Such a vector is appropriate because its direction is not changed by spatial inversion (in contrast to polar vectors: see chapter 1). Figure 3.2 shows why this is the case and compares it to the familiar example of the orbital angular momentum of a rotating sphere in classical mechanics. (Note, however, that angular momentum is time reversal odd, whereas time reversal has no effect on the axiality exhibited by the RFMO crystal structure since this is a ‘static’ rotation.) Since we would like to

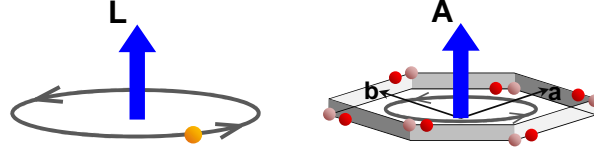


**Figure 3.2:** The orbital angular momentum of a rotating sphere is described by an axial vector  $\mathbf{L}$  whose sign is not changed by inversion (left). Similarly, one can define an axial vector  $\mathbf{A}$  resulting from a crystallographic distortion (shown schematically right). In the case of RFMO, the distortion moves the oxygen ions around the central Fe ion from the pink to the red positions, but inversion symmetry is retained.

connect the direction of  $\mathbf{A}$  to the sense of the structural rotation, it is convenient to employ a ‘right-hand rule’ (in complete analogy to the angular momentum  $\mathbf{L}$ ) in which the axial vector  $\mathbf{A}$  points along  $+$  ( $-$ )  $\mathbf{c}$  for anticlockwise (clockwise) rotation respectively. This definition will be made more rigorous in section 3.5.1.

The two senses in which the oxygen ions may rotate are entirely equivalent from an energetics point of view, so we expect a real crystal of RFMO to consist of roughly equal populations of two ‘axial’ domains: one in which the rotation is clockwise, and the other in which it is anticlockwise. The associated axial vectors are therefore of the form  $\mathbf{A} = (0, 0, \pm A_z)$ . The existence of these two axial domains will be important in explaining the neutron scattering results that follow in this chapter.

### 3.2.2 Ferroaxiality

The fact that RFMO has this axial distortion may be used to better understand why, from a symmetry point of view, materials like RFMO are multiferroic. In general terms (without any specific material in mind), assume that the onset of a magnetic structure below some temperature  $T_N$  breaks inversion symmetry and can therefore be associated with a chirality  $\sigma$ , a scalar quantity. If the point group of the crystal structure allows the existence of an axial vector  $\mathbf{A}$  (for example, symmetry elements such as mirror planes which lie along the direction of  $\mathbf{A}$  are not allowed since this would require  $\mathbf{A} = \mathbf{0}$ ) in the parent phase above  $T_N$ , then this axial vector may couple to the chirality below  $T_N$  to give rise to a polar vector  $\mathbf{P}$  of the form

$$\mathbf{P} \propto \sigma \mathbf{A}. \quad (3.1)$$

Note that this transforms correctly as a polar vector (*i.e.* is odd under spatial inversion, and even under time reversal<sup>1</sup>). Thus a ferroelectric polarisation would, by symmetry, be

<sup>1</sup>Time reversal has no effect on the magnetic chiralities (either helical or triangular – see section 3.3) that are relevant to this work.

allowed below  $T_N$ . The associated term in the free energy would have the following trilinear form:

$$F_{\text{ax}} = c\sigma \mathbf{A} \cdot \mathbf{P}, \quad (3.2)$$

where  $c$  is a coupling constant (note that  $F_{\text{ax}}$  is one of the allowed terms which sum together to give the total free energy  $F$ ). It is clear that should an external electric field  $\mathbf{E}$  be applied to the sample and used to change the direction of  $\mathbf{P}$ , the system could respond by changing the sign of the magnetic structure (parametrised by  $\sigma$ ) in order to keep the free energy at a minimum. Thus this may provide a route towards the coupling required for an electric field to stimulate a change in the magnetic structure.

Point groups in which the above scenario can occur, called here ‘ferroaxial point groups’, require:

1. that the parent phase does not allow the existence of ferroelectricity by symmetry (so that the onset of ferroelectric polarisation occurs due to the symmetry breaking of the magnetic structure and not some other effect); and
2. that the point group symmetry elements allow for the existence of a non-zero axial vector in at least one direction.

There are seven such ferroaxial groups:  $\bar{1}$ ,  $2/m$ ,  $\bar{3}$ ,  $\bar{4}$ ,  $\bar{6}$ ,  $4/m$ , and  $6/m$ . All of these, with the exception of  $\bar{1}$ , define a unique direction in which the axial vector must point. In the case of RFMO (which has  $\bar{3}$  ferroaxial symmetry), this is along the  $\mathbf{c}$  direction as shown previously.

### 3.3 Magnetic ordering

The  $\text{Fe}^{3+}$  ions ( $S = 5/2$ ) [63] are responsible for the magnetic properties of RFMO. There is one magnetic ion per unit cell, located at the origin. The system is known to exhibit a strong anisotropy, keeping the spins fixed within the  $ab$  plane [64]. Hence the magnetic moments in RFMO, which are arranged on a stacking of triangular lattices, are frustrated since the nearest neighbour in-plane interactions are all antiferromagnetic. The lowest energy configuration of the spins is therefore the  $120^\circ$  structure, in which the spins in any given  $ab$  plane are all positioned  $120^\circ$  apart<sup>2</sup>. Thus, the magnetic structure of RFMO below  $T_N \approx 4$  K [61] essentially consists of a  $120^\circ$  structure in-plane, with the spins in adjacent

<sup>2</sup>In order to determine the lowest energy configuration of a triangle of spins  $\mathbf{S}_i$  ( $i = 1, 2, 3$ ) one should minimise the exchange energy  $E = JS^2(\cos \theta_{12} + \cos \theta_{23} + \cos \theta_{31})$  where  $\theta_{ij}$  is the angle between the  $i$ th and  $j$ th spins,  $J$  is the exchange constant (taken here to be positive since the interactions are antiferromagnetic), and  $S$  is the magnitude of the spin. Since  $\theta_{31} = 360^\circ - \theta_{12} - \theta_{23}$ , we should minimise the quantity  $E/(JS^2) = \cos \theta_{12} + \cos \theta_{23} + \cos \theta_{12} \cos \theta_{23} - \sin \theta_{12} \sin \theta_{23}$ . Doing this separately with respect to both  $\theta_{12}$  and  $\theta_{23}$  leads immediately to  $\theta_{12} = \theta_{23} = \theta_{31} = 120^\circ$ .

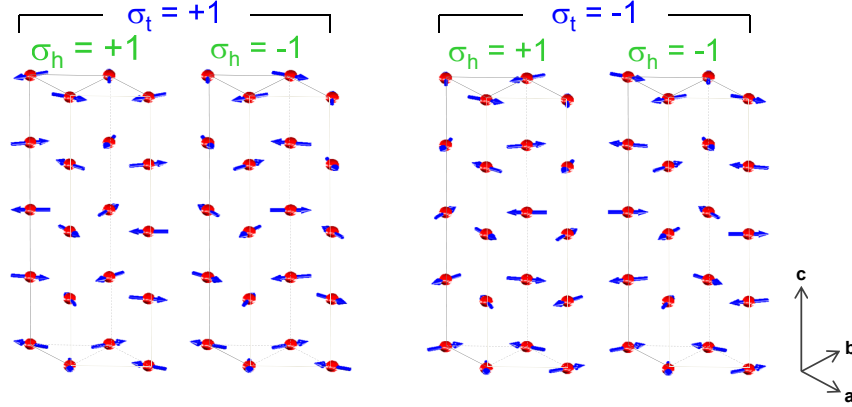


**Figure 3.3:** Sketch of the four different magnetic structures that exist in  $\text{RbFe}(\text{MoO}_4)_2$  (four unit cells are shown for each). Each structure can be associated with both a helical chirality  $\sigma_h$  and a triangular chirality  $\sigma_t$ .

planes undergoing a global rotation by some angle determined by the out-of-plane exchange constants. The magnetic propagation vectors are of the form  $\mathbf{q} = (q_1, q_1, q_2)$ , where

$$q_1 = \pm 1/3, \quad q_2 \approx \pm 0.44, \quad (3.3)$$

and satellite peaks corresponding to these values were observed in our neutron diffraction data. The structure is incommensurately modulated along the  $\mathbf{c}$  direction, and since  $q_2$  is close to  $1/2$  the spins are close to anti-aligned on adjacent layers.

As shown in figure 3.3, such an arrangement of spins leads to four ways of propagating a long range structure through the crystal [each can be thought of as corresponding to the different signs of  $q_1$  and  $q_2$  in equations (3.3); see also section 3.6]. These structures can be described by (i) a *helical chirality*  $\sigma_h$ , which determines the sense in which adjacent spins rotate as one moves along the  $\mathbf{c}$  direction, and (ii) a *triangular chirality*  $\sigma_t$  which determines the in-plane arrangement of spins. These quantities are rigorously defined in section 3.5.1.

As one would expect, the magnetic structure changes significantly under the influence of an applied magnetic field [64] as it becomes favourable for the structure to develop a ferromagnetic component along the direction of the field. The work presented here, however, is restricted to the case where a zero magnetic field is applied to the sample (indeed, this is a requirement if the technique employed in the CRYOPAD apparatus is to work: see section 2.5.2).

### 3.4 Ferroelectricity

RFMO was recently reported to exhibit a small ferroelectric polarisation below  $T_N$  [65]. Such a polarisation was successfully measured on the present samples by integrating the

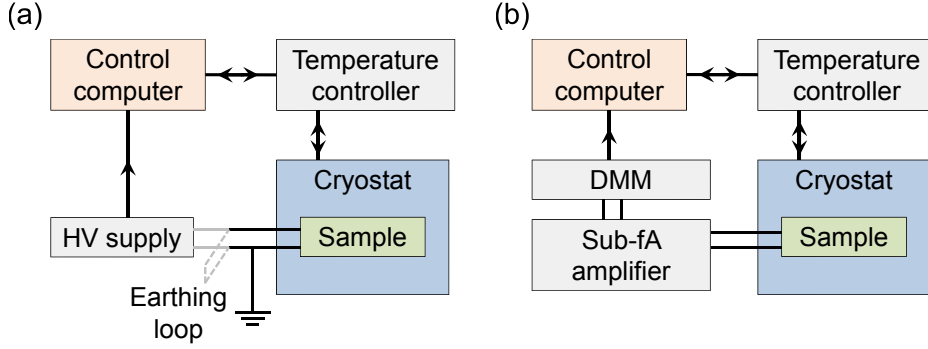


**Figure 3.4:** Experimental arrangements for (a) field cooling, and (b) measuring pyroelectric currents. Bold lines indicate data / control flow; fine lines indicate wires making up electrical circuits. HV: high voltage; DMM: digital multimeter.

pyroelectric current. This technique, which works by measuring the change in surface charges on the sample surface as a function of temperature, is described in more detail below.

### 3.4.1 Experimental arrangement

The experimental arrangement is depicted schematically in figure 3.4. A control computer communicates with an Oxford Instruments ITC503S temperature controller which is responsible for setting and reading the temperature at the sample position in a cryostat. The sample has silver paint contacts painted onto either side, and these are connected via a pair of wires to a feedthrough from the cryostat insert. For field cooling the sample, the arrangement in figure 3.4(a) is used: a Keithly high voltage (HV) power supply is connected across the sample with one contact connected to earth. The HV supply can be removed and an earthing loop connected once field cooling is complete, removing any initial surface charges that are present.

To measure the pyroelectric current, a sub-fA current to voltage amplifier is connected across the sample (using a short connector to minimise noise). This outputs a voltage which is read by a Keithley digital multimeter, the output of which is logged by the control software, along with the temperature and the time (measured by the computer's internal clock) since the start of the measurement.

### 3.4.2 Integrating the pyroelectric current measurements

Acquiring the ferroelectric polarisation  $P(t)$  as a function of time relies on being able to integrate a measured pyroelectric current at time  $t$ ,  $I(t)$ . This is given, for a sample of area



$A$ , by

$$I(t) = A \frac{dP(t)}{dt} \quad (3.4)$$

such that

$$P(t) = \frac{1}{A} \int_{t_{\text{final}}}^t dt' I(t'). \quad (3.5)$$

In order to obtain  $P$  as a function of the temperature  $T$  it is necessary to measure the temperature, as well as the time, for each data point. Thus, to be able to use this technique, one must record for the  $n$ th data point the values of  $(I_n, t_n, T_n)$ ,  $n = 1, \dots, N$ . We may then compute the integral in equation (3.5) numerically to give a set of  $(P_m, T_m^{(\text{mid.})})$  values (where  $m = 1, \dots, N - 1$ ) comprising

$$P_m = \frac{1}{A} \sum_{n=m}^{N-1} \frac{(I_n + I_{n+1})}{2} (t_{n+1} - t_n), \quad (3.6)$$

$$T_m^{(\text{mid.})} = \frac{T_{m+1} + T_m}{2}, \quad (3.7)$$

where the trapezium rule has been used to approximate the area under the  $P(t)$  curve, and  $T_m^{(\text{mid.})}$  is the average (midpoint) of the temperatures corresponding to those in the data points at either side of the  $m$ th trapezium.

### 3.4.3 Results

The pyroelectric currents were measured as described above, following cooling in an applied electric field of  $\pm 7 \text{ kV cm}^{-1}$  (*i.e.* an applied voltage along the  $\mathbf{c}$  direction of  $\pm 175 \text{ V}$  with respect to the side of the sample that was earthed, across a sample of thickness  $250 \text{ }\mu\text{m}$ ). Initially the sample was field cooled from a temperature of  $\approx 10 \text{ K}$  through  $T_N$  down to base temperature. The high voltage supply was removed and the contacts shorted out, and the sample was left (with shorted contacts) at base temperature for 5 minutes. The shorting cable was removed and the current amplifier (outputting a voltage proportional to the measured current with a factor of  $10^{12}$  gain) was connected across the sample. The voltage from the amplifier was measured, along with the sample temperature and time, as the sample was warmed through the ferroelectric transition. This process was carried out for both positive and negative field coolings, and the integrated pyroelectric currents (*i.e.* the ferroelectric polarisations) are plotted in figure 3.5(a).

Following this, another sample from the same batch was measured, this time waiting for 25 minutes at base temperature with maximum pumping on the liquid-He. This allowed the sample to cool to a lower temperature than previously, and the pyroelectric currents from  $\approx 2 \text{ K}$  were measured: these are plotted in figure 3.5(b). This sample was subsequently used for the neutron scattering experiment presented later in this chapter. Note that the

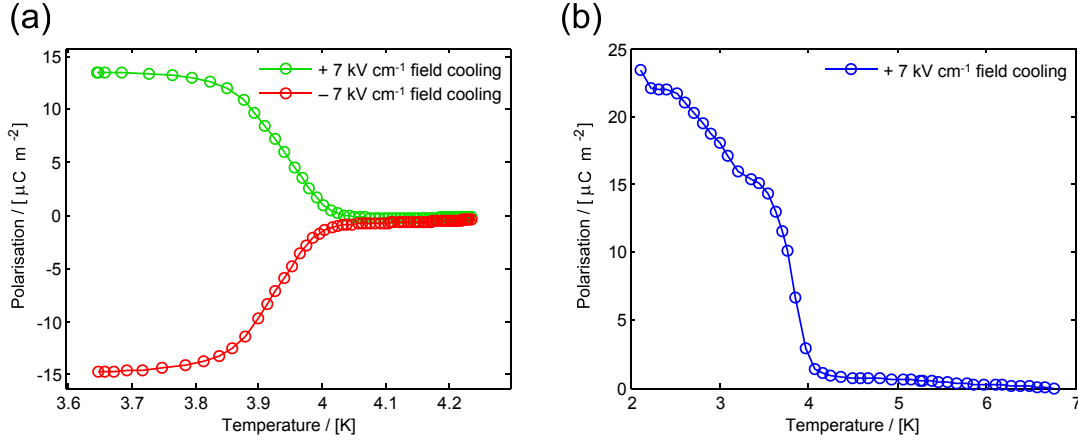


**Figure 3.5:** Ferroelectric polarisation measurements, obtained by integrating the pyroelectric currents, on  $\text{RbFe}(\text{MoO}_4)_2$ . (a) Behaviour in the proximity of the transition in both positive and negative electric field coolings. (b) Data from the neutron scattering sample (taken with positive field cooling), in which the sample was cooled to lower temperatures. The polarisation does not appear to saturate within the obtainable temperature range.

polarisation does not appear to saturate within the range of temperatures studied here. This is consistent with the data presented in [65] on the same system, although our samples show a higher value of the polarisation compared to these data.

### 3.5 Energy calculations

In this section I examine the symmetric exchange energies present in RFMO in each of the axial domains, and establish the rôle played by the axuality in separating different magnetic states in energy. I also use symmetry constraints to determine which terms are allowed to appear in the free energy, and explain the ferroaxial coupling in more detail.

#### 3.5.1 Definitions

It is necessary to provide rigorous definitions of the following key parameters:

##### Axuality, $\mathbf{A}$

The vector  $\mathbf{A}$  is an axial vector associated with the structural distortion. It is defined relative to a fixed external vector  $\mathbf{v}_{\text{ext}}$ , which is a reference vector pointing along the  $\mathbf{c}$  direction that is rigidly attached to the sample.  $\mathbf{A}$  is defined as positive ( $\mathbf{A}^+$ ) if the sense of the rotational distortion is anticlockwise with respect to  $\mathbf{v}_{\text{ext}}$  (*i.e.* with one's thumb pointing along  $\mathbf{v}_{\text{ext}}$  the rotation of the tetrahedra is described by the direction of the fingers on one's

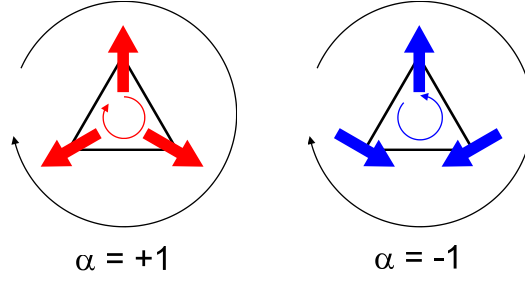


**Figure 3.6:** Examples of positive and negative staggered triangular chirality. As one circumscribes each triangle in the sense indicated by the outer black circular arrow, the spins rotate in either the same ( $\alpha = 1$ , red circular arrow) or opposite ( $\alpha = -1$ , blue circular arrow) sense.

right hand); or negative ( $\mathbf{A}^-$ ) in the opposite case (left-handed). Note that this definition reverses under  $\mathbf{v}_{\text{ext}} \rightarrow -\mathbf{v}_{\text{ext}}$ .

### Helical chirality, $\sigma_h$

The standard definition of helical chirality is adopted, namely

$$\sigma_h = \frac{(\mathbf{S}_1 \times \mathbf{S}_2) \cdot \mathbf{r}_{12}}{|(\mathbf{S}_1 \times \mathbf{S}_2) \cdot \mathbf{r}_{12}|}, \quad (3.8)$$

where  $\mathbf{S}_1$  and  $\mathbf{S}_2$  are axial vectors describing the spins at two sites linked by the polar vector  $\mathbf{r}_{12}$ . This definition is independent of the direction of  $\mathbf{v}_{\text{ext}}$ .

### Triangular chirality, $\sigma_t$

The triangular chirality is defined as

$$\sigma_t = \alpha \frac{\mathbf{v} \cdot \mathbf{v}_{\text{ext}}}{|\mathbf{v} \cdot \mathbf{v}_{\text{ext}}|}, \quad (3.9)$$

where  $\alpha$  is the staggered triangular chirality (figure 3.6) and  $\mathbf{v}$  is a vector that points along the direction of the nearest  $\text{MoO}_4$  tetrahedron to the triangle in question [see figure 3.7(b)]. In the convention used here  $\alpha$  is equal to +1 if, as one circumscribes the triangle in a certain sense, the spins rotate in the same sense; or  $-1$  if the spins rotate in the opposite sense. Since  $\alpha$  changes sign from one triangle to the next [figure 3.7(a)], obtaining a uniquely valued macroscopic quantity over the whole crystal requires the coupling to  $\mathbf{v}$  [figure 3.7(b)] which, like  $\alpha$ , also alternates sign in adjacent triangles. This definition of  $\sigma_t$ , while slightly more cumbersome than similar definitions in materials with only one triangle per unit cell<sup>3</sup>, is necessary because of the presence of both ‘up’ and ‘down’ triangles which are joined

<sup>3</sup>See, for example, the triangular chirality discussed in [66] exhibited by the langasite compound  $\text{Ba}_3\text{NbFe}_3\text{Si}_2\text{O}_{14}$ .

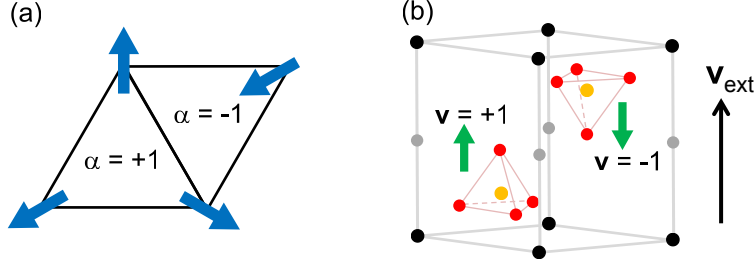


**Figure 3.7:** (a) A triangular lattice with  $120^\circ$  spin structure exhibits both positive and negative staggered triangular chirality  $\alpha$ , depending upon whether the triangle in question is pointing ‘up’ or ‘down’ the page as depicted here. (b) Invoking a coupling to the vector  $\mathbf{v} = \pm \hat{\mathbf{e}}_z$  allows one to construct a macroscopic triangular chirality.

together to form the lattice. Due to the definition in equation (3.9),  $\sigma_t$  changes sign under  $\mathbf{v}_{\text{ext}} \rightarrow -\mathbf{v}_{\text{ext}}$ .

An alternative definition of triangular chirality is given by the expression

$$\sigma_t = \frac{2}{3\sqrt{3} S^2} (\mathbf{S}_1 \times \mathbf{S}_2 + \mathbf{S}_2 \times \mathbf{S}_3 + \mathbf{S}_3 \times \mathbf{S}_1) \cdot \mathbf{v}, \quad (3.10)$$

where the prefactor ensures that  $|\sigma_t| = 1$  and the sense of rotation of the spins is determined by the cross products.

### Polarisation, $\mathbf{P}$

Since  $\mathbf{P} = (0, 0, P_z)$ , this is simply defined as positive if  $P_z$  is along  $+\mathbf{v}_{\text{ext}}$ , or negative if  $P_z$  is along  $-\mathbf{v}_{\text{ext}}$ . It therefore changes sign under  $\mathbf{v}_{\text{ext}} \rightarrow -\mathbf{v}_{\text{ext}}$ .

### 3.5.2 Symmetric exchange energies

In this part I consider the energies associated with the various symmetric exchange interactions in RFMO. The relevant super-super-exchange paths mediated by the oxygen ions are shown in figure 3.8 and described in detail below.

- $J_1$  is the in-plane nearest neighbour exchange path. This will be mediated by two routes, via the pairs of oxygens above and below the plane. Since the tetrahedra on both routes rotate in the same direction during the axial distortion, the overall effect is for this exchange path to remain unchanged below  $T_c = 190$  K.
- $J_2$  is the nearest neighbour out-of-plane exchange path. It is mediated by the oxygens as shown in figure 3.8 (dashed line) and, as with  $J_1$ , will remain unchanged during the distortion. This is because the rotation of the lower tetrahedra increases the first

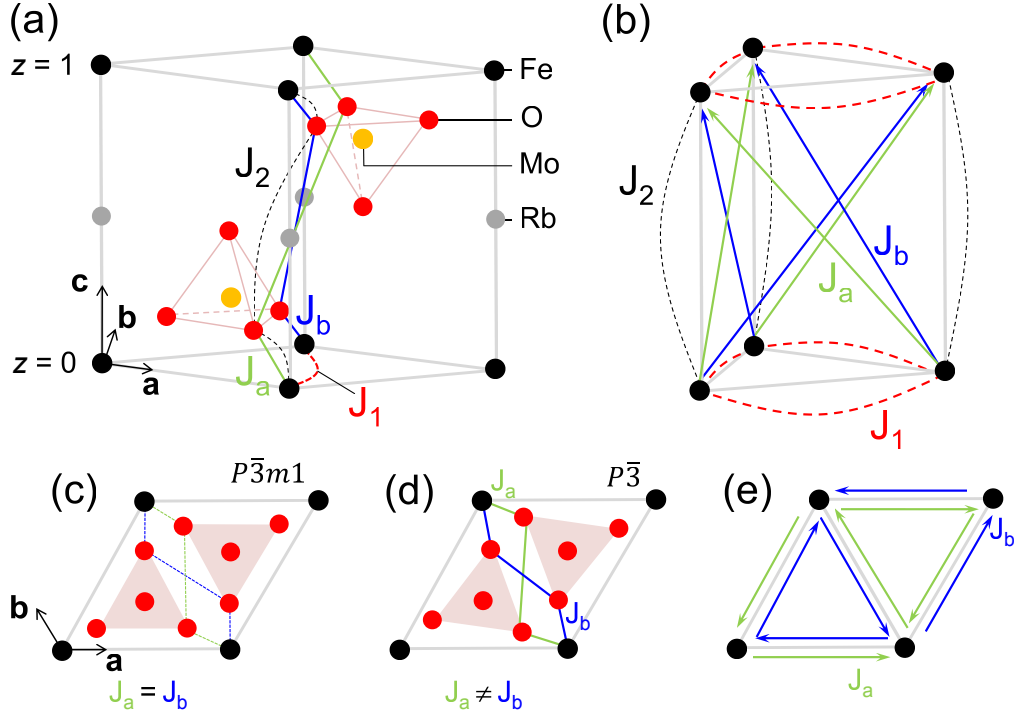


**Figure 3.8:** The exchange paths in  $\text{RbFe}(\text{MoO}_4)_2$ . (a) Three-dimensional view showing in-plane ( $J_1$ ) and vertical ( $J_2$ ) pathways, as well as the two diagonal paths ( $J_a$  and  $J_b$ ) which depend on the ferroaxial distortion. (b) The effect of applying the threefold symmetry on the interactions. (c) to (e) The difference between  $J_a$  and  $J_b$  paths arising from the axial distortion. In the high temperature phase (c) the two paths are equal, but in the low temperature  $P\bar{3}$  phase (d) they become distinct.

$\text{Fe}(z=0)$ –O distance, but the rotation of the upper one shortens the O– $\text{Fe}(z=1)$  distance by a corresponding amount.

- $J_a$  and  $J_b$ : these are the next-nearest neighbour out-of-plane exchange paths, spanning the prismatic faces. In the  $P\bar{3}m1$  structure they are equivalent, as shown in figure 3.8. But in  $P\bar{3}$  the rotation shortens one path and lengthens the other, so they are not expected to be equal.

In summary, the ferroaxial distortion will directly affect the difference  $J_a - J_b$  (such that the sign of  $J_a - J_b$  depends on the direction of  $\mathbf{A}$ ), but will leave  $J_1$  and  $J_2$  constant.

### 3.5.2.1 Energy of the different chiral magnetic structures

The magnetic structure in RFMO consists of the  $120^\circ$  structure in-plane, with incommensurate propagation along  $\mathbf{c}$  with  $q_z \approx 0.44$ . Therefore the exchange energy per Fe ion is as

follows:

$$E = 3J_1S^2 \cos(2\pi/3) + J_2S^2 \cos(2\pi q_z) + 3J_aS^2 \cos[2\pi(\sigma_t/3 + \sigma_h q_z)] + 3J_bS^2 \cos[2\pi(-\sigma_t/3 + \sigma_h q_z)]. \quad (3.11)$$

Expanding the cosines,

$$E = -3J_1S^2/2 + J_2S^2 \cos(2\pi q_z) + 3J_aS^2 \left[ -\frac{1}{2} \cos(2\pi q_z) - \sigma_t \sigma_h \frac{\sqrt{3}}{2} \sin(2\pi q_z) \right] + 3J_bS^2 \left[ -\frac{1}{2} \cos(2\pi q_z) + \sigma_t \sigma_h \frac{\sqrt{3}}{2} \sin(2\pi q_z) \right]. \quad (3.12)$$

So

$$E = E_0 + \tilde{E}(\sigma_t, \sigma_h), \quad (3.13)$$

where

$$E_0 = -3J_1S^2/2 + J_2S^2 \cos(2\pi q_z) - \frac{3(J_a + J_b)}{2}S^2 \cos(2\pi q_z) \quad (3.14)$$

is the energy common to all chiral configurations, and

$$\tilde{E}(\sigma_t, \sigma_h) = \sigma_t \sigma_h \frac{3\sqrt{3}}{2} (J_b - J_a) S^2 \sin(2\pi q_z) \quad (3.15)$$

$$\approx 0.9564 \times \sigma_t \sigma_h (J_b - J_a) S^2 \quad (3.16)$$

depends on the product of the two chiralities, and the difference in exchange paths  $a$  and  $b$ . This term goes to zero in the (hypothetical) case where there is no ferroaxial distortion.

Using the notation  $(\sigma_t, \sigma_h) = (\pm, \pm)$  to denote a pair of chiralities (see figure 3.3 and the definitions given above), in the absence of an applied electric field either:

- $J_a > J_b$ , implying that  $(+, +)$  and  $(-, -)$  configurations have lower energy: this will be referred to as ‘axial domain I’; or
- $J_a < J_b$ , implying that  $(+, -)$  and  $(-, +)$  configurations have lower energy: this will be referred to as ‘axial domain II’.

The difference in energy between  $\{(+, +), (-, -)\}$  and  $\{(+, -), (-, +)\}$  is given by

$$\Delta E_A = 3\sqrt{3}(J_b - J_a)S^2 \sin(2\pi q_z). \quad (3.17)$$

### 3.5.2.2 Helical modulation

Differentiating equation (3.13) with respect to  $q_z$  results in

$$\begin{aligned} \frac{\partial E}{\partial q_z} = & -2\pi S^2 J_2 \sin(2\pi q_z) + 2\pi S^2 \frac{3}{2} (J_a + J_b) \sin(2\pi q_z) \\ & + 2\pi S^2 \sigma_t \sigma_h \frac{3\sqrt{3}}{2} (J_b - J_a) \cos(2\pi q_z), \end{aligned} \quad (3.18)$$

and setting this to zero for a minimum in the energy gives

$$\cos(2\pi q_z) \sigma_t \sigma_h 3\sqrt{3} (J_b - J_a) = \sin(2\pi q_z) [2J_2 - 3(J_a + J_b)]. \quad (3.19)$$

Hence

$$\tan(2\pi q_z) = \frac{3\sqrt{3} \sigma_t \sigma_h (J_b - J_a)}{2J_2 - 3(J_a + J_b)}. \quad (3.20)$$

This shows that the pitch of the helix is determined by the amplitude of the axial distortion. However, since the product  $\sigma_t \sigma_h (J_b - J_a)$  does not depend on the chiralities or the sign of the axial distortion, this gives the same pitch to the helix regardless of the exact magnetic configuration or structural domain.

### 3.5.2.3 Approximate size of $J_a$ and $J_b$

Using the calculated value of  $J_2 = 0.3$  K given in [67], it is possible to use equation (3.20) to determine the approximate sizes of  $J_a$  and  $J_b$ . Taking  $\sigma_h \sigma_t = 1$  (*i.e.*  $J_a > J_b$ , axial domain I) and  $q_z = 0.44$  gives:

$$-0.0762 = \frac{J_b - J_a}{0.6 - 3(J_a + J_b)}, \quad (3.21)$$

*i.e.*

$$J_a = 0.0372 + 0.6279 J_b. \quad (3.22)$$

If we take  $J_b \approx 0$  (assuming that  $J_b \ll J_a$ ), this gives  $J_a \approx 0.04$  K. Thus an approximate value for the separation in energy of the states in different axial domains is

$$\Delta E_A \approx 0.4 \text{ K}, \quad (3.23)$$

having used  $q_z = 0.44$ ,  $S = 5/2$ , and  $|J_a - J_b| = 0.04$  K.

### 3.5.2.4 Energy difference between the two polar states

The above calculations suggest that, for axial domain I, the states described by chiralities  $\{(+, +), (-, -)\}$  should be lower in energy than those with chiralities  $\{(+, -), (-, +)\}$ . Anticipating what follows, in zero field cooling through  $T_N$  axial domain I will contain an equal population of both  $(+, +)$  and  $(-, -)$  magnetic domains, since the two configurations are

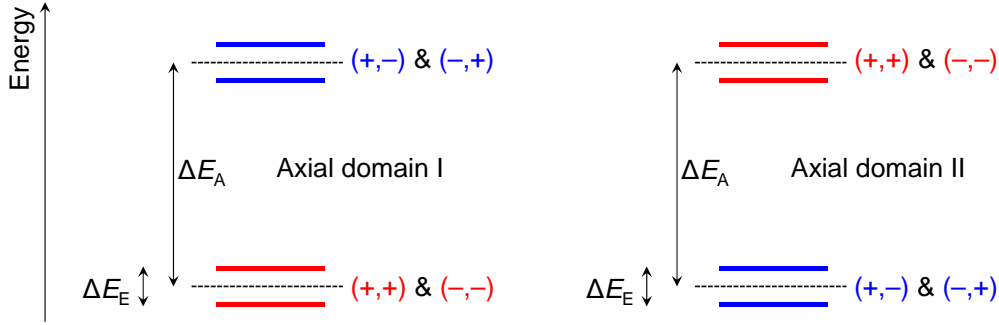


**Figure 3.9:** Energies of the different magnetic configurations. Under zero applied electric field, the axial distortion separates  $\{(+,+), (-,-)\}$  configurations from  $\{(+,-), (-,+)\}$  by an amount  $\Delta E_A$  in energy (dashed lines). The effect of the electric field is to further separate out these pairs of states (solid, coloured lines) by an amount  $\Delta E_E \ll \Delta E_A$ . The minimum energy configuration is therefore determined by the sign of the applied electric field and the axial domain in question.

degenerate in energy. However, applying an electric field removes this degeneracy (see figure 3.9) and separates the energies of the two magnetic configurations by an amount  $\Delta E_E$ . [Similarly, the two magnetic configurations which are at lowest energy in axial domain II,  $(+,-)$  and  $(-,+)$ , will also be separated by  $\Delta E_E$  in an applied electric field.] It will be useful to calculate an approximate value for this quantity in order to compare it to the separation in energy due to the axial distortion,  $\Delta E_A$ .

The approximate polarisation measured at low temperatures is  $P \approx 20 \mu\text{C m}^{-2}$  [see figure 3.5(b)]. The sample thickness is  $\approx 0.2 \text{ mm}$ , and the surface area is  $6.27 \times 10^{-6} \text{ m}^2$ , so the volume of the sample is  $\approx 1.25 \times 10^{-9} \text{ m}^3$ . Since the unit cell volume is  $208.65 \text{ \AA}^3 = 2.0865 \times 10^{-28} \text{ m}^3$ , the sample contains  $\approx 6.0125 \times 10^{18}$  unit cells, leading to an electric dipole moment per spin of

$$p_{\text{spin}} = 4.173 \times 10^{-33} \text{ C m} \quad (3.24)$$

directed along the  $c$ -axis. Such a dipole moment in an applied electric field of  $\mathcal{E} = 7.5 \times 10^5 \text{ V m}^{-1}$  has energy  $E = -p_{\text{spin}}\mathcal{E} = -3.1297 \times 10^{-27} \text{ J}$ . Hence the energy separation is

$$\Delta E_E = 3.75 \times 10^{-8} \text{ eV} \quad (3.25)$$

or, in temperature units,  $4.3478 \times 10^{-4} \text{ K}$ . We are therefore working in the regime where  $\Delta E_E \ll \Delta E_A$ .

### 3.5.3 The free energy and coupling to an electric field

As mentioned previously, the free energy is allowed to contain terms of the form  $F_{\text{ax}} = (\mathbf{A}\sigma) \cdot \mathbf{P}$ , where  $\sigma$  is a chirality of the magnetic structure and  $\mathbf{P}$  a polarisation, since these



terms are invariant under both time reversal ( $\hat{T}$ ) and spatial inversion ( $\hat{I}$ ) operations as shown in the table below:

	$\hat{T}$	$\hat{I}$
$\mathbf{A}$	even	even
$\sigma$	even	odd
$\mathbf{P}$	even	odd

Therefore:

- for axial domain I,  $\{(+, +), (-, -)\}$  structures are favoured, and the sign of  $\mathbf{E}$  will select either  $(+, +)$  or  $(-, -)$  to minimise the free energy; and
- for axial domain II,  $\{(+, -), (-, +)\}$  structures are favoured, and the sign of  $\mathbf{E}$  will select either  $(+, -)$  or  $(-, +)$  to minimise the free energy.

The exact configuration that  $\mathbf{E}$  favours depends on the precise coupling to the different  $\sigma$ 's.

The most general form for the free energy  $F$ , being invariant under time reversal and spatial inversion, is

$$F = (c_t A + c_1) \sigma_t P_z + (c_h A + c_2) \sigma_h P_z + \dots \quad (3.26)$$

where  $A = \pm|A|$  is the axial vector directed along  $z$ ,  $P_z$  is the polarisation along  $z$ ,  $c_{1,2,t,h}$  are constants, and ' $\dots$ ' stands for higher order terms in the order parameters (note that since  $\sigma_{t,h}^2 = 1$  and  $\mathbf{A} \cdot \mathbf{A} = \text{constant}$  these terms will not include any higher powers of these parameters). Since  $\sigma_t$ ,  $\sigma_h$ , and  $P_z$  change sign under inversion (but  $A$  does not), and under time reversal  $\sigma_t$  and  $\sigma_h$  are both invariant, in general all four of the terms in equation (3.26) are allowed.

However, it is also a requirement that the free energy is invariant under changing the direction of  $\mathbf{v}_{\text{ext}}$ , because this is decided arbitrarily. Since  $\mathbf{v}_{\text{ext}} \rightarrow -\mathbf{v}_{\text{ext}}$  changes the sign of  $P_z$ ,  $\sigma_t$  and  $A$ , but leaves  $\sigma_h$  unchanged, this imposes  $c_t = c_2 = 0$ , so that the free energy reduces to

$$F = c_1 \sigma_t P_z + c_h A \sigma_h P_z. \quad (3.27)$$

As shown in figure 3.8, a structure in which  $J_a < J_b$  requires a left-handed structural rotation of the tetrahedra (taking  $\mathbf{v}_{\text{ext}}$  to be along  $+\mathbf{c}$ ), so axial domain I is assigned an axuality of  $\mathbf{A}^-$ . Similarly, axial domain II has axuality  $\mathbf{A}^+$ . The four allowed sets of parameter values (for both axial domains) are as shown in table 3.1, from which it is clear that  $\sigma_t = -A\sigma_h$ . The free energy may therefore be written as

$$F = \tilde{c} A \sigma_h P_z, \quad (3.28)$$

or, equivalently, as

$$F = -\tilde{c} \sigma_t P_z, \quad (3.29)$$

$A$	$\sigma_t$	$\sigma_h$	$A\sigma_h$
+	+	-	-
+	-	+	+
-	+	+	-
-	-	-	+

**Table 3.1:** The four sets of allowed parameters (axiality, triangular chirality, and helical chirality) in  $\text{RbFe}(\text{MoO}_4)_2$ .

where  $\tilde{c}$  is a new coupling constant. This implies that one cannot determine based on symmetry (for the present system) whether the dominant coupling is to the helical or triangular chirality, since they are essentially made equivalent due to the axial distortion. Both chiralities, when combined together with the axial distortion, result in certain low-energy configurations of the magnetic spins, to which an applied electric field should couple and be able to switch.

## 3.6 Spherical neutron polarimetry

This section presents the details of the neutron scattering work before the results of the spherical neutron polarimetry experiments undertaken on RFMO are discussed in section 3.7.

### 3.6.1 Magnetic structure factor

When considering diffraction from a magnetic structure it is useful to exploit the periodicity inherent in the arrangement of spins and expand the structure as a Fourier series. Thus, where there exists a single magnetic ion per unit cell (as is the case for RFMO), one may write the magnetic moment of the  $l$ th unit cell as

$$\boldsymbol{\mu}_l \propto \sum_{\{\mathbf{q}\}} \mathbf{S}_{\mathbf{q}} e^{-i\mathbf{q} \cdot \mathbf{R}_l}, \quad (3.30)$$

where the  $\mathbf{S}_{\mathbf{q}}$  are the Fourier coefficients,  $\mathbf{R}_l$  is the lattice vector for the unit cell containing the  $l$ th moment, and the summation runs over a set of different propagation vectors  $\{\mathbf{q}\}$ . For a simple structure which can be described by a single propagation vector (all that is necessary here), this expression reduces to

$$\boldsymbol{\mu}_l \propto \mathbf{S}_{\mathbf{q}} e^{-i\mathbf{q} \cdot \mathbf{R}_l} + \mathbf{S}_{-\mathbf{q}} e^{i\mathbf{q} \cdot \mathbf{R}_l}, \quad (3.31)$$

where, because the moments must be real, we require  $\mathbf{S}_{\mathbf{q}} = \mathbf{S}_{-\mathbf{q}}^*$ .

With reference to figure 3.3, we can establish relationships between the propagation vector and the triangular and helical magnetic chiralities. The convention used here is to

always take  $q_z$  to be *positive*, such that  $\mathbf{q} = (\epsilon/3, \epsilon/3, q_z)$  where  $q_z \approx 0.44$  and  $\epsilon = \pm 1$ . The types of magnetic structures depicted in figure 3.3 may all be described in the Cartesian basis [in which  $\mathbf{R}_l = (R_l^x, R_l^y, R_l^z)$ ], as

$$\boldsymbol{\mu}_l = \begin{pmatrix} \cos(\mathbf{q} \cdot \mathbf{R}_l) \\ \delta \sin(\mathbf{q} \cdot \mathbf{R}_l) \\ 0 \end{pmatrix} = \begin{pmatrix} \cos 2\pi \left[ \epsilon \left( \frac{1}{3} R_l^x + \frac{1}{3} R_l^y \right) + q_z R_l^z \right] \\ \delta \sin 2\pi \left[ \epsilon \left( \frac{1}{3} R_l^x + \frac{1}{3} R_l^y \right) + q_z R_l^z \right] \\ 0 \end{pmatrix}. \quad (3.32)$$

Here, the two parameters  $\epsilon = \pm 1$  and  $\delta = \pm 1$  define the helical and triangular chiralities of the structure (see table 3.3). Thus, a particular magnetic structure may be described by

$$\boldsymbol{\mu}_l \propto (\hat{\mathbf{e}}_x + \delta i \hat{\mathbf{e}}_y) e^{-i\mathbf{q} \cdot \mathbf{R}_l} + (\hat{\mathbf{e}}_x - \delta i \hat{\mathbf{e}}_y) e^{i\mathbf{q} \cdot \mathbf{R}_l}, \quad (3.33)$$

where  $\hat{\mathbf{e}}_x, \hat{\mathbf{e}}_y$  are orthonormal basis vectors in the plane of the spins (*i.e.* the  $ab$  plane), and  $\mathbf{q} = \mathbf{q}_{1,2}$  (respectively for  $\epsilon = \pm 1$ ) is the propagation vector of the structure.

It is necessary to calculate the *magnetic structure factor*, defined as the Fourier transform of the function  $\mathbf{M}(\mathbf{r})$ , which describes the magnetisation as a function of position  $\mathbf{r}$  within the crystal:

$$\mathbf{M}(\mathbf{Q}) = \int d^3\mathbf{r} \mathbf{M}(\mathbf{r}) e^{-i\mathbf{Q} \cdot \mathbf{r}}. \quad (3.34)$$

To evaluate this, we take the magnetisation distribution function to be

$$\mathbf{M}(\mathbf{r}) \propto \sum_l \boldsymbol{\mu}_l m(\mathbf{r} - \mathbf{R}_l), \quad (3.35)$$

*i.e.* simply a sum over the lattice points in the crystal, each of which contains a magnetic moment  $\boldsymbol{\mu}_l$  at the origin arising from the Fe ion, and the function  $m(\mathbf{r} - \mathbf{R}_l)$  describes how the magnetisation varies throughout space in the proximity of this moment. Thus

$$\mathbf{M}(\mathbf{r}) \propto \sum_l [\mathbf{S}_\mathbf{q} e^{-i\mathbf{q} \cdot \mathbf{R}_l} + \mathbf{S}_\mathbf{q}^* e^{i\mathbf{q} \cdot \mathbf{R}_l}] m(\mathbf{r} - \mathbf{R}_l), \quad (3.36)$$

so that

$$\mathbf{M}(\mathbf{Q}) \propto \int d^3\mathbf{r} \sum_l m(\mathbf{r} - \mathbf{R}_l) [\mathbf{S}_\mathbf{q} e^{-i\mathbf{q} \cdot \mathbf{R}_l} + \mathbf{S}_\mathbf{q}^* e^{i\mathbf{q} \cdot \mathbf{R}_l}] e^{-i\mathbf{Q} \cdot \mathbf{r}}. \quad (3.37)$$

Writing  $\mathbf{r} = \mathbf{R}_l + \mathbf{x}$ , where  $\mathbf{x}$  is a position vector within the unit cell, we have that  $d^3\mathbf{r} = d^3\mathbf{x}$  and so

$$\mathbf{M}(\mathbf{Q}) \propto \sum_l [\mathbf{S}_\mathbf{q} e^{-i\mathbf{q} \cdot \mathbf{R}_l} + \mathbf{S}_\mathbf{q}^* e^{i\mathbf{q} \cdot \mathbf{R}_l}] \int d^3\mathbf{x} m(\mathbf{x}) e^{-i\mathbf{Q} \cdot (\mathbf{R}_l + \mathbf{x})} \quad (3.38)$$

$$= \sum_l [\mathbf{S}_\mathbf{q} e^{-i\mathbf{q} \cdot \mathbf{R}_l} + \mathbf{S}_\mathbf{q}^* e^{i\mathbf{q} \cdot \mathbf{R}_l}] e^{-i\mathbf{Q} \cdot \mathbf{R}_l} \int d^3\mathbf{x} m(\mathbf{x}) e^{-i\mathbf{Q} \cdot \mathbf{x}} \quad (3.39)$$

$$= \sum_l [\mathbf{S}_\mathbf{q} e^{-i\mathbf{q} \cdot \mathbf{R}_l} + \mathbf{S}_\mathbf{q}^* e^{i\mathbf{q} \cdot \mathbf{R}_l}] e^{-i\mathbf{Q} \cdot \mathbf{R}_l} f^{\text{mag}}(\mathbf{Q}) \quad (3.40)$$

$$= \sum_l [\mathbf{S}_\mathbf{q} e^{-i(\mathbf{Q} + \mathbf{q}) \cdot \mathbf{R}_l} + \mathbf{S}_\mathbf{q}^* e^{-i(\mathbf{Q} - \mathbf{q}) \cdot \mathbf{R}_l}] f^{\text{mag}}(\mathbf{Q}). \quad (3.41)$$

Since the summation runs over all of the lattice points located at  $\mathbf{R}_l$ , the phase factors in the above expressions cancel out unless  $\mathbf{Q} + \mathbf{q} = \mathbf{G}$  for the first term, or  $\mathbf{Q} - \mathbf{q} = \mathbf{G}$  for the second ( $\mathbf{G}$  is a reciprocal lattice vector). Hence

$$\mathbf{M}(\mathbf{Q}) \propto \mathbf{S}_{\mathbf{q}} \delta^{(3)}(\mathbf{G} - [\mathbf{Q} + \mathbf{q}]) f^{\text{mag}}(\mathbf{Q}) + \mathbf{S}_{\mathbf{q}}^* \delta^{(3)}(\mathbf{G} - [\mathbf{Q} - \mathbf{q}]) f^{\text{mag}}(\mathbf{Q}), \quad (3.42)$$

and so  $\mathbf{M}(\mathbf{Q}) \propto \mathbf{S}_{\mathbf{q}} f^{\text{mag}}(\mathbf{Q})$  if  $\mathbf{Q} = \mathbf{G} - \mathbf{q}$ , or else  $\mathbf{M}(\mathbf{Q}) \propto \mathbf{S}_{\mathbf{q}}^* f^{\text{mag}}(\mathbf{Q})$  if  $\mathbf{Q} = \mathbf{G} + \mathbf{q}$ .

$\mathbf{S}_{\mathbf{q}}$  is given by equation (3.33), but before one can substitute this into equation (3.42) it is necessary to change from the Cartesian coordinate system of the crystal (which has the  $x$ -axis parallel to  $\mathbf{a}$  and the  $z$ -axis parallel to  $\mathbf{c}$ ) to that of the experiment (which has the  $X$ -axis parallel to  $\mathbf{Q}$  and the  $Z$ -axis vertical, see figure 3.10). To do this, we act on the vector  $\mathbf{S}_{\mathbf{q}} = (S_{\mathbf{q}}^x, S_{\mathbf{q}}^y, 0)$  with a series of matrices to obtain

$$\tilde{\mathbf{S}}_{\mathbf{q}} = \begin{bmatrix} \cos \varphi & -\sin \varphi & 0 \\ \sin \varphi & \cos \varphi & 0 \\ 0 & 0 & 1 \end{bmatrix} \begin{bmatrix} \sqrt{3}/2 & -1/2 & 0 \\ 1/2 & \sqrt{3}/2 & 0 \\ 0 & 0 & 1 \end{bmatrix} \begin{bmatrix} 1/4 & \sqrt{3}/4 & \sqrt{3}/2 \\ \sqrt{3}/4 & 3/4 & -1/2 \\ -\sqrt{3}/2 & 1/2 & 0 \end{bmatrix} \begin{pmatrix} S_{\mathbf{q}}^x \\ S_{\mathbf{q}}^y \\ 0 \end{pmatrix}. \quad (3.43)$$

In this expression, the matrix on the right rotates the crystal coordinate axes by  $90^\circ$  about the axis

$$\hat{\mathbf{n}} = \begin{pmatrix} \cos 60^\circ \\ \sin 60^\circ \\ 0 \end{pmatrix}, \quad (3.44)$$

*i.e.* parallel to  $\mathbf{a}^* + \mathbf{b}^*$ , in order to align the  $z$ -axes of the two systems; the middle matrix rotates the crystal  $x$ - and  $y$ -axes about the  $z$ -direction such that the  $x$ -axis is now orthogonal to the plane of the sample; and the left-hand matrix further rotates the axes about the  $z$ -direction by the angle  $\varphi = \theta - \omega$  between the sample surface and the  $y$ -axis of the experiment (figure 3.10). Hence, the final expression for the magnetic structure factor for the  $\mathbf{Q} = \mathbf{G} - \mathbf{q}$  satellite is given by

$$\mathbf{M}^{(-)}(\mathbf{Q}) = p f^{\text{mag}}(\mathbf{Q}) \tilde{\mathbf{S}}_{\mathbf{q}} \quad (3.45)$$

$$= p f^{\text{mag}}(\mathbf{Q}) \begin{bmatrix} -\frac{1}{2} \sin \varphi & -\frac{\sqrt{3}}{2} \sin \varphi & \cos \varphi \\ \frac{1}{2} \cos \varphi & \frac{\sqrt{3}}{2} \cos \varphi & \sin \varphi \\ -\sqrt{3}/2 & 1/2 & 0 \end{bmatrix} \begin{pmatrix} 1 \\ \delta i \\ 0 \end{pmatrix}, \quad (3.46)$$

or for the  $\mathbf{Q} = \mathbf{G} + \mathbf{q}$  satellite by

$$\mathbf{M}^{(+)}(\mathbf{Q}) = p f^{\text{mag}}(\mathbf{Q}) \tilde{\mathbf{S}}_{\mathbf{q}}^* \quad (3.47)$$

$$= p f^{\text{mag}}(\mathbf{Q}) \begin{bmatrix} -\frac{1}{2} \sin \varphi & -\frac{\sqrt{3}}{2} \sin \varphi & \cos \varphi \\ \frac{1}{2} \cos \varphi & \frac{\sqrt{3}}{2} \cos \varphi & \sin \varphi \\ -\sqrt{3}/2 & 1/2 & 0 \end{bmatrix} \begin{pmatrix} 1 \\ -\delta i \\ 0 \end{pmatrix}, \quad (3.48)$$

where  $p$  is a constant.

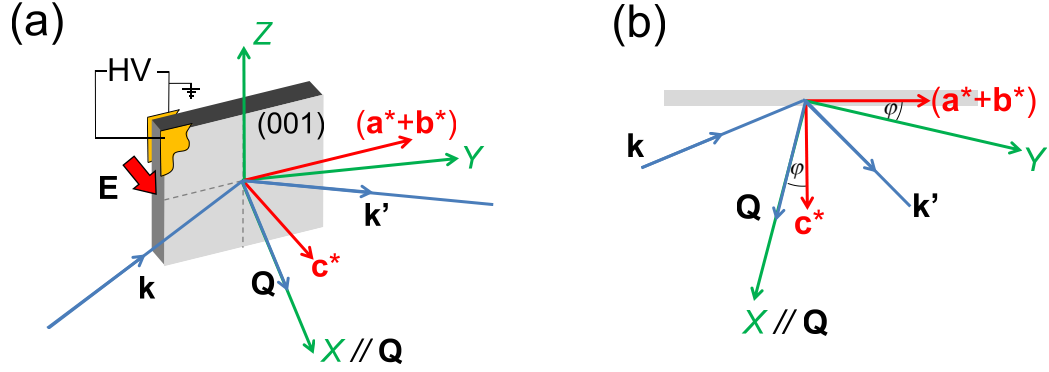


**Figure 3.10:** Experimental geometry: (a) three-dimensional view (all arrows apart from the  $Z$ -axis lie in the scattering plane); and (b) view with the  $Z$ -axis coming out of the page. The red arrows show directions of reciprocal lattice vectors, and the green show the  $\{X, Y, Z\}$  directions of the Blume reference frame (the frame of the experiment), in which the  $Z$ -axis is vertical and the  $X$ -axis is parallel to the scattering vector  $\mathbf{Q} = \mathbf{k}' - \mathbf{k}$ . A portion of the gold contacts which were evaporated onto the  $(0, 0, \pm 1)$  surfaces is shown in (a). HV: High voltage.

### 3.6.1.1 Magnetic form factor

The magnetic form factor associated with a single Fe ion,  $f^{\text{mag}}$ , depends upon the magnetisation associated with the ion as well as the scattering vector  $\mathbf{Q}$ . It is given by

$$f^{\text{mag}}(\mathbf{Q}) = \int d^3\mathbf{r} m(\mathbf{r}) e^{-i\mathbf{Q}\cdot\mathbf{r}}, \quad (3.49)$$

*i.e.* it is the Fourier transform of the function  $m(\mathbf{r})$  which describes how the magnetisation varies as a function of position in the ion.

Following [68], one can split the contributions to  $f^{\text{mag}}$  up into parts originating from the total spin and orbital angular momenta:

$$f_{\text{spin}}(\mathbf{Q}) = \frac{1}{M_S} \sum_{L=0}^{2l} i^L \langle j_L(\mathbf{Q}) \rangle \sum_{M=-L}^L S_{LM} Y_M^L(\hat{\mathbf{Q}}), \quad (3.50)$$

and

$$f_{\text{orbit}}(\mathbf{Q}) = \frac{1}{M_L} \sum_{L=0,2,\dots}^{2l} [\langle j_L(\mathbf{Q}) \rangle + \langle j_{L+2}(\mathbf{Q}) \rangle] \sum_{M=-L}^L B_{LM} Y_M^L(\hat{\mathbf{Q}}), \quad (3.51)$$

where the  $j_L$  are the spherical Bessel functions,  $Y_M^L$  the spherical harmonics, and the coefficients  $S_{LM}$  and  $B_{LM}$  can be obtained from the orbital wave function [69].  $M_S$  is the total spin moment and is given by  $S_{00}$ , and similarly the total orbital moment  $M_L$  is given by  $B_{00}$ . For the  $\text{Fe}^{3+}$  ions present in RFMO, which have  $s = j = 5/2$  and  $l = 0$ , the above

	$A$	$a$	$B$	$b$	$C$	$c$	$D$
$j_0(\tilde{q})$ :	0.3972	13.2442	0.6295	4.9034	-0.0314	0.3496	0.0044
$j_2(\tilde{q})$ :	1.3602	11.9976	1.5188	5.0025	0.4705	1.9914	0.0038

**Table 3.2:** Coefficients used for the analytical approximations to the Bessel functions in equations (3.56) and (3.57).

expressions simplify to:

$$f_{\text{spin}}(\mathbf{Q}) = \frac{1}{M_S} \langle j_0(\mathbf{Q}) \rangle S_{00} Y_0^0(\hat{\mathbf{Q}}) \quad (3.52)$$

$$= \frac{1}{2\sqrt{\pi}} \langle j_0(\mathbf{Q}) \rangle, \quad (3.53)$$

and

$$f_{\text{orbit}}(\mathbf{Q}) = \frac{1}{M_L} [\langle j_0(\mathbf{Q}) \rangle + \langle j_2(\mathbf{Q}) \rangle] B_{00} Y_0^0(\hat{\mathbf{Q}}) \quad (3.54)$$

$$= \frac{1}{2\sqrt{\pi}} [\langle j_0(\mathbf{Q}) \rangle + \langle j_2(\mathbf{Q}) \rangle]. \quad (3.55)$$

The Bessel functions  $j_0$  and  $j_2$  may be approximated by the following analytical functions [70]:

$$\langle j_0(\tilde{q}) \rangle = A e^{-a\tilde{q}^2} + B e^{-b\tilde{q}^2} + C e^{-c\tilde{q}^2} + D, \quad (3.56)$$

$$\langle j_2(\tilde{q}) \rangle = \left( A e^{-a\tilde{q}^2} + B e^{-b\tilde{q}^2} + C e^{-c\tilde{q}^2} + D \right) \tilde{q}^2, \quad (3.57)$$

where

$$\tilde{q} := \frac{\sin \theta}{\lambda} \quad (3.58)$$

is in units of  $\text{\AA}^{-1}$ , and the constant coefficients  $A$ ,  $B$ ,  $C$ ,  $D$ ,  $a$ ,  $b$ , and  $c$  are different for the two Bessel functions; they are given in table 3.2.

The overall magnetic form factor is then given by  $f^{\text{mag}}(\mathbf{Q}) = f_{\text{spin}}(\mathbf{Q}) + f_{\text{orbit}}(\mathbf{Q})$ , although for the present case of  $\text{Fe}^{3+}$  (in which the  $d$ -shell is half filled) the lack of any orbital moment will make the orbital contribution to the form factor negligible.

### 3.6.2 Diffractometer angles

Since the crystal is oriented such that  $\mathbf{Q}$  will always be a linear combination of the vectors  $\mathbf{c}^*$  and  $\mathbf{a}^* + \mathbf{b}^*$ , the accessible reflections will all be of the form  $(h, h, l)$ . Imposing the Bragg condition results in

$$\sin \theta = \frac{\lambda \sqrt{3a^{*2}h^2 + c^{*2}l^2}}{4\pi} \quad (3.59)$$

and, since the angle between  $\mathbf{Q}$  and  $\mathbf{c}^*$  is just  $\varphi$ , from the geometry in figure 3.10 we have

$$\cos \varphi = \frac{lc^*}{\sqrt{3a^{*2}h^2 + c^{*2}l^2}}, \quad (3.60)$$

$$\omega = \begin{cases} \theta - \varphi, & h > 0, \\ \theta + \varphi, & h < 0. \end{cases} \quad (3.61)$$

These equations may be used to calculate the detector angle ( $2\theta$ ) and sample angle ( $\omega$ ) which should both be set to access a particular ( $h, h, l$ ) reflection, as well as to calculate the angle  $\varphi$  which is necessary in working out the magnetic interaction vector [equations (3.46) and (3.48)].

### 3.6.3 Calculation of the neutron intensities and polarimetry components

For the present case in which the magnetic scattering does not overlap with the nuclear scattering, the Blume-Maleev equations (using the crystallography convention,  $\mathbf{Q} = \mathbf{k}' - \mathbf{k}$ ) give the scattered intensity (see also section 2.4)

$$I = \mathbf{M}_\perp \mathbf{M}_\perp^* + i \mathbf{P}^{\text{in}} \cdot (\mathbf{M}_\perp \times \mathbf{M}_\perp^*), \quad (3.62)$$

where

$$\mathbf{M}_\perp \equiv \mathbf{M}_\perp(\mathbf{Q}) = \hat{\mathbf{Q}} \times \mathbf{M}(\mathbf{Q}) \times \hat{\mathbf{Q}} \quad (3.63)$$

is the magnetic interaction vector [ $\mathbf{M}(\mathbf{Q})$  is given in equations (3.46) and (3.48)], and  $\mathbf{P}^{\text{in}}$  is a unit vector along the direction of the incident neutron beam's polarisation. The vector along the direction of the exit polarisation,  $\mathbf{P}^{\text{out}}$ , is given by

$$\mathbf{P}^{\text{out}} = \frac{1}{I} \left[ -\mathbf{P}^{\text{in}}(\mathbf{M}_\perp \cdot \mathbf{M}_\perp^*) + \mathbf{M}_\perp(\mathbf{P}^{\text{in}} \cdot \mathbf{M}_\perp^*) + \mathbf{M}_\perp^*(\mathbf{P}^{\text{in}} \cdot \mathbf{M}_\perp) - i(\mathbf{M}_\perp \times \mathbf{M}_\perp^*) \right]. \quad (3.64)$$

Therefore, in order to calculate the intensity and exit polarisation for a certain magnetic reflection, one needs to follow these steps:

- Determine the scattering vector  $\mathbf{Q}$  for the reflection; determine whether the magnetic satellite is at a position  $+\mathbf{q}$  or  $-\mathbf{q}$  with respect to the closest Bragg peak at  $\mathbf{G}$ ; and determine the direction of polarisation of the incident beam (*i.e.* the unit vector  $\mathbf{P}^{\text{in}}$ ).
- Calculate the angle  $\varphi$  [equation (3.60)]; calculate the magnetic form factor  $f^{\text{mag}}(\mathbf{Q})$  [equations (3.53) and (3.55)]; and use equations (3.46) or (3.48) as appropriate to find the magnetic structure factor  $\mathbf{M}(\mathbf{Q})$ .
- Find the magnetic interaction vector  $\mathbf{M}_\perp(\mathbf{Q})$ ; and use equations (3.62) and (3.64) to determine the scattered intensity (up to a normalisation constant which is the same for all calculated intensities) and direction of the exit neutron polarisation.

### 3.6.4 The polarimetry components

The measured quantities in a spherical neutron polarimetry experiment are the polarimetry components,  $P_{i \rightarrow j}$  where  $i, j = X, Y, Z$ . Given a fully polarised incident beam along  $i$ , the polarisation measured along  $j$  is given by

$$P_{i \rightarrow j} := \frac{I_{i \rightarrow j} - I_{i \rightarrow -j}}{I_{i \rightarrow j} + I_{i \rightarrow -j}}, \quad (3.65)$$

where  $I_{i \rightarrow j}$  is the intensity measured along the direction  $j$  given an incident neutron beam fully polarised along  $i$ . Clearly  $P_{i \rightarrow j} \in [-1, 1]$ . For a given incident polarisation direction, for example with  $\mathbf{P}^{\text{in}} = (1, 0, 0)$  (*i.e.* the incident neutrons are polarised fully along the  $+X$  direction), we may calculate the polarimetry components  $P_{x \rightarrow x}$ ,  $P_{x \rightarrow y}$ , and  $P_{x \rightarrow z}$  directly from equations (3.62) and (3.64), which give  $\mathbf{P}^{\text{out}} = (P_{x \rightarrow x}, P_{x \rightarrow y}, P_{x \rightarrow z})$ . Similarly, taking  $\mathbf{P}^{\text{in}} = (0, 1, 0)$  will give  $\mathbf{P}^{\text{out}} = (P_{y \rightarrow x}, P_{y \rightarrow y}, P_{y \rightarrow z})$ , and  $\mathbf{P}^{\text{in}} = (0, 0, 1)$  gives  $\mathbf{P}^{\text{out}} = (P_{z \rightarrow x}, P_{z \rightarrow y}, P_{z \rightarrow z})$ . Thus, by measuring the polarimetry components, one may then proceed to gain information about the magnetic interaction vector  $\mathbf{M}_\perp(\mathbf{Q})$ , from which one can infer the magnetic structure(s) present in the sample.

Evaluating the above formulae leads to simplified expressions for the polarimetry components. These are:

$$P_{x \rightarrow x} = -1, \quad (3.66)$$

$$P_{y \rightarrow y} = \frac{2M_{\perp y}M_{\perp y}^*}{|\mathbf{M}_\perp|^2} - 1, \quad (3.67)$$

$$P_{z \rightarrow z} = \frac{2M_{\perp z}M_{\perp z}^*}{|\mathbf{M}_\perp|^2} - 1, \quad (3.68)$$

$$P_{y \rightarrow x} = P_{z \rightarrow x} = \frac{2\Im\{M_{\perp y}M_{\perp z}^*\}}{|\mathbf{M}_\perp|^2}, \quad (3.69)$$

$$P_{x \rightarrow y} = P_{x \rightarrow z} = P_{y \rightarrow z} = P_{z \rightarrow y} = 0, \quad (3.70)$$

where  $\mathbf{M}_\perp = (0, M_{\perp y}, M_{\perp z})$  ( $\mathbf{M}_\perp$  by definition has no component along  $X$ ) and  $|\mathbf{M}_\perp|^2 = \mathbf{M}_\perp \cdot \mathbf{M}_\perp^*$ . One of the reasons why spherical neutron polarimetry is such a powerful technique is because of the sensitivity of the ‘off-diagonal’ terms  $P_{y \rightarrow x}$  and  $P_{z \rightarrow x}$  to the imaginary part of the magnetic structure factor. It can therefore be used to infer the sign of  $\delta$  [see equations (3.46) and (3.48)] which, together with knowledge of the scattering vector and therefore  $\epsilon$  [equation (3.32)], can be used to determine the magnetic chiralities  $\sigma_t$  and  $\sigma_h$  that are present. Table 3.3 summarises how the magnetic chiralities are related to the particular satellite and the imaginary part of the magnetic structure factor.



$\epsilon = +1$	$\delta = +1$	$\sigma_t = +1$	$\sigma_h = +1$	$\mathbf{Q} = \mathbf{G} + \mathbf{q}_1$	$\mathbf{M} \sim (1, -\delta i) = (1, -i)$
				$\mathbf{Q} = \mathbf{G} - \mathbf{q}_1$	$\mathbf{M} \sim (1, \delta i) = (1, i)$
	$\delta = -1$	$\sigma_t = -1$	$\sigma_h = -1$	$\mathbf{Q} = \mathbf{G} + \mathbf{q}_1$	$\mathbf{M} \sim (1, -\delta i) = (1, i)$
				$\mathbf{Q} = \mathbf{G} - \mathbf{q}_1$	$\mathbf{M} \sim (1, \delta i) = (1, -i)$
$\epsilon = -1$	$\delta = +1$	$\sigma_t = -1$	$\sigma_h = +1$	$\mathbf{Q} = \mathbf{G} + \mathbf{q}_2$	$\mathbf{M} \sim (1, -\delta i) = (1, -i)$
				$\mathbf{Q} = \mathbf{G} - \mathbf{q}_2$	$\mathbf{M} \sim (1, \delta i) = (1, i)$
	$\delta = -1$	$\sigma_t = +1$	$\sigma_h = -1$	$\mathbf{Q} = \mathbf{G} + \mathbf{q}_2$	$\mathbf{M} \sim (1, -\delta i) = (1, i)$
				$\mathbf{Q} = \mathbf{G} - \mathbf{q}_2$	$\mathbf{M} \sim (1, \delta i) = (1, -i)$

**Table 3.3:** Relationship between the parameters used in describing the arrangement of magnetic moments [ $\delta$  and  $\epsilon$ , see equation (3.32)], the triangular and helical chiralities  $\sigma_t$  and  $\sigma_h$ , the magnetic propagation vector  $\mathbf{q}_1 = (1/3, 1/3, q_z)$  or  $\mathbf{q}_2 = (-1/3, -1/3, q_z)$ , and the magnetic structure factor  $\mathbf{M}$ . In the above,  $\mathbf{M}$  is written in terms of two components of a vector: these refer to the  $x$  and  $y$  components of the left-most vectors in equations (3.46) and (3.48). For simplicity the matrix rotating these vectors into the Blume coordinate system, as well as the factors of  $p$  and  $f^{\text{mag}}$ , are omitted.

### 3.7 Results

Here, results from the spherical neutron polarimetry experiments, undertaken on RFMO using the CRYOPAD on beamline D3 at the ILL, are presented.

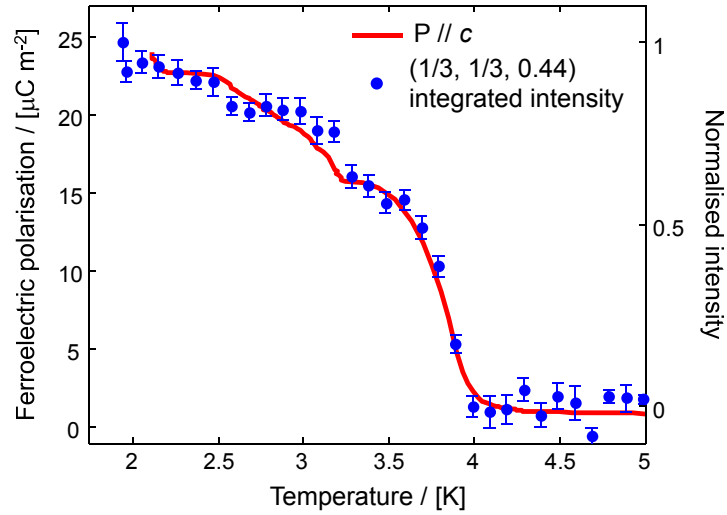


**Figure 3.11:** The ferroelectric polarisation,  $P \parallel c$ , measured along the  $c$ -axis [data from figure 3.5(b)] and the integrated intensity of the  $(1/3, 1/3, q_z)$  magnetic reflection (measured without the spin filter) as a function of temperature.

Peak position	$\mathbf{q}$	Satellite	Preferred magnetic chiralities for $+\mathbf{E}$ , $-\mathbf{E}$
$(1/3, 1/3, 0.44)$	$(1/3, 1/3, q_z)$	+ve	$(+, +), (-, -)$
$(1/3, 1/3, 0.56)$	$(-1/3, -1/3, q_z)$	-ve	$(+, -), (-, +)$
$(-1/3, -1/3, 0.44)$	$(-1/3, -1/3, q_z)$	+ve	$(+, -), (-, +)$
$(-1/3, -1/3, 0.56)$	$(1/3, 1/3, q_z)$	-ve	$(+, +), (-, -)$
$(-1/3, -1/3, 1.44)$	$(-1/3, -1/3, q_z)$	+ve	$(+, -), (-, +)$
$(-1/3, -1/3, -0.44)$	$(1/3, 1/3, q_z)$	-ve	$(+, +), (-, -)$
$(-1/3, -1/3, 0.44)$	$(-1/3, -1/3, q_z)$	+ve	$(+, -), (-, +)$

**Table 3.4:** A list of the seven magnetic satellites measured in both positive and negative field coolings. The propagation vector  $\mathbf{q}$  associated with each peak is given, as is the sign of the satellite. The final column gives the predominant contribution to the magnetic chiralities as measured in the positive and negative electric field cooling data respectively.

### 3.7.1 Temperature dependence of the magnetic peaks

As expected, scattering intensity was observed at reciprocal space positions  $\mathbf{G} \pm \mathbf{q}_{1,2}$ , consistent with the known magnetic structure (discussed above). The temperature dependence of the  $(1/3, 1/3, 0.44)$  magnetic satellite is shown in figure 3.11. The spin filter, used to determine the exit beam polarisation, was removed for this measurement and the intensity is therefore integrated over all exit polarisations. The incident neutron beam was polarised along  $Z$ .

The simultaneous onset of the ferroelectric polarisation with the magnetic scattering intensity confirms that it is the magnetic structure that is responsible for breaking the inversion symmetry, and hence that RFMO is indeed a ‘type-II’ multiferroic (this is also confirmed by measurement of the specific heat in [71], which shows only a single peak with temperature). The error bars on the integrated intensities show the standard deviation in the measurements as calculated in the data acquisition software.

### 3.7.2 Field cooling data

#### 3.7.2.1 General behaviour as a function of electric field

The plots in figure 3.12 show measured vs. calculated values of the polarimetry components for both positive and negative field cooling. For each field cooling, data were collected from seven different magnetic peaks, the details of which are in table 3.4.

From the above considerations, we expect one axial domain to contain magnetic structures with  $(+, +)$  and  $(-, -)$  chiralities, and these will give rise to satellites at  $\mathbf{q}_1 = (1/3, 1/3, q_z)$  positions. The other axial domain will contain  $(+, -)$  and  $(-, +)$  chiralities corresponding to  $\mathbf{q}_2 = (-1/3, -1/3, q_z)$  positions. The data presented here clearly demonstrate that an

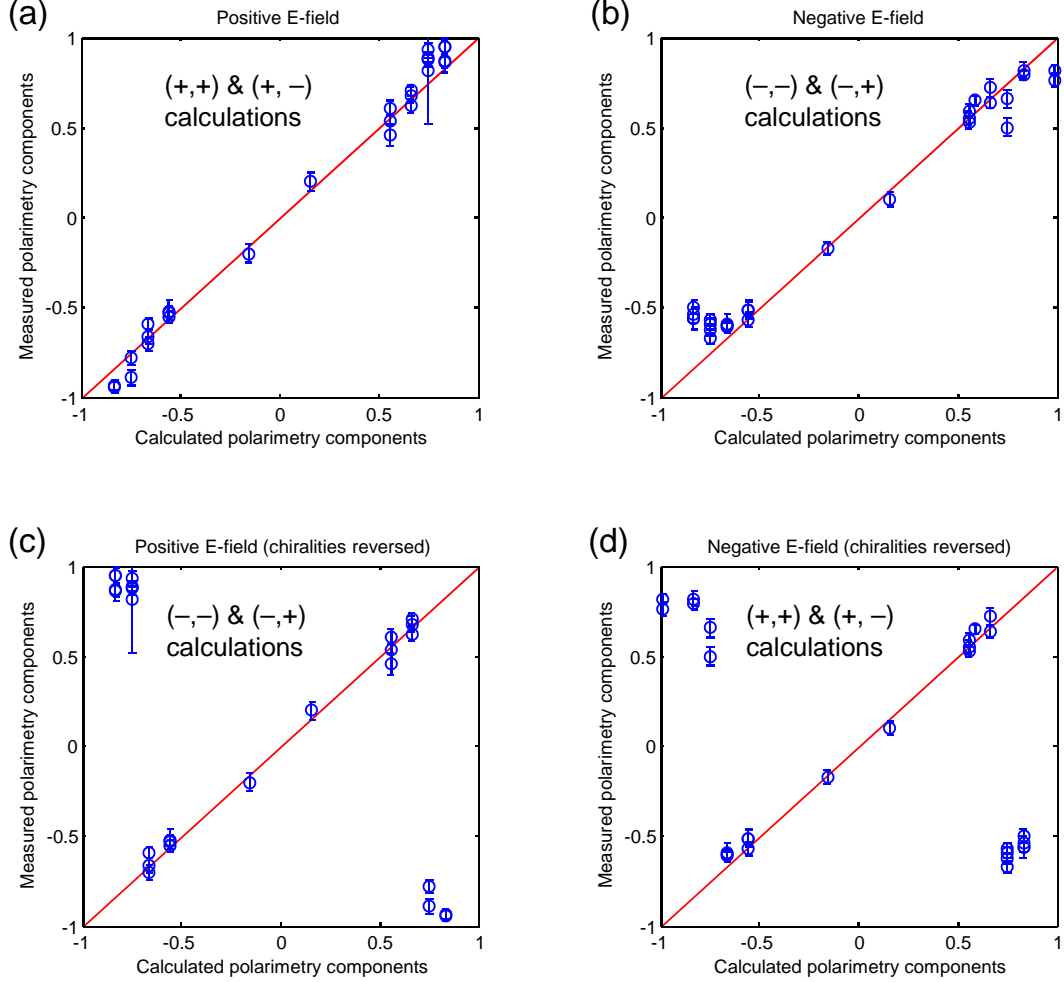


**Figure 3.12:** Comparison between measured and calculated values for the polarimetry components  $P_{y \rightarrow y}$ ,  $P_{z \rightarrow z}$ ,  $P_{y \rightarrow x}$ , and  $P_{z \rightarrow x}$  for several different magnetic reflections at 1.5 K. The calculated values in (a) and (d) are derived from calculations with the same sign of the imaginary part of the magnetic structure factor, whereas those in (b) and (c) have the opposite sign. It is clear that the off-diagonal polarimetry components (which are sensitive to this choice of sign, determined by the magnetic chiralities) switch with the direction of the applied voltage, whereas the on-diagonal components do not.

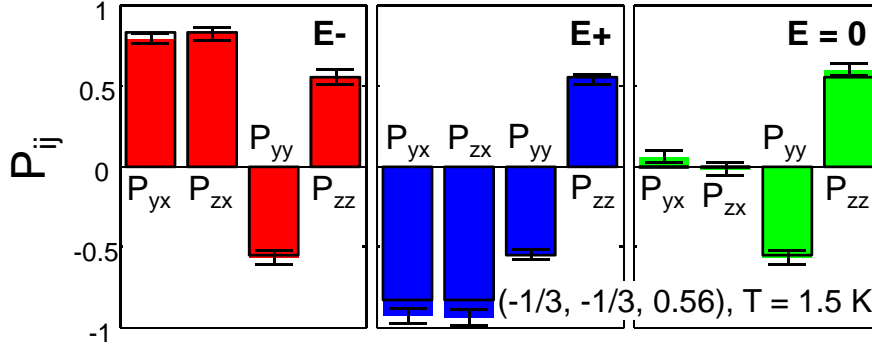


**Figure 3.13:** Polarimetry components following negative, positive, and zero field coolings (with field strength 7.5 kV/cm). Solid bars indicate observed values and rectangles show the calculations.

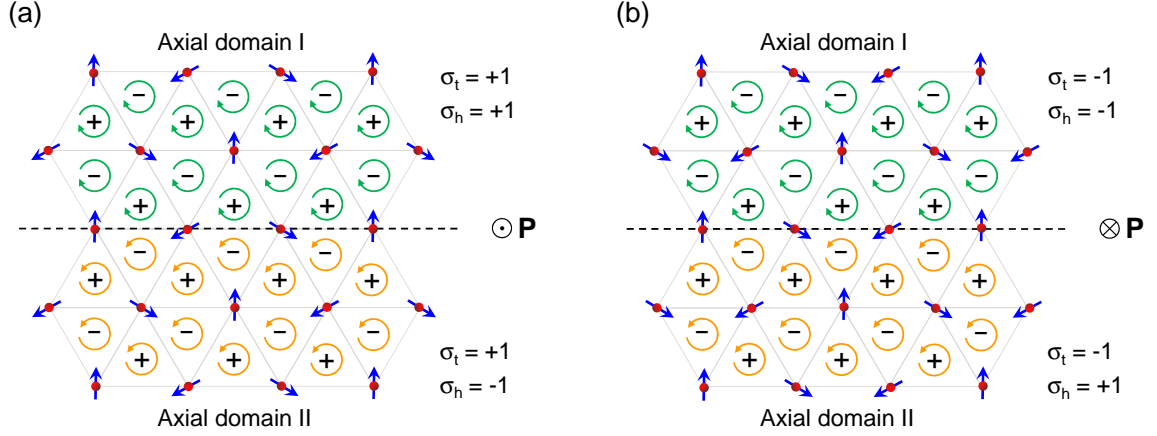
electric field can be used to preferentially select one of these two chirality ‘states’ in each axial domain simultaneously (as listed in the final column of table 3.4). For positive  $\mathbf{E}$ -field cooling these correspond to magnetic structures with  $(+, +)$  (axial domain I) and  $(+, -)$  (axial domain II) chiralities [figure 3.12(a)], and conversely  $(-, -)$  and  $(-, +)$  chiralities [figure 3.12(b)] for negative  $\mathbf{E}$ -field cooling. Figures 3.12(c) and 3.12(d) show calculations based on the opposite chiralities, which clearly do not agree with the data.

Figure 3.13 compares positive, negative, and zero voltage field coolings for four polarimetry components measured on a particular magnetic reflection at base temperature. It is clear that the off-diagonal components  $P_{y \rightarrow x}$  and  $P_{z \rightarrow x}$  are highly dependent on the applied electric field, whereas the other terms (which are not sensitive to the chiralities of the magnetic structures) remain constant throughout. This demonstrates that an electric field, in driving the direction of the ferroelectric polarisation  $\mathbf{P}$ , may couple to the magnetic structures in both axial domains simultaneously. This is summarised by figure 3.14, which shows the chiral states of both axial domains for positive and negative field cooling.

Although a reasonable agreement between measured and calculated values of the polarimetry components can be obtained by assuming a single magnetic state for each field cooling, the agreement can be improved by calculations which assume that there is a population of both allowed structures in each field cooling: this is the focus of the next section.

### 3.7.2.2 Fitting the domain populations

In order to quantify the extent to which the calculated polarimetry components agree with the values measured in experiment, I shall use (and attempt to minimise) the parameter  $r$ ,



**Figure 3.14:** The predominant magnetic structures present in (a) positive, and (b) negative field cooling, each of which has two contributions (one from each axial domain). The direction of the ferroelectric polarisation ( $\mathbf{P}$ ) is shown, and the axial distortion is indicated by the circular arrows which show the sense of rotation of the  $\text{MoO}_4$  tetrahedra. The direction of the  $\text{MoO}_4$  tetrahedron associated with each triangle of spins is shown by the  $\pm$  signs.

the average discrepancy between observations and calculations, defined as

$$r := \frac{1}{N} \sum_{\{P_{i \rightarrow j}\}} \left| P_{i \rightarrow j}^{(\text{measured})} - P_{i \rightarrow j}^{(\text{calculated})} \right|, \quad (3.71)$$

where the sum runs over the  $N$  different polarimetry components  $P_{i \rightarrow j}$  in a specific set of data.

To improve the agreement obtained in the previous section, I now assume that, in each axial domain, there exists a variable population of the two magnetic domains [either  $(+, +)$  and  $(-, -)$  for axial domain I, or  $(+, -)$  and  $(-, +)$  for axial domain II]. Since the experiment is sensitive to magnetic structures arising from the two axial domains separately, the magnetic domain populations are refined separately in each axial domain. The ‘best fit’ domain populations are shown in figure 3.15.

In these calculations,  $f \in [-1, 1]$  is used to parametrise the magnetic domain populations, according to the following scheme. For axial domain I,  $f = 1$  corresponds to 100%  $(+, +)$  population, whereas  $f = -1$  means 100%  $(-, -)$ . For axial domain II,  $f = 1$  means 100%  $(+, -)$  and  $f = -1$  means 100%  $(-, +)$ . Hence, the simple picture of figure 3.14 is described by  $f = 1$  for positive field cooling, and  $f = -1$  for negative field cooling.

As shown in figure 3.15, for both axial domains under positive field cooling the best agreement is obtained with 100% population of  $(+, +)$  (for axial domain I) or  $(+, -)$  (axial domain II). However, under negative field cooling, the system does not completely populate

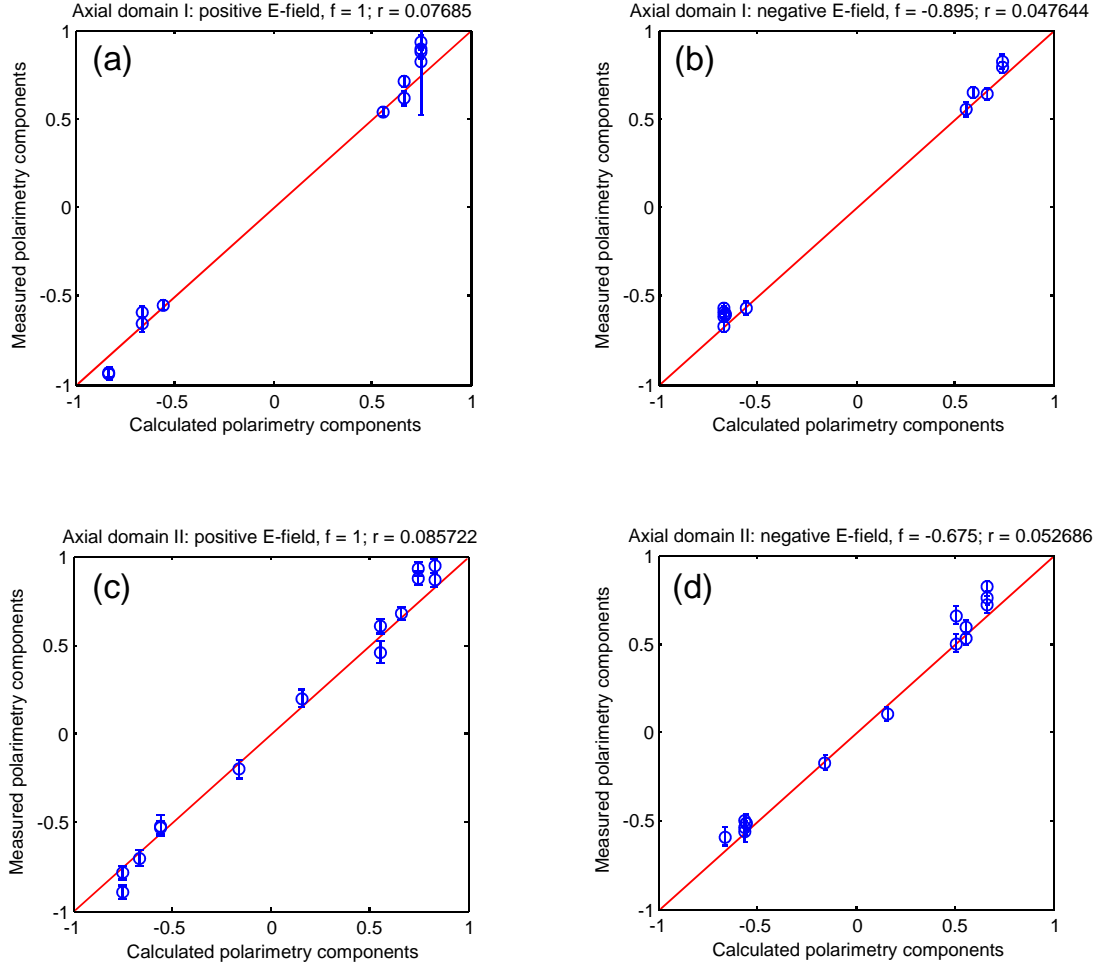


**Figure 3.15:** Improvement to the fits of figures 3.12(a) and 3.12(b), obtained by introducing one free parameter,  $f$ , which allows the magnetic domain populations to vary from 100% (see text for details). Data were collected at 1.5 K.

the opposite magnetic domains, and the best fits suggest a population in axial domain I of 94.75%  $(-, -)$  with 5.25% remnant  $(+, +)$ , and a population in axial domain II of 83.75%  $(-, +)$  with 16.25% remnant  $(+, -)$ . Therefore, although it is not possible to switch the entire magnetic domain population within the sample, a sizeable majority population *can* be controlled by the external electric field.

### 3.7.3 Zero field cooling data

Figure 3.16 compares the zero field cooled data with a model which is obtained by calculating polarimetry components for multiple magnetic domains in each axial domain as in the previous section. The effect of not applying any electric field is that each axial domain contains approximately equal populations of the two magnetic structures permitted in each

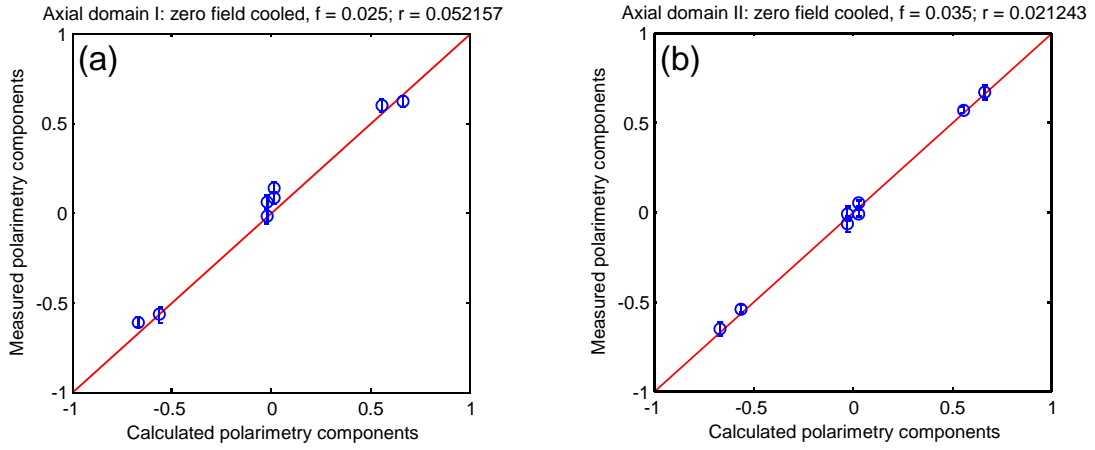


**Figure 3.16:** Comparison between calculated and measured polarimetry components for the zero field cooled data taken at 1.5 K. A good agreement is obtained with approximately equal populations of the two energetically preferred magnetic domains for each axial domain.

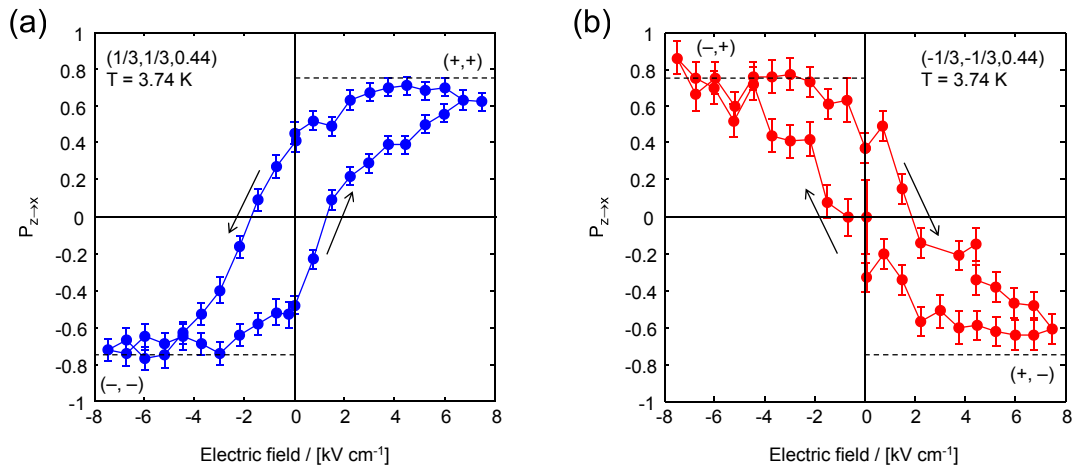


**Figure 3.17:** Hysteresis loops in the  $P_{z \rightarrow x}$  polarimetry component as a function of applied electric field. (a) Data from the  $(1/3, 1/3, q_z)$  peak, corresponding to axial domain I, in which the magnetic structure switches between  $(+, +)$  and  $(-, -)$  chiralities. (b) Data from the  $(-1/3, -1/3, q_z)$  peak, from axial domain II and with  $(+, -)$  and  $(-, +)$  chirality switching.

one. The best fits, which are shown in the figure, assume for axial domain I a magnetic structure which is 51.25%  $(+, +)$  and 48.75%  $(-, -)$ , and for axial domain II a magnetic structure which is 51.75%  $(+, -)$  and 48.25%  $(-, +)$ .

### 3.7.4 Hysteresis measurements

In the final part of the neutron polarimetry experiment, hysteresis loops in the off-diagonal polarimetry components were measured as a function of electric field. The results for two magnetic peaks (one belonging to each axial domain) are shown in figure 3.17. In order to observe hysteresis it was necessary to warm the sample much closer to the magnetic transition temperature (measurements were made at 3.74 K). These measurements demonstrate that, for this temperature, one can exercise direct control over the magnetic chiralities and switch their state by changing the applied electric field.

Also plotted in figure 3.17 are the values of  $P_{z \rightarrow x}$  corresponding to magnetic domains fully populated with the same chiral structures; these are indicated by the dashed lines. It is therefore clear that these hysteresis measurements demonstrate close to 100% switching in the chiralities, as would be expected close to the transition temperature.

## 3.8 Conclusion

Having introduced the idea of a ferroaxial coupling in systems supporting a structural axial vector, I have used the example of the proper screw multiferroic material  $\text{RbFe}(\text{MoO}_4)_2$  as an interesting system with which to test the interplay between magnetism, ferroelectricity, and axuality. Pyroelectric current measurements were carried out in order to determine how the ferroelectric polarisation varies as a function of temperature. The structural distortion that exists in RFMO below 190 K was then examined in detail with respect to the changes it induces in the exchange pathways. In this way a direct link between the structural distortion and the energetically preferred magnetic configurations was established, and minimising the symmetric exchange energy also shows how the pitch of the incommensurate helical spin structure in RFMO is directly determined by the amplitude of the axial distortion.

I have shown that, in each axial domain, the lowest energy magnetic structures are doubly degenerate, and may be described by triangular and helical chiralities  $(\sigma_t, \sigma_h) = (+, +)$  and  $(-, -)$  for one axial domain, and  $(+, -)$  and  $(-, +)$  for the other. By including a ferroaxial coupling term in the free energy, this degeneracy can be lifted by the application of an external electric field which drives the ferroelectric polarisation of the crystal. Thus, in zero electric field, a mixture of both magnetic configurations should be present in each axial domain, whereas in non-zero field some preference should be shown towards a particular configuration which is at lowest energy.



This behaviour was confirmed by spherical neutron polarimetry data collected under both field cooled and zero field cooled conditions. The polarimetry components, some of which are sensitive to the chiralities of the magnetic structures, agree well with calculations based on the magnetic structures predicted by the above reasoning. Moreover, the magnetic domain populations can be estimated by fitting the polarimetry data. Finally, hysteresis in the magnetic structure as a function of electric field demonstrates the multiferroic control (*i.e.* the power to alter the magnetic ‘state’ of a material with an applied electric field) that is possible in this class of materials.

The present work has demonstrated that unconventional spin-driven multiferroicity may be found within those materials possessing a ferroaxial point group: therefore a future direction in the search for novel multiferroics could be to investigate more closely those materials which are known to be structurally axial (and that order magnetically), but whose multiferroic properties have not yet been investigated. In the case of RFMO specifically, an inelastic neutron scattering experiment could be performed to determine experimental values for the exchange constants, which would provide direct confirmation of the effect that the axial distortion has in stabilising the different magnetic structures by coupling to the sign of  $J_a - J_b$ . In addition, a microscopic mechanism for the multiferroic properties of RFMO is still missing, and further work will be needed in order to fully understand this phenomenon and its implications for other ferroaxial materials.



# Chapter 4

---

## Charge ordering in $\text{YbFe}_2\text{O}_4$

---

### 4.1 Introduction

In the  $R\text{Fe}_2\text{O}_4$  family of compounds ( $R = \text{Ho-Lu, Y, or In}$ ) [72] the average iron valence is  $2.5^+$ , meaning that the crystal should contain an equal population of  $\text{Fe}^{2+}$  and  $\text{Fe}^{3+}$  ions across the Fe sites to maintain charge neutrality [73]. This system is therefore interesting from the point of view of multiferroicity, because the Fe ions can both magnetically order, providing a coupling to an external magnetic field, and may also order with respect to their electronic valence – a phenomenon known as *charge ordering* or charge disproportionation [74] – that could induce a macroscopic polarisation which would couple to an external electric field. Hence there is potential for a coupling between the magnetic and electric orderings in these systems, and magnetoelectric behaviour has been widely reported [75–77]. This coupling may make this family of compounds suitable for multiferroic applications, particularly since they have recently been grown as thin films [78].

A large number of experimental studies have been undertaken on the  $R\text{Fe}_2\text{O}_4$  compounds, from a wide variety of diffraction techniques using X-rays [79–82], neutrons [83–87] and electrons [88–91], together with bulk measurements of the dielectric [79, 92–99] and magnetic [92–94, 100, 101] properties. A number of optical studies [102–105] have also been reported. Most of the work published to date has been on  $\text{LuFe}_2\text{O}_4$  which has subsequently become well-established in the field as a typical example of a type-I multiferroic, whose ferroelectric properties are due to charge ordering. This is known as ‘improper’ ferroelectricity, and occurs independently of any magnetic ordering, as opposed to resulting directly from structural or magnetic transitions [5]. However, the precise nature of the charge ordering which leads to these effects is still controversial.

In this chapter, I present X-ray scattering data collected on the  $R = \text{Yb}$  system, which was found to have more stable oxygen content (to which the properties of the system are very sensitive [106–109]) than  $R = \text{Lu}$  [110]. By studying in detail the superstructure satellite

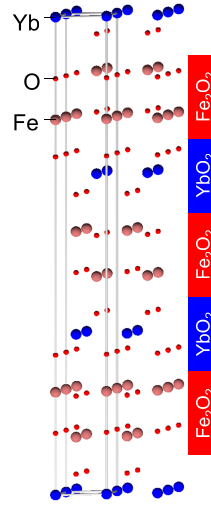


**Figure 4.1:** Crystal structure of  $\text{YbFe}_2\text{O}_4$ . The  $\text{YbO}_2$  ('U') layers and  $\text{Fe}_2\text{O}_2$  ('W') layers are indicated, and the crystallographic unit cell is shown by the grey box.

peaks in the X-ray data that result from the charge ordering, I show that the charge ordering in  $\text{YbFe}_2\text{O}_4$  is incommensurate and, consequently, incapable of providing a route towards a non-zero macroscopic ferroelectric polarisation. I develop a simple model of the effect of the charge ordering on the surrounding oxygen ions, and use this to simulate the X-ray data obtained in experiment. I also discuss the nature of the transition in which the charge ordering changes from being two-dimensional to being three-dimensional in character.

#### 4.1.1 Crystal structure and geometrical frustration

The crystal structure of the  $R\text{Fe}_2\text{O}_4$  compounds is comprised of an alternating stacking of  $\text{YbO}_2$  layers and  $\text{Fe}_2\text{O}_2$  bilayers (see figure 4.1). These are also respectively referred to as 'U-layers' and 'W-layers' in the literature [111]. The space group is  $R\bar{3}m$  and the lattice parameters at room temperature are  $a = 3.455 \text{ \AA}$  and  $c = 25.054 \text{ \AA}$  [112]. The separation of the  $\text{Fe}_2\text{O}_2$  bilayers by the rare earth ions suggests that the system may exhibit two-dimensional behaviour above a certain temperature, where the interactions between Fe ions *between* bilayers are weak but those *within* the bilayers remain strong.

Key to the behaviour of the system is the triangular lattice upon which the Fe sites are located. As shown in figure 4.2, the well-known system of Ising spins ( $S_z = \pm 1/2$ ) fixed at the vertices of a triangle with antiferromagnetic interactions between them leads to 'frustration'. In this example, the lower left site in figure 4.2(a) is arbitrarily assigned to an up-spin (coloured red). Therefore, one of the neighbours (here the lower right site) will prefer to house a down-spin (blue) to minimise the energy cost associated with the

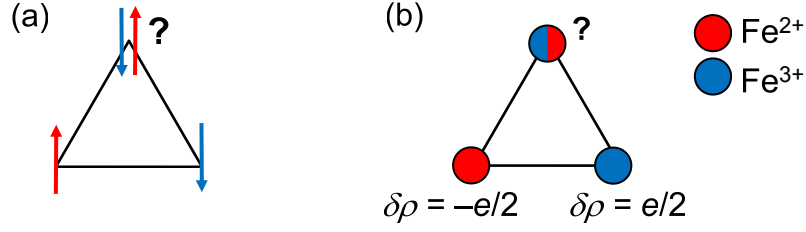


**Figure 4.2:** (a) Magnetic spins arranged at the vertices of a triangle are said to be geometrically ‘frustrated’ because it is impossible to satisfy all of the antiferromagnetic exchange interactions simultaneously. By analogy, a triangular arrangement of  $\text{Fe}^{2+}$  and  $\text{Fe}^{3+}$  ions in (b) is unable to satisfy all of the Coulomb interactions and is therefore similarly frustrated. (See also [91].)

antiferromagnetic exchange interaction. The problem comes in assigning a direction to the third spin on the upper site: both up and down are equally (un)favourable. This leads to the absence of a unique ground state configuration. Instead, the ground state is highly degenerate and the system is said to be ‘frustrated’ because it is impossible to satisfy all of the interactions simultaneously. As the frustration is due to the arrangement of the ions on a triangular lattice, this phenomenon is known as *geometrical frustration*.

Figure 4.2(b) shows how a similar scenario can occur with respect to the Fe valence. The interactions between different sites are this time electrostatic in nature, but the phenomenon is very similar to the Heisenberg  $S_z = 1/2$  case in that the system prefers to have *different* charge species (either 2+ or 3+) at either end of each edge of the triangle (*i.e.* opposite deviations  $\delta\rho$  in charge with respect to the average valence). Thus, for  $\text{RFe}_2\text{O}_4$ , we expect a high degree of geometrical frustration arising from the charge ordering, and it is this frustration that drives the interesting properties presented below.

## 4.1.2 Charge ordering

The Fe ions in  $\text{YbFe}_2\text{O}_4$  can form long range charge ordered structures both within the  $ab$  planes (two-dimensional charge ordering) and additionally, at lower temperatures, along the  $c$  direction as adjacent layers become correlated. The likely arrangements of the different charge species are discussed below.

### 4.1.2.1 Two-dimensional charge ordering

Focussing on an individual  $\text{Fe}_2\text{O}_2$  bilayer, there are a number of possible arrangements that can be used to tile an equal amount of  $\text{Fe}^{2+}$  and  $\text{Fe}^{3+}$  onto two triangular lattices stacked along the  $c$  direction. Previous measurements [91] have reported diffraction peaks that occur at  $(h, k) = (1/3, 1/3)$  positions in reciprocal space with respect to the crystallographic unit

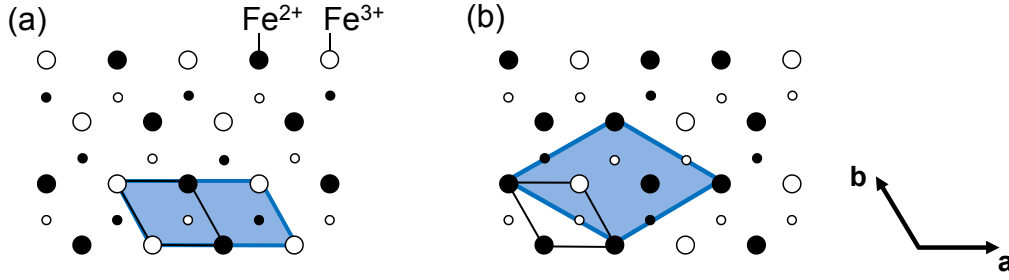


**Figure 4.3:** Two possible in-plane charge ordered supercells for the W-layers of  $\text{YbFe}_2\text{O}_4$ . The colour of each ion indicates its valence, and the large ions are on an adjacent layer to the small ones, forming the  $\text{Fe}_2\text{O}_2$  bilayer. (a) An example of a structure in which equal numbers of  $\text{Fe}^{2+}$  and  $\text{Fe}^{3+}$  ions are positioned on each separate layer, leading to a doubling of the unit cell area (this is known as the  $\text{CO}_{1/2}$  structure, see [114]). In (b) a  $\sqrt{3} \times \sqrt{3}$  structure is shown, in which each of the layers is differently charged. This arrangement would lead to a polarisation between the layers, and is consistent with satellite peaks at  $(1/3, 1/3)$  positions. Crystallographic unit cells are pictured with a thin black outline; charge ordered supercells are the blue shaded areas.

cell. These occur below a transition temperature  $T_{2D} \approx 500$  K [113]. Such satellites imply that the charge ordered supercell is three times larger than the crystallographic cell along the **a** and **b** directions, ruling out a structure in which each of the two layers carries an equal amount of both charge species, as shown in figure 4.3(a).

Instead, in order to construct a model consistent with the positions of the satellites, it is necessary to consider scenarios in which each of the two layers carries a net charge. It is then possible to obtain a structure similar to that shown in figure 4.3(b), where the charge ordering enlarges the cell by a factor of three in each of the **a** and **b** directions. The superstructure unit cell pictured is the  $\sqrt{3} \times \sqrt{3}$  cell which is conventionally used in the literature; its lattice vectors (**a'** and **b'**) are related to those of the crystallographic unit cell (**a** and **b**) by the following transformation:

$$\begin{pmatrix} \mathbf{a}' \\ \mathbf{b}' \end{pmatrix} = \begin{bmatrix} 2 & 1 \\ -1 & 1 \end{bmatrix} \begin{pmatrix} \mathbf{a} \\ \mathbf{b} \end{pmatrix}. \quad (4.1)$$

In figure 4.3(b), I have arbitrarily positioned the honeycomb structure formed by the  $3^+$  ions on the ‘small’ layer so that they are displaced by  $(\mathbf{b} - \mathbf{a})/3$  with respect to the honeycomb of  $2^+$  ions on the ‘large’ layer. However, this displacement can equivalently occur along the  $(2\mathbf{a} + \mathbf{b})/3$  and  $-(\mathbf{a} + 2\mathbf{b})/3$  directions, and one can also interchange  $2^+$  and  $3^+$  charges (equivalent to swapping the ‘large’ and ‘small’ ions in the figure), giving a total of six possible charge ordering arrangements as shown in figure 4.4, where I have numbered them W1 to W6 for convenience. The conventional unit cell intersects three such W-layers, and depending on the exact position along the *c*-axis the supercell will be translated in the

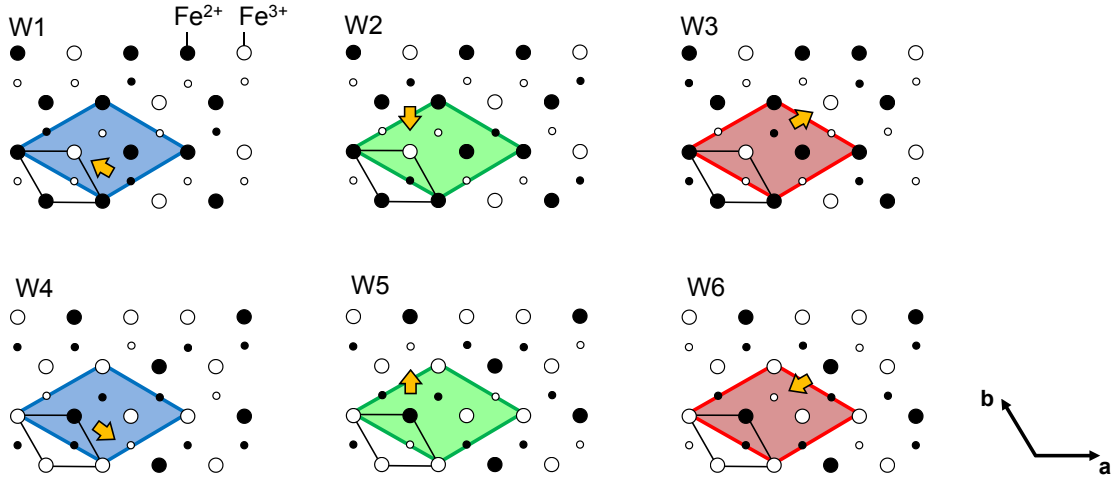


**Figure 4.4:** The six W-layers in  $\text{YbFe}_2\text{O}_4$ . Large ions are on the upper layer (*i.e.* in the positive  $c$  direction) with respect to the smaller ones on the lower layer. The direction of the ferroelectric polarisation associated with each layer is shown by the orange arrows in the plane. In addition, layers W1-W3 have a component of the polarisation along  $-c$ , and W4-W6 along  $+c$ . A choice of crystallographic unit cell and charge ordered supercell are also shown, assuming the layers are positioned between the U-layer at  $c = 0$  and the U-layer at  $c = 1/3$ . If the W-layer was instead placed between two different U-layers then the unit cells would be translated in accordance with the structure shown in figure 4.1.

$ab$  plane relative to the positions shown in figure 4.4 such that the overall position of the Fe ions is consistent with the structure in figure 4.1.

The W-layers each have a polarisation pointing in a different direction. Since W1-W3 contain twice the amount of  $\text{Fe}^{3+}$  as  $\text{Fe}^{2+}$  on the lower layer, the  $c$ -component of the polarisation will be directed along  $-c$ . Similarly, the  $c$ -component of the polarisation for W4-W6 is directed along  $+c$ . The direction of the in-plane polarisation is simply the direction by which the two honeycomb structures are displaced relative to one another. Therefore it points along  $(\mathbf{b} - \mathbf{a})$  for W1,  $-(\mathbf{a} + 2\mathbf{b})$  for W2,  $(2\mathbf{a} + \mathbf{b})$  for W3, and the reverse directions for W4, W5, and W6 respectively.

#### 4.1.2.2 Three-dimensional charge order

If the W-layers depicted in figure 4.4 stack in a regular pattern along the  $c$ -axis then the crystal will exhibit three-dimensional charge ordering. The polarity of each W-layer makes the nature of this stacking key to the ferroelectric properties of the crystal. Thus, if the layers were to stack like W1-W2-W3-W1-..., the  $c$ -axis polarisation components would all point in the same direction whilst the in-plane components would cancel, and the stacking would be ferroelectric (in this case there is no enlargement of the unit cell along  $c$ ). One could

therefore hope to measure a macroscopic polarisation along the  $\mathbf{c}$  direction. Alternatively, the layers can stack like W1-W2-W3-W4-W5-W6-W1-..., in which case the unit cell along  $\mathbf{c}$  is doubled and the alternating polarisation direction along  $\mathbf{c}$  leads to an *antiferroelectric* structure, which would provide no macroscopic polarisation to be measured.

Recent results on  $\text{LuFe}_2\text{O}_4$  have shown evidence for both a ferroelectric structure with a  $\sqrt{3} \times \sqrt{3}$  supercell and an antiferroelectric structure with a  $\sqrt{3} \times \sqrt{3} \times 2$  supercell, as deduced by the positions of the charge ordered satellite peaks along the  $\mathbf{c}^*$  direction which change with temperature [80]. The transition to a three-dimensional structure is associated with a sharp anomaly in the specific heat, and occurs at  $T^* \approx 320$  K [80]. Of the (relatively few) studies that have focussed specifically on the  $R = \text{Yb}$  compounds, electron diffraction data on the Mn-doped system have been reported that show satellites at  $(1/3, 1/3, n)$ -type positions ( $n \in \mathbb{Z}$ ) at room temperature [94], whereas electron diffraction on the undoped system at room temperature has satellites at  $(1/3, 1/3, n + 1/2)$  [89]. A further electron diffraction study at  $T = 130$  K observed satellite spots at  $(1/3, 1/3, 1/2)$ -type positions [97].

### 4.1.3 Magnetic ordering

In addition to the charge ordering,  $R\text{Fe}_2\text{O}_4$  also exhibits a magnetic ordering of the Fe spins below  $T_N \approx 240$  K. Below this transition the spins align ferrimagnetically along the  $\pm\mathbf{c}$  direction with propagation vector  $(1/3, 1/3, 0)$  [85]. There exists a further magnetic transition to a more complex (incommensurate) structure below  $T_L \approx 175$  K [85], and the exact magnetic configuration is still controversial [108]. Whilst an understanding of the magnetic ordering is clearly essential if one is to exploit the multiferroic properties of these systems, for the present work I shall be concerned only with an investigation of the charge ordering.

### 4.1.4 The use of X-ray diffraction in examining charge ordering

Non-resonant X-ray diffraction (the experimental technique of choice for this chapter) is unable to distinguish between the differently charged Fe species directly<sup>1</sup>. However, it is an ideal probe of any periodic atomic displacement patterns that may be propagating throughout the crystal as a result of the varying charges and ionic radii within a charge ordered structure. It is through this ‘secondary effect’ that one may use X-ray diffraction to observe indirectly charge ordering on a macroscopic scale throughout the illuminated volume of the sample. In the subsequent sections I shall consider the details of the way in which X-ray diffraction is sensitive to such periodic displacement patterns, present X-ray

<sup>1</sup>Resonant X-ray diffraction, on the other hand, *can* be used as a direct probe in the study of charge ordering. See *e.g.* [115] and [116].



diffraction data from both laboratory and synchrotron sources on YbFe<sub>2</sub>O<sub>4</sub>, and discuss a model of the low temperature atomic displacement structure that results from the three-dimensional charge ordered arrangement.

## 4.2 Diffraction from periodic atomic displacements

Here I shall calculate the scattering intensity for elastic X-ray diffraction (although what follows is equally applicable to neutron diffraction) from a structure which has a periodic atomic displacement pattern, for example resulting from charge ordering as in YbFe<sub>2</sub>O<sub>4</sub>.

The scattered intensity is proportional to the modulus squared of the structure factor [see equation (2.23)], which in turn is given by

$$F(\mathbf{Q}) = \sum_j f_j(\mathbf{Q}) e^{i\mathbf{Q} \cdot \mathbf{r}_j}, \quad (4.2)$$

where the sum runs over the atoms in the crystal (labelled by  $j$ ), each of which is located at a position  $\mathbf{r}_j$  with respect to some origin. (Note that the position of the origin has no effect on the intensity since replacing  $\mathbf{r}_j$  by  $\mathbf{r}_0 + \mathbf{r}_j$  just gives an extra phase factor multiplying each term in the sum, which will not alter the modulus.) In this expression,  $f_j(\mathbf{Q})$  is the atomic form factor (for X-rays) or the nuclear scattering length (for neutrons).

Consider a lattice with a basis consisting of a single atom, such as that depicted in figure 4.5(a). To this is introduced a periodic modulation in the position of the atoms, by displacing all of them sinusoidally along the  $z$ -direction, as shown in figure 4.5(b). The modulation propagates along the  $x$ -direction and can therefore be described by a propagation vector of the form

$$\mathbf{q} = (\tau, 0, 0), \quad (4.3)$$

where the parameter  $\tau$  is related to the spatial period  $la$  of the modulation ( $a$  being the lattice constant) by  $\tau = 1/l$ . In figure 4.5(b), the period is clearly  $6a$  and so the propagation vector is  $\mathbf{q} = (1/6, 0, 0)$ .

Each atom belongs to a unit cell which has lattice vector  $\mathbf{R}_n$  ( $n$  labels the unit cell, and therefore also each specific atom), and so one may write the displacement of the  $n$ th atom as

$$\mathbf{d}_n = \begin{pmatrix} 0 \\ 0 \\ d(e^{i\mathbf{R}_n \cdot \mathbf{q}} + e^{-i\mathbf{R}_n \cdot \mathbf{q}}) \end{pmatrix} \quad (4.4)$$

where  $d$  parametrises the size of the displacement. For the structure depicted in figure 4.5(a), the atomic positions are simply given by  $\mathbf{r}_n = \mathbf{R}_n$ , whereas for the modulated

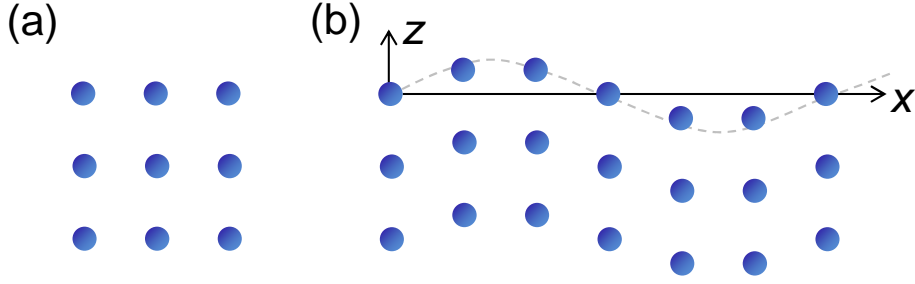


**Figure 4.5:** (a) A square lattice with a single-atom basis. In (b) the atomic positions are sinusoidally modulated.

structure [figure 4.5(b)], the positions are  $\mathbf{r}_n = \mathbf{R}_n + \mathbf{d}_n$ . Thus the structure factor for the modulated structure is

$$F(\mathbf{Q}) = \sum_n f_n(\mathbf{Q}) e^{i\mathbf{Q} \cdot (\mathbf{R}_n + \mathbf{d}_n)} \quad (4.5)$$

$$= \sum_n f_n(\mathbf{Q}) e^{i\mathbf{Q} \cdot \mathbf{R}_n} e^{iQ_z d [\exp(i\mathbf{R}_n \cdot \mathbf{q}) + \exp(-i\mathbf{R}_n \cdot \mathbf{q})]} \quad (4.6)$$

where  $\mathbf{Q} = (Q_x, Q_y, Q_z)$ . The second exponential may be expanded to give

$$F(\mathbf{Q}) = \sum_n f_n(\mathbf{Q}) e^{i\mathbf{Q} \cdot \mathbf{R}_n} \left[ 1 + iQ_z d (e^{i\mathbf{R}_n \cdot \mathbf{q}} + e^{-i\mathbf{R}_n \cdot \mathbf{q}}) + \frac{i^2 Q_z^2 d^2 (e^{i\mathbf{R}_n \cdot \mathbf{q}} + e^{-i\mathbf{R}_n \cdot \mathbf{q}})^2}{2!} + \dots \right]. \quad (4.7)$$

Since the displacements are expected to be small, one can truncate this series at quadratic order in  $d$ . Thus

$$\begin{aligned} F(\mathbf{Q}) \approx & \sum_n f_n(\mathbf{Q}) e^{i\mathbf{Q} \cdot \mathbf{R}_n} \\ & + \sum_n f_n(\mathbf{Q}) e^{i\mathbf{Q} \cdot \mathbf{R}_n} iQ_z d (e^{i\mathbf{R}_n \cdot \mathbf{q}} + e^{-i\mathbf{R}_n \cdot \mathbf{q}}) \\ & - \frac{1}{2} \sum_n f_n(\mathbf{Q}) e^{i\mathbf{Q} \cdot \mathbf{R}_n} Q_z^2 d^2 (e^{i\mathbf{R}_n \cdot 2\mathbf{q}} + e^{-i\mathbf{R}_n \cdot 2\mathbf{q}} + 2), \end{aligned} \quad (4.8)$$

and so

$$\begin{aligned} F(\mathbf{Q}) \approx & (1 - Q_z^2 d^2) \sum_n f_n(\mathbf{Q}) e^{i\mathbf{Q} \cdot \mathbf{R}_n} \\ & + iQ_z d \sum_n f_n(\mathbf{Q}) e^{i(\mathbf{Q} + \mathbf{q}) \cdot \mathbf{R}_n} + iQ_z d \sum_n f_n(\mathbf{Q}) e^{i(\mathbf{Q} - \mathbf{q}) \cdot \mathbf{R}_n} \\ & - \frac{1}{2} Q_z^2 d^2 \sum_n f_n(\mathbf{Q}) e^{i(\mathbf{Q} + 2\mathbf{q}) \cdot \mathbf{R}_n} - \frac{1}{2} Q_z^2 d^2 \sum_n f_n(\mathbf{Q}) e^{i(\mathbf{Q} - 2\mathbf{q}) \cdot \mathbf{R}_n}. \end{aligned} \quad (4.9)$$

All of the terms in equation (4.9) contain a summation over different phase factors which are of the form  $e^{i\mathbf{Q} \cdot \mathbf{R}_n}$ . These will cancel out unless the exponent  $\mathbf{Q} \cdot \mathbf{R}_n = 2\pi p$ , where

$p \in \mathbb{Z}$ . This is equivalent to saying that

$$\sum_n e^{i\mathbf{Q} \cdot \mathbf{R}_n} \propto \delta^{(3)}(\mathbf{Q} - \mathbf{G}), \quad (4.10)$$

where  $\mathbf{G}$  is a reciprocal lattice vector. Hence

$$\begin{aligned} F(\mathbf{Q}) \propto & [1 - Q_z d^2] f(\mathbf{Q}) \delta^{(3)}(\mathbf{Q} - \mathbf{G}) \\ & + iQ_z d f(\mathbf{Q}) \delta^{(3)}(\mathbf{Q} + \mathbf{q} - \mathbf{G}) + iQ_z d f(\mathbf{Q}) \delta^{(3)}(\mathbf{Q} - \mathbf{q} - \mathbf{G}) \\ & - \frac{1}{2} Q_z^2 d^2 f(\mathbf{Q}) \delta^{(3)}(\mathbf{Q} + 2\mathbf{q} - \mathbf{G}) - \frac{1}{2} Q_z^2 d^2 f(\mathbf{Q}) \delta^{(3)}(\mathbf{Q} - 2\mathbf{q} - \mathbf{G}), \end{aligned} \quad (4.11)$$

where  $f_n(\mathbf{Q}) \equiv f(\mathbf{Q})$  (all the atoms are the same). The intensity is proportional to  $|F(\mathbf{Q})|^2$  and therefore will contain the square of each of the above terms (there are no cross terms because the delta functions will always multiply to zero for non-zero  $\mathbf{q}$ ).

This shows that, to quadratic order in the displacement amplitude, one expects to see a strong Bragg peak, weak satellite peaks located at  $\mathbf{G} \pm \mathbf{q}$  due to the modulation in atomic displacement (intensity proportional to the square of the displacement magnitude), and very weak second order satellites at  $\mathbf{G} \pm 2\mathbf{q}$  (intensity proportional to the fourth power of the displacement).

#### 4.2.1 Equivalence of the supercell and propagation vector descriptions

In the case of a *commensurate* propagation vector (*i.e.* one which describes a modulation whose period is an integer number of unit cells), it is possible to calculate the scattering intensity in a different way to above by constructing a *supercell* (this will be used extensively later in this chapter). The structure of figure 4.5(b) can be described in two equivalent ways:

1. *Using the crystallographic unit cell.* The structure consists of a cubic lattice (the  $y$ -direction is not shown in the figure) convoluted with a basis of a single atom, whose position with respect to the lattice point depends on the unit cell it is in (*i.e.* the specific  $\mathbf{R}_n$  belonging to that atom). The lattice vectors are  $\mathbf{R}_n = n_1 \mathbf{a} + n_2 \mathbf{b} + n_3 \mathbf{c}$  ( $n_{1,2,3} \in \mathbb{Z}$ ) where, in the Cartesian basis,

$$\mathbf{a} = \begin{pmatrix} a \\ 0 \\ 0 \end{pmatrix}, \quad \mathbf{b} = \begin{pmatrix} 0 \\ a \\ 0 \end{pmatrix}, \quad \mathbf{c} = \begin{pmatrix} 0 \\ 0 \\ a \end{pmatrix}. \quad (4.12)$$

The atomic positions are given as above by  $\mathbf{r}_n = \mathbf{R}_n + \mathbf{d}_n$ , with

$$\mathbf{d}_n = \begin{pmatrix} 0 \\ 0 \\ d(e^{i\mathbf{R}_n \cdot \mathbf{q}} + e^{-i\mathbf{R}_n \cdot \mathbf{q}}) \end{pmatrix} \quad (4.13)$$

and  $\mathbf{q} = \frac{1}{6} \mathbf{a}^*$ .

2. *Using the supercell.* The structure consists of a tetragonal lattice whose basis vectors  $\mathbf{a}'$ ,  $\mathbf{b}'$ , and  $\mathbf{c}'$  are defined in terms of the basis vectors of the original *cubic* lattice by

$$\begin{pmatrix} \mathbf{a}' \\ \mathbf{b}' \\ \mathbf{c}' \end{pmatrix} = \begin{bmatrix} 6 & 0 & 0 \\ 0 & 1 & 0 \\ 0 & 0 & 1 \end{bmatrix} \begin{pmatrix} \mathbf{a} \\ \mathbf{b} \\ \mathbf{c} \end{pmatrix}. \quad (4.14)$$

This defines the superlattice vectors  $\mathbf{R}'_n = n_1\mathbf{a}' + n_2\mathbf{b}' + n_3\mathbf{c}'$  where, as before,  $n_{1,2,3} \in \mathbb{Z}$  (and in a similar way one can construct the reciprocal superlattice vectors  $\mathbf{G}'$ ). The structure is then generated by a convolution between this lattice and a basis of  $N$  atoms, located at

$$\mathbf{x}_m = \mathbf{R}_m + \begin{pmatrix} 0 \\ 0 \\ d(e^{i\mathbf{R}_m \cdot \mathbf{q}} + e^{-i\mathbf{R}_m \cdot \mathbf{q}}) \end{pmatrix}, \quad (4.15)$$

where  $m = 1, 2, \dots, N$ . Here  $N$  is simply the ratio of the crystallographic unit cell and supercell volumes:

$$N = \frac{\mathbf{a}' \cdot (\mathbf{b}' \times \mathbf{c}')}{\mathbf{a} \cdot (\mathbf{b} \times \mathbf{c})} \quad (4.16)$$

[also equal to the determinant of the matrix in equation (4.14)] which in the present case is clearly equal to six, and

$$\mathbf{R}_m = (m-1)\mathbf{a}, \quad m = 1, 2, \dots, 6. \quad (4.17)$$

Now, using the *crystallographic unit cell* formulation, one obtains the structure factor given in equation (4.9). However, if the *supercell* formulation is used, then the structure factor given by

$$F(\mathbf{Q}) = \sum_{j \text{ atoms in crystal}} f_j(\mathbf{Q}) e^{i\mathbf{Q} \cdot \mathbf{r}_j} \quad (4.18)$$

can be split into two parts by writing  $\mathbf{r}_j = \mathbf{R}'_n + \mathbf{x}_m$ . This gives the following lattice and basis contributions:

$$F(\mathbf{Q}) = \sum_{n \text{ lattice points}} \sum_{m \text{ basis atoms}} f_m(\mathbf{Q}) e^{i\mathbf{Q} \cdot (\mathbf{R}'_n + \mathbf{x}_m)} \quad (4.19)$$

$$= \sum_n e^{i\mathbf{Q} \cdot \mathbf{R}'_n} \sum_m f_m(\mathbf{Q}) e^{i\mathbf{Q} \cdot \mathbf{x}_m}. \quad (4.20)$$

As before, the first summation will give zero unless  $\mathbf{Q} \cdot \mathbf{R}'_n = 2\pi p$  for  $p \in \mathbb{Z}$ , which means that

$$F(\mathbf{Q}) \propto \delta^{(3)}(\mathbf{Q} - \mathbf{G}') \sum_m f_m(\mathbf{Q}) e^{i\mathbf{Q} \cdot \mathbf{x}_m} \quad (4.21)$$

$$= \delta^{(3)}(\mathbf{Q} - \mathbf{G}') \sum_{m=1}^N f_m(\mathbf{Q}) e^{i\mathbf{Q} \cdot [\mathbf{R}_m + \hat{\mathbf{e}}_z d \exp(i\mathbf{R}_m \cdot \mathbf{q}) + \hat{\mathbf{e}}_z d \exp(-i\mathbf{R}_m \cdot \mathbf{q})]}, \quad (4.22)$$

where  $\mathbf{G}'$  is a reciprocal lattice vector of the superlattice. Proceeding as before and expanding for small  $d$  gives

$$\begin{aligned}
 F(\mathbf{Q}) \propto & \delta^{(3)}(\mathbf{Q} - \mathbf{G}') [1 - Q_z^2 d^2] \sum_{m=1}^N f_m(\mathbf{Q}) e^{i\mathbf{Q} \cdot \mathbf{R}_m} \\
 & + \delta^{(3)}(\mathbf{Q} - \mathbf{G}') i Q_z d \left[ \sum_{m=1}^N f_m(\mathbf{Q}) e^{i(\mathbf{Q} + \mathbf{q}) \cdot \mathbf{R}_m} + \sum_{m=1}^N f_m(\mathbf{Q}) e^{i(\mathbf{Q} - \mathbf{q}) \cdot \mathbf{R}_m} \right] \\
 & - \delta^{(3)}(\mathbf{Q} - \mathbf{G}') \frac{1}{2} Q_z^2 d^2 \left[ \sum_{m=1}^N f_m(\mathbf{Q}) e^{i(\mathbf{Q} + 2\mathbf{q}) \cdot \mathbf{R}_m} + \sum_{m=1}^N f_m(\mathbf{Q}) e^{i(\mathbf{Q} - 2\mathbf{q}) \cdot \mathbf{R}_m} \right].
 \end{aligned} \tag{4.23}$$

This is clearly zero unless  $\mathbf{Q} = \mathbf{G}'$ . As the summations run over all the crystallographic unit cells that make up the supercell, the only values of  $\mathbf{G}'$  that do not result in the phases in the first of the above summations cancelling to zero are when  $\mathbf{G}' = \mathbf{G}$ . Hence the first summation is proportional to  $\delta^{(3)}(\mathbf{G}' - \mathbf{G})$ . Similarly, the other summations are only non-zero when  $\mathbf{Q} = \mathbf{G}' = \mathbf{G} \pm \mathbf{q}$  or  $\mathbf{Q} = \mathbf{G}' = \mathbf{G} \pm 2\mathbf{q}$ . Hence

$$\begin{aligned}
 F(\mathbf{Q}) \propto & [1 - Q_z^2 d^2] f(\mathbf{Q}) \delta^{(3)}(\mathbf{Q} - \mathbf{G}) \\
 & + i Q_z d f(\mathbf{Q}) \left[ \delta^{(3)}(\mathbf{Q} - \mathbf{G} + \mathbf{q}) + \delta^{(3)}(\mathbf{Q} - \mathbf{G} - \mathbf{q}) \right] \\
 & - \frac{1}{2} Q_z^2 d^2 f(\mathbf{Q}) \left[ \delta^{(3)}(\mathbf{Q} - \mathbf{G} + 2\mathbf{q}) + \delta^{(3)}(\mathbf{Q} - \mathbf{G} - 2\mathbf{q}) \right],
 \end{aligned} \tag{4.24}$$

which is in agreement with the expression for the structure factor calculated using the *crystallographic unit cell* formalism.

One can therefore, in principle, approximate the diffracted intensities from any incommensurate displacement pattern to an arbitrary degree of accuracy by building a supercell corresponding to a commensurate approximation of the structure and calculating the intensities using the above equations. In practice, computational power will limit the accuracy to which these results can be obtained, because a better approximation to the incommensurate pattern will clearly require a larger supercell and therefore more computation. However, one can only ever measure an incommensurate propagation vector to a certain degree of accuracy, and this level of accuracy can be replicated in constructing commensurate approximation supercells and evaluating their diffracted intensities using no more than a reasonably powerful desktop computer.

## 4.3 X-ray diffraction data

### 4.3.1 Laboratory measurements

Preliminary measurements on single crystal samples of YbFe<sub>2</sub>O<sub>4</sub> were made on an Agilent Technologies ‘SuperNova’ molybdenum source diffractometer ( $\lambda = 0.71073 \text{ \AA}$ ). The recip-

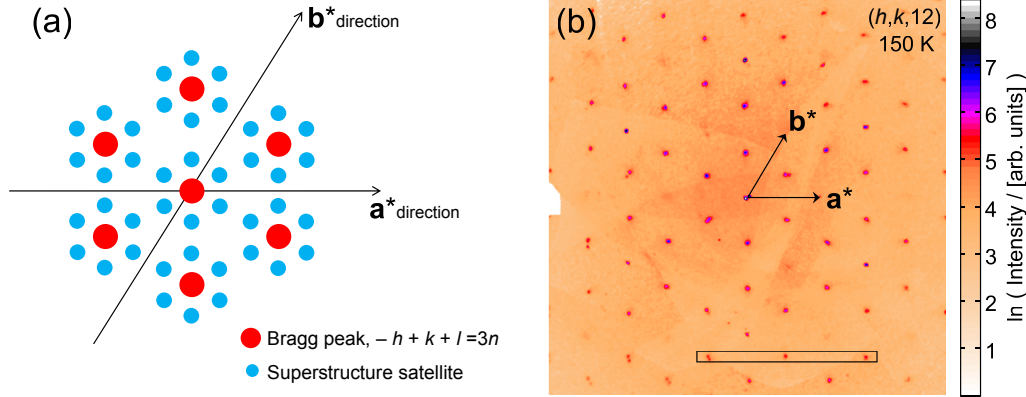


**Figure 4.6:** (a) Positions of the scattered intensity in the  $a^*b^*$  plane, assuming a propagation vector  $\mathbf{q} = (1/3, 1/3)$  and symmetry equivalents. (b) Intensity map of the  $(h, k, 12)$  plane constructed from a laboratory X-ray measurement at 150 K. Hexagons of satellites surrounding the Bragg peak positions are seen, confirming the existence of an approximate  $\sqrt{3} \times \sqrt{3}$  supercell resulting from charge ordering in the plane. The three satellites enclosed in a box are shown in figure 4.7 .

rocal space intensity maps (details of how these are generated are provided in section 2.3.1) show the presence of satellite spots at  $\mathbf{G} \pm \mathbf{q}$ , where  $\mathbf{G} = h\mathbf{a}^* + k\mathbf{b}^* + l\mathbf{c}^*$  is an allowed reciprocal lattice vector (for  $R\bar{3}m$  the rhombohedral setting requires that  $-h + k + l = 3n$ ,  $n \in \mathbb{Z}$ ), and  $\mathbf{q} \approx (1/3, 1/3)$  in the  $ab$  plane. In addition, the three-fold symmetry also allows satellites at  $\mathbf{q} \approx (1/3, -2/3)$  and  $\mathbf{q} \approx (-2/3, 1/3)$ , resulting in the hexagonal pattern of Bragg peaks and satellites shown in figure 4.6(a). No second (or higher) order satellites could be detected above the background. Figure 4.6(b) shows a  $(h, k, 12)$  intensity map where the satellite spots are clearly visible, confirming the existence of a charge ordered superstructure in the plane.

The view along the  $\mathbf{c}^*$  direction gives information about the three-dimensional charge ordering. In figure 4.7, it can be seen that the satellite peaks are not at commensurate positions, but appear to oscillate in  $h$  and  $k$  around these lines, and occur at incommensurate values of  $l$  separated by approximately  $c^*/3$ . These oscillations in the peak positions clearly indicate that the charge ordered superstructures in  $\text{YbFe}_2\text{O}_4$  are more complex than a simple  $\sqrt{3} \times \sqrt{3}$  cell would suggest, and this motivated the collection of synchrotron data before undertaking a full analysis.

### 4.3.2 Synchrotron radiation measurements

Synchrotron X-ray diffraction experiments on beamline I19 at Diamond were carried out on single crystals from the same batch as used in the laboratory measurements. Data

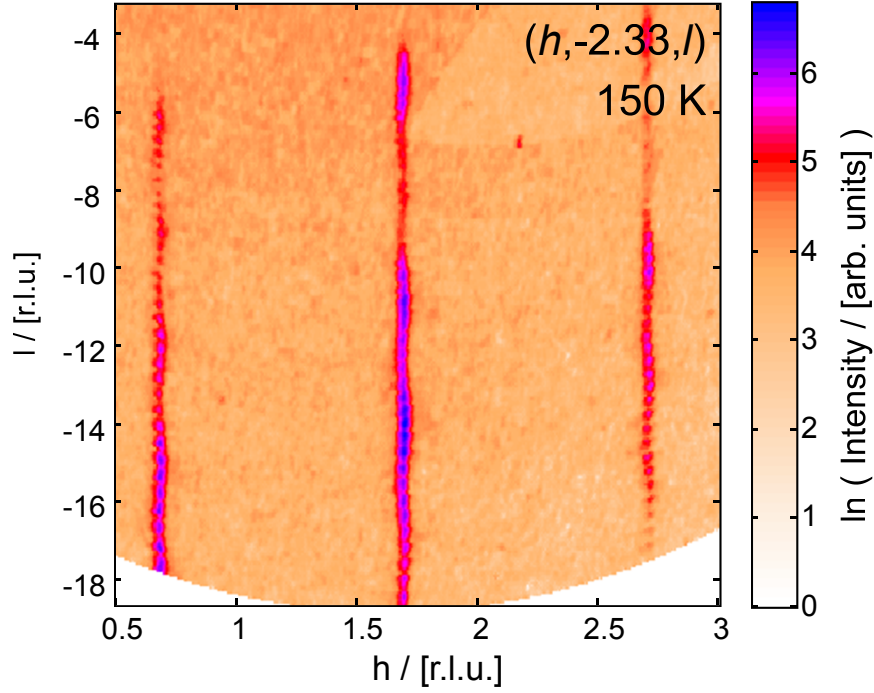


**Figure 4.7:** Intensity map of the  $(h, -7/3, l)$  plane, showing the three satellites marked with a box in figure 4.6(b).

were taken between 150 K and 360 K, covering both sides of the three-dimensional charge ordering transition which occurs at  $T^* = 320$  K.

#### 4.3.2.1 $T < T^*$

Data at 150 K show very similar ‘spotty’ satellite streaks along the  $\mathbf{c}^*$  direction to those found in the laboratory data. The intensity profile of the  $(1/3, -5/3, l)$  set of satellites collected at 150 K is shown in figure 4.8. From this the rapid oscillations separated by  $\approx c^*/3$  are apparent, together with longer scale modulations in the intensity envelope. Figure 4.9 shows the fast Fourier Transform (performed by MATLAB software) of the intensity oscillations shown in figure 4.8, as well as of the intensities of the same satellites measured at a range of other temperatures. From this one can see that the dominant oscillatory component in the intensity profile corresponds to a real space periodicity of  $\approx 2.8c$ , *i.e.* slightly less than the  $3c$  periodicity implied by peaks separated by exactly  $c^*/3$  in reciprocal space. As one warms towards the transition at  $T^*$ , the size of this Fourier component clearly diminishes, and above  $T^*$  it is no longer present as the helices of scattering become continuous.

By extracting a stack of two-dimensional intensity maps it is possible to reconstruct

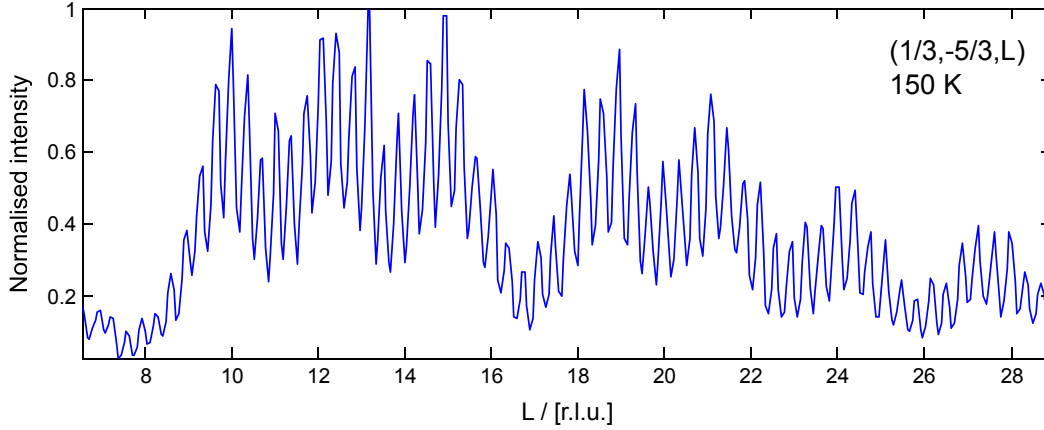


**Figure 4.8:** Intensity profile of the  $(1/3, -5/3, l)$  set of satellites at 150 K. Intensity maxima separated by  $\approx c^*/3$  can be clearly seen, as well as longer scale modulations in intensity.

three-dimensional visualisations of the reciprocal space intensity. Such an isointensity surface plot is shown in figure 4.11(a), which shows a portion of the  $(2/3, -7/3, l)$  satellite. This clearly shows that, whilst the intensity is concentrated onto peaks separated along the  $\mathbf{c}^*$  direction, there are small deviations in  $h$  and  $k$  as a function of  $l$ , generating a helical modulation. There is also a slowly varying modulation in the intensity along the rod. Figure 4.11(e) shows a schematic reciprocal space view showing several of the satellites at 150 K. The widths of each rod appear to vary since they have different intensities.

A value for the radius of the satellite helices is determined in figure 4.10, which is made by plotting the position of the maximum intensity pixel for several  $l = \text{constant}$  reciprocal space slices (in effect, determining the centre of the satellite intensity). The three-dimensional plot is fitted with a helix of radius  $\rho = 5$  pixels (red line in figure 4.10), which corresponds approximately to  $\rho \approx 0.015 a^*$  in reciprocal lattice units.

#### 4.3.2.2 $T > T^*$

Figure 4.11(a) can be directly compared to figure 4.11(b), which shows the same portion of reciprocal space above the transition at  $T^*$ . It is clear that the spotty structure of the rods [which indicates that unique mode(s) have been stabilised] is no longer present at high  $T$ , where one finds a continuous and highly diffuse distribution of intensity along  $\mathbf{c}^*$ . It should be noted however that the *pitch* of the helix in figure 4.11(b) remains very well-defined, and the loss of coherence is only in the  $\mathbf{c}^*$  direction since the intensity maxima still maintain well-defined boundaries in the  $a^*b^*$  plane.

In figures 4.11(c) and 4.11(d) the phase and handedness belonging to several helices are examined. The data show simple rules for the phase,  $\varphi$ , and handedness of each helix.



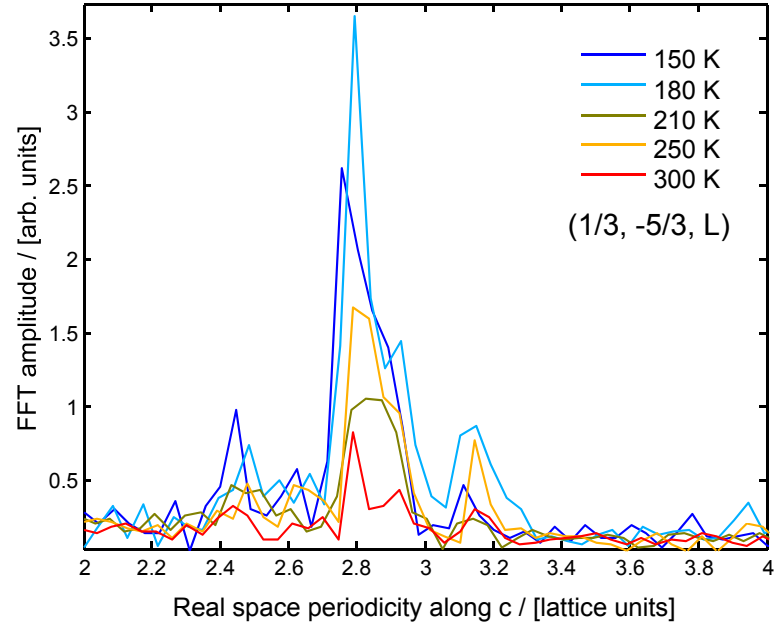


**Figure 4.9:** Fast Fourier transforms of the intensity profile in figure 4.8, as a function of sample temperature below  $T^*$ .

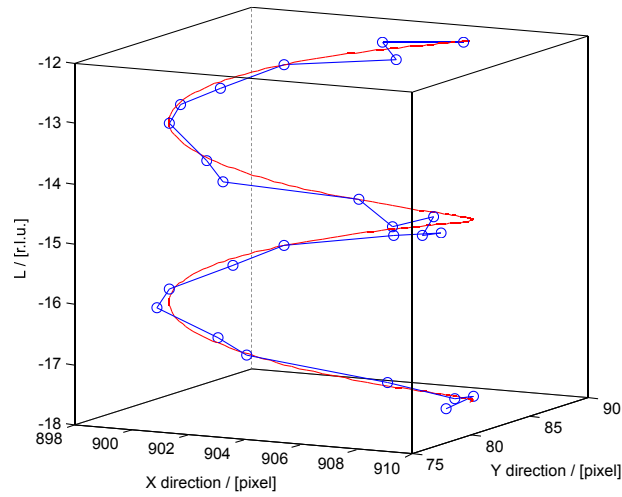


**Figure 4.10:** Positions of intensity maxima at different values of  $l$  for the  $(2/3, -7/3, l)$  satellite rod. The red line is a fit comprising a perfect helix of radius 5 pixels.

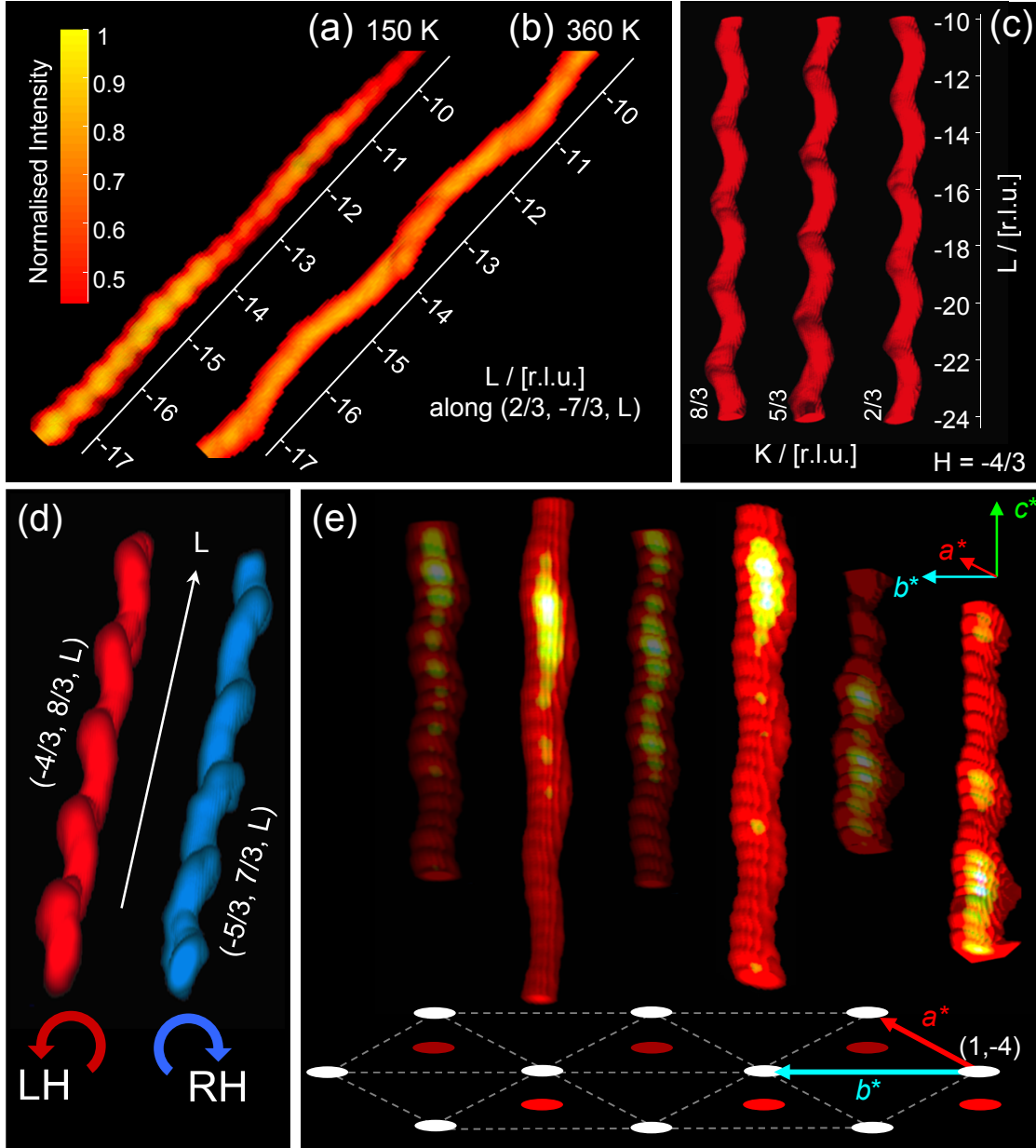


**Figure 4.11:** Three-dimensional reciprocal space isointensity plots of the satellite helices arising from the charge ordering. The data in (a) and (b) show a particular satellite below and above  $T^* = 320$  K, clearly showing the transition from a ‘spotty’ to a continuous distribution of intensity. At low temperatures intensity is concentrated onto peaks separated by  $\approx c^*/3$ . In (c) three adjacent helices ( $T = 360$  K) are plotted, demonstrating that while the pitch of each helix remains constant (at  $3c^*$ ), the phase varies according to the position in the  $a^*b^*$  plane. (d) Two helices at  $T = 360$  K, for  $24 < l < 10$  r.l.u., illustrating the selection rule for the handedness. (e) Schematic reciprocal space reconstruction of several satellites at 150 K. The reciprocal lattice is shown at the bottom (white circles) with the locations of the satellites (red circles) projected downwards.

Working in a Cartesian reciprocal space basis, the helices are described by reciprocal space vectors of the form

$$\mathbf{Q} = (Q_x + \rho \cos \theta, Q_y + \rho \sin \theta, l), \quad (4.25)$$

where

$$\theta = \pm \frac{2\pi l}{3} + \varphi \quad (4.26)$$

and the phase of each helix is given by

$$\varphi = 2\pi \frac{(h - k)}{3} + \varphi_0, \quad (4.27)$$

$\varphi_0$  being a constant phase. The  $\pm$  in equation (4.26) determines the handedness of the helix, and obeys

$$h + k = \frac{3n \pm 1}{3}, \quad (4.28)$$

where  $h$  and  $k$  are the commensurate positions of the helix in the plane, and the  $\pm$  sets the handedness as left (+) or right (−) [see figure 4.11(d)]. This is as one would expect given the  $R\bar{3}m$  symmetry, in which the handedness of the helices is fixed entirely by the chiral holohedral axes that are present along  $\mathbf{c}^*$  in the rhombohedral reciprocal lattice at  $(1/3, 1/3)$ -type positions (see figure 4.19 for more details). Phase differences between these chiral axes are also responsible for the form that the phase of the helices takes in equation (4.27).

### 4.3.3 Discussion

The striking feature of the low temperature data (below  $T^*$ ) is the observation of intensity maxima separated not by the commensurate  $c^*/2$  as reported by electron diffraction measurements (see section 4.1.2.2), but instead by an incommensurate separation of  $\approx c^*/3$ . It is also clear that, whichever modes are stabilised, they do not lead to peaks at exactly  $(1/3, 1/3)$  type positions in-plane, but deviate slightly from this commensurate value. This will be central to the modelling of the low temperature diffraction data I present in section 4.4.

The behaviour as one warms through the transition at  $T^*$  is intriguing. Typically, if one had a structure lacking in long range periodicity along the  $\mathbf{c}$  direction, the expectation would be to observe diffuse reciprocal lattice rods of scattering (extended along  $\mathbf{c}^*$ ) rather than well-defined peaks. (This is because the repeat period along  $\mathbf{c}$  is essentially infinite, leading to a vanishingly small distance between ‘Bragg peaks’ in the  $\mathbf{c}^*$  direction.) However, the present data do not show this behaviour. Whilst the diffuse element is certainly present, the helices along  $\mathbf{c}^*$  clearly demonstrate strong correlations along the  $\mathbf{c}$  direction (much greater

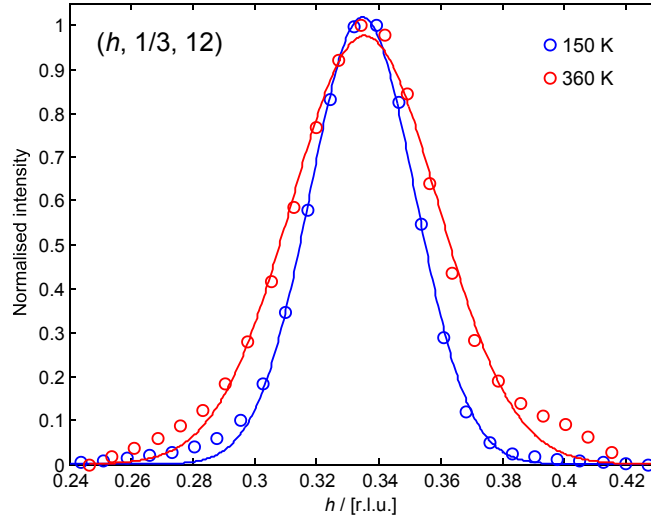


**Figure 4.12:** Intensity profiles of the  $(h, 1/3, 12)$  charge ordering satellite peak at 150 K and 360 K. The data (open circles) are fitted with a Gaussian peak shape (lines). The 150 K fit has a narrower peak shape, indicating a greater correlation length in the plane compared to 360 K.

than the interbilayer distance) since they have a very well-defined pitch. The fact that the isointensity surfaces appear to follow such a helical pattern is indicative of a real space behaviour in which there exists a progressive population of modes within a quasidegenerate helical manifold, starting from those that are closest to the ground state, so that the local coherence is maintained whilst allowing the system to explore states around the minima. This behaviour is also supported theoretically by the work of Yamada, Harris, and Yildirim [117, 118], who developed a mean field model to describe the Coulomb interactions between charges that was inspired by an equivalent problem encountered in the magnetic ordering in solid oxygen [119, 120].

Strong correlations in the charge ordering found in the  $ab$  plane, which can be quantified by the width of the diffraction satellite peaks in the  $\mathbf{a}^*$  or  $\mathbf{b}^*$  directions, are present at all temperatures including above  $T^*$  (see figure 4.12). However, the correlation length in the plane is longer at lower temperatures, as is to be expected.

#### 4.4 The low temperature structure and oxygen displacement model

In this section I shall model the X-ray intensities by considering the effect of the Fe valence ordering on the different oxygen sites in the unit cell. To begin with I shall introduce a relatively simple and intuitive oxygen displacement model assuming a commensurate charge ordering pattern. I shall then calculate the scattered intensities one would expect if such

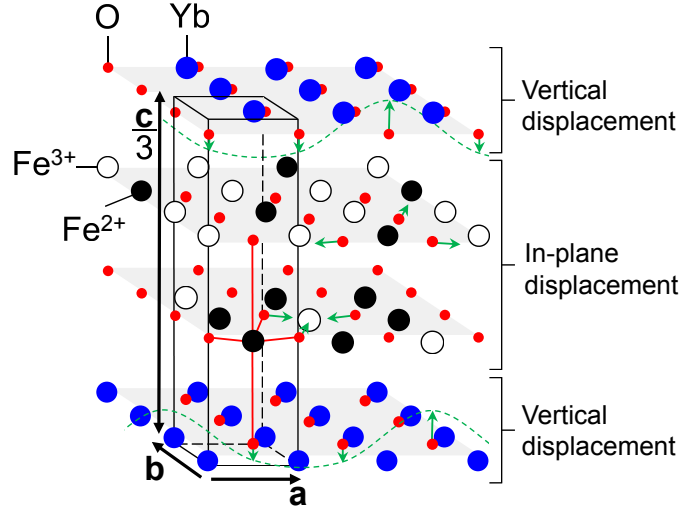


**Figure 4.13:** Part of the commensurate structure, showing the vertical displacement of apical oxygen ions in the  $\text{YbO}_2$  layers, and in-plane displacement of the oxygen ions in the  $\text{Fe}_2\text{O}_2$  layers. One third of the crystallographic unit cell is indicated by the box.

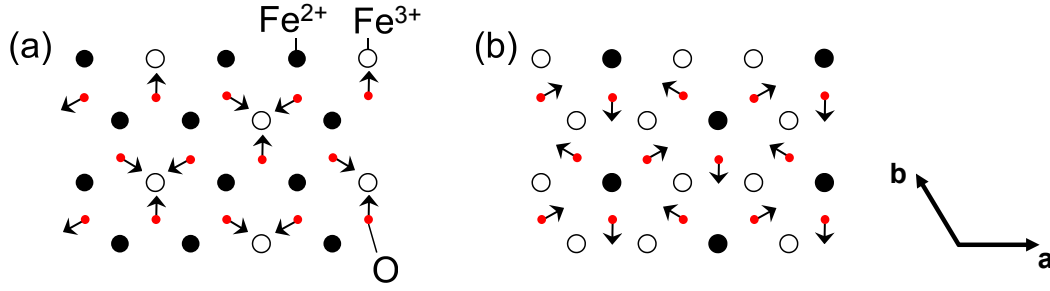
a commensurate model were correct. Following this I shall generalise the model to an incommensurate structure, whose propagation vectors form a better match to the X-ray scattering data. The final part of this section compares the intensities generated by both commensurate and incommensurate models to the data.

#### 4.4.1 Oxygen displacements in the commensurate picture

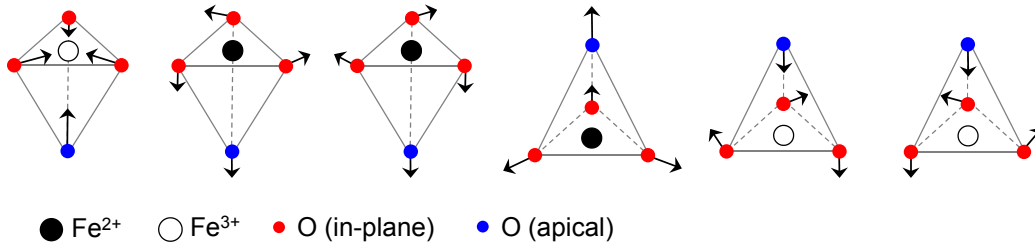
Before attempting to model the incommensurate low temperature structure, I will begin by assuming that the system orders in a commensurate way as described in section 4.1.2, and then introduce small deviations following this. The model I use modulates the positions of all of the oxygen ions in the crystal, both those in the  $\text{Fe}_2\text{O}_2$  ('in-plane' oxygens) and those in the  $\text{YbO}_2$  layers ('apical' oxygens).

Figure 4.13 shows a portion of the  $\text{YbFe}_2\text{O}_4$  structure, extending in height up to  $c/3$ . Those oxygen ions in the lowest layer are apical, and are displaced vertically following a sinusoidal envelope. The phase is chosen so that the maximum displacement is towards the  $\text{Fe}^{3+}$  ion on the layer above, and correspondingly away from the  $\text{Fe}^{2+}$  ions. The oxygens in the  $\text{Fe}_2\text{O}_2$  bilayers are displaced solely in-plane. The arrangement is such that, for a  $(2\text{Fe}^{2+} + \text{Fe}^{3+})$  layer, the oxygens displace *towards* the nearest  $\text{Fe}^{3+}$ , whereas for a  $(\text{Fe}^{2+} + 2\text{Fe}^{3+})$  layer, the displacement is *away from* the nearest  $\text{Fe}^{2+}$ .

The in-plane arrangement is shown in more detail in figure 4.14. It is clear from this that the oxygens are either moving towards a 'central'  $\text{Fe}^{3+}$  and away from the centre of



**Figure 4.14:** In-plane commensurate oxygen displacement patterns for (a) a  $(2\text{Fe}^{2+} + \text{Fe}^{3+})$  layer, and (b) a  $(\text{Fe}^{2+} + 2\text{Fe}^{3+})$  layer.



**Figure 4.15:** The six different types of oxygen tetrahedra in the commensurate displacement pattern of  $\text{YbFe}_2\text{O}_4$ . The three on the left form the  $(2\text{Fe}^{2+} + \text{Fe}^{3+})$  layer, and the three on the right the  $(\text{Fe}^{2+} + 2\text{Fe}^{3+})$  layer.

mass of two nearest neighbour  $\text{Fe}^{2+}$  ions [figure 4.14(a)], or moving away from a central  $\text{Fe}^{2+}$  towards the centre of mass of two nearest neighbour  $\text{Fe}^{3+}$ 's [figure 4.14(b)]. One way of visualising the displacement patterns in-plane is in terms of a ‘distortion field’  $\mathbf{S}$  originating from each Fe ion and obeying the Maxwell-like equation

$$\nabla \cdot \mathbf{S} = -\delta\rho, \quad (4.29)$$

where  $\delta\rho$  is the deviation of the Fe valence from the average of +2.5. Thus  $\text{Fe}^{2+}$  ions are distortion field ‘sources’ whilst the  $\text{Fe}^{3+}$  ions are distortion field ‘sinks’. Each oxygen, which is sensitive to the distortion field originating from its three nearest neighbour Fe ions, is displaced according to the total field at its position in the structure. In the commensurate displacement picture, there are six different resulting types of oxygen tetrahedra (each surrounding an Fe ion): these are displayed in figure 4.15. It is of interest to draw an analogy here between the displacement pattern of the in-plane oxygens and the  $120^\circ$  magnetic spin structure on a triangular lattice (see chapter 3).

The first  $1/3$  of the unit cell along  $c$  pictured in figure 4.13 comprises a W6 layer positioned between the two U-layers. To continue the commensurate ‘starting point’ I shall take the next W-layer along the  $c$  direction to be W5, and the next to be W4 (thereby fully

defining the crystallographic unit cell in terms of the charge ordering). The following equations can then be used to generate the oxygen displacements (described by the vector  $\mathbf{d}_{\text{Fe-O}}$  for the in-plane oxygens, and  $\mathbf{d}_{\text{Yb-O}}$  for the apical oxygens) directly from the propagation vector  $\mathbf{q}$ :

$$\mathbf{d}_{\text{Fe-O}} = (d_x, d_y, 0), \quad (4.30)$$

where

$$d_x \pm id_y = d_1 e^{i\mathbf{R}_n \cdot \mathbf{q}} e^{i\phi_j}, \quad (4.31)$$

and

$$\mathbf{d}_{\text{Yb-O}} = (0, 0, d_z), \quad (4.32)$$

where

$$d_z = d_2 \cos(\mathbf{R}_n \cdot \mathbf{q} + \phi_j). \quad (4.33)$$

The index  $j = 0, \dots, 11$  is used to label the ‘layer’ in the  $ab$  plane in which the oxygens are positioned. Thus the oxygens corresponding to  $j = 0$  are at the bottom of the unit cell and are displaced vertically (see figure 4.13),  $j = 1$  oxygens are at the bottom of the first W-layer (here a W6), *etc.* The phases  $\phi_j$  are determined by imposing a W6-W5-W4 structure (this would lead to polarisation cancelling out in the plane, but summing to give a non-zero value along  $\mathbf{c}$  in the commensurate picture).

In equations (4.30) to (4.33),  $\mathbf{R}_n$  is the crystallographic unit cell vector of the oxygen in question,  $d_1$  and  $d_2$  are displacement amplitudes (respectively for in-plane and apical oxygens),  $\mathbf{q}$  is the propagation vector, and  $d_x$ ,  $d_y$  and  $d_z$  are the displacements along the directions of the Cartesian orthonormal basis axes defined by  $\hat{\mathbf{e}}_x \parallel \mathbf{a}$ ,  $\hat{\mathbf{e}}_z \parallel \mathbf{c}$ , and  $\hat{\mathbf{e}}_y = \hat{\mathbf{e}}_z \times \hat{\mathbf{e}}_x$ .

#### 4.4.2 Propagation vectors for the commensurate structure

An immediate problem one encounters in attempting to model the low temperature data is that the intensity maxima are separated by  $\approx c^*/3$ . For the purposes of the model, this separation is taken to be *exactly* equal to  $c^*/3$  (the true value is slightly greater than this: see section 4.3.2.1). Note first that if a single propagation vector of the form  $\mathbf{q}_1 = (1/3, 1/3, 1/3)$  were present, then the  $\bar{3}$  symmetry would generate a set of three symmetry equivalent domains. This will lead to scattered intensity at the following locations with respect to the Bragg peaks:

$$\begin{array}{lll} (1/3, 1/3, 1/3), & (2/3, -1/3, -1/3), & (1/3, -2/3, 1/3), \\ (-1/3, -1/3, -1/3), & (-2/3, 1/3, 1/3), & (-1/3, 2/3, -1/3). \end{array}$$

The first row may be taken to be the propagation vectors associated with each of the three domains, and the second row comes from the fact that, for each propagation vector  $\mathbf{q}$ , intensity is scattered to positions  $\mathbf{G} \pm \mathbf{q}$ . Including now the effect of the mirror planes

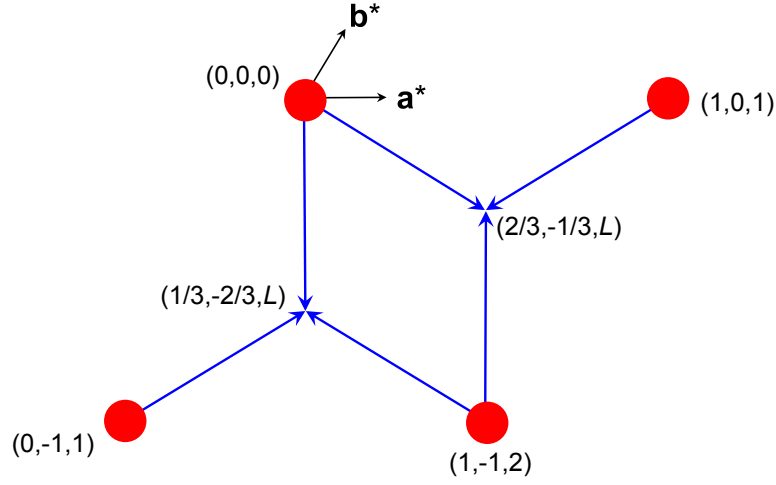


**Figure 4.16:** Reciprocal space diagram showing the contributions of the different propagation vectors  $\mathbf{q} = (1/3, 1/3, 1/3)$  and  $\mathbf{q} = (1/3, 1/3, 0)$  to the satellites in the commensurate picture ( $\mathbf{c}^*$  is directed out of the page). The reciprocal lattice nodes are indicated by the red circles, and the blue arrows show the *in-plane* projection of the propagation vectors. Each blue arrow actually contributes three satellites to the central position, with  $q_z = +1/3, 0$ , and  $-1/3$ .

(increasing the symmetry to  $\bar{3}m$ ), a further three equivalent propagation vectors are formed leading to further intensity maxima located at:

$$\begin{aligned} & (1/3, 1/3, -1/3), \quad (2/3, -1/3, 1/3), \quad (1/3, -2/3, -1/3), \\ & (-1/3, -1/3, 1/3), \quad (-2/3, 1/3, -1/3), \quad (-1/3, 2/3, 1/3). \end{aligned}$$

The problem, therefore, is that with a single propagation vector of this form one will observe intensity maxima at  $l = n \pm 1/3$  ( $n \in \mathbb{Z}$ ) positions, but not at the positions  $l = n$ . Thus, in order to obtain peaks uniformly separated by  $c^*/3$  it is necessary to include a second propagation vector with zero  $q_z$  component. Such a vector, of the form  $\mathbf{q}_2 = (1/3, 1/3, 0)$ , gives rise to six symmetry equivalent peaks (the mirror planes have no effect since the final component of  $\mathbf{q}_2$  is zero) located at:

$$\begin{aligned} & (1/3, 1/3, 0), \quad (2/3, -1/3, 0), \quad (1/3, -2/3, 0), \\ & (-1/3, -1/3, 0), \quad (-2/3, 1/3, 0), \quad (-1/3, 2/3, 0). \end{aligned}$$

Combining the effect of these domains gives rise to a reciprocal space picture similar to that depicted in figure 4.16, where a particular satellite rod will have peaks in intensity coming from propagation vectors attached to the three surrounding Bragg peaks.

#### 4.4.3 Generalisation to an incommensurate model

Having developed a model for the commensurate  $\sqrt{3} \times \sqrt{3}$  ordering, it is now straightforward to generalise the same model to that with an incommensurate propagation vector.



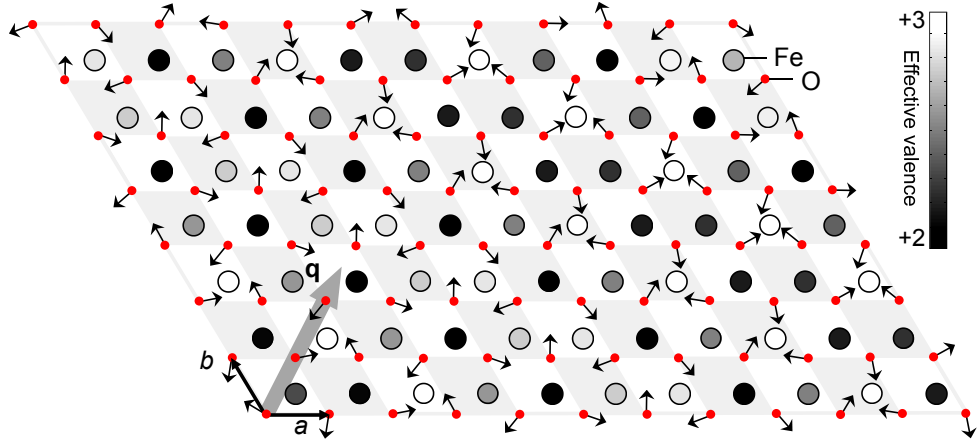


**Figure 4.17:** Representation of the in-plane oxygen displacement pattern for an incommensurate propagation vector  $\mathbf{q} = (1/3 + \delta, 1/3 + \delta)$ . Based on the oxygen displacements, an effective valence is assigned to each Fe ion, as indicated by its colour.

Equations (4.30) to (4.33) are used to generate the oxygen displacements, this time with an incommensurate value of  $\mathbf{q}$ . Once an incommensurate oxygen displacement pattern has been generated, one can assign an ‘effective’ valence to the Fe ions sitting between the oxygens, based on equation (4.29), which provides a formal link between the scalar field of the Fe charge, and the vector ‘distortion’ field.

By way of example, figure 4.17 shows schematically what such an in-plane incommensurate pattern might look like, with  $\mathbf{q} = (1/3 + \delta, 1/3 + \delta)$ , such that the oxygen displacements rotate slightly further around than the commensurate value of  $120^\circ$  between adjacent crystallographic unit cells. Notice that the Fe ion valence is assigned low values (black) when the surrounding oxygens are predominantly displaced away from it (*i.e.* the distortion field is diverging outwards), whereas it is assigned high values (white) when the reverse is true. In this way, one can see the ‘charge density wave’-like behaviour resulting from the slowly varying Fe valences propagating along the direction of  $\mathbf{q}$ . In this incommensurate model, the apical oxygens would continue to be displaced sinusoidally along the  $c$ -axis, although the period is clearly no longer equal to an integer number of unit cells. One may therefore think of the incommensurate structure as a slow variation between the configurations depicted in figure 4.15.

Calculating intensities to model the data first requires determination of the incommensurate propagation vector(s) associated with the displacement mode(s). In order to keep the model manageable I shall continue to take the  $z$ -component of the propagation vector as commensurate, such that peaks appear along the  $l$ -direction spaced *exactly*  $c^*/3$  apart. I therefore will take two non-equivalent propagation vectors as in the previous section and

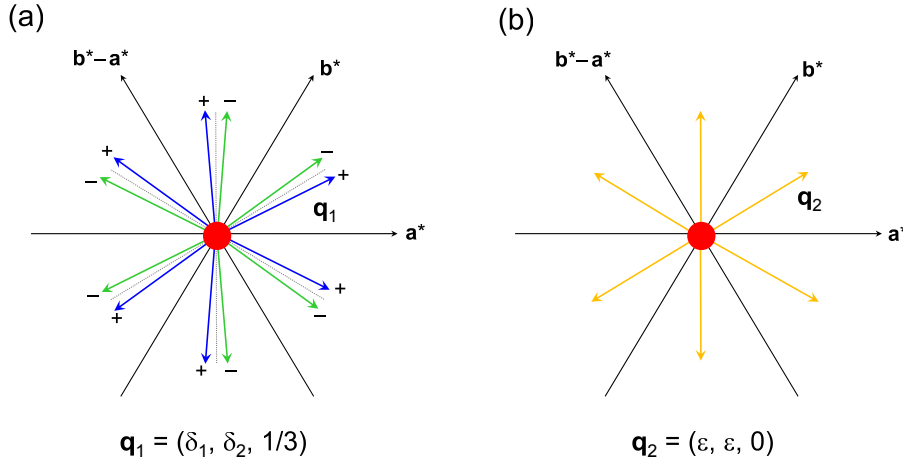


**Figure 4.18:** View of the  $a^*b^*$  plane in reciprocal space (with  $\mathbf{c}^*$  directed out of the page), showing (a)  $\mathbf{q}_1$  and the eleven symmetry equivalent positions generated by  $\bar{3}m$ , and (b)  $\mathbf{q}_2$  and the five symmetry equivalent positions. The various  $\mathbf{q}$ 's surround the central Bragg peak (red circle). In (a) the position above or below the page is indicated with + (green arrows) or - (blue arrows), whereas in (b)  $q_z = 0$ . The mirror planes contain the  $\mathbf{c}^*$  and either the  $\mathbf{a}^*$ ,  $\mathbf{b}^*$ , or  $\mathbf{b}^* - \mathbf{a}^*$  directions.

proceed in a similar way. The first propagation vector, of the form  $\mathbf{q}_1 = (\delta_1, \delta_2, 1/3)$ , generates a set of three equivalent domains due to the  $\bar{3}$  symmetry, giving scattered intensity located at:

$$\begin{aligned} &(\delta_1, \delta_2, 1/3), & (\delta_1 + \delta_2, -\delta_1, -1/3), & (\delta_2, -\delta_1 - \delta_2, 1/3), \\ &(-\delta_1, -\delta_2, -1/3), & (-\delta_1 - \delta_2, \delta_1, 1/3), & (-\delta_2, \delta_1 + \delta_2, -1/3). \end{aligned}$$

The effect of the mirror planes leads to further intensity located at:

$$\begin{aligned} &(\delta_2, \delta_1, 1/3), & (-\delta_1, \delta_1 + \delta_2, -1/3), & (-\delta_1 - \delta_2, \delta_2, 1/3), \\ &(-\delta_2, -\delta_1, -1/3), & (\delta_1, -\delta_1 - \delta_2, 1/3), & (\delta_1 + \delta_2, -\delta_2, -1/3). \end{aligned}$$

All twelve of these reciprocal space positions are shown in figure 4.18(a). The second propagation vector, of the form  $\mathbf{q}_2 = (\epsilon, \epsilon, 0)$ , gives rise to six symmetry equivalent peaks:

$$\begin{aligned} &(\epsilon, \epsilon, 0), & (2\epsilon, -\epsilon, 0), & (\epsilon, -2\epsilon, 0), \\ &(-\epsilon, -\epsilon, 0), & (-2\epsilon, \epsilon, 0), & (-\epsilon, 2\epsilon, 0), \end{aligned}$$

which are shown in figure 4.18(b).

The combined effect of all domains gives the reciprocal space picture of figure 4.19. From this it is clear that the resulting satellites will form a helical structure in reciprocal space, propagating along the  $l$ -direction with a pitch of  $3c^*$ . The radius of the helix,  $\rho$ , can be used to fix  $\mathbf{q}_1$  and  $\mathbf{q}_2$ , according to the following geometrical considerations. As shown in the inset to figure 4.19, the position of the peak at the end of the  $\mathbf{q}_2$  vector is given (with respect to the basis vectors  $\mathbf{a}^*$  and  $\mathbf{b}^*$  of the reciprocal lattice) by

$$\mathbf{P}_2 = \begin{pmatrix} 1/3 \\ -2/3 \end{pmatrix} - \alpha \begin{pmatrix} 1 \\ 1 \end{pmatrix}, \quad (4.34)$$

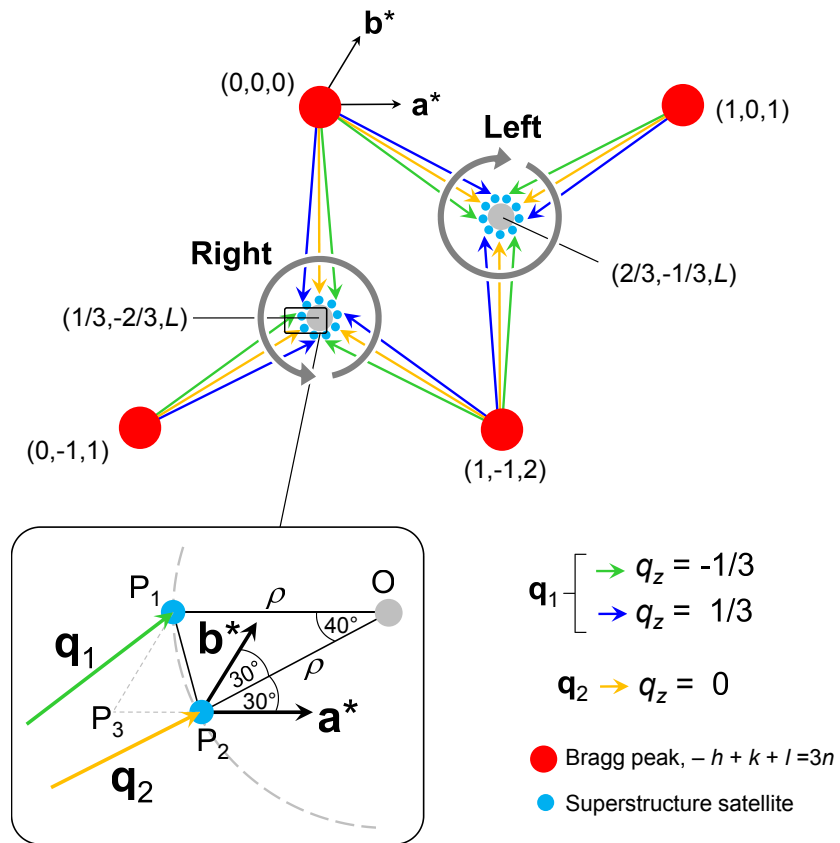


**Figure 4.19:** Contributions of the two propagation vectors  $\mathbf{q}_1 = (\delta_1, \delta_2, 1/3)$  and  $\mathbf{q}_2 = (\epsilon, \epsilon, 0)$  to the satellites (blue circles) (compare with figure 4.16). The coordinates  $(h, k, l)$  and the directions of  $\mathbf{a}^*$  and  $\mathbf{b}^*$  are indicated. Inset: geometry of two satellite peaks at points  $P_1$  and  $P_2$ , relative to the centre of the helix at  $(1/3, -2/3, l)$  (grey circle).

where the length of the second part of this vector is  $|\alpha(\mathbf{a}^* + \mathbf{b}^*)| = \rho$ . This fixes

$$\epsilon = \frac{1}{3} - \frac{\rho}{\sqrt{3}}. \quad (4.35)$$

Finding the vector  $\overrightarrow{P_2P_1}$  will then set the  $\delta_{1,2}$ . Since triangle  $P_1OP_2$  is isosceles with angle  $P_1\hat{O}P_2 = 360^\circ/9 = 40^\circ$ , we have:

$$|\overrightarrow{P_1P_2}| = \rho \sin 40^\circ / \sin 70^\circ = 0.6840\rho, \quad (4.36)$$

$$|\overrightarrow{P_3P_2}| = |\overrightarrow{P_1P_2}| \sin 40^\circ / \sin 60^\circ = 0.5077\rho, \quad (4.37)$$

$$|\overrightarrow{P_3P_1}| = |\overrightarrow{P_1P_2}| \sin 80^\circ / \sin 60^\circ = 0.7779\rho, \quad (4.38)$$

(note that  $\overrightarrow{P_3P_2} \parallel \mathbf{a}^*$  and  $\overrightarrow{P_3P_1} \parallel \mathbf{b}^*$ ). Hence, in the reciprocal basis,

$$\mathbf{P}_1 = \mathbf{P}_2 + \begin{pmatrix} 0.7779\rho \\ -0.5077\rho \end{pmatrix} = \begin{pmatrix} 0 \\ -1 \end{pmatrix} + \begin{pmatrix} \frac{1}{3} + (0.7779 - \frac{1}{\sqrt{3}})\rho \\ \frac{1}{3} + (-0.5077 - \frac{1}{\sqrt{3}})\rho \end{pmatrix}, \quad (4.39)$$

and so the components of  $\mathbf{q}_1$  are given by

$$\delta_1 = \frac{1}{3} + \left(0.7779 - \frac{1}{\sqrt{3}}\right)\rho, \quad (4.40)$$

$$\delta_2 = \frac{1}{3} + \left(-0.5077 - \frac{1}{\sqrt{3}}\right)\rho. \quad (4.41)$$

Inserting a value for the radius  $\rho \approx 0.015a^*$  (see section 4.3.2.1) results in

$$\delta_1 = 0.3363\dots, \quad \delta_2 = 0.3171\dots, \quad \text{and} \quad \epsilon = 0.3247\dots \quad (4.42)$$

#### 4.4.4 Intensity calculations

The previous sections developed the formalism needed to generate the oxygen displacement patterns associated with a general propagation vector. It is now possible to apply these models to the X-ray data collected on YbFe<sub>2</sub>O<sub>4</sub>. For the incommensurate model, one can make any commensurate approximation to the incommensurate charge ordered structure (whose propagation vector was calculated in section 4.4.3), calculate the positions of all the atoms in the commensurate unit cell (typically this will be very large if it is to be a good approximation to the incommensurate structure), and therefore calculate the scattered X-ray intensity from an array of such supercells.

The same method may be applied to the commensurate model of section 4.4.2, for which a calculation of the intensities along a particular satellite rod may be achieved by building a supercell whose dimensions are  $3a \times 3b \times 3c$  for the  $\mathbf{q}_1 = (1/3, 1/3, 1/3)$  structure, or  $3a \times 3b \times c$  for the  $\mathbf{q}_2 = (1/3, 1/3, 0)$  structure. The structure factor would then be given by

$$F(\mathbf{Q}) = \sum_{j \text{ atoms in crystal}} f_j(\mathbf{Q}) e^{i\mathbf{Q} \cdot \mathbf{r}_j} \quad (4.43)$$

where we can write

$$\mathbf{r}_j = \mathbf{R}_n^{(\text{sup.cell})} + \mathbf{x}_l \quad (4.44)$$

and

$$\sum_{j \text{ atoms in crystal}} = \sum_{n \text{ supercells}} \sum_{l \text{ atoms in supercell}}. \quad (4.45)$$

Note that the  $\mathbf{x}_l$  will be fractional coordinates since they are defined with respect to the lattice vectors of the supercell (not the crystallographic cell). Thus

$$F(\mathbf{Q}) = \sum_{n \text{ supercells}} \sum_{l \text{ atoms in supercell}} f_l(\mathbf{Q}) e^{i\mathbf{Q} \cdot (\mathbf{R}_n^{(\text{sup.cell})} + \mathbf{x}_l)} \quad (4.46)$$

$$= \sum_n e^{i\mathbf{Q} \cdot \mathbf{R}_n^{(\text{sup.cell})}} \sum_l f_l(\mathbf{Q}) e^{i\mathbf{Q} \cdot \mathbf{x}_l}. \quad (4.47)$$

As in section 4.2, the first summation is just the addition of a very large number of phase factors, which will be zero unless  $\mathbf{Q}$  is equal to a reciprocal lattice vector of the supercell, denoted  $\mathbf{G}^{(\text{sup.cell})}$ . Hence

$$F(\mathbf{Q}) \propto \delta^{(3)}(\mathbf{Q} - \mathbf{G}^{(\text{sup.cell})}) \sum_l f_l(\mathbf{Q}) e^{i\mathbf{Q} \cdot \mathbf{x}_l}. \quad (4.48)$$

The places where the delta function at the start of this expression is non-zero mark the centres of the peak profiles that will be attached to each intensity maximum<sup>2</sup>.

In the case of the incommensurate model of section 4.4.3, the following commensurate approximations were made to the propagation vectors:

$$\mathbf{q}_1 = \begin{pmatrix} 42/125 \\ 38/125 \\ 1/3 \end{pmatrix} = \begin{pmatrix} 0.336 \\ 0.304 \\ 0.333 \dots \end{pmatrix}, \quad (4.49)$$

$$\mathbf{q}_2 = \begin{pmatrix} 8/25 \\ 8/25 \\ 0 \end{pmatrix} = \begin{pmatrix} 0.320 \\ 0.320 \\ 0 \end{pmatrix}. \quad (4.50)$$

Thus, for the  $\mathbf{q}_1$  structure, a supercell of dimensions  $125a \times 125b \times 3c$  will contain 42 repeating units along the  $a$ -direction, 38 along  $b$ , and 1 along  $c$ . Likewise for the  $\mathbf{q}_2$  structure, a supercell of dimensions  $25a \times 25b \times c$  will contain 8 repeating units along the  $a$ -direction, 8 along  $b$ , and 1 along  $c$ . These are the supercell dimensions that were used in the model, and equation (4.48) is again used to calculate the structure factors.

The calculation of the scattered X-ray intensities (whether from the commensurate or incommensurate models) proceeds according to the following steps:

<sup>2</sup>In principle one could attempt to simplify this expression by including the harmonic oxygen displacement patterns described in the previous section, making explicit the dependence on  $\mathbf{q}$ . This approach is not followed however, since ultimately the Yb ions will also be displaced in accordance with the surrounding oxygen displacements, which complicates the picture somewhat. Thus the scattered intensities are calculated directly from equation (4.48).

### Generating the supercell

The starting point is the positions of the 21 atoms (3 Yb, 6 Fe, 12 O) in the rhombohedral crystallographic unit cell which are then converted to Cartesian coordinates. Thus, an atom with fractional coordinates  $u, v, w$  is positioned at  $\mathbf{r} = u\mathbf{a} + v\mathbf{b} + w\mathbf{c} = xa\hat{\mathbf{e}}_x + ya\hat{\mathbf{e}}_y + zc\hat{\mathbf{e}}_z$ , where  $|\mathbf{a}| = |\mathbf{b}| = a$  and  $|\mathbf{c}| = c$ , and the appropriate transformations are  $x = u - \frac{1}{2}v$ ,  $y = v\frac{\sqrt{3}}{2}$ . Following this, an ‘empty’ supercell lattice (in Cartesian coordinates) is constructed with dimensions matching those above (depending on the propagation vector). Finally, this lattice is convoluted with the basis of 21 atoms to form an ‘undisplaced’ supercell.

### Ionic displacements

The oxygen ions are displaced according to equations (4.30) to (4.33) and the appropriate propagation vector  $\mathbf{q}$ . The oxygen displacements are a measure of the charge ordering, and could be estimated, for example, using the bond valence sum method [121] provided that both the main Bragg peaks and satellite peaks are measured. In the synchrotron experiment, only the satellite peaks were measured (the Bragg peaks being allowed to saturate on the detector), so for the purposes of this model I shall use a nominal displacement of 0.1 Å for both in-plane and apical oxygen positions. Following this, the Yb ions are displaced slightly such that they are at the centre of mass of the surrounding four<sup>3</sup> oxygen ions (imposing periodic boundary conditions at the edges of the supercell). This is important because, since Yb is a strong scatterer of X-rays, we expect the intensity pattern to be very sensitive to the Yb positions. With oxygen displacement amplitudes of 0.1 Å, typical Yb displacements are around 0.03 to 0.05 Å.

### X-ray intensities and comparison to data

The X-ray intensity associated with particular scattering vectors  $\mathbf{Q} = h\mathbf{a}^* + k\mathbf{b}^* + l\mathbf{c}^*$  is calculated for a particular plane of the reciprocal lattice, according to

$$I(\mathbf{Q}) = |F(\mathbf{Q})|^2, \quad (4.51)$$

where the structure factor  $F(\mathbf{Q})$  is [from equation (4.48)]:

$$F(\mathbf{Q}) \propto \delta^{(3)}(\mathbf{Q} - \mathbf{G}^{(\text{sup.cell})}) \sum_j f_j(|\mathbf{Q}|) e^{2\pi i(Q_1 x_1^j + Q_2 x_2^j + Q_3 x_3^j)}. \quad (4.52)$$

In this expression,  $\mathbf{Q} = (Q_1, Q_2, Q_3) = h'\mathbf{a}^{*'} + k'\mathbf{b}^{*'} + l'\mathbf{c}^{*'}$ , where the primes refer to the reciprocal lattice vectors of the supercell, and  $\mathbf{x}_j = x_1^j\mathbf{a}' + x_2^j\mathbf{b}' + x_3^j\mathbf{c}'$  represents the position of the  $j$ th atom in the unit supercell. Expressions for the atomic form factor

<sup>3</sup>There are four nearest neighbour oxygens to each Yb in this system.

	Yb	Fe	O
$a_1$	28.6641	11.7695	3.04850
$b_1$	1.98890	4.76110	13.2771
$a_2$	15.4345	7.35730	2.28680
$b_2$	0.257119	0.307200	5.70110
$a_3$	15.3087	3.52220	1.54630
$b_3$	10.6647	15.3535	0.323900
$a_4$	2.98963	2.30450	0.867000
$b_4$	100.417	78.8805	32.9089
$c$	7.56672	1.03690	0.250800

**Table 4.1:** Coefficients used in the analytic approximation to the X-ray atomic form factors for Yb, Fe, and O [see equation (4.53)].

$f_j(|\mathbf{Q}|)$  associated with the  $j$ th atom are determined from tables in [27]. The analytic approximation for each atom's form factor is given by the following expression:

$$f(s^2) = \sum_{i=1}^4 a_i e^{-b_i s^2} + c, \quad (4.53)$$

where  $s^2 := \sin^2 \theta / \lambda^2$  and the nine coefficients  $a_{1,...,4}, b_{1,...,4}, c$  are given in [27], and reproduced here in table 4.1. From Bragg's law we have  $s^2 = \frac{Q^2}{16\pi^2}$ , so if  $\mathbf{Q} = h\mathbf{a}^* + k\mathbf{b}^* + l\mathbf{c}^*$  then

$$s^2 = \frac{1}{16\pi^2} [(h^2 + k^2 + hk)a^{*2} + l^2 c^{*2}] \quad (4.54)$$

$$= \frac{1}{16\pi^2} \left[ (h^2 + k^2 + hk) \left( \frac{4\pi}{\sqrt{3}a} \right)^2 + l^2 \left( \frac{2\pi}{c} \right)^2 \right], \quad (4.55)$$

where  $a = 3.455 \text{ \AA}$  and  $c = 25.054 \text{ \AA}$  gives  $s^2$  in the required units of  $\text{\AA}^{-2}$ .

Intensity maps (slices of reciprocal space that can be compared directly to the data) are made by multiplying  $I(\mathbf{Q})$  with a function  $P(\mathbf{Q})$  comprising an array of Gaussian peak shapes positioned at the intensity maxima (where  $\mathbf{Q} = \mathbf{G}^{(\text{sup.cell})}$ ). For a constant  $k$  slice (*e.g.* one in which  $h$  is increasing along the  $x$ -axis, and  $l$  along the  $z$ -axis) this function is given by

$$P(h, l) = \sum_m \exp \left[ -\frac{(h - h_m^{\max})^2}{2\sigma_h^2} - \frac{(l - l_m^{\max})^2}{2\sigma_l^2} \right], \quad (4.56)$$

where the summation runs over the intensity maxima (labelled by  $m$ ) that are present within the intensity map, having coordinates  $(h_m^{\max}, l_m^{\max})$ , and the widths of the peaks in the  $h$ - and  $l$ -directions are given by the respective  $\sigma_{h,l}$ . The amplitude of the 'meandering' peak positions in the intensity maps is chosen to be in approximate agreement with the data; this corresponds to a radius of roughly  $0.015 a^*$  as used in calculating the propagation vectors.

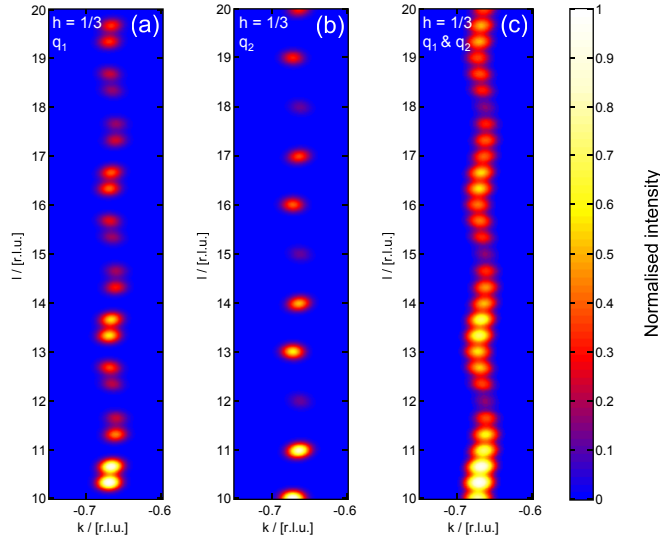


**Figure 4.20:** Combination of scattering due to the (a)  $\mathbf{q}_1$  and (b)  $\mathbf{q}_2$  modes to give a single intensity map (c), for the approximation to the incommensurate structure as detailed in section 4.4.3.

The two sets of intensities (calculated separately for the  $\mathbf{q}_1$  and  $\mathbf{q}_2$  structures<sup>4</sup>) are then combined to give a single intensity map, as shown in figure 4.20. For the purposes of the simple models presented here, the two modes are combined with essentially equal contribution (*i.e.* a scale factor is applied between them which allows for the difference in size of the corresponding supercells upon which the magnitude of the structure factor depends).

A simple background subtraction algorithm is run on the data before comparison is made to the calculated intensities, the effect of which is shown in figure 4.21. The algorithm takes two intensity profiles along  $l$ : one on the left-hand side of the rod and one on the right-hand side. It then averages the two profiles to obtain a background profile as a function of  $l$  which is subtracted from the entire plot. A selection of reciprocal space intensity maps, comparing calculations (from both commensurate and incommensurate models) with the data are presented in figures 4.22, 4.23, and 4.24. The intensity cuts chosen for the modelling comprised data that looked the most ‘clean’ and contained well-separated peaks<sup>5</sup>. Within each of these figures, the three sub-plots share the same intensity scale bar (right-hand side

<sup>4</sup>It is not necessary to calculate separately the intensities for each of the symmetry-equivalent domains associated with a particular propagation vector, since they all give rise to the same real space structure and therefore the same scattering pattern.

<sup>5</sup>Note also that the data are processed in such a way that these intensity slices are integrated over a distance of  $\approx 0.01$  r.l.u. orthogonally to the plane: thus, for the purposes of modelling the data, they are treated as a two-dimensional projection of the helix. Therefore the variation of intensity that one might expect as the helix moves orthogonally to the plane of the data slice is not taken into account.



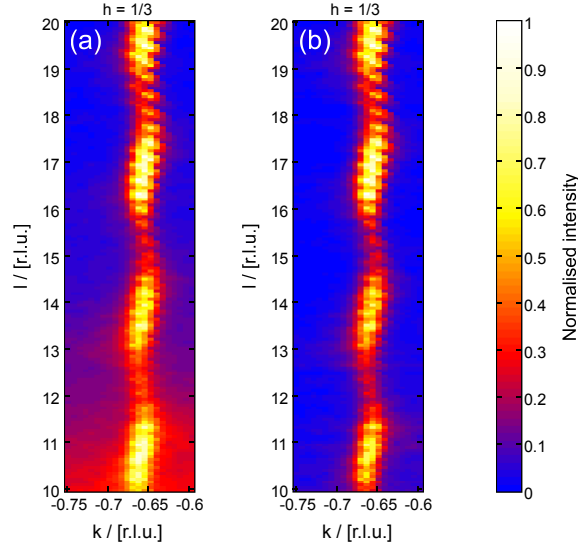


**Figure 4.21:** An example of (a) data without background subtraction, and (b) the same data with background subtraction.

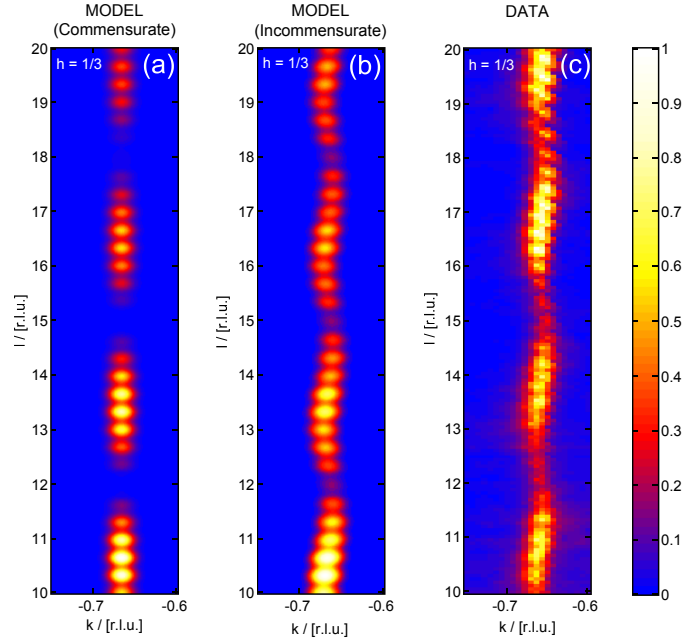


**Figure 4.22:** Intensity maps for a constant  $h$  slice through part of the  $(1/3, -2/3, l)$  set of satellites. (a) Calculated intensity from the commensurate model with  $\mathbf{q}_1 = (1/3, 1/3, 1/3)$  and  $\mathbf{q}_2 = (1/3, 1/3, 0)$ . (b) Intensity calculated by approximating incommensurate modes with propagation vectors  $\mathbf{q}_1 = (0.336, 0.304, 1/3)$  and  $\mathbf{q}_2 = (0.320, 0.320, 0)$ . (c) The background subtracted synchrotron data collected at 150 K. Normalised intensity is indicated by the colour bar on the right.

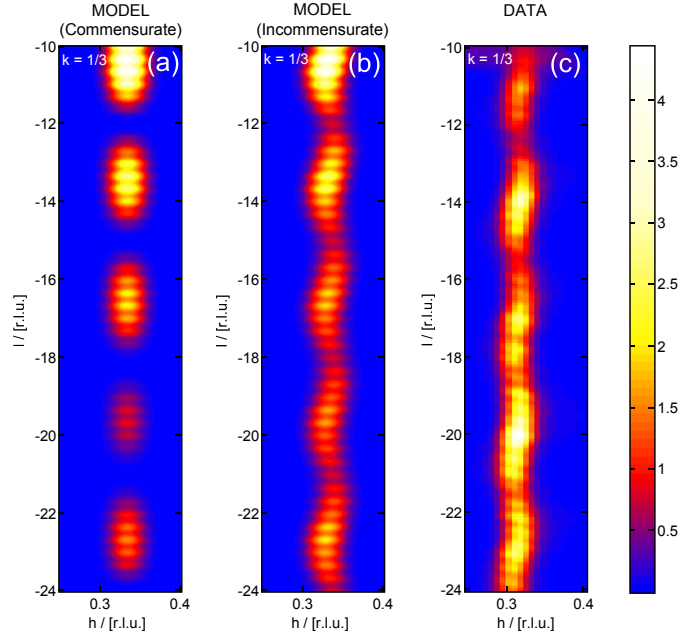


**Figure 4.23:** As figure 4.22, for a constant  $k$  slice through the  $(1/3, 1/3, l)$  set of satellites.

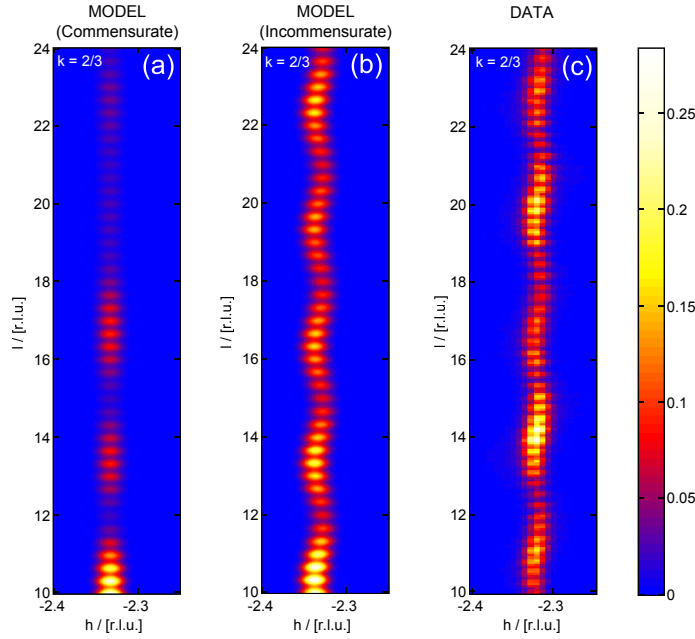


**Figure 4.24:** As figure 4.22, for a constant  $k$  slice through the  $(-7/3, 2/3, l)$  set of satellites.

of each figure). All of these intensities have been normalised to give the maximum intensity in figure 4.22 a value of 1.

Although the fits are by no means perfect, they succeed in reproducing the qualitative

behaviour of the intensities as a function of  $\mathbf{Q}$ . Some of the more subtle features are different in the data but this is to be expected from what is a relatively simple displacement model. It is clear that both these models suggest that the low temperature charge ordered structure can be thought of in terms of the population of two separate modes, presumably both deep in the energy landscape. In addition to this, the much better fits obtained by assuming an incommensurate model (this is particularly striking in figure 4.24) provide compelling evidence for the existence of a population of two *incommensurate* modes in the low temperature structure of  $\text{YbFe}_2\text{O}_4$ .

## 4.5 Conclusion

I have used high resolution synchrotron X-ray scattering data, taken above and below the phase transition at  $T^*$ , to explain the nature of the charge ordering present in  $\text{YbFe}_2\text{O}_4$ . At low temperatures, the data have been successfully simulated using an oxygen displacement model, and I have generalised the commensurate  $\sqrt{3} \times \sqrt{3}$  pattern to a large supercell approximation of the observed incommensurate structure. A primary implication of these results is that the  $R\text{Fe}_2\text{O}_4$  compounds *should not* exhibit a ferroelectric polarisation, because the charge order is incommensurately modulated. This means that a picture similar to that of figure 4.17 will describe the charges on the  $\text{Fe}_2\text{O}_2$  bilayers: therefore a polarisation exists across the bilayer but its direction will vary slowly with position within the plane. The effect of this variation will cancel out any net polarisation in the bulk, even though the bilayers are *locally* polar. In spite of this, an electrical polarisation has been measured in  $R\text{Fe}_2\text{O}_4$  and reported in the literature. A possible explanation is provided in [122], in which the authors claim that no intrinsic polarisation exists in  $\text{LuFe}_2\text{O}_4$ , and rather the reported polarisation is due to the influence of contacts. Recent results that demonstrate that the bilayers in  $\text{LuFe}_2\text{O}_4$  are actually non-polar also appear to support this idea [123].

In addition, the  $T > T^*$  data confirm theoretical predictions and show a continuous helix of scattering in reciprocal space. This was previously interpreted in terms of two-dimensional ordering, but this is incompatible with the helical structure observed here. Therefore significant  $c$ -axis correlations, much greater than the inter-bilayer distance, must be present in order to explain the diffraction data.

The exact charge ordered arrangement in  $R\text{Fe}_2\text{O}_4$  is clearly more complex than a simple commensurate model with a ferroelectric stacking of the bilayers (the model that would give rise to a bulk ferroelectric polarisation) would suggest. Further research is therefore needed in order to explain why certain samples of  $R\text{Fe}_2\text{O}_4$  appear to show bulk ferroelectricity below  $T^*$ . It would also be interesting to consider in more detail the effect of changing the rare earth ion, since diffraction data for different  $R$ 's appear to show different periodicities

in the charge ordering along  $\mathbf{c}$ , although small incommensurate deviations in-plane from the  $(1/3, 1/3)$  position are widely reported. Whilst theoretical considerations support the existence of continuous helices of scattering in reciprocal space above  $T^*$ , little light has been shed so far on a corresponding real space structure that could explain this diffraction pattern. The determination of such a structure would greatly help in understanding the true nature of the charge ordering in  $R\text{Fe}_2\text{O}_4$ .

## Chapter 5

---

### The low field phase diagram of $\text{Ba}_{0.5}\text{Sr}_{1.5}\text{Zn}_2\text{Fe}_{12}\text{O}_{22}$ hexaferrite

---

#### 5.1 Introduction

Barium hexaferrites have been studied with great interest for many years as the different structural types and the possibility of tuning the behaviour with doping (varying the relative strengths of the exchange interactions) has lead to great flexibility in the number of different magnetic phases supported by this class of materials [124, 125]. Their room temperature magnetism has also given rise to their use in permanent magnets in numerous applications, and their layered structure makes them suitable for growth by epitaxial methods [126]. Further exotic magnetic arrangements can typically be induced in these materials by altering the temperature and applied magnetic field. In particular, there has been substantial interest recently in the Z-type hexaferrites [formula  $(\text{Ba},\text{Sr})_3M_2\text{Fe}_{24}\text{O}_{41}$  where  $M$  is a divalent metal ion], which show the magnetoelectric effect at room temperature [127], as well as the Y-type hexaferrites. Of the latter, two compositions in particular have been well-studied: (i)  $\text{Ba}_2\text{Mg}_2\text{Fe}_{12}\text{O}_{22}$  and (ii)  $\text{Ba}_{2-x}\text{Sr}_x\text{Zn}_2\text{Fe}_{12}\text{O}_{22}$ . The Mg system displays helical, conical, and ferrimagnetic arrangements [128, 129] as the applied magnetic field is varied, and a ferroelectric polarisation appears in the field induced ‘tilted conical’ phase that can be controlled with the direction of the applied field [130–132]. It was also shown recently that this system displays signatures of an electric-dipole-active magnetic resonance (‘electromagnon’) measured by optical techniques [133].

However, it is the equally interesting and diverse system  $\text{Ba}_{2-x}\text{Sr}_x\text{Zn}_2\text{Fe}_{12}\text{O}_{22}$  that is the focus of this chapter. The various magnetic structures, in contrast to the Mg system, evolve from a helimagnetic arrangement in zero applied field to various ‘fan’ structures as the transverse field is increased [134, 135]. The discovery by Kimura *et al.* in 2005 that one of these fan structures also exhibits ferroelectricity [136] (this has also been reported recently

in aluminium doped systems where a conical component of the magnetic structure develops [137, 138]) has sparked renewed interest in practical applications since these systems have been shown to display multiferroic properties at room temperature. Electron diffraction experiments have also shown that the various magnetic structures induce modulations in the crystal lattice [139].

Soft X-ray diffraction is an excellent tool with which to study the magnetism in these hexaferrites because, by tuning the X-ray energy to be resonant with the Fe edge, a large resonant enhancement in the magnetic scattering can be obtained. This has recently been used by Mulders *et al.* [140] where circularly polarised X-rays were used to examine the zero field helical structure. This technique was subsequently used to great effect in [141] where the contrast in the diffracted signals from the helical spin arrangement between right and left circularly polarised X-rays was exploited to map the spatial distribution of chiral domains present in these materials.

In this chapter I present a soft X-ray diffraction study of the hexaferrite's magnetism in the low applied field region of the phase diagram. This technique is very sensitive to changes in the magnetic propagation vector(s) associated with the different phases of the material, and is therefore highly suited to studying the complex interactions between the many different proposed structures. Polarisation analysis is employed to improve sensitivity to the magnetic signal. Following this is a discussion of the various phases that are observed in the data, and a construction of the field / temperature phase diagram. One of the principal findings of this chapter is the suggestion of a new '6-fan' structure that gives rise to magnetic scattering with propagation vector  $\mathbf{q} = (0, 0, 1)$ , and energy calculations are carried out to demonstrate that this is a feasible candidate structure for this new phase.

### 5.1.1 Crystal structure

The magnetoplumbite-related Y-type hexaferrites have a relatively complex crystal structure with a large unit cell<sup>1</sup>, as depicted in figure 5.1 (see also [142]). The structure consists of an alternate stacking of spinel 'short' blocks (conventionally referred to as 'S' blocks), and hexagonal 'long' blocks ('L' blocks). The doping  $x$  measures the relative amounts of Ba and Sr: the system studied here has  $x = 1.5$ . The space group is  $R\bar{3}m$  and the lattice parameters of the sample used in the synchrotron experiment were measured at room temperature using a laboratory 'SuperNova' X-ray source to be  $a = 5.852(6)$  Å and  $c = 43.54(4)$  Å. A further parameter  $\gamma$  is necessary to describe the mixing of Fe and Zn on the  $6c$  sites:  $\gamma$  is the fraction of Fe on the  $6c$  sites in the L block (which is equal to the fraction of Zn on the

<sup>1</sup>The correspondingly small size of  $c^*$  makes soft X-ray diffraction (*i.e.* long X-ray wavelengths) particularly appropriate for the study of this system.

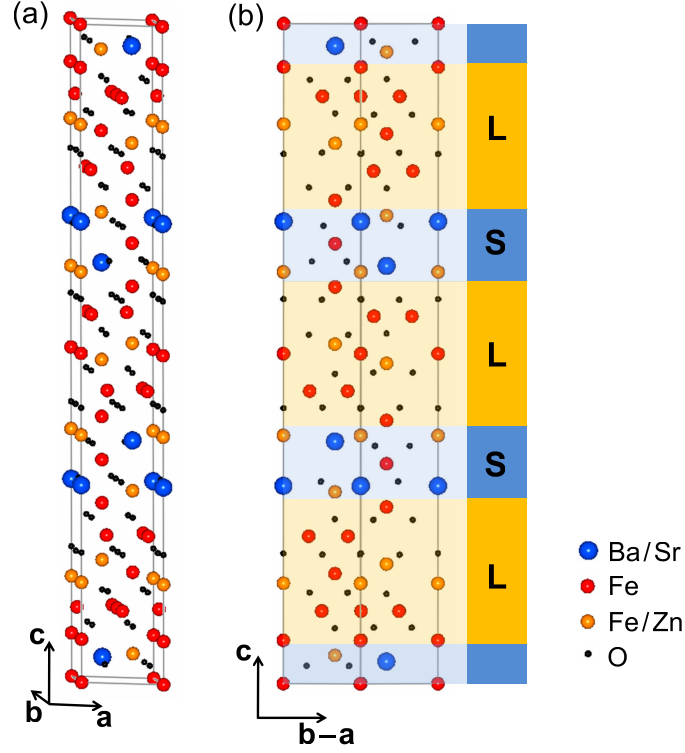


**Figure 5.1:** Crystal structure of the Y-type hexaferrite  $\text{Ba}_{2-x}\text{Sr}_x\text{Zn}_2\text{Fe}_{12}\text{O}_{22}$ . (a) A perspective view of a single unit cell, which is shown in projection in (b). The locations of the S and L blocks are indicated. The atoms depicted in yellow (labelled Fe / Zn) have mixed Fe and Zn occupation, parametrised by  $\gamma$ .

6c sites in the S block) [143]. In [134] a value of  $\gamma = 0.661$  is reported for  $x$  close to 1.5, and this is the value that is used in describing the moments of the spin blocks in section 5.6. However,  $\gamma$  is known to vary between samples of nominally identical composition [143], so this value may not be exactly correct for the sample studied here. This is of little consequence for the work that follows though, as the only effect will be to adjust slightly the exchange parameters derived to fit the data.

### 5.1.2 Magnetic structures

Here I introduce in more detail the various reported magnetic structures, determined by neutron scattering in [135], that are known to be present in this hexaferrite. These systems have many different sites containing magnetic ions, and as such the possibility exists for a large number of complex and varied magnetic structures to appear in the material. However, a substantial simplification can be made because all of the magnetic moments within each L or S block can be viewed as being ferromagnetically aligned perpendicularly to  $\mathbf{c}$ , such that

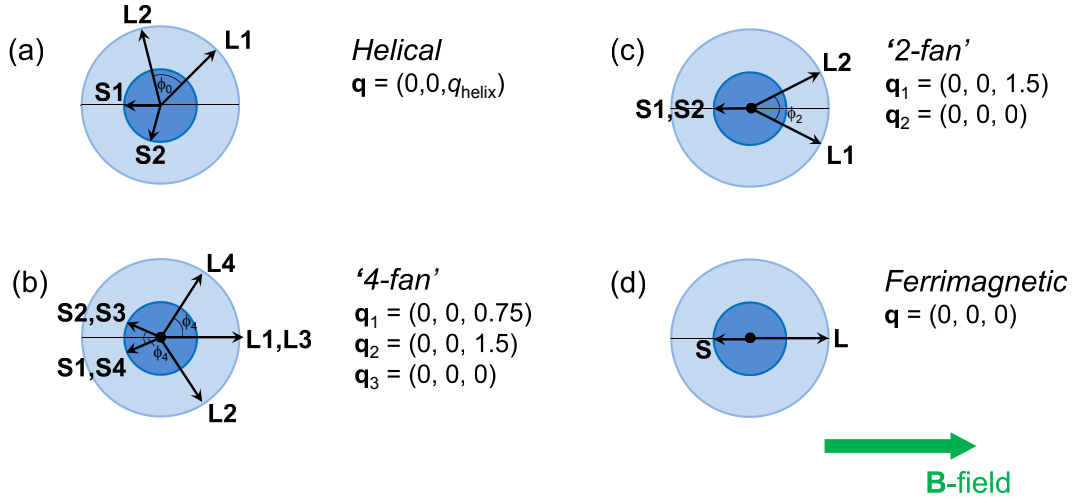


**Figure 5.2:** Plan views (along  $\mathbf{c}$ ) of the various previously reported magnetic phases of the hexaferrite [135]. Moving from (a) to (d) corresponds to increasing the applied magnetic field from zero (the direction of  $\mathbf{B}$  is indicated). The propagation vector(s)  $\mathbf{q}_i$  associated with each phase are given (see also [135]), along with the labelling used for the angles between the spin blocks. The blocks stack in the order S1-L1-S2-L2-... as one moves along the positive  $\mathbf{c}$  direction.

the spin blocks can be treated essentially as separate effective magnetic moments stacked along  $\mathbf{c}$ .

The magnetic phases that the material exhibits as a function of increasing applied magnetic field are summarised in figure 5.2. In zero field an incommensurate helical structure is stabilised [figure 5.2(a)], with the L blocks and S blocks out of phase by an angle of  $180^\circ + \phi_0/2$ . Applying a transverse field causes the structure to change such that more of the moment is aligned with the field: this results in the ‘4-fan’ oscillatory structure of figure 5.2(b) (this is also known in the literature as the ‘Intermediate-I’ phase), and at higher fields the ‘2-fan’ structure of figure 5.2(c) (the ‘Intermediate-II’ phase). Note that a strong antiferromagnetic exchange interaction between nearest neighbour spin blocks tends to align the S blocks antiparallel to the field. As the field is increased, the system enters the multiferroic ‘Intermediate-III’ phase in which a ferroelectric polarisation is reported [136]. However, the exact structure of this phase remains controversial, since all of the diffraction data collected thus far point to a ‘2-fan’ structure [identical to figure 5.2(c)], but this magnetic arrangement retains inversion symmetry and cannot, therefore, be polar. At still higher fields all of the moments align (or anti-align) with the field direction producing the ferrimagnetic configuration depicted in figure 5.2(d). The propagation vectors describing the different phases can be calculated via the standard Fourier expansion of the collection



of moments  $\mu_l$  from which the structure is generated:

$$\mu_l \propto \sum_j (\mathbf{S}_j e^{-i\mathbf{q}_j \cdot \mathbf{r}_l} + \mathbf{S}_j^* e^{i\mathbf{q}_j \cdot \mathbf{r}_l}), \quad (5.1)$$

where  $\mathbf{S}_j$  is the Fourier component for the  $j$ th propagation vector, and  $\mathbf{r}_l$  is the position of the moment  $\mu_l$ . The phase diagram summarising the above can be found in [136], and shows that the system very quickly changes from one phase to another as the applied field is increased. Thus, the motivation of the present work is to examine the behaviour of the system in low applied fields, where the energies of the different phases are closely spaced, and to perform a detailed measurement of the field dependence of the different phase populations.

## 5.2 Magnetisation measurements

Before discussing the X-ray scattering measurements it is desirable to examine the behaviour of the bulk magnetisation of the sample as a function of temperature and applied magnetic field. These measurements are useful in revealing information about the size of the moment belonging to a particular magnetic structure.

### 5.2.1 Experimental details

Magnetometry of the hexaferrite sample used in the X-ray scattering experiment was performed using a Quantum Design Magnetic Property Measurement System (MPMS) XL Superconducting Quantum Interference Device (a ‘SQUID’ magnetometer). In such an arrangement two Josephson junctions are connected in parallel to create a superconducting loop, the voltage across which can be used to measure the trapped flux quanta and thereby the magnetic flux originating from the sample.

Practically speaking, the sample is mounted inside a plastic straw which is then attached to the end of the MPMS insert. This in turn is connected to a translation stage which enables the sample to be moved through the detector coils. A small field must be applied in order to induce a non-zero net magnetisation in the sample. The sample is then moved through the detectors and the resulting plot of the SQUID’s output against the sample position is fitted by the software: the amplitude is taken to be the magnetisation of the sample. The advantage of this technique is that background contributions (for example from the plastic holding the sample) are largely eliminated.

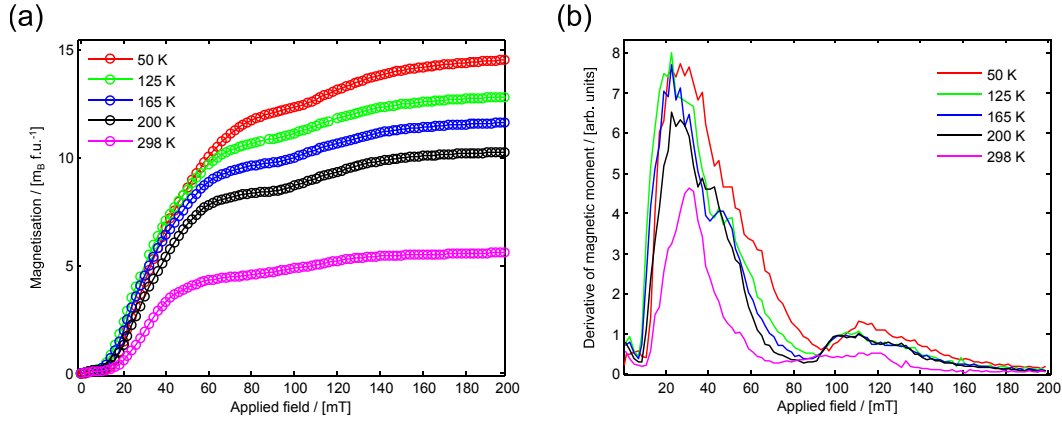


**Figure 5.3:** SQUID magnetisation measurements on the hexaferrite sample used for the X-ray scattering experiment. (a) The bulk magnetisation as a function of applied magnetic field for several temperatures. (b) The magnetic field derivatives of the data in (a).

## 5.2.2 Results

The dependence of the magnetisation on the applied magnetic field (which was oriented within the plane of the spin blocks, orthogonally to the  $c$  direction) was measured at five separate temperatures ranging from 50 K to room temperature. The data can be seen in figure 5.3, which also plots the magnetic field derivative of the data. As expected, the system quickly moves out of its zero field helical phase (which has a very low magnetisation) when the field is applied and, within the field range measured here<sup>2</sup>, appears to tend to a saturation value that is inversely related to the temperature.

As can be seen from the differentiated data, the system displays one main transition in its magnetisation (only very weakly dependent on the temperature) at  $\approx 30$  mT: this signals the onset of a non-helical structure which then saturates close to 90 mT. There are also some very broad peaks in the differentiated data which indicate a change in the magnetisation between 80 and 140 mT.

## 5.3 Resonant X-ray scattering

Resonant magnetic X-ray diffraction was carried out at beamline I10 at Diamond, and employed the RASOR diffractometer. Details of the setup are given in the following section.

<sup>2</sup>This field range was chosen as it matches those fields currently obtainable with the X-ray diffraction setup (section 5.3). At stronger fields it is expected that the data would show a number of further transitions, ultimately resulting in a ferrimagnetic arrangement being stabilised at which point the magnetisation would saturate.

### 5.3.1 Experimental details

#### 5.3.1.1 Determination of the propagation vectors

When evaluating the magnetic resonant cross section, one finds that the intensity is proportional to the square of the magnetic scattering amplitude [see equation (2.32)]:

$$F_{\text{RES}}^{\text{mag}}(\mathbf{Q}) = \sum_j f_{j,\text{RES}} e^{i\mathbf{Q}\cdot\mathbf{r}_j}, \quad (5.2)$$

where the summation runs over the magnetic ions of the crystal<sup>3</sup> indexed by  $j$ . Thus, since  $f_{j,\text{RES}}$  is proportional to the  $j$ th magnetic moment (for fixed polarisation and scattering angle, and for scattering into the first order magnetic satellites), the scattering amplitude is proportional to

$$\sum_j \sum_n (\mathbf{S}_n e^{-i\mathbf{q}_n\cdot\mathbf{r}_j} + \mathbf{S}_n^* e^{i\mathbf{q}_n\cdot\mathbf{r}_j}) e^{i\mathbf{Q}\cdot\mathbf{r}_n} \quad (5.3)$$

$$= \sum_j \sum_n [\mathbf{S}_n e^{i(\mathbf{Q}-\mathbf{q}_n)\cdot\mathbf{r}_j} + \mathbf{S}_n^* e^{i(\mathbf{Q}+\mathbf{q}_n)\cdot\mathbf{r}_j}] \quad (5.4)$$

which, when summed over the magnetic moments, is non-zero only at scattering vectors  $\mathbf{Q} = \mathbf{G} \pm \mathbf{q}_n$ , where  $\mathbf{G}$  is a reciprocal lattice vector<sup>4</sup>. Thus one can determine easily the magnetic propagation vector associated with a particular phase in the experiment, simply by looking for the position of the magnetic satellite peaks as the scattering vector is varied (by changing the diffractometer angles) and indexing these peaks appropriately.

#### 5.3.1.2 Sample environment

In order to both apply and accurately measure magnetic fields at the sample position, a custom designed sample holder was built. The hexaferrite single crystal is attached with silver paint to a copper holder, which is screwed onto the cryostat cold finger. This holder (see figure 5.4) allows up to two square neodymium permanent magnets to be housed underneath the sample, carefully positioned such that their magnetic field lies within the plane of the sample (the magnets are 1 cm wide so the field is very uniform over the 2 mm sample width<sup>5</sup>). The vertical distance between these magnets and the sample position can be varied by inserting copper spacers: this allows one to make coarse changes to the magnetic field strength at the sample.

The sample holder also contains an Arepoc HHP-NU Hall sensor, designed to operate at any temperature between 1.5 K and 350 K and in a magnetic field range up to 5 T,

<sup>3</sup>Or, in the present case, magnetic spin blocks.

<sup>4</sup>This can be shown by exploiting the periodicity of the lattice, *i.e.* by writing  $\mathbf{r}_j = \mathbf{R}_l + \mathbf{r}'_p$  where  $\mathbf{R}$  is a lattice vector and  $\mathbf{r}'$  is a position vector within the unit cell. See appendix A for a more rigorous treatment.

<sup>5</sup>This was checked when the sample holder was constructed using a commercial calibrated Gaussmeter.

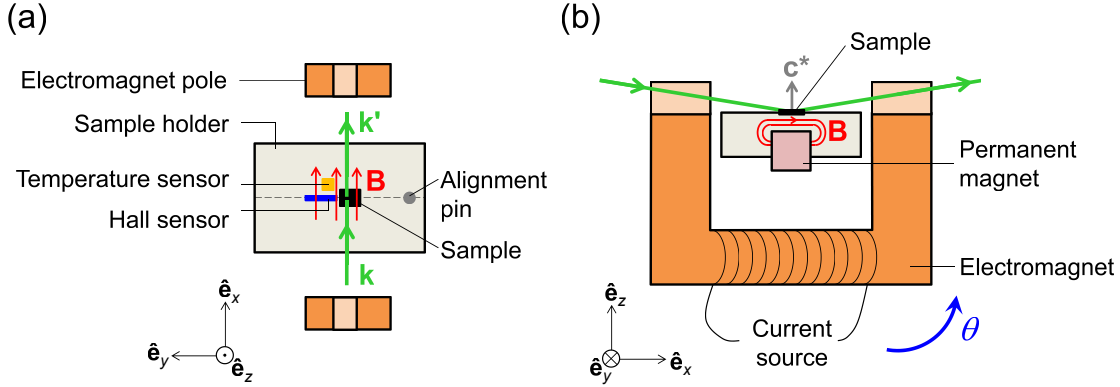


**Figure 5.4:** The RASOR sample mount seen in two different orientations (the  $\hat{e}_{x,y,z}$  directions, as defined in figure 2.1, are indicated). The electromagnet has two central sections removed to allow the X-ray beam to access the sample (shown in light orange). The entire assembly is rigidly attached to the  $\theta$  arm and rotates with it, the positive sense being depicted by the arrow in (b). Therefore the magnetic field at the sample position is the same regardless of the diffractometer orientation. A fine pin is attached to the end of the mount to assist in alignment and finding the centre of rotation of the chamber.

sunk into the copper slightly so that the active area is level with the sample and sits immediately next to it. The Hall sensor was supplied with a constant current of 10 mA using a Lakeshore model 120 current source, and the Hall voltage was read out by a Keithley model 182 voltmeter. The sensor was calibrated offline using a calibrated Hirst transverse probe Gaussmeter. The Hall sensor is an invaluable addition to the sample mount as it allows precise recording of the applied field throughout the experiment. In addition, a Cernox<sup>TM</sup> temperature sensor is also mounted close to the sample position. Cables for the Hall and temperature sensors are connected via the dedicated feedthroughs on RASOR's  $\theta$ -rotation.

Also attached to the  $\theta$ -rotation of the instrument is a custom built iron core electromagnet, supplied by a high current source, designed to apply a magnetic field directed to be both within the plane of the sample and within the scattering plane. The poles are large enough to ensure that the magnetic field is uniform over the width of the sample, but are shaped with a small indent to allow the incident and exit X-ray beams to pass through unobstructed. Preliminary measurements of this electromagnet demonstrate that, combined with the permanent magnets fixed to the sample mount, one can achieve continuously variable fields in the range 0 to 250 mT (see figure 5.5).

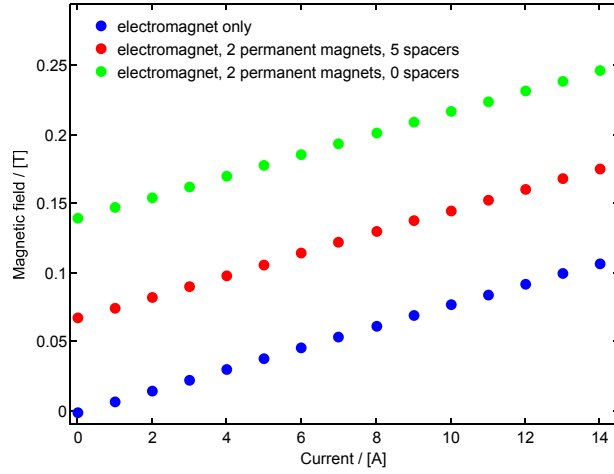


**Figure 5.5:** Magnetic field measured at the sample position as a function of electromagnet current, for various permanent magnet configurations.

### 5.3.1.3 Polarisation analysis

Here I give further details of how the polarisation analysis employed in the X-ray scattering experiment works. As explained above, the resonant magnetic scattering amplitude is given by

$$F_{\text{RES}}^{\text{mag}}(\mathbf{Q}) = \sum_j f_{j,\text{RES}} e^{i\mathbf{Q}\cdot\mathbf{r}_j} \quad (5.5)$$

where, from equation (2.33),

$$f_{j,\text{RES}} = -iF^{(1)} \begin{bmatrix} 0 & \boldsymbol{\mu}_j \cdot (\hat{\mathbf{e}}_x \cos \theta - \hat{\mathbf{e}}_z \sin \theta) \\ -\boldsymbol{\mu}_j \cdot (\hat{\mathbf{e}}_z \sin \theta + \hat{\mathbf{e}}_x \cos \theta) & \boldsymbol{\mu}_j \cdot \hat{\mathbf{e}}_y \sin 2\theta \end{bmatrix} \quad (5.6)$$

describes the polarisation dependence<sup>6</sup> in the  $\{\sigma, \pi\}$  basis. In this expression the  $j$ th magnetic moment is written  $\boldsymbol{\mu}_j$ ,  $\theta$  is half of the scattering angle, and the basis vectors  $\hat{\mathbf{e}}_x$ ,  $\hat{\mathbf{e}}_y$ , and  $\hat{\mathbf{e}}_z$  are shown in figure 5.4.  $F^{(1)}$  is a constant provided the incident wavelength is unchanged. Since charge scattering does not alter the X-ray polarisation (*i.e.* the only non-zero elements would be contained along the diagonal in the above matrix representation), it is desirable, if one is to measure the magnetic contribution to the scattering with the greatest sensitivity, to measure one of the off-diagonal components. For the present work, this is done by measuring in the  $\sigma \rightarrow \pi$  channel, and the orientation of the applied magnetic field ensures that the magnetic moments are aligned in a direction giving a relatively large cross section. This is because the moments will tend to align along the  $\hat{\mathbf{e}}_x$  direction, which

<sup>6</sup>Note that the other term in the resonant magnetic scattering amplitude, which gives rise to second order magnetic satellites, is not considered here because no such satellites were observed in the diffraction from the zero field incommensurate spiral structure (this is the only magnetic configuration that could result in these second order satellites [31]).

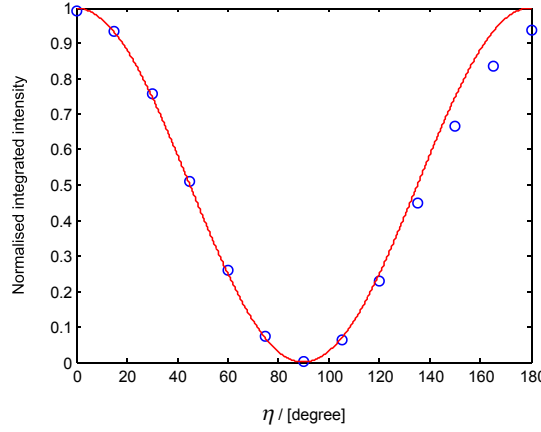


**Figure 5.6:** Integrated intensities from the direct beam obtained by rocking the PA crystal, as a function of  $\eta$  (rotation about the beam direction). The red line shows the ideal  $\cos^2 \eta$  dependence. Data from [144].

appears (along with a factor of  $\cos \theta$ ) in the off-diagonal part. By contrast, placing the magnetic field orthogonally to this will tend to reduce the  $\hat{\mathbf{e}}_x$  component of the moment as the field is increased, lowering the magnetic scattering cross section in  $\sigma \rightarrow \pi$ .

The incident X-rays are set to be  $\sigma$  polarised by the soft X-ray APPLE II undulator and are close<sup>7</sup> to 100% polarised [145]. After interacting with the magnetism in the sample, the polarisation of the scattered beam is analysed by Bragg scattering from a polarisation analyser (PA). For soft X-rays this is a specifically grown multilayer crystal whose inter-layer spacing has been chosen such that the Bragg condition is met with scattering angle  $\theta_{\text{PA}} = 45^\circ$  at the resonant scattering energy of 706.9 eV (although slight changes in incident wavelength may require very small deviations from this  $\theta_{\text{PA}}$  value in order to maintain the diffraction condition). The channeltron detector employed within RASOR is positioned at an angle  $2\theta_{\text{PA}} = 90^\circ$  to detect those X-rays that are diffracted from the PA. Whilst maintaining the scattering condition from the analyser crystal, both the PA crystal and the detector may be rotated about the direction of the scattered X-ray beam (*i.e.* the axis of rotation is along  $\mathbf{k}'$ ) by an angle  $\eta$ . Therefore, as shown in figure 5.6, one is able to differentiate between the two scattering channels  $\sigma \rightarrow \sigma, \pi$ . This figure shows data collected with the direct beam diffracting from the PA crystal as a function of  $\eta$  at 706.9 eV [144]. The leakthrough (*i.e.* the X-ray intensity scattered into the detector by the PA when  $\eta = 90^\circ$ ) is 0.1%. Although this energy is not the precise value of the resonance measured from

<sup>7</sup>In [145] the experimentally determined value of the Stokes parameter  $P_1$  for the I10 undulators, measuring the extent to which the polarisation is linear, was found to vary between 100.1% (horizontally polarised) and -99.3% (vertically polarised).

the hexaferrite magnetism (see figure 5.8), it is sufficiently close for the leakthrough not to change significantly from this value.

#### 5.3.1.4 Detectors

The RASOR diffractometer is equipped with two detectors: a photodiode connected to a current amplifier, and a channeltron (electron multiplier) detector. Whilst the photodiode is useful for alignment purposes and preliminary measurements as (unlike the channeltron) it is able to view the direct beam and strong Bragg peaks, the channeltron detector was found to have less noise and subsequently was used to collect all the data presented from figure 5.9 onwards.

### 5.3.2 Results

#### 5.3.2.1 $\theta$ - $2\theta$ scans

As shown in figure 5.4(b), the hexaferrite crystal was oriented prior to the experiment and polished such that the  $\mathbf{c}^*$  axis was pointing along the  $\hat{\mathbf{e}}_z$  direction. Thus, a scan that increases the sample rotation  $\theta$  at half the rate at which the detector rotation  $2\theta$  is increased will scan along the  $(0, 0, l)$  reciprocal space direction<sup>8</sup>. This is the fundamental type of scan from which the majority of the data presented in this chapter will be extracted. An example is shown in figure 5.7, which is a  $\theta$ - $2\theta$  scan taken with the photodiode detector in zero applied field and at room temperature, in the absence of polarisation analysis (*i.e.* the measurement is made in  $\sigma \rightarrow \sigma + \pi$ ) at the resonant energy. The  $x$ -axis has been converted into reciprocal lattice units via the relation

$$l = \frac{4\pi \sin\left(\frac{2\theta}{2}\right)}{c^* \lambda}. \quad (5.7)$$

In the above  $c^* = 2\pi/c$  is determined by fitting the  $(0, 0, 3)$  Bragg peak, and  $\lambda$  is the X-ray wavelength.

In the centre of the scan is the very intense  $(0, 0, 3)$  charge reflection [note that, due to the rhombohedral centring, only those Bragg peaks  $(h, k, l)$  satisfying  $-h + k + l = 3n$  for  $n \in \mathbb{Z}$  are allowed]. Surrounding this there are two magnetic reflections at  $l = 2.36$  and  $l = 3.64$  which are due to the helical spin block structure. Further out there are two very weak peaks positioned at  $l = 1.5$  and  $l = 4.5$ , appearing due to a small second harmonic (*i.e.* twice the energy) contribution to the undulator spectrum: this means that the strong charge reflections at  $(0, 0, 3)$  and  $(0, 0, 9)$  have second harmonics positioned at  $(0, 0, 1.5)$  and  $(0, 0, 4.5)$  respectively. Finally, at low  $l$  (corresponding to low scattering angles) there is a substantial increase in the background. This is due to the specular geometry employed in

<sup>8</sup>Offsets in  $\theta$  have to be determined during the sample alignment and corrected.

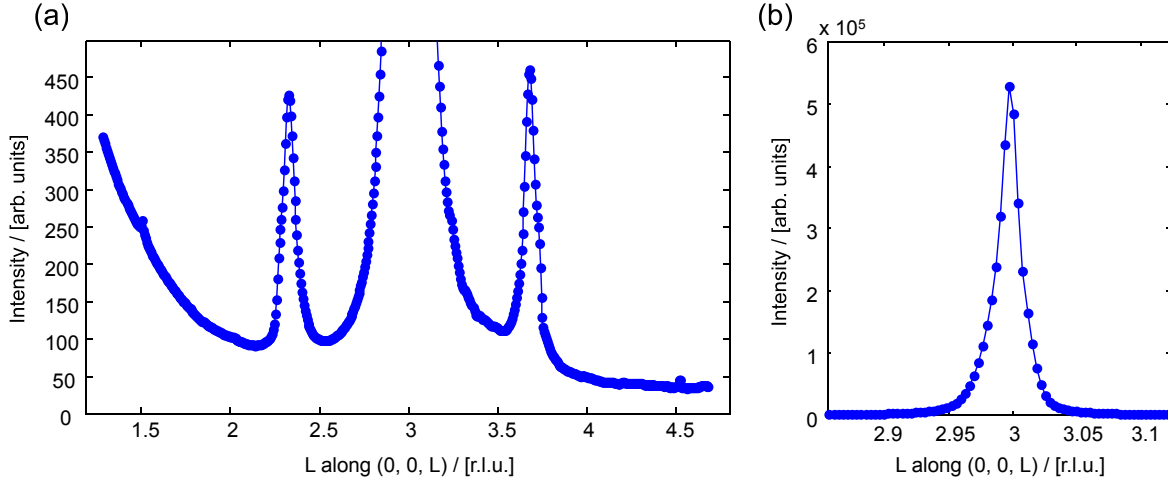


**Figure 5.7:** (a)  $l$ -scan of the hexaferrite sample at room temperature and in zero applied magnetic field. The full Bragg peak is shown in (b) [the intensity scale is the same as in (a)].

this experiment and is simply a surface effect that results in reflection of the soft X-ray beam. The presence of both the second harmonic charge peaks and the specular intensity can be reduced to below background with polarisation analysis by measuring in the  $\sigma \rightarrow \pi$  channel.

### 5.3.2.2 Energy dependence

It is important to examine the behaviour of the diffracted intensity as a function of incident X-ray energy in order to determine where the greatest resonant enhancement in the signal may be obtained. Figure 5.8 plots the energy dependence of the magnetic peak associated with the helical phase at room temperature and zero field: a clear enhancement is seen close to 708.6 eV (the energy at which the remainder of the experiment took place<sup>9</sup>) and an additional feature is visible at  $\approx 720$  eV. These are due, respectively, to the Fe  $L_3$   $2p_{3/2}$  and Fe  $L_2$   $2p_{1/2}$  atomic transitions, whose elemental binding energies are 706.8 eV and 719.9 eV respectively [146].

<sup>9</sup>The energy calibration was checked by fitting a room temperature  $\theta$ - $2\theta$  scan of the (0, 0, 3) peak (taken at the resonant energy) to determine the centre in  $2\theta$ . The room temperature lattice parameter (determined from laboratory X-ray diffraction) was then used to extract the X-ray wavelength, using equation (5.7). This gives an accurate value for the energy of the resonance, which is offset with respect to the nominal energy to which the monochromator is set. Data at non-resonant energies (these only appear in figure 5.8) have had this offset removed.



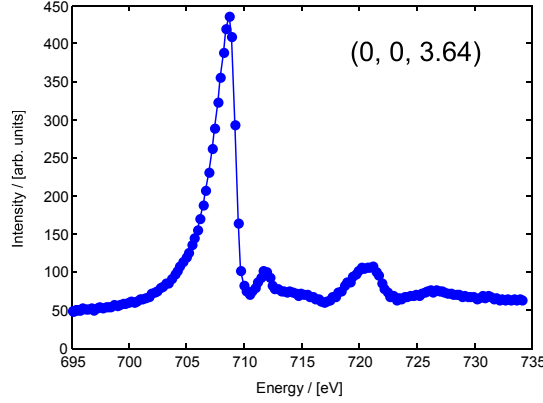


**Figure 5.8:** Constant  $\mathbf{Q}$  scan showing the intensity of the  $(0, 0, 3.64)$  magnetic satellite as a function of incident X-ray energy. The data were collected in zero applied field and at room temperature.

### 5.3.2.3 $l$ -scans as a function of magnetic field

Here I give an overview of the data and discuss the general trends present within it. Figures 5.9, 5.10, and 5.11 show a detailed magnetic field dependence of the positions and intensities of the magnetic satellites from the  $l$ -scans (on the left of the Bragg peak only) at 298 K, 165 K, and 50 K respectively. The data were all collected in the  $\sigma \rightarrow \pi$  channel.

The room temperature data (figure 5.9) show a strong contribution from the helix at  $\mathbf{q} = (0, 0, q_{\text{helix}}) \approx (0, 0, 0.65)$ , which diminishes with applied field and is almost entirely gone by 50 mT. As the helical phase disappears, a peak onsets with  $\mathbf{q} = (0, 0, 1.5)$  and is strongest at  $\approx 80$  mT. At higher fields this peak then also decreases, leaving no magnetic satellites above 130 mT [although there is a significant increase in the intensity of the  $(0, 0, 3)$  peak as the ferrimagnetic component develops – see figure 5.13]. A transition close to 130 mT is also visible in the MPMS data of figure 5.3. In addition there are very small intensities measured at peaks with propagation vectors  $\mathbf{q} = (0, 0, 1)$  and  $\mathbf{q} = (0, 0, 0.75)$  to be found in the room temperature data.

The data taken at 165 K (see figure 5.10) are different from the room temperature data in three main ways: (i) they show a marked increase in the intensity of the  $\mathbf{q} = (0, 0, 1)$  peak over several of the intermediate fields; (ii) the propagation vector of the helix has changed to be much closer to  $\mathbf{q} = (0, 0, 0.5)$ , making the very small  $\mathbf{q} = (0, 0, 0.75)$  peak more obvious; and (iii) within the range of fields studied here there are still satellites present with  $\mathbf{q} = (0, 0, 1.5)$ , in contrast to the room temperature data.

The 50 K data (figure 5.11) are fairly similar to the data taken at 165 K, although the peak corresponding to the helical phase appears stronger in low fields, relative to the other

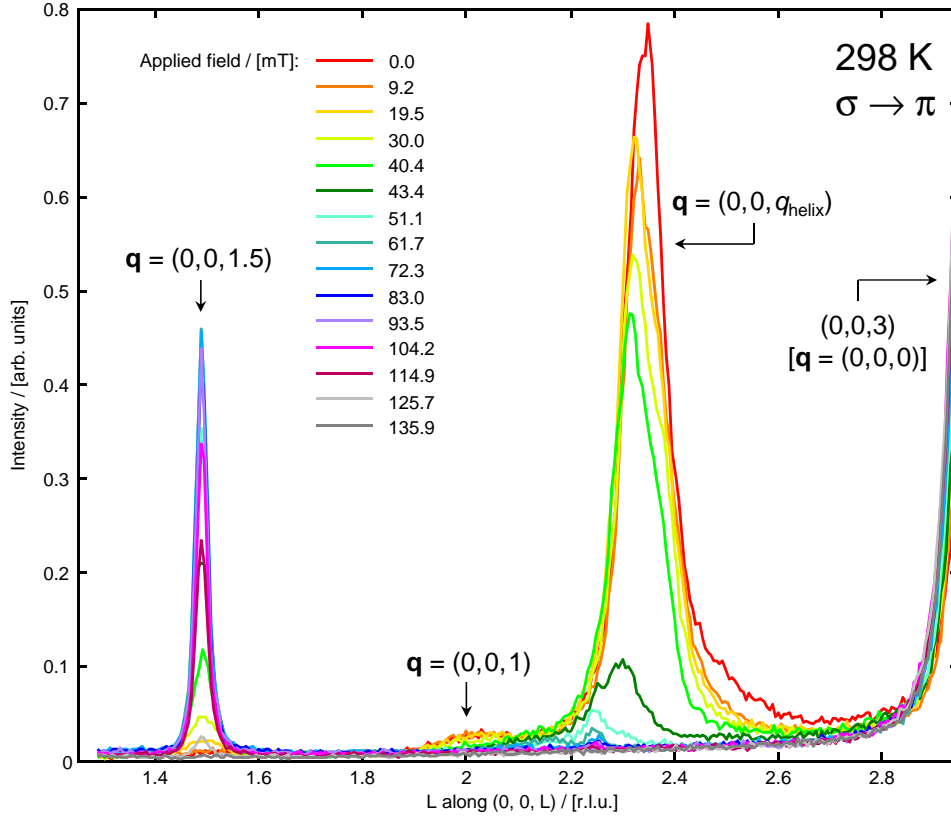


**Figure 5.9:**  $l$ -scans at various magnetic fields, taken in the  $\sigma \rightarrow \pi$  channel at 298 K. Peaks are labelled with the corresponding propagation vectors  $\mathbf{q}$ , and the position of the  $(0, 0, 3)$  Bragg peak is indicated.

magnetic satellites, than in the 165 K data set.

#### 5.3.2.4 Further data processing

From the  $l$ -scans discussed above, the background regions on both sides of each individual peak were fitted with a linear intensity profile<sup>10</sup> which was then subtracted. The resulting peak shape was fitted (using either a Gaussian or Lorentzian function in order to obtain the closest fit) to find the exact position of the peak. Finally the integrated intensities were determined from the background subtracted peaks.

Following this, it is possible to gain a complete picture of how the magnetic structures present in the sample depend on both applied field and temperature by constructing a phase diagram, including in particular information concerning the hitherto unreported phase with propagation vector  $\mathbf{q} = (0, 0, 1)$ .

<sup>10</sup>Higher order terms in the polynomial used to generate the background function were not found to be necessary over the typical width of a peak.

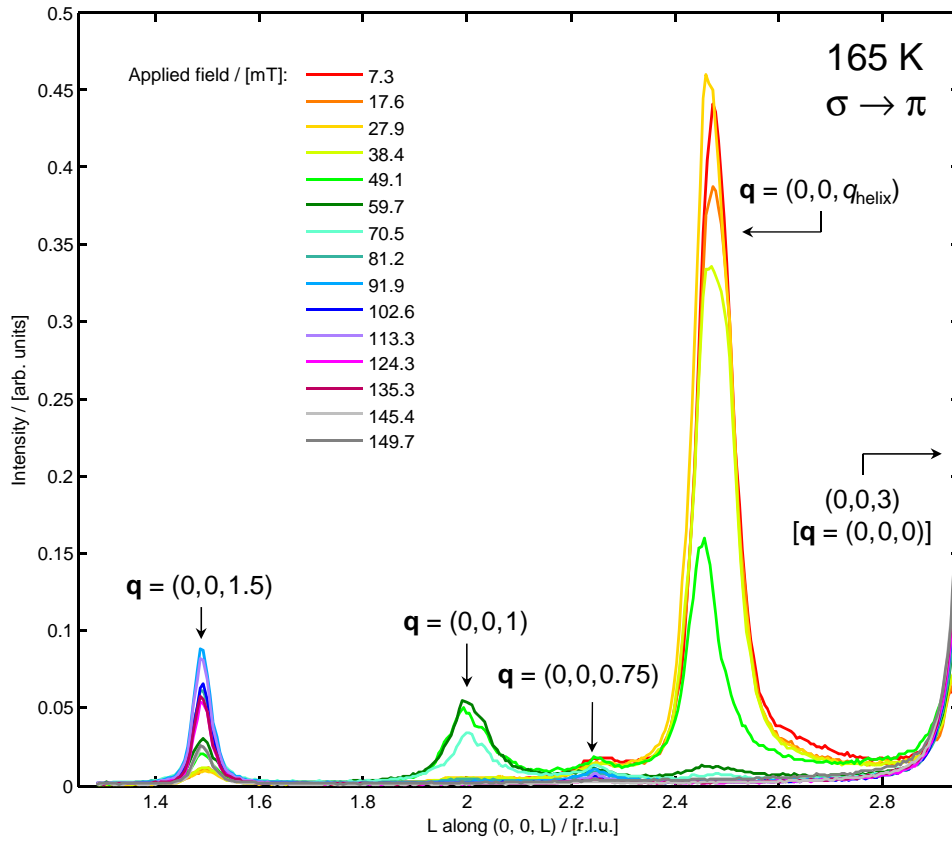


**Figure 5.10:** As figure 5.9, with data taken at 165 K.

## 5.4 Low field phase diagram

Having integrated the peak intensities it is possible to compare the relative sizes of each peak as a function of applied field and temperature. This comparison is made in figure 5.12, which shows the sizes of the helical [*i.e.*  $(0, 0, q_{\text{helix}})$ ],  $(0, 0, 1)$ , and  $(0, 0, 1.5)$  propagation vector peaks as a scatter plot (the size of each data point is scaled relative to the particular measurement of the peak in question that had the highest integrated intensity). Once this is done it becomes clear that the phase diagram can be split approximately into four regions according to the different propagation vectors [the region labelled  $(0, 0, 0)$  corresponds to those fields and temperatures where no satellites are seen and magnetic intensity is observed purely at the ferrimagnetic position  $\mathbf{q} = (0, 0, 0)$ ]. It should be emphasised that this is very much a qualitative treatment, the idea being to determine the approximate behaviour of the system and identify those areas of phase coexistence. Therefore the ‘phase boundaries’ indicated in figure 5.12 with the dashed lines are really only suggested (approximate) positions.

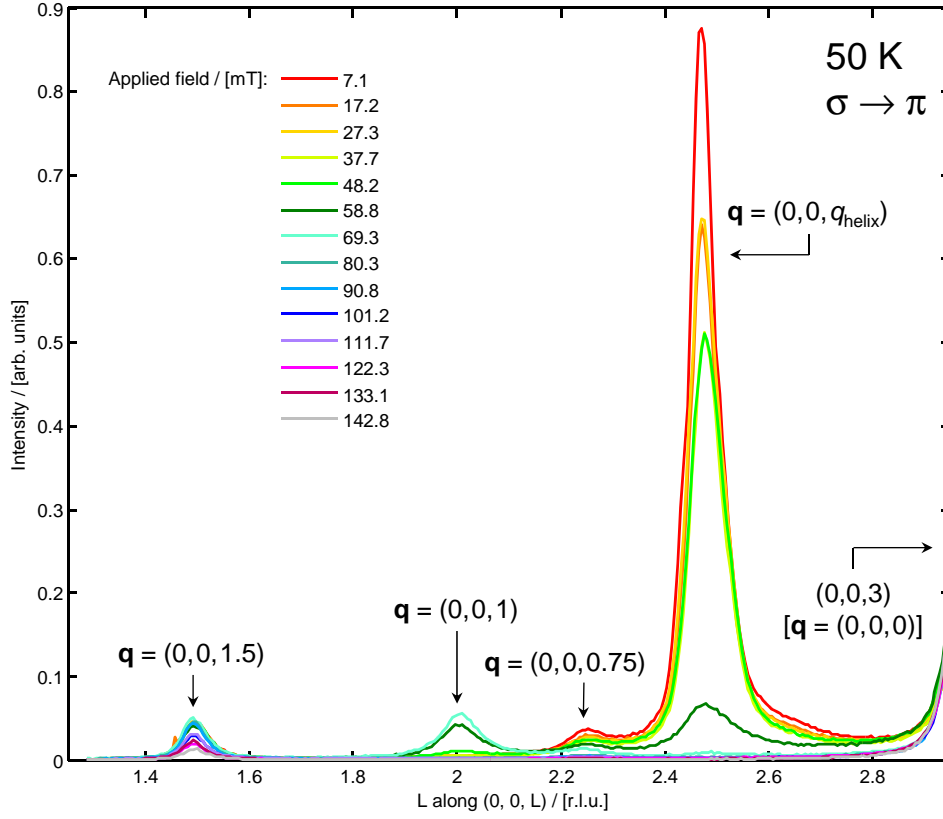


**Figure 5.11:** As figure 5.9, with data taken at 50 K.

The weak  $\mathbf{q} = (0, 0, 0.75)$  peaks observed in the data are not considered further in this treatment because, as can be seen from the 4-fan structure in figure 5.2, the  $\mathbf{q} = (0, 0, 0.75)$  component only describes a modulation in the magnetic structure that is orthogonal to the applied field direction. However, by measuring the intensity scattered into the  $\sigma \rightarrow \pi$  channel one is sensitive only to the components of the magnetic structure along  $\hat{\mathbf{e}}_x$  and  $\hat{\mathbf{e}}_z$  [equation (5.6)], *i.e.* in effect the X-rays measure only a projection of the magnetic structure onto the scattering plane. Since the geometry used for this experiment has the scattering plane aligned with the field direction, in principle any magnetic satellites corresponding to out-of-scattering-plane modulations [of which the  $\mathbf{q} = (0, 0, 0.75)$  is one] should not be observed. The fact that a very small peak is seen here is most likely due to the scattering plane not being perfectly aligned to the applied field direction. Thus, the 4-fan structure should only appear to give satellites in the diffraction at  $\mathbf{q} = (0, 0, 1.5)$  and  $\mathbf{q} = (0, 0, 0)$ . The same reasoning can be used to infer that, for the 2-fan structure, one should not observe a peak at  $\mathbf{q} = (0, 0, 1.5)$ , the sole contribution to the magnetic scattering in this phase appearing at  $\mathbf{q} = (0, 0, 0)$ . This is summarised in table 5.1.

Phase	Magnetic satellites observed in $\sigma \rightarrow \pi$	Propagation vectors, $\mathbf{q}$
Helical	$(0, 0, 3 \pm q_{\text{helix}})$	$(0, 0, q_{\text{helix}})$
6-fan	$(0, 0, 2)$ and $(0, 0, 4)$	$(0, 0, 1)$
	$(0, 0, 3)$	$(0, 0, 0)$
4-fan	$(0, 0, 1.5)$ and $(0, 0, 4.5)$	$(0, 0, 1.5)$
	$(0, 0, 3)$	$(0, 0, 0)$
2-fan	$(0, 0, 3)$	$(0, 0, 0)$

**Table 5.1:** Reciprocal space positions of the magnetic satellites  $(0, 0, l)$  observed in diffraction from the various hexaferrite magnetic structures in  $\sigma \rightarrow \pi$  (the ‘6-fan’ phase will be discussed in section 5.5). The associated propagation vectors are given.

Based upon these considerations, the main findings from figure 5.12 are:

1. As the field is increased at room temperature, the system moves from a helical phase via the 4-fan phase with  $\mathbf{q} = (0, 0, 1.5)$  to the 2-fan phase with  $\mathbf{q} = (0, 0, 0)$ . There is significant phase coexistence between the helical and 4-fan phase, as evidenced by the small  $(0, 0, 1.5)$  peaks that are present at low fields, and the growing  $\mathbf{q} = (0, 0, 0)$  contribution with field can be seen at the  $(0, 0, 3)$  peak position (figure 5.13). This contribution does not appear to saturate in the range measured here, indicating that the angle  $\phi_2$  of the 2-fan structure is continuing to reduce at the highest measured fields and that the system has not reached a pure ferrimagnetic phase.
2. At intermediate temperatures (165 K) the system behaves similarly, with the addition of a new peak at  $\mathbf{q} = (0, 0, 1)$  that appears close to the region between the helical and 4-fan phases. The phase responsible for this peak has not been previously reported.
3. At lower temperatures, evidence of the new phase with  $\mathbf{q} = (0, 0, 1)$  is still present, but the fact that the intensity of the  $(0, 0, 3)$  peak levels out above  $\approx 70$  mT (see figure 5.13), and at a much lower value than is observed in the higher temperature data, suggests that the 2-fan phase has not been stabilised and one is instead observing the ferrimagnetic component belonging to the 4-fan structure, whose angle  $\phi_4$  does not appear to be changing with field.
4. Generally the measurements show a good deal of phase overlap (due to different parts of the crystal stabilising into different phases), suggesting that all of the observed phases are very close in energy.

In the next section I consider a candidate structure that may explain the appearance of the  $\mathbf{q} = (0, 0, 1)$  peaks, and I undertake energy calculations to determine which phases should be the most stable as a function of applied magnetic field.

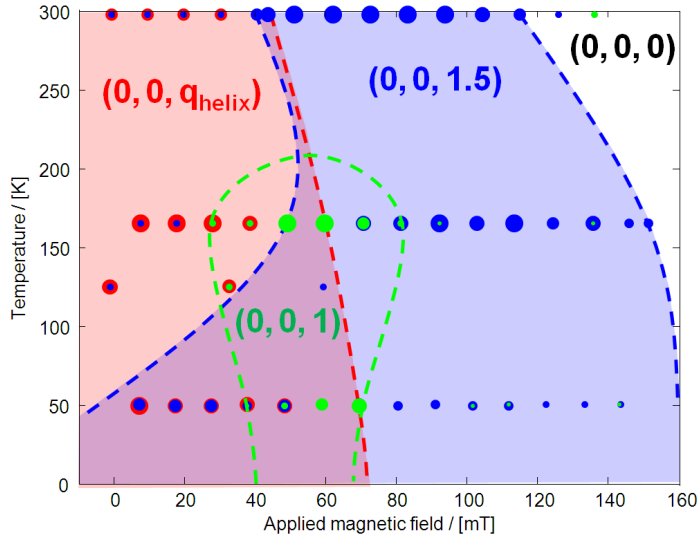


**Figure 5.12:** Low field phase diagram based on the diffraction data of figures 5.9 to 5.11. The points are coloured according to the propagation vector of the diffraction peak they represent, and sized according to their relative intensities.

## 5.5 Energy calculations for the various phases

The energy of a particular magnetic structure may be calculated via

$$E_j = \sum_i J_{ij} \mathbf{S}_j \cdot \mathbf{S}_i - g\mu_B \mathbf{B} \cdot \mathbf{S}_j, \quad (5.8)$$

which gives the energy<sup>11</sup> of the  $j$ th spin block, and the summation is understood to run over all of the other spin blocks surrounding  $\mathbf{S}_j$ . For the present work, however, the only non-zero exchange constants  $J_{ij}$  are taken to be between nearest neighbour and second-nearest neighbour spin blocks (*i.e.*  $\mathbf{S}_i$  is next to  $\mathbf{S}_j$  or else is separated from it by one spin block if it is to contribute to the summation). Once  $E_j$  is calculated for each spin block species (*i.e.* for  $j = \text{L}$  and  $j = \text{S}$ ), the average energy per  $(\text{L} + \text{S})$  block can be determined, and its behaviour as a function of field calculated.

### 5.5.1 Helical phase (zero field)

Following [135], one may describe the zero applied magnetic field structure as a simple helix formed by the S and L blocks, with a turn angle of  $180^\circ + \phi_0/2$  between adjacent blocks (*i.e.* an angle  $\phi_0$  between next-nearest neighbour blocks which are of the same type – see figure 5.14 which also shows the exchange interactions). As there are three S and three L

<sup>11</sup>Note that this convention uses  $J > 0$  to mean an antiferromagnetic coupling,  $J < 0$  to be ferromagnetic, and that the magnetic moment  $\boldsymbol{\mu}_j = g\mu_B \mathbf{S}_j$ .

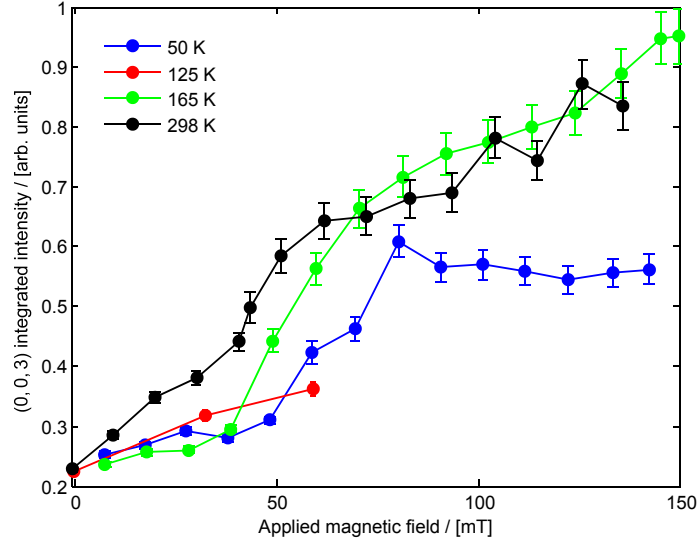


**Figure 5.13:** Intensities of the  $(0,0,3)$  peaks, measured in  $\sigma \rightarrow \pi$  as a function of applied magnetic field and at different temperatures.

blocks per unit cell, the angle  $\phi_0$  is related to the propagation vector of the structure via

$$\mathbf{q}_{\text{helix}} = \left( 0, 0, \frac{3\phi_0}{360^\circ} \right). \quad (5.9)$$

The energy of a single S block is given by

$$E_S = 2J_{LS}S_S S_L \cos(180^\circ + \phi_0/2) + 2J_{SS}S_S^2 \cos \phi_0, \quad (5.10)$$

and for a single L block by

$$E_L = 2J_{LS}S_S S_L \cos(180^\circ + \phi_0/2) + 2J_{LL}S_L^2 \cos \phi_0. \quad (5.11)$$

Thus, the total energy per  $(L + S)$  spin block (of which there are  $N$ ) is

$$\frac{E}{N} = -2J_{LS}S_S S_L \cos(\phi_0/2) + (J_{SS}S_S^2 + J_{LL}S_L^2) \cos \phi_0. \quad (5.12)$$

Minimising this with respect to  $\phi_0$  gives

$$\cos\left(\frac{\phi_0}{2}\right) = \frac{J_{LS}S_S S_L}{2(J_{SS}S_S^2 + J_{LL}S_L^2)}. \quad (5.13)$$

### 5.5.2 ‘4-fan’ phase

The 4-fan phase has an angle of  $\phi_4$  (see figure 5.2) between L blocks, and also between S blocks. Therefore, proceeding in a similar way to above, the energies per spin block are given by

$$E_S = J_{SS}S_S^2 \cos \phi_4 + J_{SS}S_S^2 - 2J_{LS}S_L S_S \cos\left(\frac{\phi_4}{2}\right) + g\mu_B S_S B \cos\left(\frac{\phi_4}{2}\right) \quad (5.14)$$

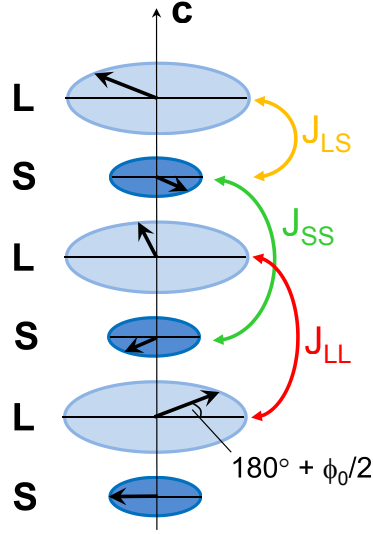


**Figure 5.14:** Spin block arrangement in the helical phase, with the exchange interactions labelled.

and

$$E_L = 2J_{LL}S_L^2 \cos \phi_4 - 2J_{LS}S_L S_S \cos \left( \frac{\phi_4}{2} \right) - \frac{1}{2}g\mu_B S_S B (1 + \cos \phi_4). \quad (5.15)$$

The energy per (L + S) block is therefore

$$\begin{aligned} \frac{E}{N} = & J_{LL}S_L^2 \cos \phi_4 + \frac{J_{SS}}{2}S_S^2 \cos \phi_4 + \frac{J_{SS}}{2}S_S^2 - 2J_{LS}S_L S_S \cos \left( \frac{\phi_4}{2} \right) \\ & - \frac{1}{2}g\mu_B B S_L (1 + \cos \phi_4) + g\mu_B B S_S \cos \left( \frac{\phi_4}{2} \right). \end{aligned} \quad (5.16)$$

Minimising with respect to the angle  $\phi_4$  results in

$$\cos \left( \frac{\phi_4}{2} \right) = \frac{J_{LS}S_L S_S - \frac{1}{2}g\mu_B B S_S}{2J_{LL}S_L^2 + J_{SS}S_S^2 - g\mu_B B S_L}. \quad (5.17)$$

### 5.5.3 '2-fan' phase

In the 2-fan phase the angle between L blocks is denoted  $\phi_2$ . The energies of the individual spin blocks may be written

$$E_S = J_{LS}S_S S_L \cos(180^\circ - \phi_2/2) + J_{LS}S_S S_L \cos(180^\circ + \phi_2/2) + 2J_{SS}S_S^2 + g\mu_B S_S B \quad (5.18)$$

and

$$\begin{aligned} E_L = & J_{LS}S_S S_L \cos(180^\circ - \phi_2/2) + J_{LS}S_S S_L \cos(180^\circ + \phi_2/2) \\ & + 2J_{LL}S_L^2 \cos \phi_2 - g\mu_B S_L \cos(\phi_2/2) B. \end{aligned} \quad (5.19)$$



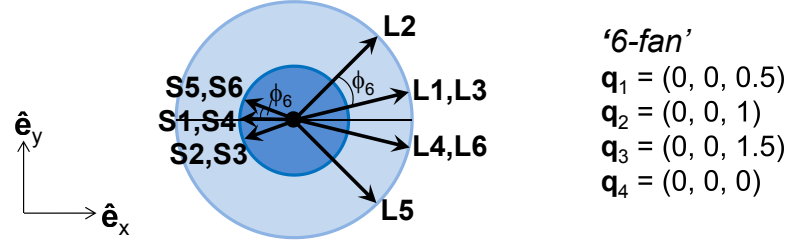


**Figure 5.15:** Plan view of the magnetic structure of the proposed '6-fan' phase (compare to figure 5.2). The four propagation vectors belonging to this structure are given.

Therefore

$$\frac{E}{N} = -2J_{LS}S_S S_L \cos(\phi_2/2) + J_{LL}S_L^2 \cos \phi_2 + J_{SS}S_S^2 - g\mu_B B S_L \cos(\phi_2/2) + g\mu_B B S_S, \quad (5.20)$$

which is minimised when

$$\cos\left(\frac{\phi_2}{2}\right) = \frac{J_{LS}S_S S_L + \frac{1}{2}g\mu_B S_L B}{2S_L^2 J_{LL}}. \quad (5.21)$$

#### 5.5.4 Ferrimagnetic phase

The ferrimagnetic structure (considered here and in the following for completeness, although it is not observed in the data because stronger fields are required for it to stabilise) is equivalent to the '2-fan' structure with the angle  $\phi_2$  set to zero. Thus, from equation (5.20), the energy is

$$\frac{E}{N} = -2J_{LS}S_S S_L + J_{LL}S_L^2 + J_{SS}S_S^2 - g\mu_B B S_L + g\mu_B B S_S. \quad (5.22)$$

#### 5.5.5 Possible explanation for the $\mathbf{q} = (0, 0, 1)$ peaks: a '6-fan' phase

Finally, a slightly more complex 6-fan phase is proposed (see figure 5.15) which would include a propagation vector of  $(0, 0, 1)$  together with  $(0, 0, 0.5)$ ,  $(0, 0, 1.5)$ , and  $(0, 0, 0)$  contributions. The angle between the L blocks (and also between the S blocks) is  $\phi_6$ , and the energies here are:

$$E_L = 2J_{LL}S_L^2 \cos \phi_6 - 2J_{LS}S_S S_L \cos\left(\frac{\phi_6}{2}\right) - \frac{g\mu_B B S_L}{3} \left[ \cos\left(\frac{3\phi_6}{2}\right) + 2 \cos\left(\frac{\phi_6}{2}\right) \right] \quad (5.23)$$

and

$$E_S = \frac{4}{3}J_{SS}S_S^2 \cos \phi_6 + \frac{2}{3}J_{SS}S_S^2 - 2J_{LS}S_L S_S \cos\left(\frac{\phi_6}{2}\right) + \frac{g\mu_B B S_S}{3} [1 + 2 \cos \phi_6]. \quad (5.24)$$

Therefore

$$\begin{aligned} \frac{E}{N} = & J_{\text{LL}}S_{\text{L}}^2 \cos \phi_6 + \frac{2}{3}J_{\text{SS}}S_{\text{S}}^2 \cos \phi_6 + \frac{1}{3}J_{\text{SS}}S_{\text{S}}^2 - 2J_{\text{LS}}S_{\text{L}}S_{\text{S}} \cos \left( \frac{\phi_6}{2} \right) \\ & - \frac{g\mu_{\text{B}}BS_{\text{L}}}{3} \left[ \cos \left( \frac{3\phi_6}{2} \right) + 2 \cos \left( \frac{\phi_6}{2} \right) \right] + \frac{g\mu_{\text{B}}BS_{\text{S}}}{3} [1 + 2 \cos \phi_6]. \end{aligned} \quad (5.25)$$

The minimum energy value of  $\phi_6$  must subsequently satisfy

$$A' \cos^2 \left( \frac{\phi_6}{2} \right) + B' \cos \left( \frac{\phi_6}{2} \right) + C' = 0, \quad (5.26)$$

where

$$A' := 2g\mu_{\text{B}}BS_{\text{L}}, \quad (5.27)$$

$$B' := -2J_{\text{LL}}S_{\text{L}}^2 - \frac{4}{3}J_{\text{SS}}S_{\text{S}}^2 - \frac{4}{3}g\mu_{\text{B}}BS_{\text{S}}, \quad (5.28)$$

$$C' := -J_{\text{LS}}S_{\text{L}}S_{\text{S}} - \frac{1}{6}g\mu_{\text{B}}BS_{\text{L}}. \quad (5.29)$$

The full Fourier decomposition of this 6-fan structure is given in the appendix, section A.1. As explained above, the present experiment is sensitive only to modulations in the component of the moments along  $\hat{\mathbf{e}}_x$ , so the 6-fan structure will result in satellites located at  $\mathbf{q} = (0, 0, 1)$  and  $\mathbf{q} = (0, 0, 0)$  as observed in the data. Furthermore, it is of interest to note that a careful examination of the peak shape (as shown in figure 5.16) at  $l \approx 3.5$  reveals a certain amount of asymmetry, motivating fitting the peak with multiple Gaussian line shapes. The figure shows that the best fit is obtained when two overlapping peaks, one centred at  $l = 3.54$  (due to the incommensurate helical structure) and the other commensurate at  $l = 3.5$ , both contribute to the intensity profile. This is therefore highly suggestive of a very weak  $\mathbf{q} = (0, 0, 0.5)$  contribution which is originating from the 6-fan phase and which is seen here, as for the  $\mathbf{q} = (0, 0, 0.75)$  peaks, due to slight misalignment between the direction of the applied field and the scattering plane.

## 5.6 Model for the room temperature phase diagram

Before calculating the exchange constants and energies of the various phases it is necessary to establish the size of the L and S block moments at room temperature. The sizes of these moments are given by

$$\mu_{\text{L}} = (3 + 2\gamma)\mu_{\text{Fe}}, \quad (5.30)$$

$$\mu_{\text{S}} = (2\gamma - 1)\mu_{\text{Fe}}, \quad (5.31)$$

where  $\gamma = 0.661$  for the stoichiometry in question, and  $\mu_{\text{Fe}}$  is the average moment on the iron site [134, 136, 147]. The SQUID data (section 5.2) show, for  $T = 298$  K, a magnetisation

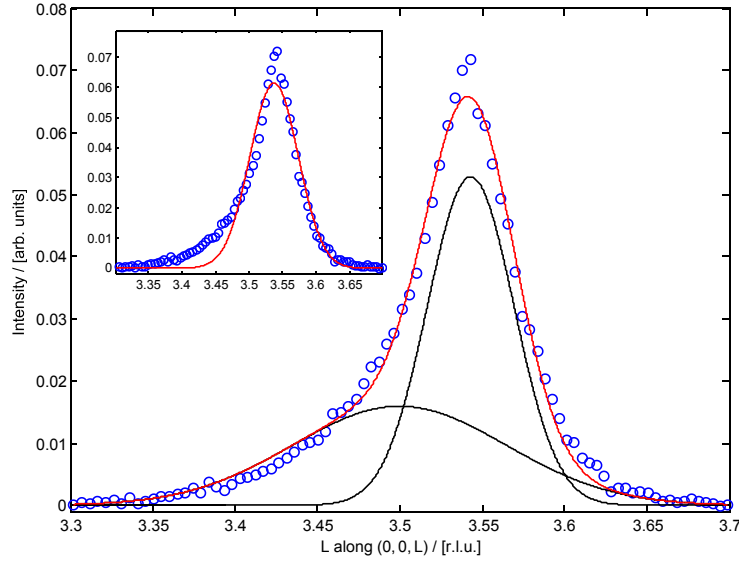


**Figure 5.16:** Fits to the peak close to  $(0, 0, 3.5)$  (data taken at 165 K and 49 mT). A good fit (red line) to the data (blue points) is obtained with two Gaussians (black lines), one centred at  $l = 3.5$  and other at an incommensurate value. The inset demonstrates the best obtainable fit with a single Gaussian peak shape.

of  $5.60 \mu_B \text{ f.u.}^{-1}$  at 200 mT, where the system is in the 2-fan phase. Since one formula unit is equivalent to a single  $(L + S)$  block, this means that

$$\mu_L \cos\left(\frac{\phi_2}{2}\right) - \mu_S = 5.60 \mu_B. \quad (5.32)$$

Writing  $|\mu_j| = g\mu_B S_j$  where  $j = L, S$  and  $g = 2$  for the pure spin moment of the  $\text{Fe}^{3+}$  ion, this can be related to the exchange constants via equation (5.21) to give

$$\frac{J_{LS}S_S S_L + \frac{1}{2}g\mu_B S_L B}{2S_L J_{LL}} = \frac{5.6}{g} + S_S, \quad (5.33)$$

where  $B = 200$  mT and [from equations (5.30) and (5.31)]

$$\frac{\mu_L}{\mu_S} = \frac{S_L}{S_S} = 13.422. \quad (5.34)$$

In addition to this, from the propagation vector  $\mathbf{q}_{\text{helix}} = (0, 0, 0.656)$  measured in the X-ray diffraction data at 298 K in zero field, the turn angle of the helix is given by

$$\phi_0 = \frac{360^\circ \times 0.656}{3} = 78.72^\circ, \quad (5.35)$$

which can be used in equation (5.13) to give another condition on the sizes of the exchange constants and absolute sizes of the moments.

Two more constraints can also be imposed: namely that the helical and 4-fan phases are of the same energy at 40 mT (the approximate position of the phase boundary) and that

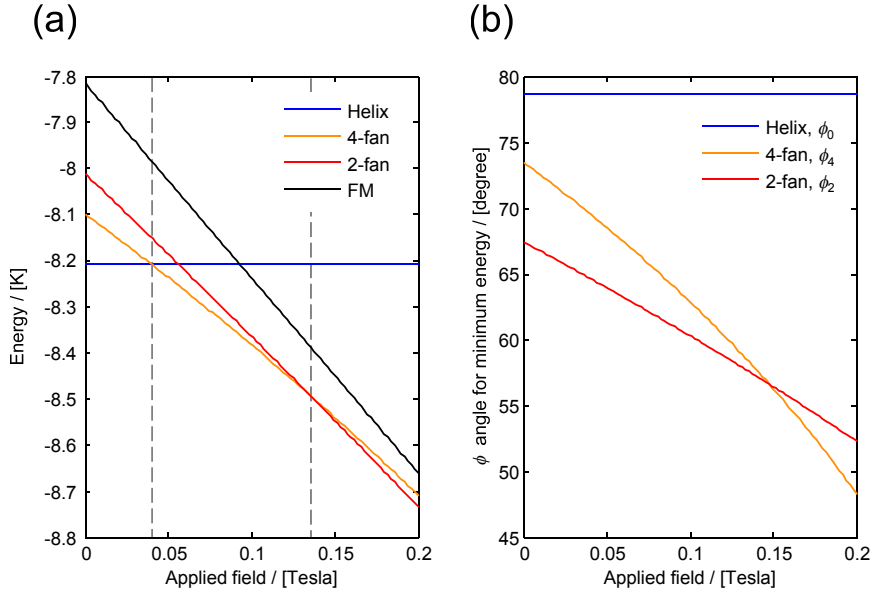


**Figure 5.17:** (a) Energies (in temperature units) of the helical, 4-fan, 2-fan, and ferrimagnetic structures as a function of field at room temperature (dashed lines indicate phase boundaries). (b) The angles  $\phi_0$  (helical phase),  $\phi_4$  (4-fan phase) and  $\phi_2$  (2-fan phase) as a function of field, showing that the amplitude of the fan-like oscillations becomes smaller (*i.e.* the spins are bunched more closely around the field direction) as the field is increased, as expected.

the 4-fan and 2-fan phases are of the same energy at 130 mT. These two conditions, along with equations (5.13) and (5.33), can be used to determine uniquely the four unknowns  $J_{\text{LS}}$ ,  $J_{\text{LL}}$ ,  $J_{\text{SS}}$  and  $S_{\text{S}}$ . The exchange constants are found to be (in temperature units)

$$J_{\text{LS}} = 6.7 \text{ K}, \quad J_{\text{SS}} = 4.1 \text{ K}, \quad J_{\text{LL}} = 0.3 \text{ K}, \quad (5.36)$$

and the block moments are

$$S_{\text{L}} = 3.4014, \quad S_{\text{S}} = 0.2534. \quad (5.37)$$

The positive signs of the exchange constants show that every interaction is antiferromagnetic in nature. Figure 5.17 plots the energy of the phases (helix, 4-fan, 2-fan, and ferrimagnetic), as well as the angles  $\phi_0$ ,  $\phi_4$ , and  $\phi_2$ , as a function of field. This clearly shows that the helical phase is stabilised below 40 mT. Above this field the 4-fan structure has the lowest energy, but as the field tends towards 130 mT the energy of the 2-fan structure tends to the same value. The ferrimagnetic structure, by comparison, remains significantly higher in energy than the other phases, confirming that the ferrimagnetic phase is not stabilised until fields substantially higher than those used in the present experiment are applied.

## 5.7 Model for the phase diagram at low temperatures

I shall now explain the phases that appear at low temperatures, working from the experimental data collected at 165 K. These data show significant contributions from all of the propagation vectors (and therefore all of the phases) shown in figures 5.2 and 5.15. In particular I hope to confirm that the candidate ‘6-fan’ structure, that would explain the appearance of the  $\mathbf{q} = (0, 0, 1)$  peaks in the diffraction, is plausible based on energy considerations.

Firstly, the 165 K data show that the helical phase turn angle has now reduced to  $\phi_0 = 63.6^\circ$ , from which (as before) a constraint on the exchange constants can be inferred from equation (5.13). Since the 6-fan phase exists alongside the other phases, in a simple model another condition can be obtained by requiring that the minimum energy of the 6-fan phase occurs in the middle of the region it occupies in the phase diagram: this is at  $\approx 50$  mT. The third condition used here is that the exchange constants  $J_{\text{LS}}$  and  $J_{\text{LL}}$  scale in the same way with temperature (this is reported in [135]) whereas  $J_{\text{SS}}$  scales differently. Applying these three conditions gives the following three exchange constants:

$$J_{\text{LS}} = 32.7 \text{ K}, \quad J_{\text{SS}} = 6.6 \text{ K}, \quad J_{\text{LL}} = 1.5 \text{ K}. \quad (5.38)$$

Thus, relative to the room temperature values,  $J_{\text{LS}}$  (and therefore  $J_{\text{LL}}$ ) have increased by factors of  $\approx 5$ , whereas  $J_{\text{SS}}$  has increased by a factor of only 1.6. This is consistent with the findings of [135], in which  $J_{\text{LL}}$  and  $J_{\text{LS}}$  are reported to decrease with temperature down to  $\approx 77$  K, but  $J_{\text{SS}}$  remains constant below  $\approx 280$  K.

Figure 5.18 shows the energies and angles of all the different phases as a function of applied field. It is clear from this that the 6-fan structure is the minimum energy configuration between  $\approx 30$  mT and 50 mT, after which the competing 4-fan structure becomes slightly lower in energy. However, in the lowest field regions there is very little difference between the energies of these phases, so it is reasonable that the diffraction data show a peak corresponding to the 6-fan structure up until  $\approx 75$  mT. This analysis also shows that towards the upper end of the phase diagram, with fields of approximately 200 mT, the 2-fan phase becomes most stable.

The fact that this model allows for a 6-fan phase to be stabilised confirms that a structure of this type is a good candidate for the hexaferrite at low fields, in order to give rise to the observed peaks at  $\mathbf{q} = (0, 0, 1)$  in the diffraction. In addition, the calculations confirm that, as in all magnetically frustrated systems, there exist a large number of states which are all very close in energy to that of the ground state. This explains why the phase diagram shows large regions of phase coexistence (for example, at 50 mT and 165 K signatures of the

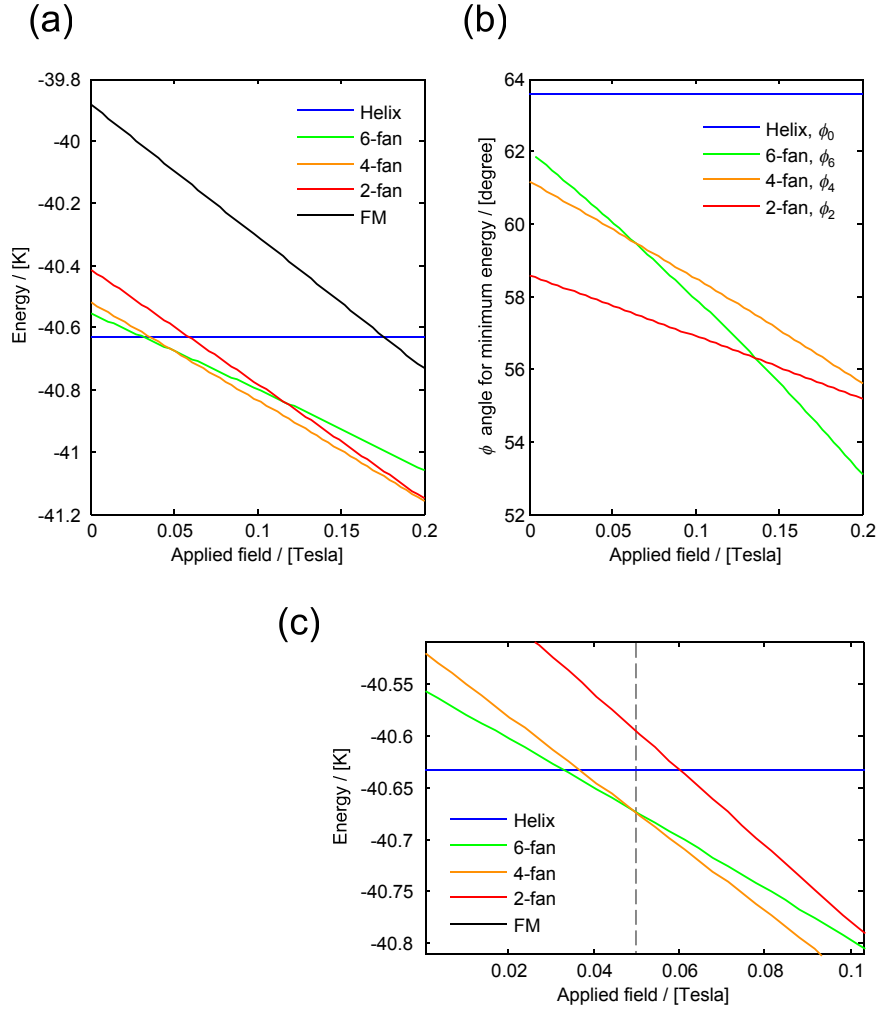


**Figure 5.18:** (a) Energies (in temperature units) of the various structures as a function of field at 165 K. (b) The angles associated with each structure as a function of field. (c) The low field detail from (a), with the point at which the 6-fan phase reaches its minimum energy indicated by the dashed line (this value having been extracted from the data in order to determine the exchange constants).

helical, 6-fan, and 4-fan phases are all present in the diffraction data) and why a striking variety of different orderings appears in this system.

## 5.8 Intensity calculations

Now that the lowest energy magnetic configurations are known as a function of field, it is possible to calculate the scattered intensities and compare these to the values measured in the experiment (I shall do this for the 165 K data as they show the full range of phases). The intensities originating from each phase are calculated separately (details of the derivation

are presented in appendix A). Firstly, the 6-fan structure gives contributions at  $(0, 0, 3)$  and  $(0, 0, 3 \pm 1)$  positions in reciprocal space, with corresponding intensities  $I_{(0,0,3)}^{6\text{-fan}}$  [equation (A.34)] and  $I_{(0,0,3\pm1)}^{6\text{-fan}}$  [equations (A.38) and (A.40)]. Similarly, the 4-fan structure gives intensity at  $(0, 0, 3)$  and  $(0, 0, 3 \pm 1.5)$ , denoted  $I_{(0,0,3)}^{4\text{-fan}}$  [equation (A.43)] and  $I_{(0,0,3\pm1.5)}^{4\text{-fan}}$  [equations (A.45) and (A.47)]. The only contribution from the 2-fan is at  $(0, 0, 3)$  and the intensity is  $I_{(0,0,3)}^{2\text{-fan}}$  [equation (A.49)]. The integrated intensities of each peak can therefore be calculated via the following equations:

$$I_{(0,0,3\pm1)}^{\text{calc.}} = f_{6\text{-fan}} I_{(0,0,3\pm1)}^{6\text{-fan}}, \quad (5.39)$$

$$I_{(0,0,3\pm1.5)}^{\text{calc.}} = f_{4\text{-fan}} I_{(0,0,3\pm1.5)}^{4\text{-fan}}, \quad (5.40)$$

$$I_{(0,0,3)}^{\text{calc.}} = f_{6\text{-fan}} I_{(0,0,3)}^{6\text{-fan}} + f_{4\text{-fan}} I_{(0,0,3)}^{4\text{-fan}} + f_{2\text{-fan}} I_{(0,0,3)}^{2\text{-fan}}, \quad (5.41)$$

where the  $f$ 's are the phase fractions (summing to unity), and a global scaling factor is to be applied between calculated and measured intensities.

Before comparing these intensities to the data, the background in the measurements (which appears to increase at high angle) is fitted empirically using a sum of two exponential functions (these were found to describe the variation in intensity more closely than a polynomial function). The integrated intensities measured in the data (on the low angle side of the Bragg peak) are then compared to those given by equations (5.39) to (5.41) and the phase fractions extracted. The shapes of the magnetic satellites at both high and low angle are then fitted to the data, subject to their integrated intensities being consistent with the calculated phase fractions. The results (calculations of the intensity profiles at 165 K for two separate fields) are shown along with the measured data in figure 5.19. Note that the data in figure 5.19(a) show small peaks with propagation vectors  $\mathbf{q} = (0, 0, 0.75)$ : as explained above, these appear because of the modulation associated with the 4-fan phase which is not precisely out of the scattering plane (due to slight misalignment of the applied magnetic field). There is also a very weak peak in this plot at  $l = 2.5$ : this indicates that a very small part of the sample remains in the helical phase even at 70.5 mT (this was not considered in the phase fraction calculations).

The calculated phase fractions give a more detailed picture of how the system as a whole responds to changes in the applied field. At  $\approx 70$  mT there is a mixture of all three phases, although a relatively small part of the sample appears to have stabilised in the 6-fan phase (this is because, at 70 mT, the 4-fan phase is slightly lower in energy). The majority of the structure stabilises in the 4-fan phase as expected, although in order to explain the intensity measured at  $(0, 0, 3)$  a significant portion ( $\approx 30\%$ ) of the sample is made up of the higher energy 2-fan structure. At  $\approx 150$  mT none of the 6-fan phase remains, and the majority

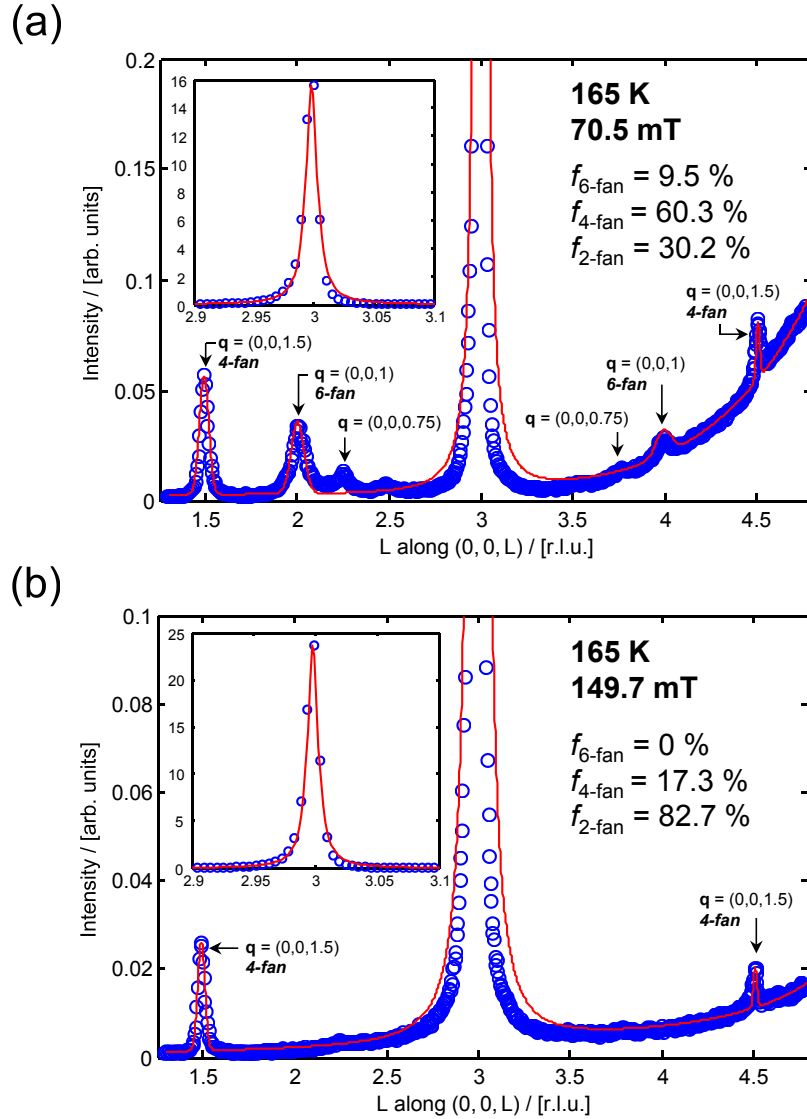


**Figure 5.19:** Measured (blue circles) and calculated (red lines) intensities for two  $l$ -scans at 165 K. Data were obtained in the  $\sigma \rightarrow \pi$  channel. In (a) the field is 70.5 mT and the intensities are calculated for a three-phase model (comprising 6-fan, 4-fan, and 2-fan structures). The phase fractions are indicated. All three phases contribute intensity to the  $(0,0,3)$  peak, and the 4-fan and 6-fan structures result in magnetic satellites as indicated. In (b) the field is 149.7 mT and only the 4-fan and 2-fan structures remain. The insets show the full Bragg peak measured in each scan.

of the sample exists in the 2-fan structure. This is due to the ever decreasing difference in energy between 4-fan and 2-fan structures as the applied field is increased.



## 5.9 Conclusion

Having undertaken a detailed soft X-ray diffraction study of this hexaferrite at low fields, the system appears to explore a multitude of phases which are all close in energy. The helical phase is shown to exist only for the lowest fields, becoming unstable as the field is increased and other magnetic fan structures become more favourable energetically. At room temperature the system rapidly enters the 2-fan phase, whereas at lower temperatures the 4-fan phase is stable up to higher applied fields.

Simple exchange energy arguments have been used to calculate the differences in energy between competing phases and, in particular, I have found that a new ‘6-fan’ phase, existing somewhere between the helical and ‘4-fan’ (intermediate-I) structures, is a likely candidate for the previously unreported peaks in the diffraction data. Based on the calculated inter-spin-block angles in each of the commensurate magnetic structures, scattering intensities are calculated and shown to fit the data. Phase fractions are extracted to quantify the degree of phase coexistence at 165 K. The use of a diffraction technique was crucial for the discovery of this new phase since its net magnetisation and energy are very similar to the competing phases: the only real signature of its existence is a change in the periodicity of the magnetic arrangement to which diffraction is extremely sensitive.

An extension of the current work could be to undertake a similar soft X-ray diffraction measurement with a greater magnetic field applied across the sample (this will most likely require the construction of a much larger water-cooled electromagnet), enabling one to enter the phase in which a ferroelectric polarisation is reported. By undertaking measurements in both  $\sigma \rightarrow \pi$  and  $\pi \rightarrow \pi$  channels, one would be sensitive to modulations in the magnetic structure both within and orthogonally to the scattering plane. In this way any small deviations from the 2-fan structure that might be responsible for breaking the inversion symmetry could be uncovered. A more ambitious experiment could also be designed in which an electric field is applied across the sample in an orthogonal direction to the magnetic field. With this arrangement one could measure (in the multiferroic phase) any changes that appear in the magnetic structure as a result of switching the direction of the electric field, leading to greater insights as to the precise origin of the ferroelectricity in this type of hexaferrite.



## Chapter 6

---

# Nonlinear optical measurements on $\text{MnWO}_4$

---

### 6.1 Introduction

I present in this chapter the design details and testing of a new optical second harmonic generation (SHG) experimental setup. Examining multiferroics with SHG is highly desirable because, in many cases, it provides complementary information to that obtainable by diffraction techniques. In particular, the technique is very sensitive to (changes in) the point symmetry, and the existence or otherwise of several key tensor components is generally enough to establish the point group of a material. This is in contrast to diffraction techniques where X-ray or neutron refinements will often converge upon several candidate space groups with equally good fits. This is important for the study of multiferroics and the search for new materials, since the point symmetry is intimately related to the allowable ferroic properties of the system.

I shall begin by examining the technical details of the experimental arrangement, and then go on to discuss the results of tests undertaken on the multiferroic system  $\text{MnWO}_4$ . This is a good system with which to optimise and characterise the experimental arrangement as its non-zero tensor components are well-known, and it also exhibits several different magnetic phases as a function of temperature that can be measured by SHG. The final part of this chapter is devoted to time-resolved pump-probe measurements on this system: this is principally to demonstrate the flexibility of the technique but also to discuss the observed enhancement of the SHG signal generated by  $(0, 1, 0)$  oriented crystals in response to a perturbation by an optical (800 nm) pulse.

### 6.2 Design of the experiment

One of the key aims of the work presented in this thesis is to build and test an experiment to measure SHG in various samples of interest. Here I describe the main components of the

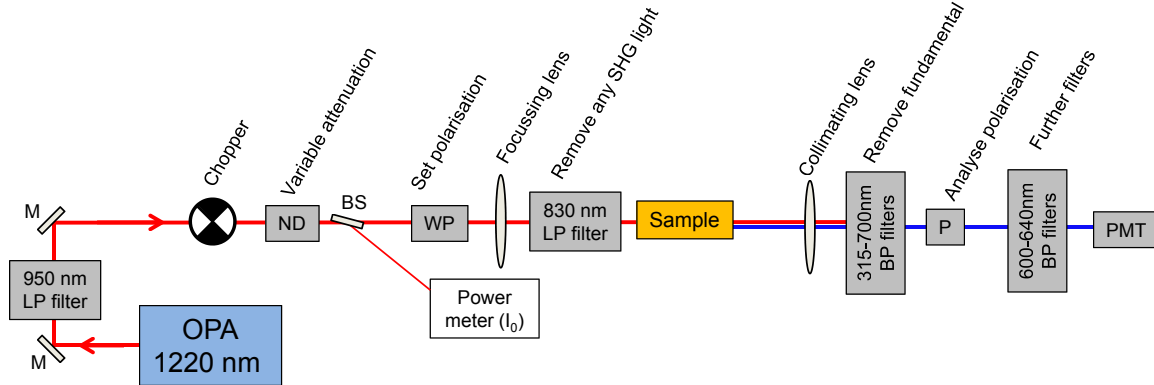


**Figure 6.1:** Schematic arrangement of the static SHG experiment. OPA: Optical parametric amplifier; M: Mirror; LP: Long pass; ND: Neutral density filter; BS: Pellicle beam splitter; WP: Wave plate; BP: Band pass; P: Polariser; PMT: Photomultiplier tube.

experimental setup. Once the light leaves the source (whether that be 800 nm light from the femtosecond laser, or light at different wavelengths from the OPA – see chapter 2), it is directed through a number of optical components into the sample, before the SHG light is detected.

A typical setup for static SHG measurements is shown schematically in figure 6.1, demonstrating the arrangement used when the OPA is producing light with  $\lambda_{\text{sig}} = 1220$  nm. The light leaves the OPA and immediately encounters a pair of dichroic mirrors which separate the signal from the idler beam and dump the idler (not shown in the figure). The beam is then reflected from a pair of gold mirrors which are used to steer it onto a pair of irises (not shown) that define the path. Between these a long pass (LP) filter removes the higher frequency harmonics generated by the OPA. The beam then passes through an optical chopper, and before reaching the variable neutral density (ND) filters that attenuate the beam to the desired intensity the light passes through a translation stage (not shown) that can be used to adjust the path length in time-resolved experiments. A beam splitter directs some of the beam into a power meter. Next the beam passes through a liquid crystal retarder, which acts as a variable wave plate (WP), typically of  $\lambda/2$  to rotate the incident polarisation with respect to the crystal axes of the sample. A lens (of focal length  $f = 17.5$  cm) focusses the beam onto the sample, and a further long pass filter removes any spurious SHG light that may have been generated by the optical components so far. After exiting the sample, the beam is collimated and passes through a number of band pass (BP) filters to remove all of the 1220 nm fundamental, leaving only 610 nm SHG light. Finally the light is analysed with a polariser and passes into a photo multiplier tube (PMT) where it is detected. Automation and control has been built into the setup to reduce data

collection time and improve precision. Custom designed code has been written in Python to oversee all of the data acquisition and plot the data in real time.

### **Optical chopper**

The light, upon leaving the OPA, passes through a chopper wheel which has a separate unit to set and control the frequency of rotation (throughout a chopping frequency of 385 Hz is used, to avoid chopping at the same frequency as any harmonics of the 1 kHz repetition rate of the laser). The control unit also provides the reference frequency which is sent to the lock-in amplifier.

### **Power meter**

After the chopper the light passes through a pellicle beam splitter which diverts a small fraction (typically around 5%) of the incident beam into a power meter. This provides a measure of  $I_0$ , proportional to the fundamental beam intensity incident on the sample, which can be used to normalise the measured signal. The power meter readings are logged automatically during data collection.

### **Liquid crystal retarder**

This variable retarder is controlled by an AC voltage which sets the retardance. Hence it may be made to act like a  $\lambda/4$  or, more commonly, a  $\lambda/2$  waveplate for a variety of different wavelengths simply by changing the voltage applied across it. The retarder is mounted within a rotation stage to allow the polarisation direction of the light incident onto the sample to be set arbitrarily (in the case of linearly polarised light). Both the retarder power supply and rotation stage are computer controlled. The variable retarder must be calibrated before use to establish the value of the applied AC voltage necessary to make the retarder behave correctly as a  $\lambda/2$  waveplate (this voltage depends on the precise value of the fundamental wavelength). To do this, a series of measurements were carried out in which light exiting the variable retarder was allowed to pass directly onto the analyser polariser before being detected by the PMT. Since linearly polarised light incident onto a  $\lambda/2$  waveplate leaves with a rotated linear polarisation (rotated by twice the rotation angle of the waveplate), a series of two-dimensional scans (waveplate angle vs. analyser polariser angle) were carried out for different voltages, until the correct behaviour was observed.

### **Sample environment**

The sample is housed inside an Oxford Instruments Optistat CF-V liquid-He flow cryostat which provides two temperature sensors (one mounted onto the heat exchanger and a second

Cernox<sup>TM</sup> sensor that can be mounted next to the sample) and a heater. Two Oxford Instruments ITC503S units are used to control and monitor the temperatures, and these are interfaced to the control software. The cryostat is mounted onto two heavy-duty translation stages that can be used to position the sample accurately (the nominal positioning resolution is  $0.1 \mu\text{m}$ ) within the beam, and again can be computer controlled.

### Analysers polariser

This is a Glan Thompson polariser which is used to analyse the polarisation of the SHG beam. It is mounted within a computer controlled rotation stage.

### Detection system

The PMT detector has a variable gain set by a small DC voltage supply unit, and is connected to the lock-in amplifier which is interfaced to the software. This ensures that the measured SHG signal originates from fundamental light that has passed through the chopper, vastly reducing the size of the background.

## 6.3 Static measurements on $\text{MnWO}_4$

Static measurements on  $\text{MnWO}_4$  have already been performed by Meier *et al.* [148,149], who reported the existence of several tensor components of both crystallographic and magnetic origin. Thus, the results obtained in this section (which agree with the previously reported findings) form a good test of the newly developed experimental setup and a check that the observed signals are indeed from the second harmonic light, as confirmed by their temperature dependences.

### 6.3.1 Introduction to $\text{MnWO}_4$

$\text{MnWO}_4$  has a monoclinic crystal structure (space group  $Pc/2$ ) [151] and a view of the atomic arrangement is given in figure 6.2. The lattice parameters were measured at room temperature using a ‘SuperNova’ diffractometer and were  $a = 4.824 \text{ \AA}$ ,  $b = 5.753 \text{ \AA}$ ,  $c = 4.995 \text{ \AA}$ ,  $\beta = 91.12^\circ$ . The magnetic  $\text{Mn}^{2+}$  ions stack in chains along the  $\mathbf{c}$  axis. In the AF1 phase, below  $T_{N1} \approx 7 \text{ K}$ , the system forms a commensurate magnetic structure with propagation vector  $\mathbf{q}_{\text{AF1}} = (\pm \frac{1}{4}, \frac{1}{2}, \frac{1}{2})$ , in which the moments are aligned along the easy axis of magnetisation which lies approximately  $36^\circ$  from the  $\mathbf{a}$  axis and is within the  $ac$  plane. In the AF2 phase, the propagation vector is incommensurate:  $\mathbf{q}_{\text{AF2}} = (-0.214, \frac{1}{2}, 0.457)$ . The structure in this phase is cycloidal. Above  $T_{N2} = 12.5 \text{ K}$ , the structure maintains the same incommensurate propagation vector but becomes sinusoidally modulated: this is the

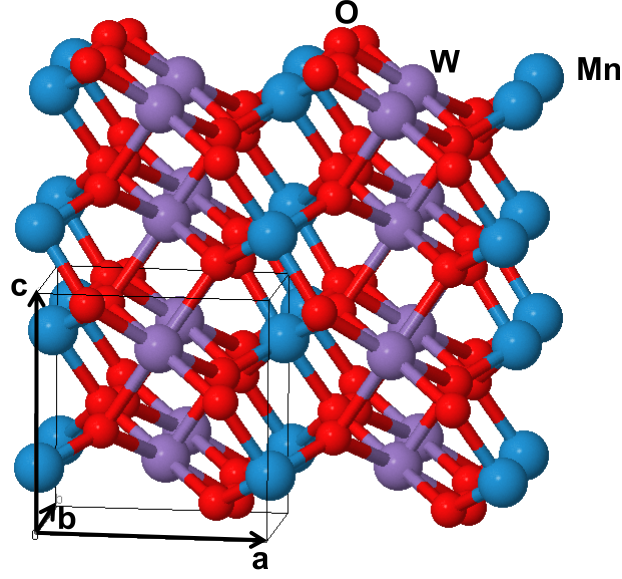


**Figure 6.2:** The crystal structure of  $\text{MnWO}_4$  with constituent species labelled [150].

AF3 phase which lasts up until  $T_{N3} = 13.5$  K, above which the system is paramagnetic. Further details can be found in [152].

In 2006 it was reported in [152, 153] that in the AF2 phase the system develops a ferroelectric polarisation  $\mathbf{P}$  which can be explained by the cycloidal spin structure via the ‘inverse Dzyaloshinskii-Moriya interaction’  $\mathbf{P} \propto \hat{\mathbf{r}}_{ij} \times (\mathbf{S}_i \times \mathbf{S}_j)$  (see also section 3.1). The polarisation therefore appears as a consequence of the inversion symmetry breaking by the cycloid, and this makes  $\text{MnWO}_4$  a spin driven type-II multiferroic.

From the point of view of SHG,  $\text{MnWO}_4$  is a very interesting system to study since one should be sensitive both to the inversion symmetry breaking in the polar AF2 phase, which will give a large contribution to the susceptibility via  $\chi^{\text{ED}}$ , and to symmetry breaking by the magnetic structure which also allows for non-zero components of  $\chi^{\text{MD}}$  below  $T_{N3}$ . The symmetry-allowed tensor components have been calculated in [148] and are reproduced here in table 6.1. The Cartesian coordinate system labelling the tensor components has  $\hat{\mathbf{e}}_y \parallel \mathbf{b}$ ,  $\hat{\mathbf{e}}_z \parallel \mathbf{c}$ , and  $\hat{\mathbf{e}}_x = \hat{\mathbf{e}}_y \times \hat{\mathbf{e}}_z$ .

One technical challenge that must be overcome in order to measure SHG in the transmission arrangement described here is that the crystals must be very thin, typically of thickness 50-100  $\mu\text{m}$  [154], as crystals of greater thickness will start to generate second harmonic light part way through the sample which will be out of phase with that generated at the start: thus the light will destructively interfere. It is also desirable to have the crystals as thin as possible to reduce the absorption of the SHG signal by the sample, and the surface needs

Point group	Incident light							
$2_y/m_y1'$ (AF1, AF3)	$k \parallel x$	$\chi_{yyy}^{\text{MD}}$	$\chi_{yzz}^{\text{MD}}$	$\chi_{zyz}^{\text{MD}}$				
	$k \parallel y$							
	$k \parallel z$	$\chi_{yyy}^{\text{MD}}$	$\chi_{yxx}^{\text{MD}}$	$\chi_{xyx}^{\text{MD}}$				
$2_y1'$ (AF2)	$k \parallel x$	$\chi_{yyy}^{\text{MD}}$	$\chi_{yzz}^{\text{MD}}$	$\chi_{zyz}^{\text{MD}}$	$\chi_{yyy}^{\text{ED}}$	$\chi_{yzz}^{\text{ED}}$	$\chi_{zyz}^{\text{ED}}$	
	$k \parallel y$							
	$k \parallel z$	$\chi_{yyy}^{\text{MD}}$	$\chi_{yxx}^{\text{MD}}$	$\chi_{xyx}^{\text{MD}}$	$\chi_{yyy}^{\text{ED}}$	$\chi_{yxx}^{\text{ED}}$	$\chi_{xyx}^{\text{ED}}$	

**Table 6.1:** Non-zero susceptibility tensor elements for  $\text{MnWO}_4$  in the three magnetic phases (after [148]).

to be of very high quality.

### 6.3.2 Results and discussion

Static measurements were made on two separate samples: one with a  $(0, 1, 0)$  orientation (*i.e.* the incident light has  $k \parallel y$ ) and one with a  $(0, 0, 1)$  orientation ( $k \parallel z$ ). The static SHG signal can be plotted as a function of the incident fundamental (set by the waveplate) and exit second harmonic (set by the analyser polariser) light polarisations simultaneously. The angle that the incident fundamental light makes relative to the  $x$ - ( $x'$ -) axis of the crystal is denoted  $\phi_\omega$ , and the angle made by the exit SHG light relative to the same crystal axis is  $\phi_{2\omega}$ . Figure 6.3 shows the measured SHG intensity as a function of these two angles for the two sample orientations, both collected at a temperature of 10.5 K.

In both cases there is a single tensor element that dominates all other effects (the plots show a single peak). In the case of  $k \parallel z$  [figure 6.3(a)], the  $\chi_{yxx}^{\text{ED,MD}}$  component is clearly seen. However, if the incident (fundamental frequency) photons are absorbed in ED-type transitions, the  $\chi^{\text{MD}}$  tensor components are not allowed since the associated magnetisation  $M_i \propto \chi_{ijk}^{\text{MD}} E_j E_k$  changes sign under time reversal, whereas  $E_{j,k}$  do not ( $\chi_{ijk}^{\text{MD}}$  also cannot change sign as the magnetic point group contains  $1'$ ). Therefore their inclusion in table 6.1 is only for completeness: in principle these components can be non-zero should an MD-type transition occur when the incident photons are absorbed, but this is a higher order contribution and therefore the  $\chi^{\text{MD}}$  are expected to be very small (none of the  $\chi^{\text{MD}}$  components were observed in the data).

The existence of a signal with  $k \parallel y$  [figure 6.3(b)] seems more puzzling since there should be no contribution here at all according to the symmetry analysis. The reason for this signal (as proposed by Meier *et al.* [148]) is a result of the incommensurate modulation in the magnetic structure of the material, which is responsible for breaking the  $2_y$  symmetry locally (on the order of the wavelength of the fundamental light), giving rise to a weak



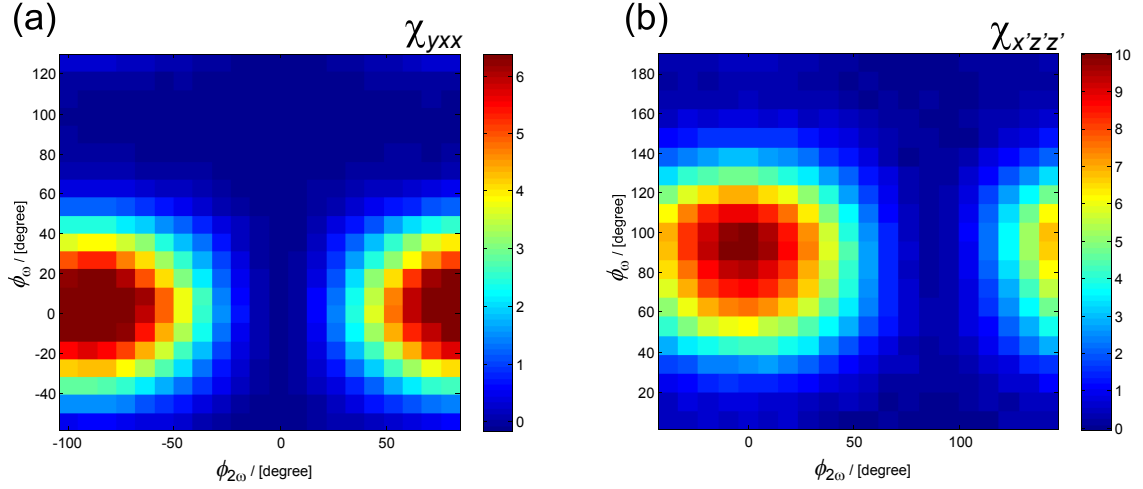


**Figure 6.3:** Static intensity plots of two susceptibility tensor components as a function of the incident ( $\omega$ ) and exit ( $2\omega$ ) polarisation angles. The angles are arranged in (a) such that  $\phi = 0^\circ \parallel x$ ,  $\phi = 90^\circ \parallel y$ ; and in (b) such that  $\phi = 0^\circ \parallel x'$ ,  $\phi = 90^\circ \parallel z'$ . Note that the intensities are in arbitrary units and are not scaled in the same way. Both sets of data were collected in the AF2 phase at  $T = 10.5$  K.

SHG signal along the  $x'$  direction for fundamental light polarised along  $z'$  (the primed coordinates are related to the direction of the incommensurate propagation vector of the magnetic structure, such that  $x'$  is within the plane of the AF2 cycloid: for details see [148]).

The fact that both of these components are clearly seen is an encouraging confirmation that the setup is working and that it can be used to identify the non-zero second order susceptibility components. Further confirmation is provided by the temperature dependence of the two peaks, which is shown in figure 6.4. The temperature dependence of the SHG signal is essentially flat in the AF1, AF3, and paramagnetic regions, but grows linearly with cooling in the AF2 region. This is in good agreement with the data published in [148], including the ratio of the SHG intensities at the AF1-AF2 phase boundary which is  $\approx 45$ .

## 6.4 Pump-probe measurements on $\text{MnWO}_4$

Having tested the experimental setup by measuring the static SHG response of  $\text{MnWO}_4$ , I now move on to discuss the time-resolved measurements I have undertaken on the same system.

### 6.4.1 The pump-probe setup

Fundamentally, the idea of a pump-probe experiment is that one introduces a large perturbation to the sample in the form of a strong optical pulse (the pump), which is then

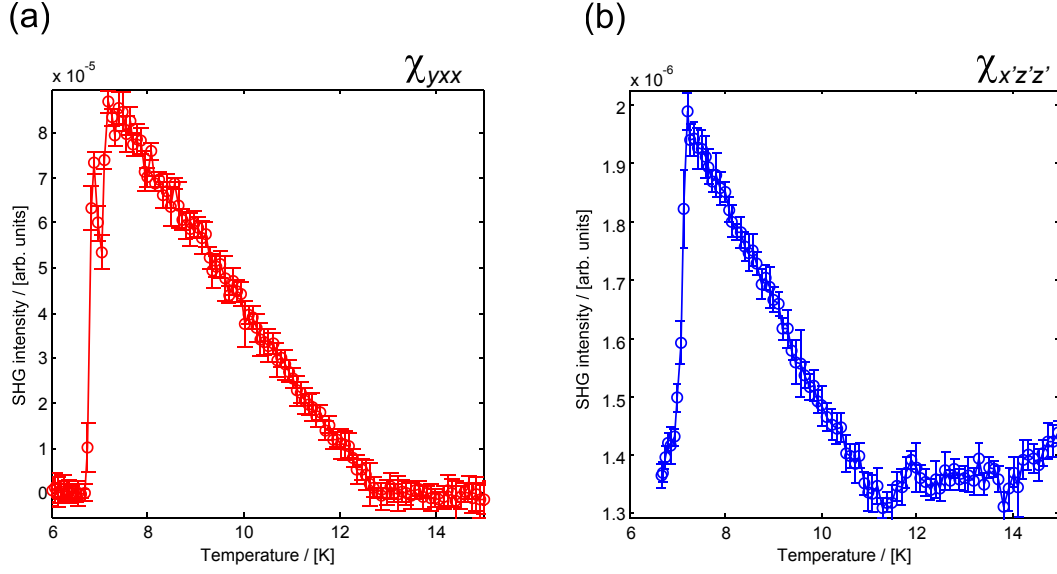


**Figure 6.4:** Temperature dependence of (a) the  $\chi_{yxx}$ , and (b) the  $\chi_{x'z'z'}$  susceptibility components. The linear increase in intensity during the AF2 phase can easily be seen. Note that both (a) and (b) use the *same* arbitrary scale.

followed some time  $\Delta t$  after this by the probe pulse and the signal resulting from the probe measured. By using a translation stage in the setup it becomes possible to vary the time delay  $\Delta t$  and this enables one to examine the dynamics of the system in response the pump pulse on ultrafast time scales.

A diagram of the setup is shown in figure 6.5. The probe branch is very similar to that used in the static experiments presented in the previous section, with the addition of a delay stage that is used to vary the path length of the branch. In addition there is a pump branch, which takes the ‘raw’ 800 nm light from the laser, sets its polarisation with an 800 nm  $\lambda/2$  waveplate (followed by a polariser, not shown in the figure) and then directs it at a slight angle to the probe beam (approximately  $10^\circ$ ) onto the sample. The pump beam that has passed through the sample is dumped. Filters are again used to reduce contamination of the SHG signal by anything that is generated by the upstream optics. The band pass filters positioned in front of the PMT are now crucial, since they are responsible for removing any potential sum-frequency-generated signal between pump and probe beams [the wavelength of such a sum frequency signal being  $\lambda_{\text{pump}}\lambda_{\text{probe}}/(\lambda_{\text{pump}} + \lambda_{\text{probe}}) = 483 \text{ nm}$ ] and any second harmonic signal arising purely from the pump beam (of wavelength 400 nm).

It is necessary to ensure that the two beams, pump and probe, are overlapped both in space and (for an appropriate position of the translation stage) in time. The latter is achieved by ensuring that the total path length of both branches are equal. The spatial

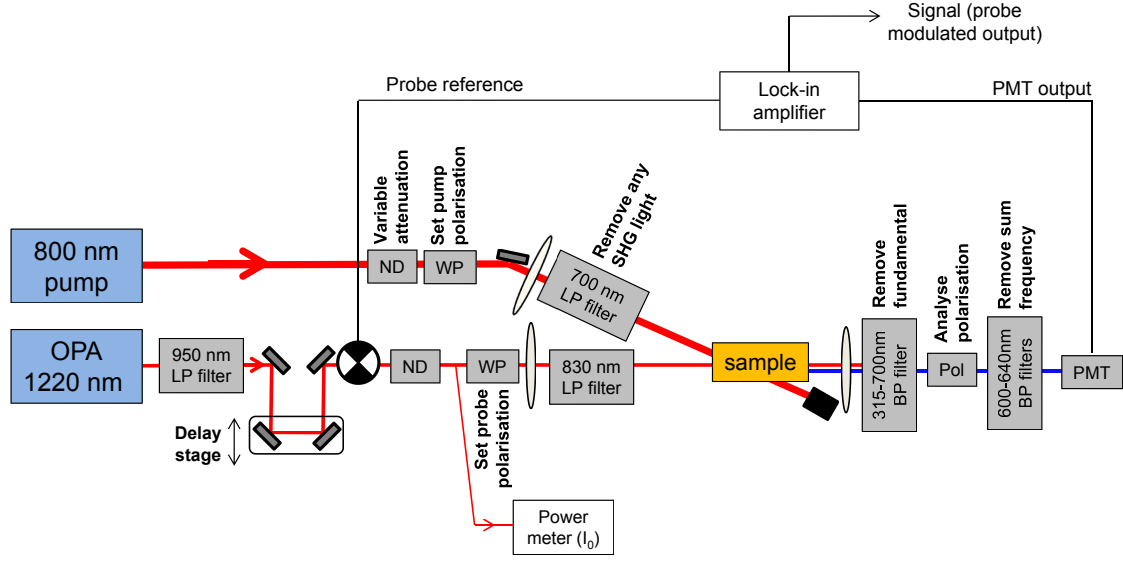


**Figure 6.5:** Schematic of the pump-probe experimental arrangement (abbreviations as figure 6.1).

overlap is ensured by aligning both beams through a pinhole mounted just above the sample position. Once this alignment is complete then the sample is simply translated into the position of the pinhole. In addition, the spot size of the probe at the sample position should be smaller than that of the pump, since one only wants to examine the volume of the crystal that is perturbed by the pump beam. To this end, the probe beam is strongly focussed at the sample position with a spot size of  $\approx 120 \mu\text{m}$ , whereas the pump beam is slightly defocussed to give a spot size of  $\approx 250 \mu\text{m}$ .

The aim of this experiment is to use the 800 nm light to pump the  $(0, 1, 0)$  oriented sample in the AF2 phase where there is a relatively large  $\chi_{x'z'z'}$  contribution to the SHG. This component arises from the incommensurate modulation in the crystal structure that is derived from the incommensurate magnetism in this phase. The effect that this optical pumping has on the crystal structure can then be measured by probing with the SHG technique developed above.

## 6.4.2 Results

Figure 6.6 plots a typical pump-probe trace for the measured SHG intensity as a function of time delay  $\Delta t$  between pump and probe, with the pump polarised along the  $x'$  direction, and the probe branch waveplate and polariser set to examine the  $\chi_{x'z'z'}$  tensor component as measured in the static scans. In this plot, the zero on the  $x$ -axis has been positioned to coincide with the peak of the data, and the shaded bar gives an approximate indication

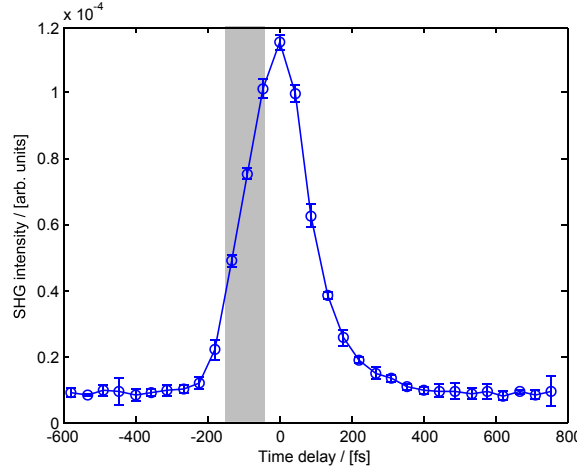


**Figure 6.6:** Pump-probe trace of the SHG intensity from the  $\chi_{x'z'z'}$  susceptibility component, with the pump polarised along  $x'$ . The shaded area gives an indication of the pump pulse duration.

of the full width at half maximum of the pulse duration of the laser (120 fs). At negative times (*i.e.* a measurement of the static SHG signal before the pump pulse has arrived) the signal is very flat. The pump pulse then appears to cause an enhancement of roughly an order of magnitude in the SHG signal. This enhancement lasts for an amount of time equal to several pulse durations before it has completely decayed back to the static signal.

In order to confirm that the observed signal close to  $t = 0$  really is an enhancement in the SHG from the probe, as opposed to an extra signal due to sum frequency mixing or SHG from the pump beam, a dependence was measured on the incident probe power whilst keeping the pump power constant (a time delay scan similar to figure 6.6 having been collected for each power). The results of this can be seen in figure 6.7 (data were collected at 10.5 K). Figure 6.7(a) plots the size of the  $t = 0$  peak as a function of the incident normalising power,  $I_0$ , as measured by the power meter, for five different probe intensities. Linear and quadratic fits are both shown: the behaviour shows a distinctly quadratic dependence which suggests the enhancement must really be in SHG as generated by the probe beam. By way of further confirmation, figure 6.7(b) plots the size of the static SHG response (measured far from  $t = 0$ ) vs. the  $t = 0$  response. The linear behaviour again confirms that the signal measured in this experiment is true SHG from the 1220 nm probe beam, and is not contaminated by light originating from any other nonlinear process in the sample.

Finally, figure 6.8 shows SHG intensity plots as a function of the incident probe polarisation angle ( $\phi_\omega$ ) and the exit SHG polarisation angle ( $\phi_{2\omega}$ ), both collected at 10.5 K (note

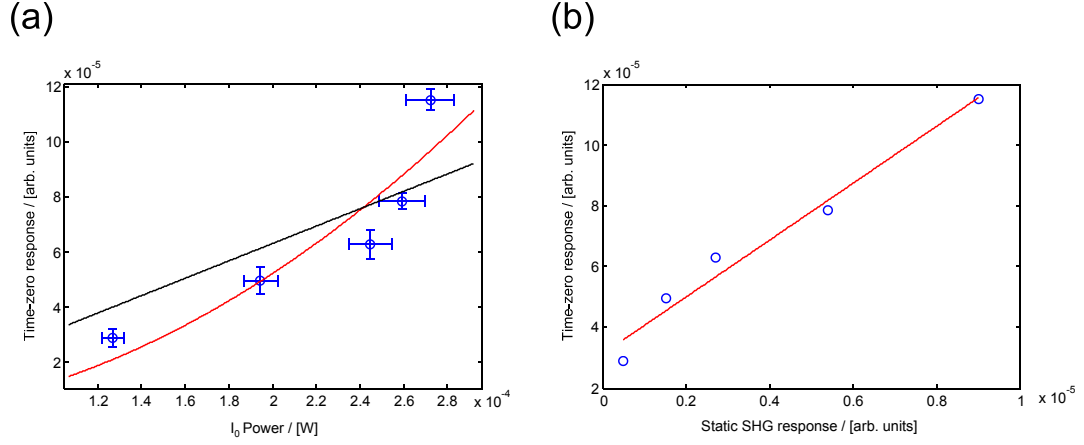


**Figure 6.7:** Data derived from similar pump-probe traces to that shown in figure 6.6, with various probe intensities. (a) The size of the  $t = 0$  peak plotted against  $I_0$  (which is proportional to the incident probe intensity), with quadratic (red) and linear (black) fits. (b) The linear relationship between the static SHG response and the height of the  $t = 0$  peak.

that the arbitrary scale is not the same as before). In figure 6.8(a), the pump is polarised along the  $z'$  direction, and a clear peak in the  $t = 0$  data is present at the  $\chi_{x'z'z'}$  position (note though that the time trace shows that the enhancement with this pump polarisation is only by a factor of  $\approx 2$ , rather than the factor of  $\approx 10$  observed with the orthogonal polarisation). Figure 6.8(b) shows the equivalent dependence on the probe polarisation with the pump now polarised along the  $x'$  direction. Here one can see a small contribution at  $(\phi_{2\omega}, \phi_{\omega}) = (0^\circ, 90^\circ)$ , *i.e.* from the  $\chi_{x'z'z'}$  component whose time delay dependence was discussed above (note that the SHG intensity scale is not the same as in figure 6.6), but much more significant is a very large contribution at  $(\phi_{2\omega}, \phi_{\omega}) = (90^\circ, 0^\circ)$  which I shall refer to as the  $\chi_{z'x'x'}$  component.

### 6.4.3 Discussion

As far as the  $\chi_{x'z'z'}$  component is concerned, it seems that the pump induces an enhancement in this component regardless of whether it is polarised along the  $z'$  or  $x'$  direction, although when polarised along  $x'$  the enhancement is  $\approx 5$  times larger than when it is polarised along  $z'$ . However, a much larger contribution to the SHG that appears only when the pump is polarised along  $x'$  is also observed: the  $\chi_{z'x'x'}$  component (this is not present in the static measurements). For such an enhancement to exist, the point symmetry must be lowered in some way (this is a necessary condition for new tensor elements to appear). One possibility may be that the effect of the pump beam, in introducing disorder, locally

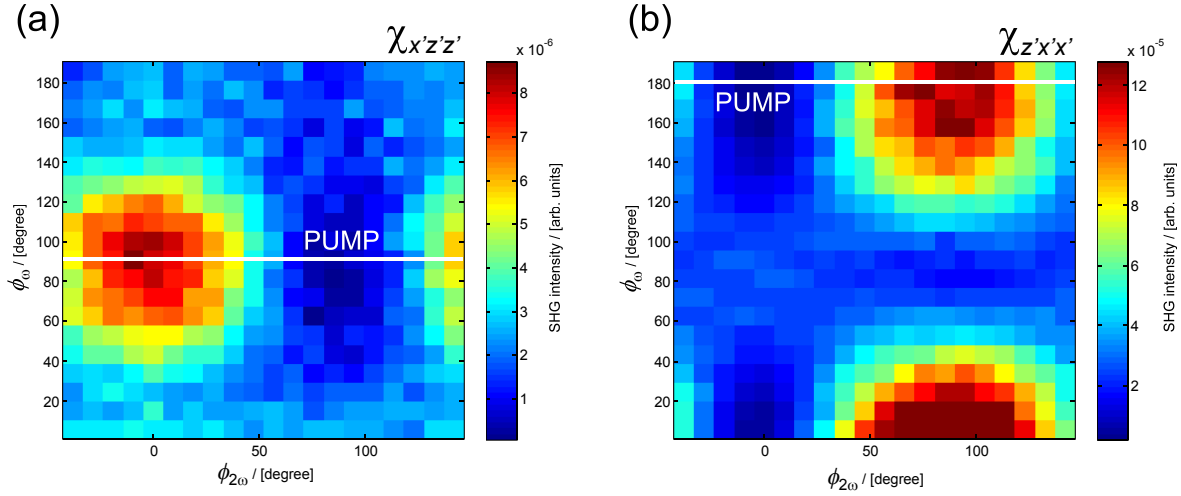


**Figure 6.8:** Pump-probe intensity maps taken at  $t = 0$ , for two different pump polarisations (the angle of which is indicated by a white line on each plot). In (a) the pump is polarised along  $z'$  (perpendicular to the spin cycloid), whereas in (b) the polarisation is along  $x'$  (within the plane of the cycloid). The corresponding tensor components giving rise to the strongest signal are indicated.

distorts the crystal lattice to a greater extent than the incommensurate magnetic structure does alone. If these local perturbations are connected spatially to the direction of the pump beam polarisation then this ‘extra’ local distortion would appear within the plane of the spin cycloid for the pump polarised along  $x'$ , and out of the plane for the pump polarised along  $z'$ . This may explain why the largest enhancements in the SHG are observed with the pump polarised along  $x'$ , when the pump can distort the lattice within the same plane as those distortions caused by the magnetic structure, as opposed to along  $z'$  where the distortions are orthogonal to this. However, as remarked in [148] in relation to SHG by relaxor ferroelectrics (which contain randomly distributed polar clusters [155]), one would expect that these local distortions would lead to the second harmonic signal they generate summing incoherently across the crystal.

## 6.5 Conclusion and further work

In this chapter I have explained the design of a new second harmonic generation experiment, set up to assist in determining the point symmetry of multiferroic crystals. The system allows one to probe all non-zero susceptibility tensor elements providing that two orthogonal thin crystal cuts are available. Temperature dependent studies are also possible, and the entire cryostat/sample setup is mounted on a pair of high-precision translation stages which

can be used to scan the sample surface whilst measuring the SHG efficiency: this may be of future use in imaging magnetic domains in cases where a contrast exists in the second harmonic light they radiate.

The system has been thoroughly tested with two samples of the multiferroic  $\text{MnWO}_4$ . Static measurements reveal an easily measurable signal whose temperature dependence agrees with the published literature. In addition, the setup has been adjusted to carry out time-resolved measurements with optical pumping. Data using 800 nm pump / 610 nm SHG probe collected on  $\text{MnWO}_4$  show a large enhancement in the SHG signal generated by a sample in the  $(0, 1, 0)$  orientation. The enhancement is dependent on the pump polarisation and is greatest when the polarisation is within the plane of the spin cycloid. This suggests that an incoherent SHG signal, resulting from the local distortions of the crystal caused by the pump beam, may be responsible for the observed enhancement, although further work will be needed to fully understand this effect.





## Appendix A

### Calculation of the hexaferrite scattering intensities

In this appendix I shall derive expressions for the scattered X-ray intensities originating from the 6-fan, 4-fan, and 2-fan phases of the hexaferrite, as used in calculating the intensity profiles in section 5.8 [equations (5.39) to (5.41)].

#### A.1 Fourier descriptions of the commensurate magnetic structures

Before calculating the intensities it is necessary to obtain the Fourier descriptions of the magnetic phases: these are given below for the three commensurate fan structures.

For the *6-fan* phase, splitting each moment  $\mu_{L,S}$  into components along  $\hat{\mathbf{e}}_x$  and  $\hat{\mathbf{e}}_y$  (figure 5.15), one has for the L blocks:

$$\mu_L^x(\mathbf{r}) = A_L^x + B_L^x \cos[(0, 0, 1) \cdot \mathbf{r} + \phi_L^x], \quad (\text{A.1})$$

$$\mu_L^y(\mathbf{r}) = A_L^y \cos[(0, 0, 0.5) \cdot \mathbf{r} + \phi_L^y] + B_L^y \cos[(0, 0, 1.5) \cdot \mathbf{r} + \phi_L^y], \quad (\text{A.2})$$

where  $\mathbf{r} = \mathbf{0}, \frac{\mathbf{c}}{3}, \frac{2\mathbf{c}}{3}, \dots$  is the position of the (L + S) block belonging to the moment, the row vectors are defined with respect to the reciprocal lattice basis vectors, the constants  $A_L^{x,y}$  and  $B_L^{x,y}$  depend on the angles of the magnetic structure in the following way:

$$A_L^x = \frac{S_L}{3} \cos\left(\frac{\phi_6}{2}\right) (1 + 2 \cos \phi_6), \quad (\text{A.3})$$

$$B_L^x = \frac{4S_L}{3} \cos\left(\frac{\phi_6}{2}\right) (1 - \cos \phi_6), \quad (\text{A.4})$$

$$A_L^y = \frac{4S_L}{3} \sin\left(\frac{\phi_6}{2}\right) (\cos \phi_6 + 1), \quad (\text{A.5})$$

$$B_L^y = \frac{2S_L}{3} \sin\left(\frac{\phi_6}{2}\right) \left(\cos \phi_6 - \frac{1}{2}\right), \quad (\text{A.6})$$

and the phase angles are

$$\phi_L^x = \frac{\pi}{3}, \quad \phi_L^y = -\frac{\pi}{3}, \quad \phi_L^z = \pi. \quad (\text{A.7})$$

Similarly, the S blocks may be described by

$$\mu_S^x(\mathbf{r}) = A_S^x + B_S^x \cos[(0, 0, 1) \cdot \mathbf{r} + \phi_S^x], \quad (\text{A.8})$$

$$\mu_S^y(\mathbf{r}) = A_S^y \cos[(0, 0, 0.5) \cdot \mathbf{r} + \phi_S^y], \quad (\text{A.9})$$

with

$$A_S^x = -\frac{S_S}{3} (1 + 2 \cos \phi_6), \quad (\text{A.10})$$

$$B_S^x = \frac{2S_S}{3} (\cos \phi_6 - 1), \quad (\text{A.11})$$

$$A_S^y = \frac{2S_S}{\sqrt{3}} \sin \phi_6, \quad (\text{A.12})$$

and

$$\phi_S^x = 0, \quad \phi_S^y = \frac{\pi}{2}. \quad (\text{A.13})$$

In the *4-fan* magnetic structure, the L block moments are

$$\mu_L^x(\mathbf{r}) = C_L^x + D_L^x \cos[(0, 0, 1.5) \cdot \mathbf{r}], \quad (\text{A.14})$$

$$\mu_L^y(\mathbf{r}) = C_L^y \cos\left[(0, 0, 0.75) \cdot \mathbf{r} - \frac{\pi}{2}\right], \quad (\text{A.15})$$

where

$$C_L^x = \frac{S_L}{2} (1 + \cos \phi_4), \quad (\text{A.16})$$

$$D_L^x = \frac{S_L}{2} (1 - \cos \phi_4), \quad (\text{A.17})$$

$$C_L^y = -S_L \sin \phi_4. \quad (\text{A.18})$$

The S block moments are given by

$$\mu_S^x = -S_S \cos\left(\frac{\phi_4}{2}\right), \quad (\text{A.19})$$

$$\mu_S^y(\mathbf{r}) = D_S^y \cos\left[(0, 0, 0.75) \cdot \mathbf{r} - \frac{3\pi}{4}\right], \quad (\text{A.20})$$

where

$$D_S^y = \sqrt{2} S_S \sin\left(\frac{\phi_4}{2}\right). \quad (\text{A.21})$$

For the *2-fan* structure, the moments are described by:

$$\mu_L^x = S_L \cos\left(\frac{\phi_2}{2}\right), \quad (\text{A.22})$$

$$\mu_L^y(\mathbf{r}) = S_L \sin\left(\frac{\phi_2}{2}\right) \cos[(0, 0, 1.5) \cdot \mathbf{r} + \pi], \quad (\text{A.23})$$

$$\mu_S^x = -S_S, \quad (\text{A.24})$$

$$\mu_S^y = 0. \quad (\text{A.25})$$

## A.2 X-ray intensities

The intensities may be calculated from the square of the resonant magnetic structure factor [see equation (2.32)], given by

$$F_{\text{mag}}(\mathbf{Q}) = \sum_j f_{j,\text{RES}} e^{i\mathbf{Q} \cdot \mathbf{r}_j}, \quad (\text{A.26})$$

where the sum runs over the magnetic blocks in the sample (labelled by  $j$ ), and for scattering into the  $\sigma \rightarrow \pi$  channel the resonant magnetic form factor is given by [using equation (2.33)]:

$$f_{j,\text{RES}} = -iF^{(1)}\mu_j^x \cos \theta, \quad (\text{A.27})$$

where  $F^{(1)}$  is a constant (the wavelength of the incident X-rays being fixed),  $\theta$  is half of the scattering angle, and I have neglected the contribution from  $\mu_j^z$  because there is no moment in this direction. Since everything will be scaled by an overall constant from here onwards I shall take  $F^{(1)} = 1$ .

In order to calculate the structure factors for the commensurate magnetic fan structures described above, it will be necessary to work with a supercell that contains six ( $L + S$ ) blocks, which will contain two periods of the  $\mathbf{q} = (0, 0, 1)$  modulation, and three periods of the  $\mathbf{q} = (0, 0, 1.5)$  modulation. Thus, the structure factor can be written

$$F_{\text{mag}}(\mathbf{Q}) = -i \cos \theta \sum_n \sum_{p=1}^6 \left[ \mu_L^x(\mathbf{r}_p) e^{i\mathbf{Q} \cdot (\mathbf{R}_n + \mathbf{r}_p)} + \mu_S^x(\mathbf{r}_p) e^{i\mathbf{Q} \cdot (\mathbf{R}_n + \mathbf{r}_p - \frac{\mathbf{c}}{6})} \right], \quad (\text{A.28})$$

where I have replaced the summation over  $j$  by two summations over  $n$  and  $p$  (both  $\in \mathbb{Z}$ ), and have written  $\mathbf{r}_j = \mathbf{R}_n + \mathbf{r}_p$ . Here,  $\mathbf{R}_n = 2n\mathbf{c}$  and  $\mathbf{r}_p = (p-1)\mathbf{c}/3$ . There is an extra  $-\mathbf{c}/6$  appearing in the second exponential in equation (A.28) because the S blocks are displaced along the  $\mathbf{c}$  direction by this amount relative to the L blocks. Therefore

$$F_{\text{mag}}(\mathbf{Q}) = -i \cos \theta \sum_n e^{i\mathbf{Q} \cdot \mathbf{R}_n} \sum_{p=1}^6 \left[ \mu_L^x(\mathbf{r}_p) e^{i\mathbf{Q} \cdot \mathbf{r}_p} + \mu_S^x(\mathbf{r}_p) e^{i\mathbf{Q} \cdot \mathbf{r}_p} e^{-\frac{i\pi l}{3}} \right], \quad (\text{A.29})$$

where  $\mathbf{Q} = l\mathbf{c}^*$ . Finally, the summation over  $n$  will be zero unless  $\mathbf{Q} \cdot \mathbf{R}_n = 2\pi \times \text{integer}$ . This restricts  $l$  to half-integer values, and so this summation can be rewritten as

$$\sum_n e^{i\mathbf{Q} \cdot \mathbf{R}_n} = \alpha \delta(l - m/2), \quad m \in \mathbb{Z}, \quad (\text{A.30})$$

where  $\alpha$  is a constant.

### A.2.1 6-fan structure

The structure factor for the 6-fan arrangement is

$$\begin{aligned} F_{\text{mag}}^{6\text{-fan}} = & -i \cos \theta \alpha \delta(l - m/2) \sum_{p=1}^6 \left\{ A_L^x + \frac{B_L^x}{2} \left[ e^{i(\mathbf{q} \cdot \mathbf{r}_p + \phi_L^x)} + e^{-i(\mathbf{q} \cdot \mathbf{r}_p + \phi_L^x)} \right] \right\} e^{i\mathbf{Q} \cdot \mathbf{r}_p} \\ & - i \cos \theta \alpha \delta(l - m/2) \sum_{p=1}^6 \left\{ A_S^x + \frac{B_S^x}{2} \left[ e^{i\mathbf{q} \cdot \mathbf{r}_p} + e^{-i\mathbf{q} \cdot \mathbf{r}_p} \right] \right\} e^{i\mathbf{Q} \cdot \mathbf{r}_p} e^{-\frac{i\pi l}{3}}, \end{aligned} \quad (\text{A.31})$$

where  $\mathbf{q} = (0, 0, 1)$ . This can be split into three contributions, the first of which does not depend on  $\mathbf{q}$  and is given by

$$F_{\text{mag}}^{6\text{-fan}(1)} = -i \cos \theta \alpha \delta(l - m/2) \sum_{p=1}^6 \left[ A_L^x + A_S^x e^{-\frac{i\pi l}{3}} \right] e^{i\mathbf{Q} \cdot \mathbf{r}_p} \quad (\text{A.32})$$

$$= -i \cos \theta \alpha \delta(l - m/2) \left[ A_L^x + A_S^x e^{-\frac{i\pi l}{3}} \right] \left( 1 + e^{2\pi i \frac{l}{3}} + e^{2\pi i \frac{2l}{3}} + e^{2\pi i \frac{3l}{3}} + e^{2\pi i \frac{4l}{3}} + e^{2\pi i \frac{5l}{3}} \right). \quad (\text{A.33})$$

Given that one must have  $l = m/2$ , the term in round brackets will go to zero whenever  $l$  is odd-half integer, and also for other integers unless  $l = 3m$  (in which case the term is equal to 6). Thus this piece of the structure factor will lead to scattering at  $l = 3m$  (*i.e.* Bragg peak) positions, with an intensity given by

$$I_{(0,0,3m)}^{6\text{-fan}} \propto \left| -i \cos \theta 6\alpha \left( A_L^x + A_S^x e^{-i\pi m} \right) \right|^2. \quad (\text{A.34})$$

The second contribution to the structure factor is given by

$$F_{\text{mag}}^{6\text{-fan}(2)} = -i \cos \theta \alpha \delta(l - m/2) \sum_{p=1}^6 \left( \frac{B_L^x}{2} e^{i\phi_L^x} + \frac{B_S^x}{2} e^{-\frac{i\pi l}{3}} \right) e^{i(\mathbf{Q} + \mathbf{q}) \cdot \mathbf{r}_p} \quad (\text{A.35})$$

$$= -i \cos \theta \alpha \delta(l - m/2) \left( \frac{B_L^x}{2} e^{i\phi_L^x} + \frac{B_S^x}{2} e^{-\frac{i\pi l}{3}} \right) \sum_{p=1}^6 e^{i(\mathbf{Q} + \mathbf{q}) \cdot \mathbf{r}_p}. \quad (\text{A.36})$$

Since  $\mathbf{q} = (0, 0, 1)$ , expanding the summation will give

$$1 + e^{2\pi i \frac{(l+1)}{3}} + e^{2\pi i \frac{2(l+1)}{3}} + e^{2\pi i \frac{3(l+1)}{3}} + e^{2\pi i \frac{4(l+1)}{3}} + e^{2\pi i \frac{5(l+1)}{3}}, \quad (\text{A.37})$$

which is the same as before except that  $l$  has been replaced by  $l + 1$ . Thus this summation is zero unless  $l + 1 = 3m$ , and this will lead to intensity on the low angle side of the Bragg peaks. Therefore

$$I_{(0,0,3m-1)}^{6\text{-fan}} \propto \left| -i \cos \theta \, 6\alpha \left[ \frac{B_L^x}{2} e^{i\phi_L^x} + \frac{B_S^x}{2} e^{-\frac{i\pi(3m-1)}{3}} \right] \right|^2. \quad (\text{A.38})$$

The final contribution to the structure factor is

$$F_{\text{mag}}^{6\text{-fan}(3)} = -i \cos \theta \, \alpha \, \delta(l - m/2) \left[ \frac{B_L^x}{2} e^{-i\phi_L^x} + \frac{B_S^x}{2} e^{-\frac{i\pi l}{3}} \right] \sum_{p=1}^6 e^{i(\mathbf{Q}-\mathbf{q}) \cdot \mathbf{r}_p}, \quad (\text{A.39})$$

which will correspondingly lead to peaks at  $l - 1 = 3m$ . Therefore

$$I_{(0,0,3m+1)}^{6\text{-fan}} \propto \left| -i \cos \theta \, 6\alpha \left[ \frac{B_L^x}{2} e^{-i\phi_L^x} + \frac{B_S^x}{2} e^{-\frac{i\pi(3m+1)}{3}} \right] \right|^2. \quad (\text{A.40})$$

### A.2.2 4-fan structure

The 4-fan structure factor is

$$\begin{aligned} F_{\text{mag}}^{4\text{-fan}} = & -i \cos \theta \, \alpha \, \delta(l - m/2) \sum_{p=1}^6 \left[ C_L^x + \frac{D_L^x}{2} (e^{i\mathbf{q} \cdot \mathbf{r}_p} + e^{-i\mathbf{q} \cdot \mathbf{r}_p}) \right] e^{i\mathbf{Q} \cdot \mathbf{r}_p} \\ & - i \cos \theta \, \alpha \, \delta(l - m/2) \sum_{p=1}^6 \left[ -S_S \cos \left( \frac{\phi_4}{2} \right) \right] e^{i\mathbf{Q} \cdot \mathbf{r}_p} e^{-\frac{i\pi l}{3}}, \end{aligned} \quad (\text{A.41})$$

where now  $\mathbf{q} = (0, 0, 1.5)$ . Proceeding in a similar way to before, the first part of the structure factor is

$$F_{\text{mag}}^{4\text{-fan}(1)} = -i \cos \theta \, \alpha \, \delta(l - m/2) \left[ C_L^x - S_S \cos \left( \frac{\phi_4}{2} \right) e^{-\frac{i\pi l}{3}} \right] \sum_{p=1}^6 e^{i\mathbf{Q} \cdot \mathbf{r}_p}, \quad (\text{A.42})$$

leading to intensity at the Bragg peak positions given by

$$I_{(0,0,3m)}^{4\text{-fan}} \propto \left| -i \cos \theta \, 6\alpha \left[ C_L^x - S_S \cos \left( \frac{\phi_4}{2} \right) e^{-i\pi m} \right] \right|^2. \quad (\text{A.43})$$

The second part is

$$F_{\text{mag}}^{4\text{-fan}(2)} = -i \cos \theta \, \alpha \, \delta(l - m/2) \frac{D_L^x}{2} \sum_{p=1}^6 e^{i(\mathbf{Q}+\mathbf{q}) \cdot \mathbf{r}_p}, \quad (\text{A.44})$$

which gives intensity in the first magnetic satellite equal to

$$I_{(0,0,3m-1.5)}^{4\text{-fan}} \propto \left| -i \cos \theta \, 6\alpha \frac{D_L^x}{2} \right|^2. \quad (\text{A.45})$$

The final part is

$$F_{\text{mag}}^{4\text{-fan}(3)} = -i \cos \theta \alpha \delta(l - m/2) \frac{D_L^x}{2} \sum_{p=1}^6 e^{i(\mathbf{Q}-\mathbf{q}) \cdot \mathbf{r}_p}, \quad (\text{A.46})$$

giving an intensity in the second satellite equal to

$$I_{(0,0,3m+1.5)}^{4\text{-fan}} \propto \left| -i \cos \theta 6\alpha \frac{D_L^x}{2} \right|^2. \quad (\text{A.47})$$

### A.2.3 2-fan structure

The 2-fan structure factor is

$$F_{\text{mag}}^{2\text{-fan}} = -i \cos \theta \alpha \delta(l - m/2) \sum_{p=1}^6 \left[ S_L \cos \left( \frac{\phi_2}{2} \right) - S_S e^{-\frac{i\pi l}{3}} \right] e^{i\mathbf{Q} \cdot \mathbf{r}_p}. \quad (\text{A.48})$$

This results in intensity at the Bragg peak positions, given by

$$I_{(0,0,3m)}^{2\text{-fan}} \propto \left| -i \cos \theta 6\alpha \left[ S_L \cos \left( \frac{\phi_2}{2} \right) - S_S e^{-i\pi m} \right] \right|^2. \quad (\text{A.49})$$

---

## References

---

- [1] N. Spaldin, M. Fiebig, and M. Mostovoy, [J. Phys.: Condens. Mat.](#) **20**, 434203 (2008).
- [2] S. Blundell, *Magnetism in condensed matter* (Oxford University Press, 2001).
- [3] N. A. Spaldin, [J. Solid State Chem.](#) **195**, 2 (2012).
- [4] J. Valasek, [Phys. Rev.](#) **17**, 475 (1921).
- [5] S.-W. Cheong and M. Mostovoy, [Nat. Mater.](#) **6**, 13 (2007).
- [6] W. J. Merz, [Phys. Rev.](#) **76**, 1221 (1949).
- [7] J. Teague, R. Gerson, and W. James, [Solid State Commun.](#) **8**, 1073 (1970).
- [8] R. Seshadri and N. A. Hill, [Chem. Mater.](#) **13**, 2892 (2001).
- [9] T. Kimura, T. Goto, H. Shintani, K. Ishizaka, T. Arima, and Y. Tokura, [Nature](#) **426**, 55 (2003).
- [10] K. Yamauchi and S. Picozzi, [Phys. Rev. Lett.](#) **105**, 107202 (2010).
- [11] M. Bibes, [Nat. Mater.](#) **11**, 354 (2012).
- [12] H. Schmid, [Journal Phys.: Condens. Matter](#) **20**, 434201 (2008).
- [13] B. Van Aken, J. Rivera, H. Schmid, and M. Fiebig, [Nature](#) **449**, 702 (2007).
- [14] A. Gorbatsevich and Y. Kopaev, [Ferroelectrics](#) **161**, 321 (1994).
- [15] E. Ascher, H. Rieder, H. Schmid, and H. Stössel, [J. Appl. Phys.](#) **37**, 1404 (1966).
- [16] G. Smolenskii, V. Isupov, and A. Agranovskaya, *Sov. Phys. Solid State* **1**, 150 (1959).
- [17] H. Schmid, [Ferroelectrics](#) **162**, 317 (1994).

- [18] M. Kenzelmann, A. B. Harris, S. Jonas, C. Broholm, J. Schefer, S. B. Kim, C. L. Zhang, S.-W. Cheong, O. P. Vajk, and J. W. Lynn, [Phys. Rev. Lett.](#) **95**, 087206 (2005).
- [19] R. D. Johnson, L. C. Chapon, D. D. Khalyavin, P. Manuel, P. G. Radaelli, and C. Martin, [Phys. Rev. Lett.](#) **108**, 067201 (2012).
- [20] M. Bibes and A. Barthélémy, [Nat. Mater.](#) **7**, 425 (2008).
- [21] R. Ramesh and N. Spaldin, [Nat. Mater.](#) **6**, 21 (2007).
- [22] C. A. F. Vaz, [J. Phys.: Condens. Matter](#) **24**, 333201 (2012).
- [23] S. H. Chun, Y. S. Chai, B.-G. Jeon, H. J. Kim, Y. S. Oh, I. Kim, H. Kim, B. J. Jeon, S. Y. Haam, J.-Y. Park, S. H. Lee, J.-H. Chung, J.-H. Park, and K. H. Kim, [Phys. Rev. Lett.](#) **108**, 177201 (2012).
- [24] M. Blume, [J. Appl. Phys.](#) **57**, 3615 (1985).
- [25] F. De Bergevin and M. Brunel, [Acta Cryst. A](#) **37**, 314 (1981).
- [26] M. Blume and D. Gibbs, [Phys. Rev. B](#) **37**, 1779 (1988).
- [27] P. J. Brown, A. G. Fox, E. N. Maslen, M. A. O’Keefe, and B. T. M. Willis, [International Tables for Crystallography, Vol. C, Chapter 6.1](#) (Wiley Online Library, 2006).
- [28] J. Als-Nielsen and D. McMorrow, [Elements of modern X-ray physics \(Second Edition\)](#) (Wiley Chichester, 2011).
- [29] S. Gasiorowicz, [Quantum physics, second edition](#) (John Wiley & Sons, 2007).
- [30] J. Hill and D. McMorrow, [Acta Cryst. A](#) **52**, 236 (1996).
- [31] J. P. Hannon, G. T. Trammell, M. Blume, and D. Gibbs, [Phys. Rev. Lett.](#) **61**, 1245 (1988).
- [32] L. Landau, V. Berestetskii, E. Lifshitz, and L. Pitaevskii, [Relativistic quantum theory](#) (Pergamon Press, 1971).
- [33] J. C. Lang, D. R. Lee, D. Haskel, and G. Srajer, [J. Appl. Phys.](#) **95**, 6537 (2004).
- [34] S. Lovesey, E. Balcar, and Y. Tanaka, [J. Phys.: Condens. Matter](#) **20**, 272201 (2008).
- [35] W. R. Busing and H. A. Levy, [Acta Cryst.](#) **22**, 457 (1967).



- [36] CrysAlis PRO, Developed by Agilent Technologies Ltd., Yarnton, UK.
- [37] H. Nowell, S. A. Barnett, K. E. Christensen, S. J. Teat, and D. R. Allan, [J. Synchrotron Rad.](#) **19**, 435 (2012).
- [38] T. A. W. Beale, T. P. A. Hase, T. Iida, K. Endo, P. Steadman, A. R. Marshall, S. S. Dhesi, G. van der Laan, , and P. D. Hatton, [Rev. Sci. Instrum.](#) **81**, 073904 (2010).
- [39] G. L. Squires, *Introduction to the theory of thermal neutron scattering* (Cambridge University Press, 2012).
- [40] L. D. Barron, [J. Am. Chem. Soc.](#) **108**, 5539 (1986).
- [41] L. Barron, [Space Sci. Rev.](#) **135**, 187 (2008).
- [42] V. Simonet, M. Loire, and R. Ballou, [Eur. Phys. J. Special Topics](#) **213**, 5 (2012).
- [43] R. M. Moon, T. Riste, and W. C. Koehler, [Phys. Rev.](#) **181**, 920 (1969).
- [44] M. Blume, [Phys. Rev.](#) **130**, 1670 (1963).
- [45] S. Maleev, V. Bar'yakhtar, and R. Suris, *Sov. Phys. Solid State* **4**, 2533 (1963).
- [46] F. Tasset, [Physica B](#) **297**, 1 (2001).
- [47] F. Tasset, P. Brown, E. Lelievre-Berna, T. Roberts, S. Pujol, J. Allibon, and E. Bourgeat-Lami, [Physica B](#) **267**, 69 (1999).
- [48] F. Tasset, [Physica B](#) **156**, 627 (1989).
- [49] E. Lelivre-Berna, E. Bourgeat-Lami, P. Fouilloux, B. Geffray, Y. Gibert, K. Kakurai, N. Kernavanois, B. Longuet, F. Mantegazza, M. Nakamura, S. Pujol, L.-P. Regnault, F. Tasset, M. Takeda, M. Thomas, and X. Tonon, [Physica B](#) **356**, 131 (2005).
- [50] E. Lelivre-Berna, E. Bourgeat-Lami, Y. Gibert, N. Kernavanois, J. Locatelli, T. Mary, G. Pastrello, A. Petukhov, S. Pujol, R. Rouques, F. Thomas, M. Thomas, and F. Tasset, [Physica B](#) **356**, 141 (2005).
- [51] B. Ouladdiaf, J. Archer, G. McIntyre, A. Hewat, D. Brau, and S. York, [Physica B](#) **385**, 1052 (2006).
- [52] P. A. Franken, A. E. Hill, C. W. Peters, and G. Weinreich, [Phys. Rev. Lett.](#) **7**, 118 (1961).
- [53] M. Fiebig, V. Pavlov, and R. Pisarev, [J. Opt. Soc. Am. B](#) **22**, 96 (2005).

- [54] R. R. Birss, *Symmetry and magnetism* (North-Holland, Amsterdam, 1964).
- [55] R. F. S. Hearmon, *An introduction to applied anisotropic elasticity* (Oxford University Press, 1961).
- [56] R. L. Fork, C. V. Shank, C. Hirlimann, R. Yen, and W. J. Tomlinson, *Optics Lett.* **8**, 1 (1983).
- [57] M. Kenzelmann, A. B. Harris, A. Aharony, O. Entin-Wohlman, T. Yildirim, Q. Huang, S. Park, G. Lawes, C. Broholm, N. Rogado, R. J. Cava, K. H. Kim, G. Jorge, and A. P. Ramirez, *Phys. Rev. B* **74**, 014429 (2006).
- [58] I. A. Sergienko and E. Dagotto, *Phys. Rev. B* **73**, 094434 (2006).
- [59] H. Katsura, N. Nagaosa, and A. V. Balatsky, *Phys. Rev. Lett.* **95**, 057205 (2005).
- [60] R. D. Johnson, S. Nair, L. C. Chapon, A. Bombardi, C. Vecchini, D. Prabhakaran, A. T. Boothroyd, and P. G. Radaelli, *Phys. Rev. Lett.* **107**, 137205 (2011).
- [61] T. Inami, *J. Solid State Chem.* **180**, 2075 (2007).
- [62] A. Waśkowska, L. Gerward, J. S. Olsen, W. Morgenroth, M. Maczka, and K. Hermanowicz, *J. Phys.: Condens. Matter* **22**, 055406 (2010).
- [63] T. Inami, Y. Ajiro, and T. Goto, *J. Phys. Soc. Jpn.* **65**, 2374 (1996).
- [64] L. E. Svistov, A. I. Smirnov, L. A. Prozorova, O. A. Petrenko, L. N. Demianets, and A. Y. Shapiro, *Phys. Rev. B* **67**, 094434 (2003).
- [65] M. Kenzelmann, G. Lawes, A. Harris, G. Gasparovic, C. Broholm, A. Ramirez, G. Jorge, M. Jaime, S. Park, Q. Huang, *et al.*, *Phys. Rev. Lett.* **98**, 267205 (2007).
- [66] K. Marty, V. Simonet, E. Ressouche, R. Ballou, P. Lejay, and P. Bordet, *Phys. Rev. Lett.* **101**, 247201 (2008).
- [67] A. J. Hearmon, F. Fabrizi, L. C. Chapon, R. D. Johnson, D. Prabhakaran, S. V. Streltsov, P. J. Brown, and P. G. Radaelli, *Phys. Rev. Lett.* **108**, 237201 (2012).
- [68] T. Chatterji, *Neutron scattering from magnetic materials* (Elsevier Science Ltd, 2006).
- [69] W. Marshall and S. W. Lovesey, *Theory of thermal neutron scattering: the use of neutrons for the investigation of condensed matter* (Clarendon Press, Oxford, 1971).
- [70] P. J. Brown, A. J. Dianoux, and G. Lander, *Neutron Data Booklet (Magnetic Form Factors section)*, 2nd ed. (OCP Science, 2003).

- [71] G. Jorge, C. Capan, F. Ronning, M. Jaime, M. Kenzelmann, G. Gasparovic, C. Broholm, A. Shapiro, and L. Demianets, *Physica B* **354**, 297 (2004).
- [72] N. Kimizuka, E. Muromachni, and K. Siratori, *Handbook on the Physics and Chemistry of Rare Earths*, Vol. 13 (Elsevier Science Press, North-Holland, 1990).
- [73] J. Akimitsu, Y. Inada, K. Siratori, I. Shindo, and N. Kimizuka, *Solid State Commun.* **32**, 1065 (1979).
- [74] M. Imada, A. Fujimori, and Y. Tokura, *Rev. Mod. Phys.* **70**, 1039 (1998).
- [75] M. Subramanian, T. He, J. Chen, N. Rogado, T. Calvarese, and A. Sleight, *Adv. Mater.* **18**, 1737 (2006).
- [76] J. Y. Park, J. H. Park, Y. K. Jeong, and H. M. Janga, *Appl. Phys. Lett.* **91**, 152903 (2007).
- [77] N. Ikeda, K. Saito, K. Kohn, H. Kito, J. Akimitsu, and K. Siratori, *Ferroelectrics* **161**, 111 (1994).
- [78] W. Wang, Z. Gai, M. Chi, J. D. Fowlkes, J. Yi, L. Zhu, X. Cheng, D. J. Keavney, P. C. Snijders, T. Z. Ward, J. Shen, and X. Xu, *Phys. Rev. B* **85**, 155411 (2012).
- [79] N. Ikeda, H. Ohsumi, K. Ohwada, K. Ishii, T. Inami, K. Kakurai, Y. Murakami, K. Yoshii, S. Mori, Y. Horibe, *et al.*, *Nature* **436**, 1136 (2005).
- [80] M. Angst, R. Hermann, A. Christianson, M. Lumsden, C. Lee, M. Whangbo, J. Kim, P. Ryan, S. Nagler, W. Tian, *et al.*, *Phys. Rev. Lett.* **101**, 227601 (2008).
- [81] A. M. Mulders, S. M. Lawrence, U. Staub, M. Garcia-Fernandez, V. Scagnoli, C. Mazzoli, E. Pomjakushina, K. Conder, and Y. Wang, *Phys. Rev. Lett.* **103**, 077602 (2009).
- [82] M. Bartkowiak, A. M. Mulders, V. Scagnoli, U. Staub, E. Pomjakushina, and K. Conder, *Phys. Rev. B* **86**, 035121 (2012).
- [83] J. Wen, G. Xu, G. Gu, and S. M. Shapiro, *Phys. Rev. B* **80**, 020403 (2009).
- [84] N. Ikeda, Y. Yamada, S. Nohdo, T. Inami, and S. Katano, *Physica B* **241**, 820 (1998).
- [85] A. D. Christianson, M. D. Lumsden, M. Angst, Z. Yamani, W. Tian, R. Jin, E. A. Payzant, S. E. Nagler, B. C. Sales, and D. Mandrus, *Phys. Rev. Lett.* **100**, 107601 (2008).

- [86] A. M. Mulders, M. Bartkowiak, J. R. Hester, E. Pomjakushina, and K. Conder, [Phys. Rev. B](#) **84**, 140403 (2011).
- [87] J. Bourgeois, G. André, S. Petit, J. Robert, M. Poienar, J. Rouquette, E. Elkaim, M. Hervieu, A. Maignan, C. Martin, and F. Damay, [Phys. Rev. B](#) **86**, 024413 (2012).
- [88] Y. Matsui, [J. Appl. Crystallogr.](#) **13**, 395 (1980).
- [89] Y. Murakami, N. Abe, T. Arima, and D. Shindo, [Phys. Rev. B](#) **76**, 24109 (2007).
- [90] Y. Zhang, H. X. Yang, C. Ma, H. F. Tian, and J. Q. Li, [Phys. Rev. Lett.](#) **98**, 247602 (2007).
- [91] Y. Yamada, S. Nohdo, and N. Ikeda, [J. Phys. Soc. Jpn.](#) **66**, 3733 (1997).
- [92] K. Oka, M. Azuma, N. Hayashi, S. Muranaka, Y. Narumi, K. Kindo, S. Ayukawa, M. Kato, Y. Koike, Y. Shimakawa, *et al.*, [J. Phys. Soc. Jpn.](#) **77**, 064803 (2008).
- [93] K. Yoshii, N. Ikeda, Y. Matsuo, Y. Horibe, and S. Mori, [Phys. Rev. B](#) **76**, 024423 (2007).
- [94] K. Yoshii, N. Ikeda, T. Michiuchi, Y. Yokota, Y. Okajima, Y. Yoneda, Y. Matsuo, Y. Horibe, and S. Mori, [J. Solid State Chem.](#) **182**, 1611 (2009).
- [95] N. Ikeda, K. Kohn, H. Kito, J. Akimitsu, and K. Siratori, [J. Phys. Soc. Jpn.](#) **64**, 1371 (1995).
- [96] N. Ikeda, K. Odaka, E. Takahashi, K. Kohn, and K. Siratori, [Ferroelectrics](#) **190**, 191 (1997).
- [97] N. Ikeda, R. Mori, S. Mori, and K. Kohn, [Ferroelectrics](#) **286**, 175 (2003).
- [98] N. Ikeda, K. Kohn, N. Myouga, E. Takahashi, H. Kitôh, and S. Takekawa, [J. Phys. Soc. Jpn.](#) **69**, 1526 (2000).
- [99] C.-H. Li, X.-Q. Zhang, Z.-H. Cheng, and Y. Suna, [Appl. Phys. Lett.](#) **92**, 182903 (2008).
- [100] J. Iida, S. Kakugawa, G. Kido, Y. Nakagawa, S. Takekawa, and N. Kimizuka, [Physica B](#) **155**, 307 (1989).
- [101] M. Phan, N. Frey, M. Angst, J. De Groot, B. Sales, D. Mandrus, and H. Srikanth, [Solid State Commun.](#) **150**, 341 (2010).

- [102] X. S. Xu, M. Angst, T. V. Brinzari, R. P. Hermann, J. L. Musfeldt, A. D. Christianson, D. Mandrus, B. C. Sales, S. McGill, J.-W. Kim, and Z. Islam, [Phys. Rev. Lett.](#) **101**, 227602 (2008).
- [103] L. Chang-Hui, L. Yi, W. Fen, L. Xuan, S. Yu-Ping, Z. Xiang-Qun, C. Zhao-Hua, and S. Yang, [Chinese Phys. Lett.](#) **26**, 127501 (2009).
- [104] F. M. Vitucci, A. Nucara, C. Mirri, D. Nicoletti, M. Ortolani, U. Schade, and P. Calvani, [Phys. Rev. B](#) **84**, 153105 (2011).
- [105] C. Lee, J. Kim, S. W. Cheong, and E. J. Choi, [Phys. Rev. B](#) **85**, 014303 (2012).
- [106] S. Mori, S. Shinohara, Y. Matsuo, Y. Horibe, K. Yoshii, and N. Ikeda, [Jpn. J. Appl. Phys.](#) **47**, 7595 (2008).
- [107] M. Kishi, S. Miura, Y. Nakagawa, N. Kimizuka, I. Shindo, and K. Siratori, [J. Phys. Soc. Jpn.](#) **51**, 2801 (1982).
- [108] T. Maruyama, Y. Murakami, D. Shindo, N. Abe, and T. Arima, [Phys. Rev. B](#) **86**, 054202 (2012).
- [109] J. Bourgeois, M. Hervieu, M. Poienar, A. M. Abakumov, E. Elkaim, M. T. Sougrati, F. Porcher, F. Damay, J. Rouquette, G. Van Tendeloo, A. Maignan, J. Haines, and C. Martin, [Phys. Rev. B](#) **85**, 064102 (2012).
- [110] A. J. Hearmon, D. Prabhakaran, H. Nowell, F. Fabrizi, M. J. Gutmann, and P. G. Radaelli, [Phys. Rev. B](#) **85**, 014115 (2012).
- [111] J. Iida, M. Tanaka, Y. Nakagawa, S. Funahashi, N. Kimizuka, and S. Takekawa, [J. Phys. Soc. Jpn.](#) **62**, 1723 (1993).
- [112] K. Kato, I. Kawada, N. Kimizuka, and T. Katsura, [Z. Kristallogr.](#) **141**, 314 (1975).
- [113] A. Nagano and S. Ishihara, [J. Phys.: Condens. Matt.](#) **19**, 145263 (2007).
- [114] M. Naka, A. Nagano, and S. Ishihara, [Phys. Rev. B](#) **77**, 224441 (2008).
- [115] S.-C. Weng, Y.-R. Lee, C.-G. Chen, C.-H. Chu, Y.-L. Soo, and S.-L. Chang, [Phys. Rev. Lett.](#) **108**, 146404 (2012).
- [116] G. L. Pascut, R. Coldea, P. G. Radaelli, A. Bombardi, G. Beutier, I. I. Mazin, M. D. Johannes, and M. Jansen, [Phys. Rev. Lett.](#) **106**, 157206 (2011).
- [117] Y. Yamada, K. Kitsuda, S. Nohdo, and N. Ikeda, [Phys. Rev. B](#) **62**, 12167 (2000).

- [118] A. B. Harris and T. Yildirim, [Phys. Rev. B](#) **81**, 134417 (2010).
- [119] E. Rastelli and A. Tassi, [J. Phys. C: Solid State Phys.](#) **19**, L423 (1986).
- [120] E. Rastelli and A. Tassi, [J. Phys. C: Solid State Phys.](#) **20**, L303 (1987).
- [121] I. Brown and D. Altermatt, [Acta Cryst. B](#) **41**, 244 (1985).
- [122] D. Niermann, F. Waschkowski, J. de Groot, M. Angst, and J. Hemberger, [Phys. Rev. Lett.](#) **109**, 016405 (2012).
- [123] J. de Groot, T. Mueller, R. A. Rosenberg, D. J. Keavney, Z. Islam, J.-W. Kim, and M. Angst, [Phys. Rev. Lett.](#) **108**, 187601 (2012).
- [124] E. Gorter, [Proc. IEE-Part B: Radio and Electronic Engineering](#) **104**, 255 (1957).
- [125] U. Enz, [J. Appl. Phys.](#) **32**, 22S (1961).
- [126] H. L. Glass and F. S. Stearns, [Magnetism, IEEE Transactions](#) **13**, 1241 (1977).
- [127] Y. Kitagawa, Y. Hiraoka, T. Honda, T. Ishikura, H. Nakamura, and T. Kimura, [Nat. Mater.](#) **9**, 797 (2010).
- [128] N. Momozawa, Y. Yamaguchi, and M. Mita, [J. Phys. Soc. Jpn.](#) **55**, 1350 (1986).
- [129] S. Ishiwata, D. Okuyama, K. Kakurai, M. Nishi, Y. Taguchi, and Y. Tokura, [Phys. Rev. B](#) **81**, 174418 (2010).
- [130] S. Ishiwata, Y. Taguchi, H. Murakawa, Y. Onose, and Y. Tokura, [Science](#) **319**, 1643 (2008).
- [131] K. Taniguchi, N. Abe, S. Ohtani, H. Umetsu, and T. Arima, [Appl. Phys. Express](#) **1**, 31301 (2008).
- [132] H. Sagayama, K. Taniguchi, N. Abe, T.-h. Arima, Y. Nishikawa, S.-i. Yano, Y. Kousaka, J. Akimitsu, M. Matsuura, and K. Hirota, [Phys. Rev. B](#) **80**, 180419 (2009).
- [133] N. Kida, D. Okuyama, S. Ishiwata, Y. Taguchi, R. Shimano, K. Iwasa, T. Arima, and Y. Tokura, [Phys. Rev. B](#) **80**, 220406 (2009).
- [134] N. Momozawa, Y. Yamaguchi, H. Takei, and M. Mita, [J. Phys. Soc. Jpn.](#) **54**, 771 (1985).
- [135] N. Momozawa and Y. Yamaguchi, [J. Phys. Soc. Jpn.](#) **62**, 1292 (1993).

- [136] T. Kimura, G. Lawes, and A. Ramirez, *Phys. Rev. Lett.* **94**, 137201 (2005).
- [137] H. B. Lee, Y.-S. Song, J.-H. Chung, S. H. Chun, Y. S. Chai, K. H. Kim, M. Reehuis, K. Prokeš, and S. Mat’áš, *Phys. Rev. B* **83**, 144425 (2011).
- [138] S. H. Chun, Y. S. Chai, Y. S. Oh, D. Jaiswal-Nagar, S. Y. Haam, I. Kim, B. Lee, D. H. Nam, K.-T. Ko, J.-H. Park, J.-H. Chung, and K. H. Kim, *Phys. Rev. Lett.* **104**, 037204 (2010).
- [139] T. Asaka, X. Z. Yu, Y. Hiraoka, K. Kimoto, T. Hirayama, T. Kimura, and Y. Matsui, *Phys. Rev. B* **83**, 130401 (2011).
- [140] A. M. Mulders, S. M. Lawrence, A. J. Princep, U. Staub, Y. Bodenthin, M. García-Fernández, M. Garganourakis, J. Hester, R. Macquart, and C. D. Ling, *Phys. Rev. B* **81**, 092405 (2010).
- [141] Y. Hiraoka, Y. Tanaka, T. Kojima, Y. Takata, M. Oura, Y. Senba, H. Ohashi, Y. Wakabayashi, S. Shin, and T. Kimura, *Phys. Rev. B* **84**, 064418 (2011).
- [142] P. B. Braun, *Philips Res. Rep.* **12**, 491 (1957).
- [143] P. Novák, K. Knížek, and J. Rusz, *Phys. Rev. B* **76**, 024432 (2007).
- [144] The data points presented in this figure were provided courtesy of Dr. Tom Beale, who undertook this particular measurement.
- [145] H. Wang, P. Bencok, P. Steadman, E. Longhi, J. Zhu, and Z. Wang, *J. Synchrotron Rad.* **29**, 944 (2012).
- [146] A. C. Thompson *et al.*, *X-ray data booklet* (Lawrence Berkeley National Laboratory, University of California Berkeley, CA, 2009).
- [147] K. Knížek, P. Novak, and M. Küpferling, *Physical Review B* **73**, 153103 (2006).
- [148] D. Meier, N. Leo, G. Yuan, T. Lottermoser, M. Fiebig, P. Becker, and L. Bohatý, *Phys. Rev. B* **82**, 155112 (2010).
- [149] D. Meier, N. Leo, M. Maringer, T. Lottermoser, M. Fiebig, P. Becker, and L. Bohatý, *Phys. Rev. B* **80**, 224420 (2009).
- [150] Structure visualisation generated using Jmol: an open-source Java viewer for chemical structures in 3D, <http://www.jmol.org/>.
- [151] J. Macavei and H. Schulz, *Z. Kristallogr.* **207**, 193 (1993).

- 
- [152] A. H. Arkenbout, T. T. M. Palstra, T. Siegrist, and T. Kimura, [Phys. Rev. B](#) **74**, 184431 (2006).
  - [153] O. Heyer, N. Hollmann, I. Klassen, S. Jodlauk, L. Bohat, P. Becker, J. A. Mydosh, T. Lorenz, and D. Khomskii, [J. Phys.: Condens. Mat.](#) **18**, L471 (2006).
  - [154] A. M. Fox, *Optical properties of solids* (Oxford University Press, 2001).
  - [155] M. Pavel, I. Rychetsky, and J. Petzelt, [J. Appl. Phys.](#) **89**, 5036 (2001).